Mapping the Ancient Milky Way and its Relic Dwarf Galaxies

by

Anirudh Chiti

B.A., Cornell University (2014)

Submitted to the Department of Physics
in partial fulfillment of the requirements for the degree of

Doctor of Philosophy

at the

MASSACHUSETTS INSTITUTE OF TECHNOLOGY

June 2021

Author .....
Department of Physics
May 14, 2021

Certified by .....
Anna Frebel
Professor of Physics
Thesis Supervisor

Accepted by .....
Deepto Chakrabarty
Professor of Physics
Associate Department Head

Mapping the Ancient Milky Way and its Relic Dwarf Galaxies

by

Anirudh Chiti

Submitted to the Department of Physics
on May 14, 2021, in partial fulfillment of the
requirements for the degree of
Doctor of Philosophy

Abstract

In the first billion years after the Big Bang, the first stars and galaxies began transforming the dark, primitive universe into the rich, complex one that we observe today. These primitive objects thus govern crucial, foundational rungs in our understanding of how the universe came to be. However, little is directly known of their properties since their large distances render direct, detailed observations difficult.

Fortunately, the Milky Way hosts populations of ancient, "metal-poor" stars and satellite dwarf galaxies that function as nearby time capsules for investigations of early star formation, galaxy formation, and chemical evolution. The study of these objects is known as Galactic Archaeology, and has led to significant advances in our understanding of the first stars, supernovae, and galaxies. However, the most primitive, metal-poor stars are rare, and the difficulty of discovering them continues to bottleneck this promising approach.

In this thesis, I present several pioneering studies of the ancient stellar populations in the Milky Way including (1) a large-scale mapping of low-metallicity stars in the Galaxy, (2) first insights into the early evolution of carbon in several satellite dwarf galaxies and implications on the early assembly of the Milky Way, and (3) a detection of an extended "halo" of stars around a tiny ($\sim$3000 stars) relic galaxy; the first direct evidence that primitive galaxies formed in massive, extended dark matter halos, and that even the tiniest galaxies may have had an early merger history. These discoveries were enabled by my development of novel imaging analyses that has led to nearly an order of magnitude improvement in the efficiency of identifying the most metal-poor stars relative to traditional spectroscopic techniques. Such analyses will be readily scalable with upcoming surveys (e.g., LSST) for the next generation of Galactic Archaeology studies.

Thesis Supervisor: Anna Frebel
Title: Professor of Physics

Contents

List of Figures

List of Tables

Acknowledgments

I find that as I have come closer to the end of graduate school, the rush of job applications, research, and writing a thesis has left me with less time to sit down and reflect on the journey that has brought me to this point. I am, however, incrediby grateful for the support of everyone that has helped over the years. In my middle school graduation in 2006, I had listed that I had wanted to be a physicist when I grew up (see Figure 0-1). It was a very naive and wide-eyed statement, informed by my fascination with NOVA documentaries and popular science books in the local library. Its hard to believe that 15 years later, I am about to accomplish that goal by receiving a PhD in physics from MIT. This would have been beyond the scope of what I had thought was possible, and the journey to this point has been an immense source of gratitude, joy, and perspective. I have many people to thank.

Figure 0-1 Ani in 2006.

I will start by thanking my advisor, Anna Frebel, for playing the most important and influential role in shaping my development as a scientist over the past seven years. Anna's time, insights, and feedback on all aspects of the PhD– research, observing, writing papers and proposals, presenting at conferences– has really been a boon in helping me come into my own as an independent researcher. I am especially grateful to her for showing me (1) how to stay grounded through the inevitable ups and downs of the PhD, (2) by example, a knack for asking interesting, probing scientific questions, and (3) the value of being committed and invested in your students, and more broadly, those around you. I found large stretches of my time in graduate school, right as I was becoming an independent researcher, to be incredibly professionally satisfying. I owe a lot of this success to Anna's mentorship.

I would also like to thank my collaborators, including Josh Simon, Alexander Ji, Mohammad Mardini, Lina Necib, Rana Ezzeddine, Laura Chang, Helmut Jerjen, Dongwon Kim, and many others. I would especially like to thank: Josh for functioning as a co-advisor on several of my dwarf galaxy projects and for greatly improving my own rigor as a scientist; Alex, who was a senior graduate student in Anna's group when I joined, for convincing me to come to MIT to work with Anna and for his constant advice and support over the years; Rana, for her support and for teaching me about the assumptions and intricacies involved in deriving stellar chemical abundances; and Mohammad, for our fruitful collaboration and frequent conversations over the past year which were especially helpful during the COVID-related lockdown. I also feel incredibly lucky to have mentored and collaborated with two stellar MIT undergraduates, Kylie Hansen and Tatsuya Daniel.

I am also grateful to the other members of Anna's group that I have overlapped with, including Heather Jacobson, Brendan Griffen, Greg Dooley, Kaley Brauer, Xiaowei Ou, and Duane Lee. I especially want to thank Heather for introducing me to stellar spectral analysis when I was a first-year graduate student, Greg for introducing me to the MOSTEC program and for our many conversations in the first half of my PhD, and Duane for his support, insights on galactic chemical evolution, and for involving me in the Sidewalk Astronomy club at MIT.

I feel incredibly lucky to have overlapped with several generations of graduate students at MIT whom, along with faculty and staff, have helped make MKI feel like a second home. I enjoyed getting to know my cohort, Liang, Sherry, Ryan M, Fei, and Hang, as we navigated classes, quals, and grad school in general, and have enjoyed the quirky grad student culture of MKI (foosball, "Winston" the mouse, the nap room, among other things) with David B, Michael, Sylvia, Kaley, Nick D, Nick M, David D, Lisa, Danielle, Dhruva, Rahul, Honggeun, Ben, Calvin, Halston, Ethan, Geoffrey, Ken, Mason, Tri, Stephanie, Champ, Kaitlyn, and Chris. The older graduate students when I joined MKI (Abraham, Aaron, Jeff, Keaton, Nancy, Uchupol, Lu, Tom, David H, Reed, Ryan L) were helpful during my first few years of grad school. I especially want to thank Liang, Nancy, and Uchupol for our hang-outs, conversations and friendship at the beginning of grad school, and the entire 37-602 office (Michael, Champ, Honggeun, Stephanie) for their friendship and conversations in the latter half of my PhD. Al Levine, Mike McDonald, Deepto Chakrabarty, and Paul Schechter have been a source of advice (and telescope time) over the years, and the staff at MKI, including Jack, Ricky, Kenton, Paul, Debbie, Thea, helped everything run smoothly.

I am grateful to a number of friends and mentors over the years, and by no means is the below list comprehensive. To my research mentors in undergrad: Shami Chatterjee, Jim Cordes, Martha Haynes, Thomas Searles, and Shunrong Zhang– thank you for giving me my start in research. To my high school teachers, including but not limited to Ms. Bonnette, Mrs. Jay, Mr. Mushal, and Mrs. Ward– thank you for shaping my academic beginnings; I appreciate and remember your influence more than you may realize. To Shu– our friendship over the past 9 years has been a constant source of joy and perspective, and your clarity of thought, independence, and selflessness have been a source of guidance. To Andrew– I could not have asked for a better roommate in grad school; your companionship, conversations, and hangouts form fond memories of "growing up" together in Boston. To Priscilla, Jed, Dan, Ellis, Olivia, and Allison– thank you for adding some color to my life and showing me a different world during the PhD, whether it be at Phoenix Landing, or Bar Harbor,

Maine. To Maytee, Grace, and Jai– I will always have fond memories of Anime Boston, Sweet Kingdom, Taco Tuesdays at the Common Ground, and playing Mario Kart with water speakers; I feel lucky to have shared my mid-20s with you. To Brittany- It was fun exploring Boston with you when I first moved here. To Frances, Lucy, and Di– I likely wouldn't be in this position without your kindness and close support through my formative years; I could not have asked for better people to have shaped my personality. To Ratnika, Jyotika, and Mohnish– The last push of this thesis would have been far more difficult without your love and support, and in particular to Ratnika, I am so optimistic about our future together.

But most importantly, I would like to thank my aunt and uncle, my extended family, and our community of friends in Houston. I first came to the US to be raised by my aunt and uncle after my immediate family had passed away when I was 11 years old. The arc from that incident to where I find myself today is something that I still can't quite fathom, and I feel truly blessed when I think of the selfless love and support of everyone involved. Their actions have turned what was a potentially traumatic experience to a foundation from which I have built a life where I am happy, grounded, optimistic, and that fills me with wonder. I have learned to approach every day with a sense of gratitude and perspective. This thesis is dedicated to them, my friends & mentors, and my mother, Anupama Damera.

Chapter 1

Introduction

1.1 The Early Evolution of the Universe

Our understanding of the history of the universe is largely informed by the observation of light from stars, galaxies, and gas in the night sky. By applying basic physics to interpret this observed light, we can derive a plethora of properties of these sources, including distances, chemical compositions, intrinsic brightnesses, velocities, and so on. But most remarkably, light takes a finite amount of time to travel across space (e.g., it takes a billion years for light to traverse a distance of a billion light years). Consequentially, this implies that we can observe the state of the universe at its earliest times and map out its evolution over cosmic time, if we simply strain our ever-larger telescopes to observe the most distant sources and then observe progressively nearer sources. Most of what is discussed in this section concerns the evolution of the early universe (within ~ 1 billion years of the Big Bang), right at the point where sources become so distant, faint, and crowded by interloping nearby objects/signals that it is difficult to directly observe this epoch of the universe. However, using indirect clues and recent, precise observations[66] of the Cosmic Microwave Background– radiation from $\sim 380,000$ years after the Big Bang– we can reconstruct a broad history of the early universe. I provide a brief summary of that early history in this section.

1.1.1 Upto the Cosmic Dark Ages

We can define the beginning of our universe to be $\sim$ 13.8 billion years ago, when it began expanding from an initial state of high temperature and density. This point in time is commonly known as the "Big Bang." After this point, the universe continually expanded, cooled, and become less dense. The very earliest epochs of the universe (within a few $\sim$100,000 years after the Big Bang) are not directly observable, and thus still remain in the realm of speculation. However, multiple important events must have occurred in this time to set the initial conditions for the later epochs of the universe that we can observe. Fundamental particles (quarks, electrons, etc.) and hydrogen, helium, and trace amounts of lithium must have formed during this time. The four fundamental forces– gravity, electromagnetism, and the strong and weak nuclear forces, must have emerged and shaped the interplay of matter and radiation. All of these developments set the base initial conditions that led to the emergence of the universe that we observe today.

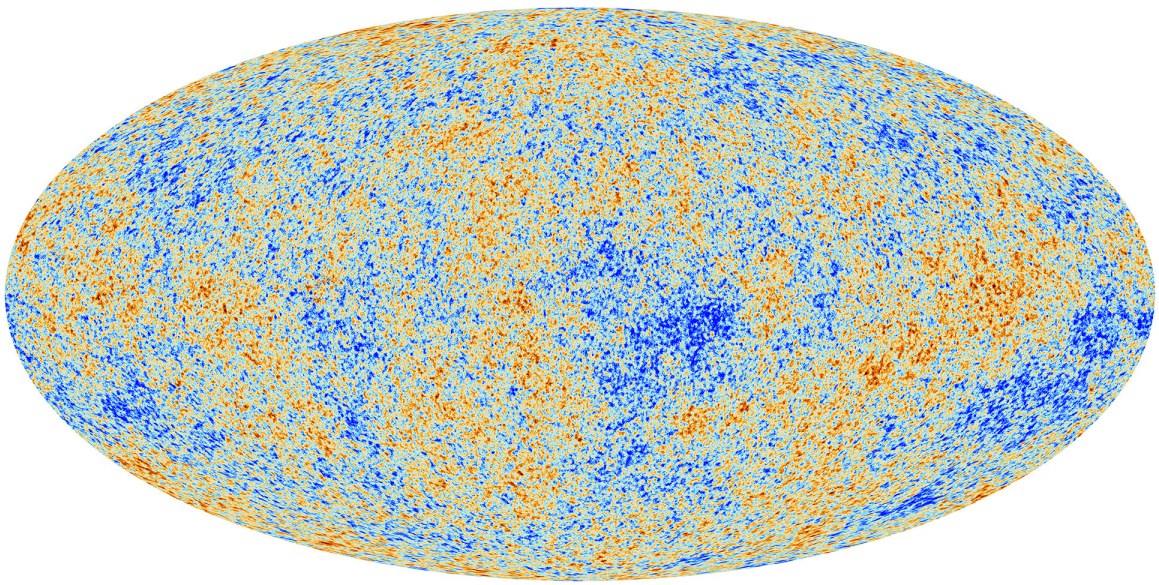

Figure 1-1 Image of the Cosmic Microwave Background– radiation from just $\sim$ $380,000$ years after the Big Bang, as imaged by the Planck mission. Credit: ESA.

Until $\sim 380,000$ years after the Big Bang, the universe would still have been too hot ($\gtrsim$3000 K) for electrons to remain bound to atoms. The interplay of free electrons with photons would have prevented light from being emitted due to a process known

as Thomson scattering, in which photons interact, "scatter" and are thus trapped by surrounding electrons. The first light we can observe from the universe was emitted when the universe became sufficient cool to allow for these free electrons to bind with protons and consequently decrease the prevalence of Thomson scattering. This initial binding of electrons to protons ∼380,000 years ago is known as the epoch of *Recombination*. We observe this first light from the Universe today as the Cosmic Microwave Background (see Figure 1-1).

The Cosmic Microwave Background (CMB) conveys a remarkable amount of information about the early universe. First, the fluctuations in the CMB are remarkably low (at the 10^{-5} level) suggesting the universe is isotropic and smooth on large scales. Second, the regions of slightly higher density in the CMB are the seeds of future structure in the universe, as these slightly over-dense regions will disproportionally continue to attract matter through gravity and thereby grow to form large galactic structures. Third, the location and relative strengths of peaks in the power spectrum of fluctuations in the CMB are sensitive to fundamental cosmological parameters, including the matter density of the universe (Ω_m), the cosmological constant (Ω_Λ), the baryon density of the universe (Ω_b), and the curvature of the universe. The exact nature of deriving these properties from the CMB is beyond the scope of this introduction, but I refer the interested reader to the paper from the Planck Collaboration on their derivation of cosmological parameters [66] and an excellent review by Max Tegmark [67].

Notably, the CMB suggests that the formation of the first galactic structures was shaped by dark matter. Dark matter is a form of matter whose only means of interaction with baryonic matter (the "regular" matter that we are familiar with) is through gravity, and forms $\sim 85\%$ of the matter in the universe. For the interested reader, Peter [68] provides an excellent review of the evidence for dark matter and our current understanding of its properties. Since dark matter only interacts with baryonic matter through gravity, it evaded interacting with photons and began "clumping" before the time of the CMB. In this way, dark matter formed gravitational potential wells that baryonic matter could settle into after the epoch of recombination. Indeed, if

these underlying clumps of dark matter did not exist at the time of recombination, then the over-densities of baryonic matter as inferred from the CMB would not have grown enough to form the galactic structures that we see today.

After recombination and the emission of the CMB, the next notable event in the universe was the formation of the first stars and galaxies several ~ 100 million years after the Big Bang. These sources are associated with the Epoch of Reionization, as the radiation emitted by these objects ionized the neutral hydrogen gas that was distributed throughout the universe. This event is known as the cosmic dawn, as the formation of these stars and galaxies in the nascent universe marks the end of the cosmic dark ages.

1.1.2 The Formation of the First Stars and Galaxies

As mentioned, the first stars and galaxies formed a few 100 million years after the Big Bang [69, 70]. There is both theoretical and observational evidence for this fact. On the observational end, galaxies hosting supermassive black holes have been observed out to a redshift $z \sim 11$ (~ 400 million years after the Big Bang) [71]. That age is therefore a hard upper bound on the time of formation of the earliest galaxies. Additionally, a direct absorption signature of the epoch of reionization was detected by Bowman et al. [72] from ~ 200 to ~ 300 million years after the Big Bang. From a more theoretical standpoint, simulations suggest that the first galaxies that could host successive generations of star formation formed around a redshift of $z \sim 10$ (~ 400 million years after the Big Bang) [73]. A timeline of the universe, including the epoch of reionization and the formation of the first stars and galaxies, is shown in Figure 1-2.

The first stars formed before the first galaxies, around redshifts of $z \sim 20$ to $z \sim 30$, in dark matter halos of mass $\sim 10^6$ solar masses [74, 75]. We note that a "galaxy" is typically defined as an object that can host multiple generations of star formation [70]. Larger halos of 10^8 solar masses can host successive generations of star formation, but the "minihalos" that hosted the formation of the first stars likely did not have enough mass to accomplish this [73]. The feedback (e.g., supernovae,

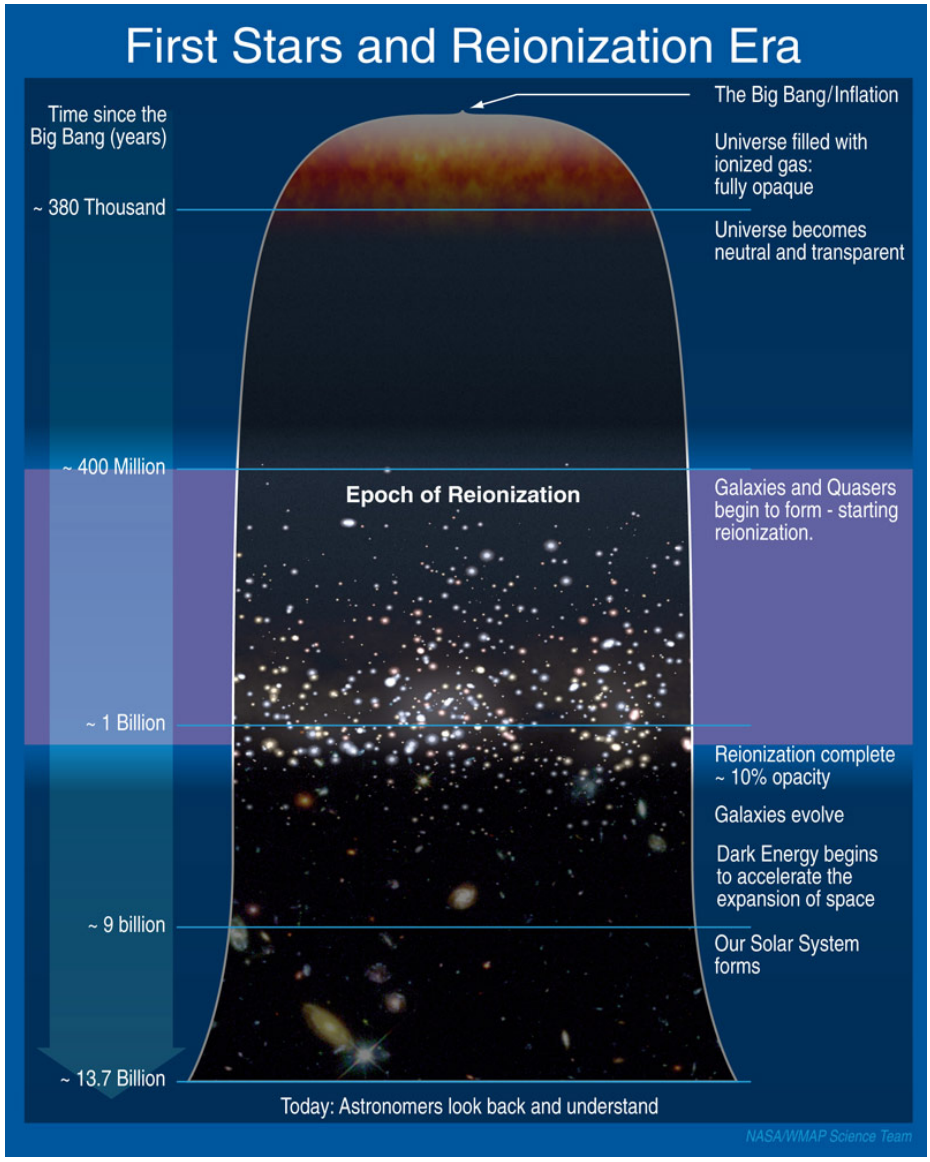

Figure 1-2 A timeline of the history of the universe, from the Big Bang to the current day. Notable points in the universe's evolution are highlighted, including the Big Bang, recombination and the emission of the CMB ($\sim 380,000$ years after the Big Bang), and Epoch of Reionization and the formation of the first stars and galaxies. Credit: NASA/Caltech

ionizing radiation) from the first stars would likely blow any remaining gas out of the tiny halos that hosted the first stars. Such feedback effects are significant, as the first stars are thought to have been massive ($\gtrsim$ 100 solar masses) due to inefficient H_2 cooling, which would have been the only molecular compound that could cool gas prior to the first stars [76]. Such large stars would exhaust their fuel early and have short lifespans, which explains why we have not yet observed any surviving "first stars" today. However, recent work has suggested that disk fragmentation effects could lead to the formation of a rarer class of low-mass first stars [77]. Regardless, it seems likely that the vast majority of the first stars were massive and their feedback effects likely blew the gas out of their tiny host minihalos. This gas would have to be re-accreted by galaxies before successive generations of star formation.

In the current paradigm of hierarchical galaxy formation, larger galaxies formed by the hierarchical merging of smaller systems (see Figure 1-3). Consequently, the minihalos that hosted the first stars merged to form larger halos that hosted the first galaxies, and the successive merging and growth of these structures led to the formation of all galactic structure that we observe today. This hierarchical assembly of galaxies is a prediction of the ΛCDM paradigm of cosmology, in which a cosmological constant Λ, "cold" dark matter, and baryonic matter are used to parametrize cosmological models of the universe. The ΛCDM paradigm has been very successful in replicating several properties of the observable universe, including the CMB, the expansion rate of the universe, and much of the large-scale distribution of mass. However, there are several tensions between ΛCDM and observations when it comes to replicating the mass distribution at smaller scales [78].

In summary, the appearance of the first stars and galaxies marks the transition from the primitive universe to one that more resembles the rich, complex system that we observe today. The first stars ushered this transformation by lighting the universe and producing the first heavy elements, and the first galaxies by assembling the first galactic structures and hosting successive generations of star formation.

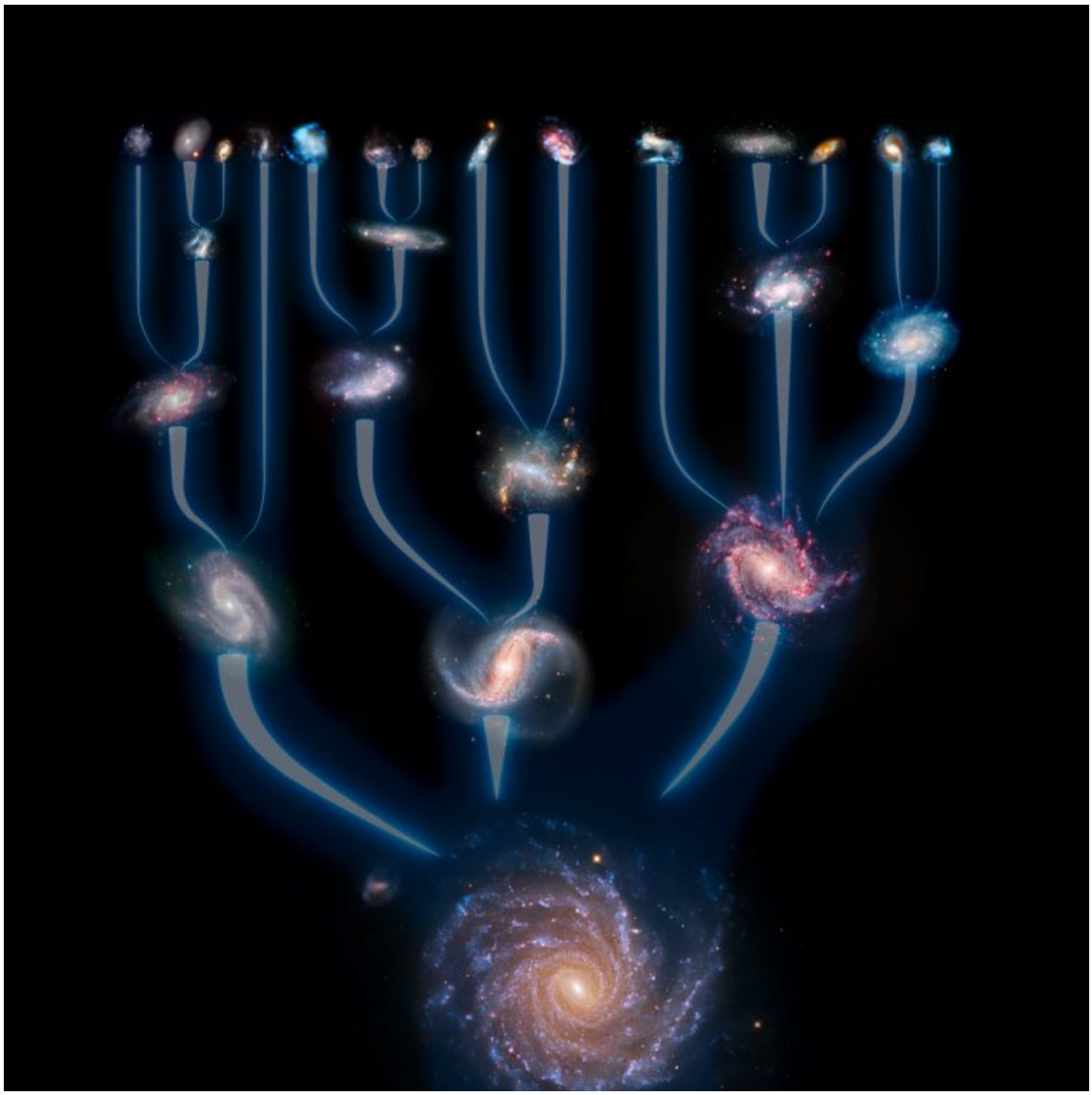

Figure 1-3 A merger tree cataloging the different galaxies that merged to form one large galaxy. At each successive step in the tree, larger galaxies are formed by the merger of smaller systems. Credit: ESA/Hubble and NASA.

1.1.3 The Drivers of Early Chemical Evolution

As previously noted, the only elements produced in the Big Bang were hydrogen, helium, and trace amounts of lithium. Successive generations of stars, supernovae, and other astrophysical events (e.g., neutron star mergers) converted these initial elements into the plethora of elements that we observe today. The astrophysical processes that lead to the formation of each element are fairly well identified, and are shown in Figure 1-4. In this subsection, I will briefly review some relevant drivers of chemical enrichment in the early universe.

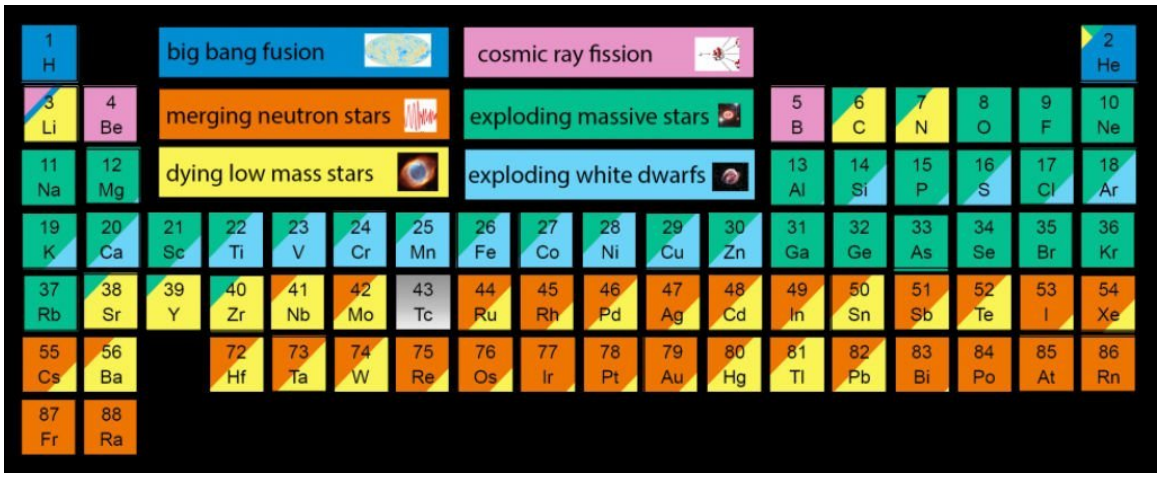

Figure 1-4 A periodic table in which the origin or each element is linked to an astrophysical source. Typically, elements lighter than iron are fused in stars, those from exploding white dwarfs are produced in Type 1a supernovae, those from neutron stars mergers are produced by the r-process, and those from dying low-mass stars are produced in the s-process. These processes are briefly detailed in Section 1.1.3. Credit: Jennifer Johnson.

The elements in the periodic table up to iron are generally fused in the cores of stars. Stars progressively fuse elements in their cores to produce light. These fusion pathways are well-known [79]. The low mass stars ($\sim$ 1 solar masses) only have sufficient density and temperature in their cores to fuse up to carbon. However, the highest mass stars are able to fuse elements up to iron. A schematic comparing the elements in the interior of a low-mass star and a high-mass star is shown in Figure 1-5. However, even the most massive stars are unable to use iron as an input to fuse heavier elements and produce energy, as iron has the largest binding energy per nucleon of

any element.

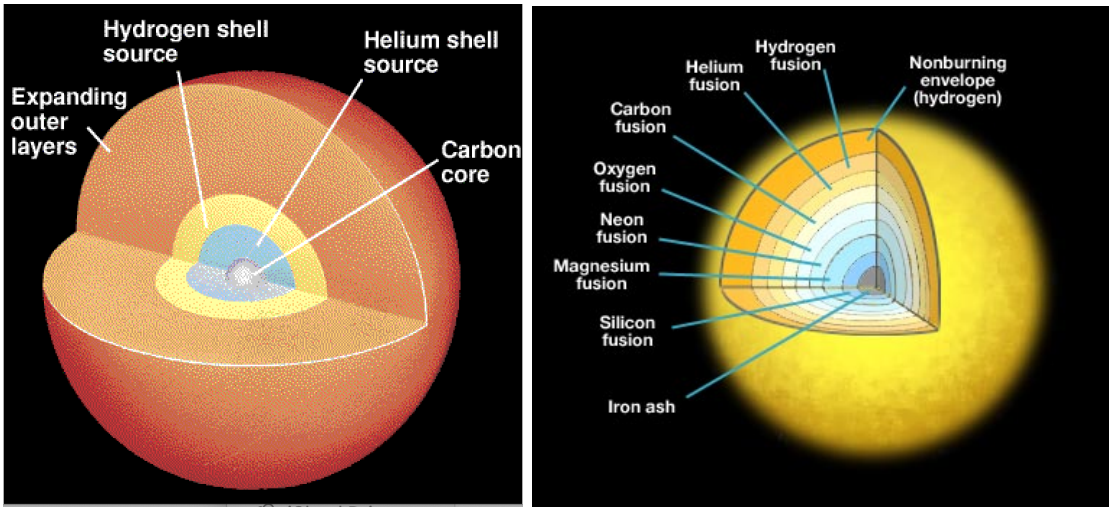

Figure 1-5 Left: Schematic of the interior of a low-mass star at the end of its life. Note that only elements up to carbon have been fused. Credit: University of Alberta Right: Schematic of the interior of a high-mass star at the end of its life. Note that elements up to iron have been fused. Credit: Penn State Astronomy & Astrophysics.

The elements heavier than iron are produced through a variety of processes, the most prominent of which are the r-process and the s-process. Both of these processes produce heavier elements through a process of neutron capture and β decay. The r and s refer to the rate of neutron capture. If atoms capture neutrons on a timescale faster than the timescale of β decay (r-process), then nuclei will accumulate a number of neutrons and then undergo decay. Otherwise, nuclei will slowly accumulate neutrons and will β decay once an unstable isotope is formed. A different set of stable elements are formed through each of these processes. The s-process is thought to occur in neutron-rich environments, such as Asymptotic Giant Branch stars (e.g., low-mass and intermediate-mass stars at the end of their life cycles)[80]. The site of the r-process has been long debated, but recent evidence suggests that neutron star mergers contribute significantly [81, 82, 83]. Although, sources beyond neutron stars mergers may be needed to explain the full pattern of r-process element abundances in the galaxy [84, 85, 86].

Another prominent site of element production is supernovae. There are a variety of classes of supernovae (Type Ia, Type Ib, Type Ic, Type II) which can be further

grouped by two main mechanisms. Type Ia supernovae occur when a white dwarf accretes mass from a companion star until its mass reaches the Chandrasekhar limit ($\sim$1.4 solar masses). At this point, a runaway explosion occurs that unbinds the white dwarf. Core Collapse Supernovae (CCSNe) occur in the rapid collapse and explosion at the end of the life cycle of a massive star ($\gtrsim$ 8 solar masses). CCSNe tend to dominate chemical evolution in the early universe, as their progenitor massive stars tend to have short lifetimes ($\lesssim$50 million years). Type Ia supernovae contribute somewhat to early chemical evolution, but generally dominate chemical evolution some time after the onset of CCSNe. This is because the progenitors of white dwarfs are low and intermediate-mass stars ($\lesssim$ 8 solar masses) that have a longer lifespan than the progenitors of CCSNe. Furthermore, there is a delay time associated with the accretion of matter onto white dwarfs until the onset of a Type Ia supernova [87]. The onset of Type Ia supernovae can actually be traced with observations of ancient stars (see Section 1.2.2) since CCSNe produce α-elements (Mg, Si, Ti, Ca) at an elevated level relative to iron ([α/Fe] = 0.4) relative to Type 1a supernovae ([α/Fe] = 0.0) [88, 89].

1.2 The Ancient Milky Way

Popular depictions of our own galaxy, the Milky Way, typically show a simple, aesthetically pleasing, blue spiral of stars (see Figure 1-6). This depiction undersells the complexity of our Galaxy's ecosystem. Notably, it excludes the extended, spherical distribution of dark matter (known as the Milky Way's dark matter "halo") which envelopes this blue spiral of stars. This vast distribution of dark matter stretches out to $\sim$ 20 times the length of the disk and accounts for $\sim$ 90% of the mass of the Milky Way. The investigation of dark matter, the mysterious substance that gravitationally binds our galaxy and comprises $\sim$ 86% percent of the matter in the universe, is an incredibly rich and intrinsically interesting area. But in this section, I will largely discuss the ancient stars, tiny galaxies, and vast stellar streams that are embedded in this extended distribution of dark matter, in addition to the other stellar components

of the Milky Way. A schematic of these objects, and the entire Milky Way ecosystem, is shown in the bottom panel of Figure 1-6.

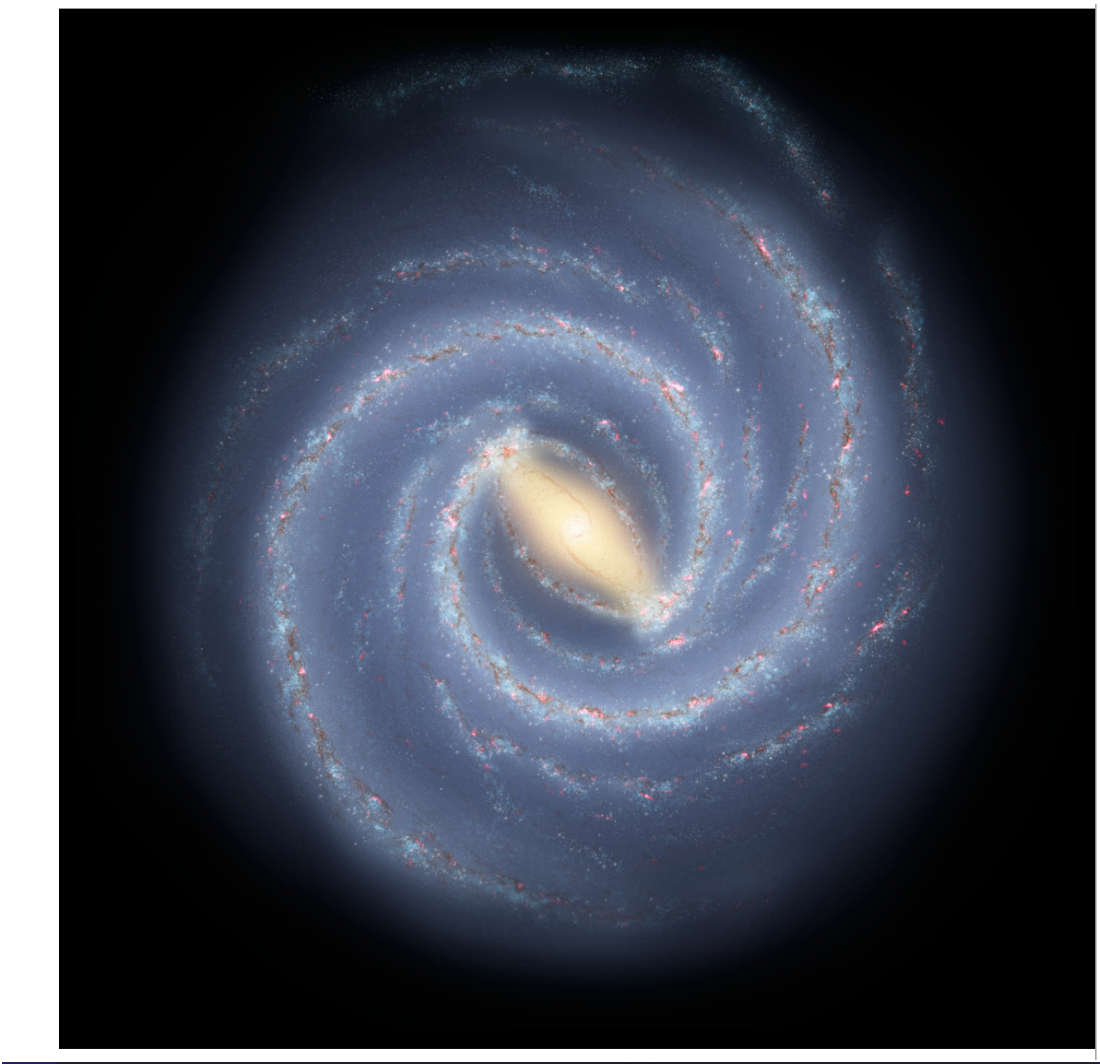

Figure 1-6 Top: Schematic of the dominant stellar components of the Milky Way: the central bulge, and the disk. Credit: NASA/JPL-Caltech/R. Hurt (SSC/Caltech). Bottom: Schematic of the entire Milky Way ecosystem, including the larger stellar halo, satellite dwarf galaxies, and globular clusters. Credit: Kaley Brauer.

1.2.1 The Structure of our Galaxy

The two most prominent stellar components of the Milky Way are the dense grouping of stars at the center of our Galaxy (aka “the Bulge"), and the blue spiral arms (aka “the Disk"). These two components comprise the overwhelming majority of the ~ 100 billion stars in our Galaxy. The Bulge is a slightly flattened spherical distribution of stars at the center of our galaxy extending out to ∼kiloparsec scales. The kinematics of these stars are likely heavily influenced by the presence of a supermassive black hole, Sgr A*, at the center of our galaxy (as manifested in the e.g., well-known $M-\sigma$ relation [90]). The Milky Way disk can be separated into two components: the thin disk and the thick disk. The thin disk extends out to a scale length of $\sim 3\,\mathrm{kpc}$ and has a scale height of $\sim 300\,\mathrm{pc}$ [91], and contains younger Population I stars as it is an active site of star formation. This is shown by the presence of young, blue stars in the thick disk that give it a characteristically blue color. The thick disk is composed of generally older stars and extends to a scale height of $\sim 1\,\mathrm{kpc}$ and roughly the same scale length as the thin disk [92]. Each of these components is scientifically interesting. The stars in the Milky Way’s Bulge have been used to e.g., calculate the mass of the Milky Way’s Supermassive Black Hole through their orbital dynamics [93]. The stars and gas in the disk have been used to trace the star formation history of the Milky Way, map the local distribution of dark matter, and constrain the formation history of our own Galaxy[94, 95, 96].

The Milky Way’s dark matter halo is studded with a population of ancient stars, dwarf galaxies, and stellar streams. The stars in the Milky Way halo comprise a sort of “cosmic junkyard,” in which stars have been deposited by galaxies that have accreted onto the Milky Way during its hierarchical assembly. As a matter of fact, we also see a number of dwarf galaxies caught in the Milky Way’s dark matter halo today, and some galaxies (e.g., the Sagittarius dwarf galaxy) show dramatic signs of being tidally ripped apart by the Milky Way. A schematic of all the known dwarf galaxies orbiting the Milky Way as of 2015 is shown in Figure 1-7. These dwarf galaxies have stellar masses ranging from a few ~ 1000 stars [37] to 10^9 stars [97]. This population of stars

and galaxies provide remarkable insights to the assembly history of the Milky Way, early chemical evolution, and the earliest galaxies, as further detailed in Sections 1.2.2 and 1.2.3.

For completeness, we also note that there are a number of star clusters in the Milky Way. These star clusters are distinct from dwarf galaxies due to their lack of dark matter. There are young, metal-rich clusters known as open clusters (few $\sim$100 stars) found near the galactic disk, and old, metal-poor globular clusters ($\sim 10^5$ stars) found near the Milky Way halo. The formation mechanism of these systems still remains a mystery, and an informative review is presented in Bastian and Lardo [98].

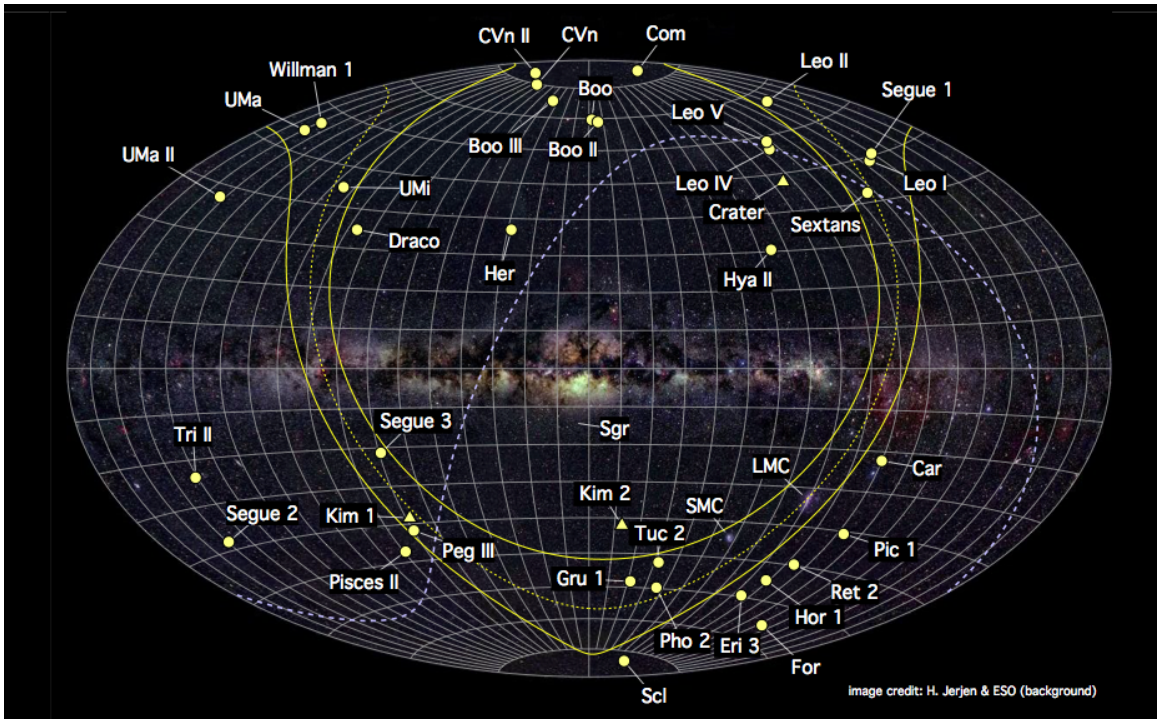

Figure 1-7 Schematic of all known Milky Way satellite galaxies as of 2015. Several dozen more have been discovered in the past 6 years. Credit: H. Jerjen & ESO.

1.2.2 Stellar Archaeology with Metal-poor stars

The chemical composition of a star's atmosphere remains unchanged throughout 90% of its life. Consequently, the stellar atmospheres of ancient, still living stars display

a chemical signature that is notably deficient in heavy elements (or "metals"). This deficiency is due to the fact that the universe continually produces heavy elements as it ages through e.g., stars, supernovae, so stars that formed at early times will reflect the chemically primitive nature of the young universe. The identification and chemical characterization of these "metal-poor" stars is a powerful, indirect technique to study the early chemical evolution of the universe, the first stars and yields from the earliest supernovae, and early star and galaxy formation processes.

Formally, we define the abundance of various elements in stars on a logarithmic scale relative to the elemental abundances in the Sun. The overall metal-content (or "metallicity") of a star is defined as $[\mathrm{Fe/H}] = \log_{10}(N_{\mathrm{Fe}}/N_{\mathrm{H}})_{\star} - \log_{10}(N_{\mathrm{Fe}}/N_{\mathrm{H}})_{\odot}$ [99], where the first term is the ratio of the number of iron to hydrogen atoms in a given star, and the second term is the number ratio of iron to hydrogen in the Sun. Formally, a metal-poor star is defined as having a relative iron abundance less than 1/10th of the Sun ($[\mathrm{Fe/H}] < -1.0$). Further classes of very, and extremely metal-poor stars have iron abundances $[\mathrm{Fe/H}] < -2.0$ and < -3.0, respectively. The bracket notation for elemental abundances can be extended to elements beyond iron (e.g., $[\mathrm{C/H}] = \log_{10}(N_{\mathrm{C}}/N_{\mathrm{H}})_{\star} - \log_{10}(N_{\mathrm{C}}/N_{\mathrm{H}})_{\odot}$). The detailed chemical abundances of extremely ($[\mathrm{Fe/H}] < -3.0$) and ultra ($[\mathrm{Fe/H}] < -4.0$) metal-poor stars are particularly useful, as these metallicity regimes indicate that a star has only been enriched by a handful of early supernovae. Consequently, the metallicity of stars maps, to first-order, to their time of formation, making the most metal-poor stars relics from the young universe. A schematic of chemical evolution is shown in Figure 1-8.

By chemically characterizing metal-poor stars in the Milky Way and its surrounding dwarf galaxies, we can learn more about the processes that drove chemical evolution. For instance, some well-known phenomena among metal-poor stars in the Milky Way halo are (1) a flat plateau of α-element (Ca, Ti, Mg, Si) abundances at low metallicities, and then a progressive trend toward lower $[\alpha/\mathrm{Fe}]$ at higher metallicities, and (2) the increasing prevalence of stars highly abundant in carbon at low metallicities. Both of these trends are shown in Figure 1-9. Trend (1) is a well-described phenomenon, in which the decreasing $[\alpha/\mathrm{Fe}]$ ratio at high metallicities indicates the

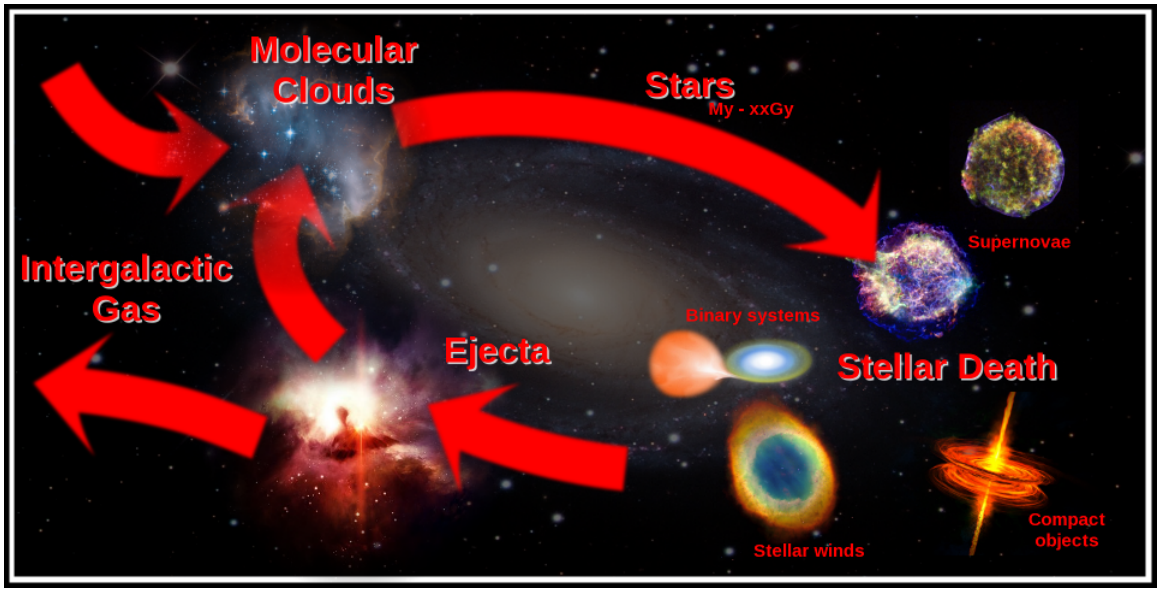

Figure 1-8 A schematic of the process by which chemical evolution continually occurs in the universe. Molecular clouds form stars, which along with their supernovae, generate heavy elements that enrich successive generations of stars. Credit: Richard Longland.

onset of Type Ia supernovae which suppresses the [α/Fe] ratio. The metallicity at which this decrease occurs can be used to e.g., gauge the efficiency of star formation in a galaxy [89]. Trend (2) indicates that the sources of chemical evolution in the early universe preferentially imprinted a carbon enhancement on stars. The exact cause of this carbon-enhancement remains debated, but faint supernovae [100] or stellar winds from rapidly rotating "spinstars" at low metallicities [101] have been proposed to explain this signature. At a more intricate level, the detailed chemical abundances of the most metal-poor stars ([Fe/H] < -4.0) can be fit with yields from a single supernova assuming progenitor mass, supernova energy, etc. are free parameters [102]. This way, the detailed chemistry of the most metal-poor stars can be used to indirectly infer the properties (e.g., initial mass functions [103]) of the first stars and the earliest supernovae.

A bottleneck of studies of the most metal-poor stars is the difficulty in identifying them, given their rarity. A fairly comprehensive summary of past efforts to identify metal-poor stars is given in Section 8.1. But some relevant numbers are that for each 1 dex decrease in metallicity, stars become roughly ~ 10 times less frequent, and

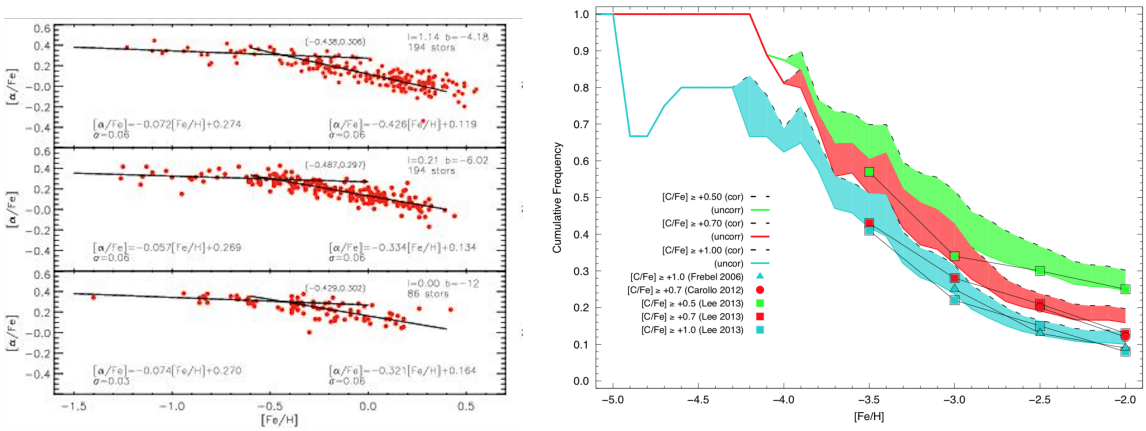

Figure 1-9 Left: [α/Fe] as a function of [Fe/H] for stars in the Milky Way Bulge. The beginning of the trend toward lower [α/Fe] indicates the onset of chemical enrichment from Type Ia supernovae. Adapted from Gonzalez et al. [7]. Right: The fraction of stars enhanced in carbon as a function of metallicity. There is a clear trend towards carbon enhancement at the lowest metallicities. Replicated from Placco et al. [8].

one star with [Fe/H] = -3.0 may be found among every 65,000 stars, and one star with [Fe/H] = -3.5 among 200,000 stars. Around 20 stars are known to have [Fe/H] < -4.0 [104].

The methodology of deriving chemical abundances of stars from spectra is outlined in many excellent textbooks (e.g., chapter 2 of Choudhuri [105]). I briefly outline the process here. The basic ingredients are a stellar spectrum, a "line list" of atomic data of spectral lines, a model stellar atmosphere, and a radiative transfer code. Individual absorption lines in stellar spectra have a line strength (quantitatively measured as a reduced equivalent width) that is a function of the intrinsic strength of the line (reflected in the atomic data), and the stellar parameters of the star (effective temperature $T_{\rm Teff}$, surface gravity $\log g$, and microturbulence $v_{\rm mic}$). The effective temperature and surface gravity of the star map to physical properties, but the microturbulence is a common input nuisance parameter for radiative transfer codes. After measuring the reduced equivalent width of each line, each reduced equivalent width is mapped to a chemical abundance using the radiative transfer code, with the atomic line data and an initial guess of stellar parameters. Then, the stellar parameters are refined

until the iron abundances[1] show no trend as a function of reduced equivalent width and line excitation potential, and the Fe I and Fe II abundances match. A final, empirical correction is applied to the effective temperature to account for a discrepancy between spectroscopically-derived temperatures and photometrically-derived temperatures, and stellar parameters are re-adjusted until the trend as a function of reduced equivalent width is removed, and the Fe I and Fe II abundances match. This full procedure is outlined in Frebel et al. [59]. A schematic of spectra of stars at different metallicities in shown in Figure 1-10.

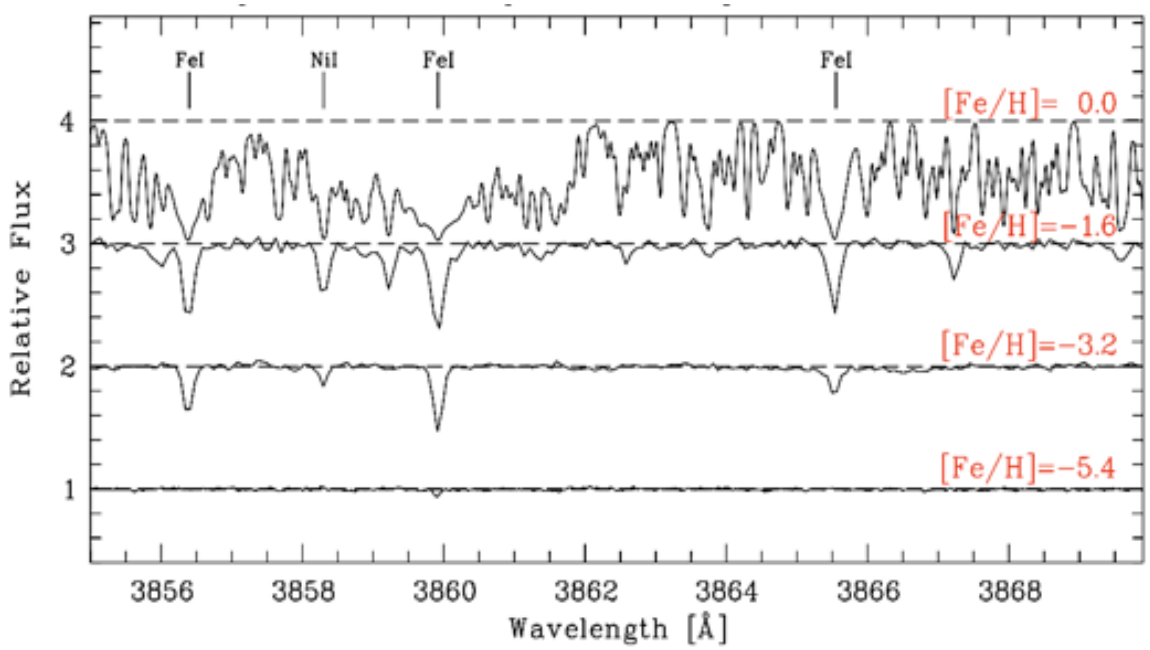

Figure 1-10 Sample spectra of stars at various metallicities. Note the systematically weaker absorption lines at lower metallicities. Credit: Anna Frebel.

1.2.3 Dwarf Galaxy Archaeology with Satellite Galaxies

The Milky Way is surrounded by dozens of dwarf galaxies. The largest of these dwarf galaxies have been known for decades (e.g., Sculptor, Sagittarius, the Magellanic Clouds). Dozens of smaller, "ultra-faint" dwarf galaxies have been discovered in the past 15 years with the advent of large-scale digital sky surveys [106, 107, 37].

[1] the iron abundance is used as the iron lines are the most ubiquitous in optical stellar spectra

These smaller, ultra-faint dwarf galaxies (UFDs) have several distinct properties. First is their remarkably low stellar mass: these systems typically have $\sim 10^3$ to $\sim 10^5$ stars. Thus, UFDs are the smallest galaxies of which we know, and provide insights to galaxy formation and evolution on the smallest scales. A corollary of their small size is that these systems may be surviving analogs of some of the earliest galaxies to have formed in the universe. Second, UFDs are the most dark-matter dominated stellar systems that we observe in the universe, with mass to light ratios approaching $M/L \sim 1000$ [91]. This makes them appealing targets for searches for indirect signatures of dark matter (e.g., annihilation signals [108]). And third, the star formation histories of UFDs indicate that they formed the bulk of their stars before reionization (e.g., Brown et al. [109]). This, coupled with the low metallicities of their stars ($\langle$[Fe/H]$\rangle < -2.0$) suggests that these galaxies are truly relics from the early universe. UFDs thus provide a nearby population of surviving early galaxies for early galaxy evolution and galaxy formation studies.

The larger, classical dwarf spheroidal galaxies are also simple, self-contained environments to study early chemical and galactic evolution. In particular, the localized nature of these dwarf galaxy environments facilitates connecting the interpretation of the chemical abundances of metal-poor stars to galactic evolution processes (e.g., star formation histories, accretion events, enrichment events). The remarkable similarities of the abundances of the most metal-poor stars ([Fe/H] < -3.0) in dwarf galaxies to Milky Way halo stars suggest some level of universality in early chemical evolution, or that the most metal-poor stars in the Milky Way halo plausibly accreted from dwarf galaxy analogs [20]. This points to the intrinsic cosmological importance of dwarf spheroidal galaxies, as the accretion of dwarf spheroidal mass galaxies are thought to have contributed the bulk of the very and extremely metal-poor stellar populations to the Milky Way halo [110]. Thus, studying the most metal-poor populations in these dwarf galaxies can provide observational tests of the assembly history of the ancient Milky Way halo.

1.3 Outline

In this thesis, I present several notable discoveries relating to the metal-poor stellar populations of the Milky Way and its satellite dwarf galaxies. These studies were facilitated by my development and implementation of novel photometric analysis techniques to identify the most metal-poor stars. These techniques, when combined with astrometry from the Gaia mission[111, 112], increased the efficiency in detecting the most metal-poor stars in dwarf galaxies by an order of magnitude relative to traditional techniques. The paper presenting these analysis techniques and applying them to the Tucana II UFD comprises Chapter 2 of this thesis.

As a result of the techniques in Chapter 2, I revealed a population of metal-poor stars at very large distances ($\sim 0.3\,\mathrm{kpc}$ to $\sim 1\,\mathrm{kpc}$; out to $\sim$9 half-light radii) from the center of Tucana II. Chapter 3 presents detailed chemical abundances from a high-resolution spectroscopic analysis of newly discovered stars out to $\sim 0.35\,\mathrm{kpc}$ from the center of Tucana II. In particular, Chapters 3.4 and 3.4.5 provide brief, but comprehensive overviews on interpreting the detailed chemical abundances of stars in the UFD context. Chapter 4 presents the kinematic confirmation and metallicities of stars out to $\sim$1 kpc ($\sim$ 9 half-light radii) from the center of Tucana II. This result is the first detection of a population of stars beyond $\sim$4 half-light radii from the center of any UFD. Intriguingly, we find that these stars appear to be bound to Tucana II; the first direct evidence that UFDs (and thus, relic early galaxies) inhabit extended, massive dark matter halos. The stars in the dark matter halo around Tucana II suggest that the system may have been shaped by an early galactic merger or strong, early supernova feedback. But more excitingly, this detection demonstrates that the stellar halos of relic galaxies are now accessible with efficient selection techniques.

Chapters 5 through 7 present the metallicities and carbon abundances of a number of very and extremely metal-poor stars in the Sculptor and Sagittarius dwarf spheroidal galaxies. These studies $\sim$tripled the known extremely metal-poor stars in Sculptor and the known very metal-poor stars in Sagittarius, allowing for robust insights on the early chemical evolution of these systems. Notably, Chapter 5 presents

a first detection of a population of carbon-enhanced metal-poor stars in any dwarf spheroidal galaxy, and suggests that the fraction of carbon-enhanced stars in Sculptor is similar to that of the Milky Way halo when [Fe/H] < -3.0. This contrasted the prior lack of known carbon-enhanced stars in dwarf spheroidal galaxies, and suggested that the carbon-enhanced population at the lowest metallicities in the Milky Way halo originated from accreted analogs of dwarf spheroidal galaxies. Interestingly, we find no such carbon-enhanced stars among the very metal-poor stars in the Sagittarius dwarf galaxy in Chapters 6 and 7.

In Chapters 8 and 9, I apply the photometric metallicity analysis techniques from Chapter 2 to the public second data release of the SkyMapper Southern Sky Survery (SkyMapper DR2) [113]. I demonstrate that these photometric metallicity techniques, when combined with Gaia EDR3 data [111, 114], can be used to derive precise metallicities of stars down to the extremely metal-poor regime. I use these techniques, along with *Gaia* EDR3 distances [115] to generate maps of the low-metallicity stellar populations of the Milky Way within $\sim 8\,\mathrm{kpc}$ in Chapter 9.

Part I

The Milky Way's dwarf galaxies

Chapter 2

Stellar metallicities from SkyMapper photometry I: A study of the Tucana II ultra-faint dwarf galaxy

The content of this chapter was published in the Astrophysical Journal as [39] in March 2020.

Abstract

We present a study of the ultra-faint Milky Way dwarf satellite galaxy Tucana II using deep photometry from the 1.3 m SkyMapper telescope at Siding Spring Observatory, Australia. The SkyMapper filter-set contains a metallicity-sensitive intermediate-band v filter covering the prominent Ca II K feature at 3933.7 Å. When combined with photometry from the SkyMapper u, g, and i filters, we demonstrate that v band photometry can be used to obtain stellar metallicities with a precision of ~ 0.20 dex when [Fe/H] > -2.5, and ~ 0.34 dex when [Fe/H] < -2.5. Since the u and v filters bracket the Balmer Jump at 3646 Å, we also find that the filter-set can be used to derive surface gravities. We thus derive photometric metallicities and surface gravities for all stars down to a magnitude of $g \sim 20$ within $\sim$75 arcminutes of Tucana II. Photometric metallicity and surface gravity cuts remove nearly all foreground contamination. By incorporating *Gaia* proper motions, we derive quantitative membership probabilities which recover all known members on the red giant branch of Tucana II. Additionally, we identify multiple likely new members in the center of the system and candidate members several half-light radii from the center of the system. Finally, we present a metallicity distribution function derived from the photometric metallicities of likely Tucana II members. This result demonstrates the utility of

wide-field imaging with the SkyMapper filter-set in studying UFDs, and in general, low surface brightness populations of metal-poor stars. Upcoming work will clarify the membership status of several distant stars identified as candidate members of Tucana II.

2.1 Introduction

The Milky Way's satellite dwarf galaxies test paradigms of the formation and evolution of the local universe. These systems are thought to be similar to those that were accreted to form the old Milky Way halo [99]. Consequently, studying the stellar content of these ancient dwarf galaxies and comparing their stars to those in the Milky Way halo can probe potential connections between the these stellar populations [e.g., 116, 20]. The relatively simple nature of dwarf galaxies also enables the modeling of their early chemical evolution [e.g., 117, 118, 119, 120] and the nature and properties of the earliest nucleosynthesis events [e.g., 82].

Of particular interest in this regard are the Milky Way's ultra-faint dwarf galaxies (UFDs). These systems have stellar populations that are old ($\gtrsim$ 10 Gyr) and metal-poor (average [Fe/H] $\lesssim -2.0$) (see Simon 121 for a review), where a metal-poor star is defined as having an iron abundance [Fe/H] ≤ -1, in which [Fe/H] $= \log_{10}(N_{\rm Fe}/N_{\rm H})_{\star} - \log_{10}(N_{\rm Fe}/N_{\rm H})_{\odot}$. Hence, UFDs are particularly interesting targets both from the perspective of chemical evolution, since they are thought to have undergone only a few cycles of chemical enrichment and star formation, and from a cosmological perspective, since at least some of them are hypothesized to be surviving first galaxies [122].

However, the faintness of UFDs makes it difficult to study their stellar population in detail. Each system has only a handful of stars that are bright enough ($V \lesssim$ 19) to obtain detailed chemical abundances. Thus, the number of foreground stars generally outnumbers the number of bright(er) UFD stars in images of the galaxy. This makes identifying UFD member stars for follow-up observations time-consuming, since stars along the giant branch in a color-magnitude diagram (CMD) must first be spectroscopically followed up with low or medium-resolution spectroscopy to measure

velocities (and metallicities) to identify true member stars. Only for those confirmed member stars it is useful to obtain reliable chemical abundances, usually from high-resolution spectroscopy.

One can principally bypass the time-intensive intermediate step of low or medium-resolution spectroscopy by deriving metallicities from photometry, since UFD stars have collectively been shown to be metal-poor ([Fe/H] $\lesssim -2.0$), and thus generally more metal-poor than foreground halo stars [123]. Indeed, Pace and Li [124] demonstrated that one can increase the efficiency in identifying member stars of UFDs by using metallicity-sensitive colors in Dark Energy Survey photometry. Deriving reliable metallicities of individual metal-poor stars from photometry is a relatively recent techique [i.e., 125], building on previous studies that demonstrated that photometry could be used to identify metal-poor stars [126]. Photometric metallicities are generally computed by using a narrow-band imaging filter that is sensitive to the overall metallicity of the star due to the presence of a prominent metal absorption feature (i.e., the Ca II K line) within the bandpass of the filter [e.g., 127, 125, 128]. Photometry has the additional benefit of being able to provide information on all stars within the field of view of the camera, whereas in spectroscopy, one is limited by e.g., slit arrangements, number of fibers, or pixels in the CCD mosaic.

The SkyMapper Southern Sky Survey [127, 9] pioneered the search for metal-poor stars using a filter set that contains an intermediate-band ~ 300 Å wide v filter that encompasses the Ca II K line within its bandpass, making the flux through the v filter dependent on the overall stellar metallicity. This narrow-band v filter has already been used to identify a number of extremely metal-poor stars and several stars with [Fe/H] < -6 [129, 3, 130]. Recent work from the Pristine Survey [125], which uses a narrow-band filter centered on the Ca II K line at 3933.7 Å to obtain photometric metallicities, has been successful in applying this technique to find halo metal-poor stars [e.g., 131, 132] and also study UFDs to derive their metallicity distribution functions [133, 134].

A goal of this paper is to demonstrate that the SkyMapper filter set [135] can be used to chemically characterize UFDs via photometric measurements of stellar param-

eters. Besides metallicities from the v filter, the relative flux through the SkyMapper u and v filters is sensitive to the surface gravity ($\log g$) of stars since those filters surround the Balmer Jump at 3646 Å [e.g., 136]. The $\log g$ of stars is of additional use as a discriminant when studying UFDs, since their member stars that are bright enough for spectroscopy are generally on the red giant branch (RGB) and should thus have low surface gravities. We note that we do not analyze horizontal branch stars in this study, as it is difficult to discriminate their metallicities due to their relatively high effective temperatures. Given this difficulty in discriminating metallicities, photometry with higher precision than the data presented in this paper would be required to derive photometric metallicities for stars on the horizontal branch of Tucana II (g$\sim$19.2).

The Tucana II UFD was discovered in the Dark Energy Survey [13, 37]. Tucana II is relatively nearby (57 kpc) and has a half-light radius of 9.83′ [13]. It was confirmed as a UFD by Walker et al. [1], who measured a large velocity dispersion ($\sigma_{\rm v_{los}} = 8.6\,{\rm km\,s^{-1}}$), a low mean metallicity of $\langle$[Fe/H]$\rangle = -2.23$, and identified eight stars as probable members. Ji et al. [2] and later Chiti et al. [12] presented chemical abundances from high-resolution spectroscopy of seven stars in Tucana II. Interestingly, two of the stars from the Chiti et al. [12] sample were new member stars that were approximately two half-light radii from the center of Tucana II. These stars were originally selected for spectroscopic follow-up based on the SkyMapper photometry described here. If not for these data, they would likely have been missed by traditional low or medium resolution spectroscopic selection techniques.

We obtained deep images (down to $g \sim 22$) of the Tucana II UFD using the u, v, g, and i filters on the 1.3 m SkyMapper telescope to demonstrate that we can 1) use the photometry to efficiently identify bright members for follow-up high resolution spectroscopy, and 2) use the photometric metallicities of the member stars to derive a metallicity distribution function (MDF) of dwarf galaxies. Since UFD members should have similar proper motions, we also use *Gaia* DR2 proper motion data [111, 112] to further improve our selection of likely members. As shown in e.g., Pace and Li [124] and Chiti and Frebel [137], *Gaia* proper motion data is especially useful in

removing foreground contaminants when studying dwarf galaxy member stars.

The paper is arranged as follows. In Section 2.2, we discuss the observations, data reduction procedure, and precision and depth of our photometry; in Section 2.3, we discuss generating a grid of synthetic photometry which we later use to derive stellar parameters; in Section 2.4, we outline our derivation of photometric metallicities and photometric $\log g$ values, and discuss our sources of uncertainty; in Section 2.5, we speculate on properties of Tucana II (i.e., the MDF) from our analysis; in Section 2.6, we summarize our results.

2.2 Observations & Data Reduction

2.2.1 Photometry

Observations of the Tucana II UFD were taken between July 19, 2015 and December 15, 2015 with the 1.35 m SkyMapper telescope at Siding Springs Observatory, Australia, as part of an auxillary program to obtain deep photometry of UFDs. Table 2.1 summarizes our photometric observations. The SkyMapper camera has 32 4k×2k CCD chips covering a 2.34° by 2.40° field of view, which enabled the imaging of the entire Tucana II UFD [$r_{1/2} \sim 10'$; 13, 37] in each frame. Images were taken with the custom SkyMapper u, v, g, and i filters [135].

We developed a data reduction pipeline for these data separately from the one used by the SkyMapper collaboration [9], since no pipeline existed when the data for this project were collected in late 2015. The reduction procedure for SkyMapper data is not trivial due to the presence of systematic pattern-noise signatures in the raw data that, if not properly removed, would impair any photometric measurements, as can be seen in Figure 2-1. We therefore explicitly outline each step of our data reduction procedure in Section 2.2.1.1 and describe our handling of the pattern-noise removal process in Section 2.2.1.2. We then discuss the precision and completeness of our photometry in Section 2.2.1.3.

2.2.1.1 Data Reduction

Data reduction was mostly performed following standard procedures [138] using python scripts that utilized the `astropy` package [139]. Bias-subtraction was done on a row-by-row basis using the overscan region that was 50 pixels wide. Flat-field corrections were applied using master flat-field frames that were generated for each filter on each night data was taken. Each master flat-field frame was generated by median-filtering 5 to 10 individual frames. We note that we used the master flat-field frames from July 20, 2015 for the u and v data on July 26, 2015, since an insufficient number of individual flat-field frames were obtained for those filters on that date.

Then, we derived astrometric solutions for each frame following a two-step procedure. First, an estimate of the astrometric solutions was computed using `astrometry-net` [140]. These astrometric solutions were subsequently corrected with SCAMP [141].

We derived photometric zero-point corrections for each of our exposures by comparing our measured instrumental magnitudes to calibrated magnitudes in the public SkyMapper DR1.1 catalog (released on December 2017) that were derived with the analysis pipeline used by the SkyMapper collaboration [9]. We first compiled source catalogs for each of our exposures using the default configuration of the Source Extractor program [142] except for the following parameters to ensure appropriate background subtraction: `BACKPHOTO_TYPE=LOCAL`, `BACKSIZE=100,100`, and `BACKPHOTO_THICK=10`. Then, for each exposure, we cross-matched our source catalog to the public SkyMapper DR1.1 catalog and derived a zeropoint offset for our magnitudes by taking the weighted average of the difference between our measured instrumental magnitudes and those in the SkyMapper DR1.1 catalog. To improve the precision of our measured offsets, we only compared the magnitudes of unblended stars brighter than 16th magnitude, and compared our aperture photometry, based on the MAG_AUTO keyword in Source Extractor, to the aperture photometry in the SkyMapper catalog, denoted by the *_petro* flag.

Since each of the 32 CCD chips of the SkyMapper camera have slightly different sensitivities, we needed to apply additional photometric zeropoint corrections for data

taken with each of the 64 readout amplifiers. We derived these offsets by first applying the overall zeropoint offsets computed for each exposure and combining the source catalogs from each night. We then repeated the procedure outlined in the previous paragraph, except we computed the residual zeropoint offset for sources on each of the 64 readout amplifiers.

For each night, our images were then stacked by sigma-clipping 5σ outliers to remove cosmic rays after incorporating the above magnitude zeropoint corrections using the SWARP package [143]. Then, a final mosaic was generated by stacking the nightly images following the aforementioned procedure. Final source catalogs were computed with Source Extractor package with the same configuration as used in deriving initial catalogs for the zeropoint calibration. All the magnitudes reported in this paper are from the MAG_AUTO keyword in Source Extractor, which are magnitudes obtained with elliptical apertures. We opted not to use magnitudes derived from fitting a point spread function (PSF) of the images as the PSF appeared to not be stable over the full field of view of the SkyMapper images. Our final source catalogs were de-reddening following Wolf et al. [9], based on reddening maps from Schlegel et al. [144]. An additional zero-point correction was applied to the u and v magnitudes following equations 4 and 5 in Casagrande et al. [145] to account for a reddening overcorrection for sources close to the Galactic plane.

2.2.1.2 Pattern-Noise Removal

Before deriving the astrometric solution, we had to remove pattern-noise signatures that were imprinted on each image. This issue is illustrated in the left panel of Figure 2-1. These signatures are composed of a high-frequency interference pattern and low-frequency waves with row-dependent zeropoint offsets. These pattern-noise signatures changed between exposures and between each of the 64 readout amplifiers.

We performed the following steps to remove the pattern-noise after bias subtraction and flat-field correction. To remove the low-frequency components of this signature, a 5th order polynomial was iteratively fit to each row of data from each readout amplifier after sigma-clipping outliers 2σ above the fit and 3σ below the fit.

After this process, the high-frequency interference pattern was found to be identical across all CCD chips of a given image, after accounting for the orientation of each chip. Consequently, we aligned the orientation of each CCD chip and median-filtered the data from two sets of 32 amplifiers to obtain two templates of the high-frequency signature. Each template was then fit, using a scaling factor and a zero-point offset as free parameters, to the appropriate readout amplifier and subtracted to remove the high-frequency pattern. Figure 2-1 shows a comparison of images before and after pattern noise removal. Visually, the dominant systematic patterns appear to be removed. Quantitatively, the standard deviation of the values of the background pixels drops by ∼30% after our pattern noise removal procedure.

2.2.1.3 Completeness & Photometric Precision

We measure the completeness of our SkyMapper source catalog by comparing the number of stars in the DES Y1A1 gold catalog [146] and in our catalog within $60'$ of the center of Tucana II. We first convert the g_{DES} magnitudes to SkyMapper $g_{\rm SM}$ magnitudes using the following formula, which we derive by fitting a polynomial to our SkyMapper photometry using magnitudes from the DES Y1A1 gold catalog as independent variables: $g_{\rm SM} = 0.983 \times g_{\rm DES} - 0.144 \times (g_{\rm DES} - i_{\rm DES}) + 0.431$. We find that the cumulative 95% completeness limits correspond to the following SkyMapper magnitude limits: $g_{\rm SM} = 22.3$ for the SkyMapper g filter, $g_{\rm SM} = 22.1$ for the SkyMapper i filter, $g_{\rm SM} = 20.8$ for the SkyMapper v filter, and $g_{\rm SM} = 20.1$ for the SkyMapper u filter. We further find that the typical uncertainty in our photometry, as reported by `magerr_auto` in Source Extractor, reaches 0.05 mags at the following DES magnitudes: $g_{\rm SM} \sim 22.0$ for the SkyMapper g filter, $g_{\rm SM} \sim 21.6$ for the SkyMapper i filter, $g_{\rm SM} \sim 19.6$ for the SkyMapper v filter, and $g_{\rm SM} \sim 19.2$ for the SkyMapper u filter.

As an additional check that our photometry is well-characterized, we compared the magnitudes derived from our pipeline to those in SkyMapper DR1.1 for stars in common between the two catalogs. We find that the residuals between our magnitudes and those in SkyMapper DR1.1 are distributed as gaussians, therefore implying that our photometry is well-behaved with respect to the public SkyMapper data. The

Table 2.1. Photometric Observations of Tucana II

Date	filter	Exposure time (s)
2015 Jul 19	u	24×300
2015 Jul 20	u	21×300
2015 Jul 26	u	9×300
2015 Aug 09	u	20×300
2015 Aug 10	u	15×300
2015 Jul 19	v	24×300
2015 Jul 20	v	20×300
2015 Jul 26	v	5×300
2015 Aug 09	v	22×300
2015 Aug 10	v	16×300
2015 Aug 09	g	4×300
2015 Dec 02	g	4×300
2015 Dec 03	g	4×300
2015 Dec 07	g	4×300
2015 Dec 13	g	4×300
2015 Dec 14	g	4×300
2015 Dec 02	i	8×300

standard deviation in the residuals reaches 0.05 mags for $g_{\rm SM}$ magnitudes when $g_{\rm SM} \sim 15.8$, $i_{\rm SM}$ magnitudes when $i_{\rm SM} \sim 15.5$, $v_{\rm SM}$ magnitudes when $v_{\rm SM} \sim 15.4$, and $u_{\rm SM}$ magnitudes when $u_{\rm SM} \sim 15.8$. We note that the scatter is driven by the uncertainty in the SkyMapper DR1.1 catalog, as our photometry is substantially deeper.

2.3 Grid of synthetic photometry

We generated a grid of flux-calibrated, synthetic spectra over a range of stellar parameters and metallicities specifically covering that expected for red giant branch (RGB) and main sequence turn off (MSTO) stars in Tucana II and the Milky Way halo. The stellar parameters of this grid are given in Table 2.2. We then computed the expected flux through each of the SkyMapper filters from these synthetic spectra.

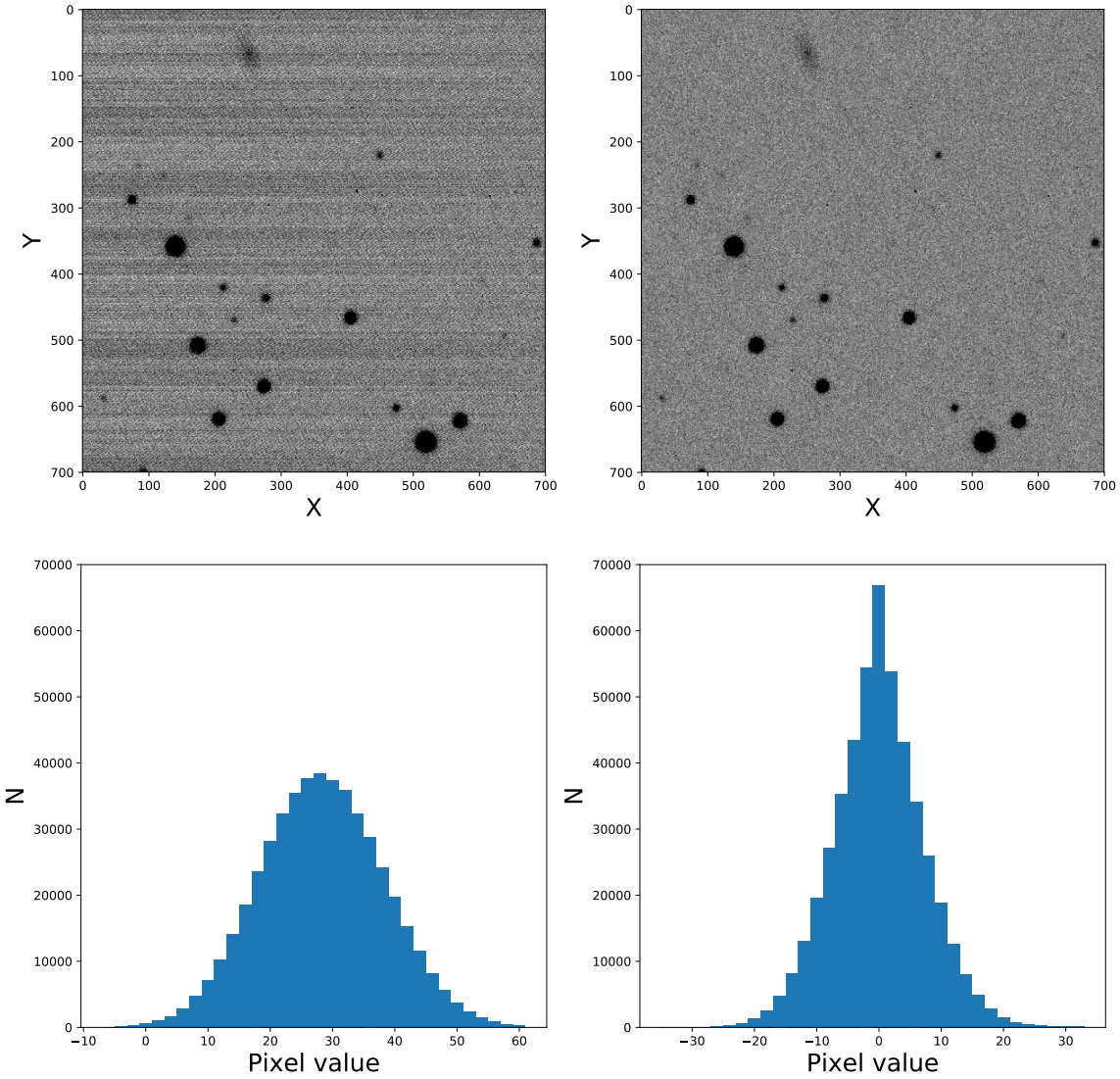

Figure 2-1 Top: Comparison of a portion of an image immediately before (left) and after (right) pattern noise removal (see Section 2.2.1.2). Bottom: A histogram of pixel values in each image before pattern noise removal (left) and after removal (right). After pattern-noise removal, the standard deviation of the values of the pixels in this image is ∼7 counts. This spread agrees with the range of readout noises reported for the SkyMapper readout amplifiers in Wolf et al. [9].

Table 2.2. Stellar parameters of grids of synthetic spectra

Parameter	Minimum	Maximum	Step
	RGB Grid		
λ	3000 Å	9000 Å	0.01 Å
$T_{\rm eff}$	4000 K	5700 K	100 K
$\log g$	1.0	3.0	0.5
[Fe/H]	−4.0	−0.5	0.5
	MSTO Grid		
λ	3000 Å	9000 Å	0.01 Å
$T_{\rm eff}$	5600 K	6700 K	100 K
$\log g$	3.0	5.0	0.5
[Fe/H]	−4.0	−0.5	0.5

2.3.1 Generating synthetic spectra

We used the Turbospectrum synthesis code [147, 148], MARCS model atmospheres [149], and a linelist composed of all lines between 3000 Å to 9000 Å available in the VALD database [150, 151] to generate our grid of flux-calibrated synthetic spectra. We replaced the lines of the CN molecule in the VALD line list with those from Brooke et al. [152] and Sneden et al. [153], those of CH with lines from Masseron et al. [53] and Brooke et al. [154], and those of C_2 with lines from Ram et al. [155]. This resulted in a linelist with $\sim 800,000$ lines. An example of two synthetic spectra with different metallicities is shown in Figure 2-2. The $^{12}C/^{13}C$ isotope ratio was assumed following the relation presented in Kirby et al. [4], which is based on figure 4 in Keller et al. [156]. We note that solar abundances for the MARCS model atmospheres are adopted from Grevesse et al. [157].

For the analysis of RGB stars, we generated a grid of spectra with stellar parameters ranging from $T_{\rm eff} = 4000$ K to 5700 K, $\log g = 1.0$ to 3.0, and [Fe/H] $= -4.0$ to -0.5. We opted to use the "standard" spherical model geometry within the MARCS model atmospheres. We used a microturbulence of $2\,{\rm km\,s^{-1}}$. The α-enhancement was set to $[\alpha/{\rm Fe}] = 0.4$ for stars with [Fe/H] < -1.0, and linearly decreased between $-1 <$ [Fe/H] < 0 such that $[\alpha/{\rm Fe}] = 0$ when [Fe/H] $= 0$.

For the analysis of MSTO stars, we generated a grid of spectra with stellar parameters ranging from $T_{\rm eff} = 5600\,{\rm K}$ to $6700\,{\rm K}$, $\log g = 3.0$ to 5.0, and [Fe/H] $= -4.0$ to -0.5. We opted to use plane-parallel model geometries as part of the MARCS model atmospheres, and used the same microturbulence value and [α/Fe] trends as for the RGB grid.

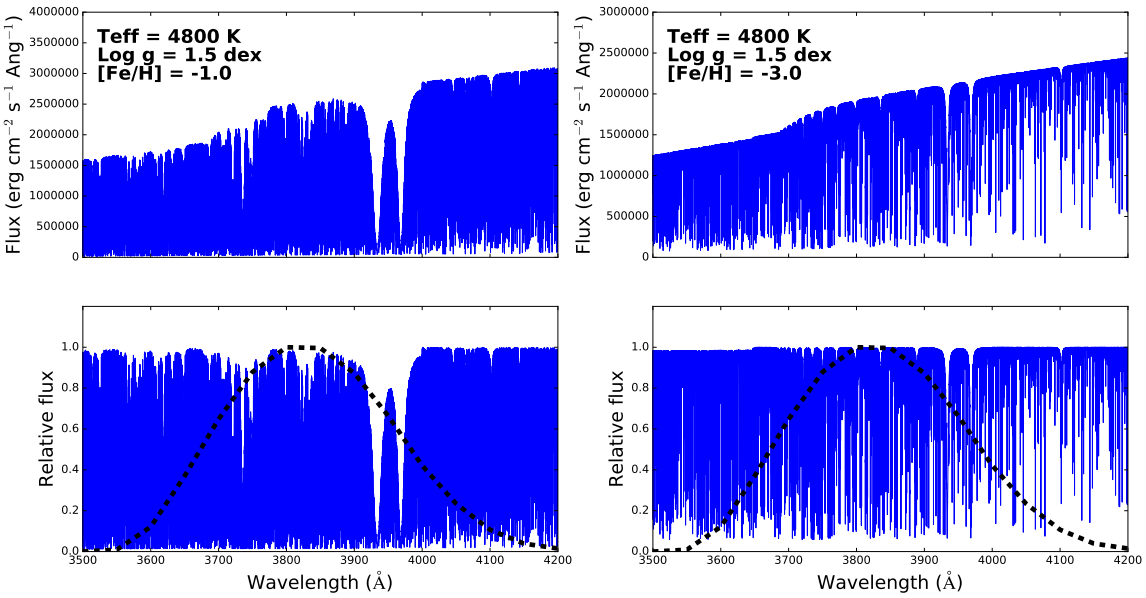

Figure 2-2 Top: Flux-calibrated synthetic spectra for two stars with the same stellar parameters, but different metallicities. Bottom: Normalized synthetic spectra for the same two stars, with the bandpass of the SkyMapper v filter overplotted as a dashed line. The strength of the Ca II K line measurably affects the flux through the v filter. The CN absorption feature at 3870 Å is also sufficiently prominent to affect the flux through the filter, and its impact on the measured photometric metallicity is discussed in Section 2.4.3.

2.3.2 Generating synthetic photometry

For each synthetic spectrum, we calculated the absolute magnitude from the flux through each of the SkyMapper u, v, g, and i filters. First, we retrieved the bandpasses of each of the SkyMapper filters [135] from the Spanish Virtual Observatory (SVO) Filter Profile Service [158][1]. We then closely followed the methodology in Casagrande and VandenBerg [159] to generate synthetic magnitudes for each of our synthetic

[1] http://svo2.cab.inta-csic.es/svo/theory/fps3/

spectra. We computed synthetic AB magnitudes, in which a flux density of $F_\nu = 3.63 \times 10^{-20}\,\mathrm{erg\,cm^{-2}\,s^{-1}\,Hz^{-1}}$ is defined as having $\mathrm{m_{AB}} = 0$, through each filter by applying the following formula

$$m_{\mathrm{AB}} = -2.5 \log \frac{\int_{\nu_i}^{\nu_f} \nu^{-1}\, F_\nu\, T_\eta\, d\nu}{\int_{\nu_i}^{\nu_f} \nu^{-1}\, T_\eta\, d\nu} - 48.60 \tag{2.1}$$

where F_ν is the flux from a flux-calibrated synthetic spectrum as a function of wavelength, T_η is the system response function over the bandpass of the filter, and ν_i and ν_f are the lowest and highest wavelengths of the bandpass filter. We note that small zero point offsets on the order of ~ 0.02 are possible in this formalism, as briefly mentioned in Casagrande and VandenBerg [159]. We, however, find that we need to apply an a zero-point correction of $+0.06$ mags to our synthetic v magnitudes to derive accurate metallicities, as described in the second to last paragraph of Section 2.4.4.

2.4 Analysis

One aim of this study is to demonstrate that SkyMapper photometry can be used to derive stellar parameters and metallicities to ultimately derive a metallicity distribution function for the Tucana II UFD. For that purpose, it is necessary to carefully characterize the sources of uncertainty in our photometric metallicities. Therefore, we first describe our methodology in measuring photometric metallicities and surface gravities in Sections 2.4.1 and 2.4.2. Then, in Sections 2.4.3 through Section 2.4.6, we attempt to quantify the impact of (strong) carbon molecular features within the bandpass of the v filter on our photometric metallicities, and compare our photometric metallicities to available spectroscopic metallicities in the literature.

2.4.1 Measuring metallicities from photometry

The SkyMapper v filter has been designed to be sensitive to stellar metallicity [e.g., 127]. This sensitivity arises from the presence of the strongest metal absorption line,

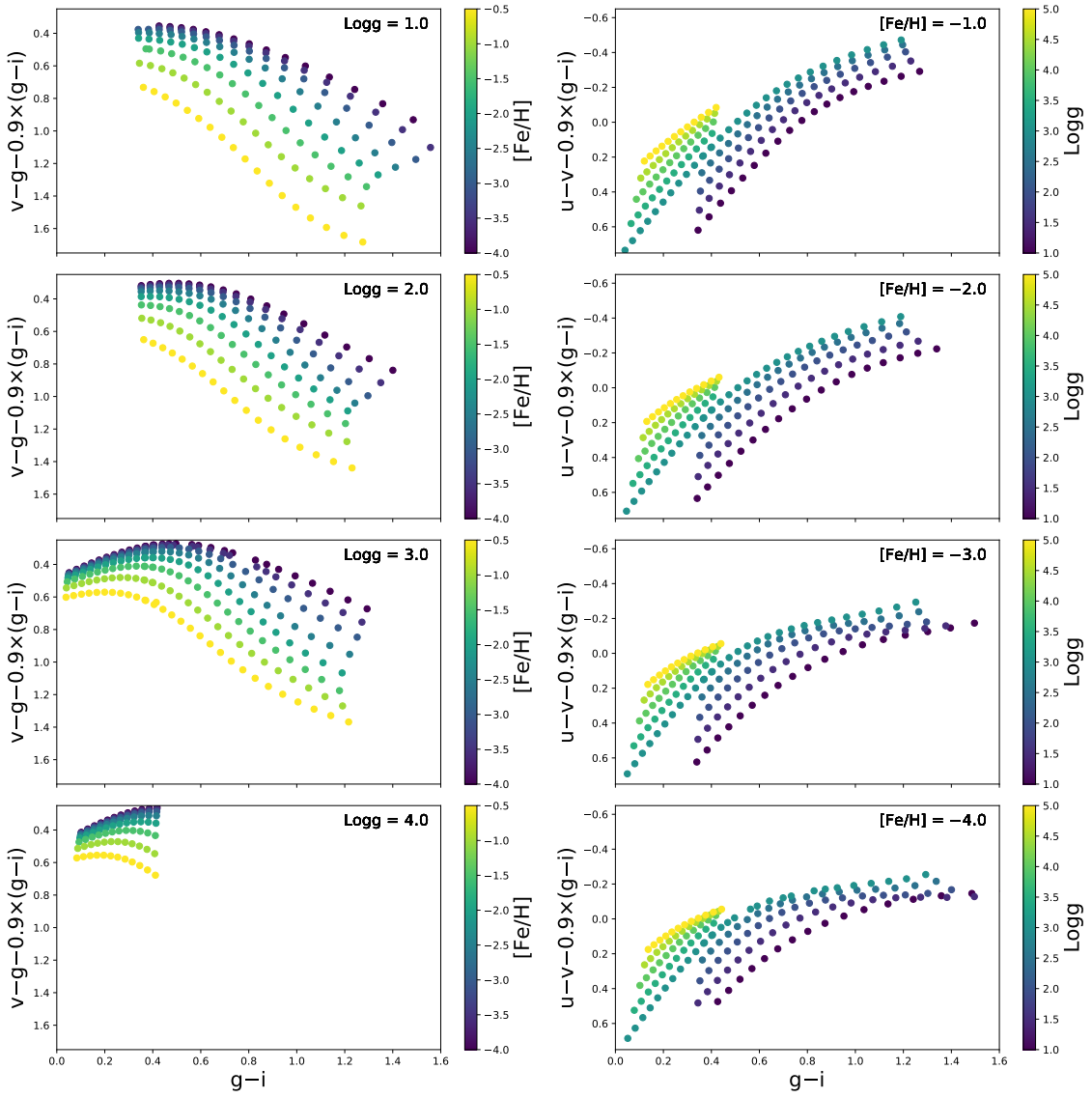

Figure 2-3 Left: Contours used to measure photometric metallicities from the SkyMapper photometry for several log g values. Right: Contours used to measure photometric surface gravities from SkyMapper photometry for several [Fe/H] values.

Ca II K, at 3933.7 Å in the bandpass. Since the strength of the Ca II K line scales with the overall metallicity of the star, the overall flux measured through the filter is thus governed by the stellar metallicity. An example is illustrated in Figure 2-2, where synthetic spectra of stars with [Fe/H] $= -1.0$ and -3.0 are juxtaposed, and the bandpass of the v filter is overplotted.

Making use of the relation between Ca II K absorption and metallicity, previous work by Keller et al. [160] suggested that metal-poor stars can be discriminated from metal-rich ones in the $v - g - 2 \times (g - i)$ vs. $g - i$ space. Inspired by this, we instead choose to utilize $v - g - 0.9 \times (g - i)$ vs. $g - i$ as a discriminator, which we have already successfully used to identify metal-poor dwarf galaxy stars using our custom SkyMapper data and SkyMapper DR1.1 [12, 137].

As part of this work, we plotted $v - g - 0.9 \times (g - i)$ vs. $g - i$ of the photometry from the synthetic spectra (described in Section 2.3) on the left panels of Figure 2-3. We did so for four different $\log g$ values, from 1 to 4. As can be seen, stars of a given metallicity form well-behaved contours allowing us to easily interpolate between these contours to derive quantifiable stellar metallicities. Hence, we interpolated between these metallicity contours with a piecewise 2d cubic spline interpolator using the `scipy.interpolate.griddata` function, and thereby derived photometric metallicities for every star with v, g, and i photometry. We flagged each star with photometry placing them beyond the upper (most metal-poor) bounds given of these contours, and set their metallicity to the boundary value (i.e., [Fe/H] $= -4.0$).

As is shown on the left panel in Figure 2-3, the contours used for measuring metallicity depend on the surface gravity $\log g$. It is thus necessary to assume an initial $\log g$ before attempting any metallicity calculations. We initually assume $\log g = 2$ which should roughly correspond to the surface gravity of stars on the RGB of Tucana II.

Upon obtaining these initial metallicities, photometric surface gravities were then derived as described in Section 2.4.2. After that, the photometric surface gravities were used to determine our final photometric metallicities. The average change in the photometric metallicities upon updating the surface gravity is marginal (~ 0.02 dex

for stars with $\log g < 3.0$), suggesting that one iteration is sufficient for convergence. Section 2.4.7 discusses our final adopted metallicity uncertainties.

2.4.2 Measuring surface gravities from photometry

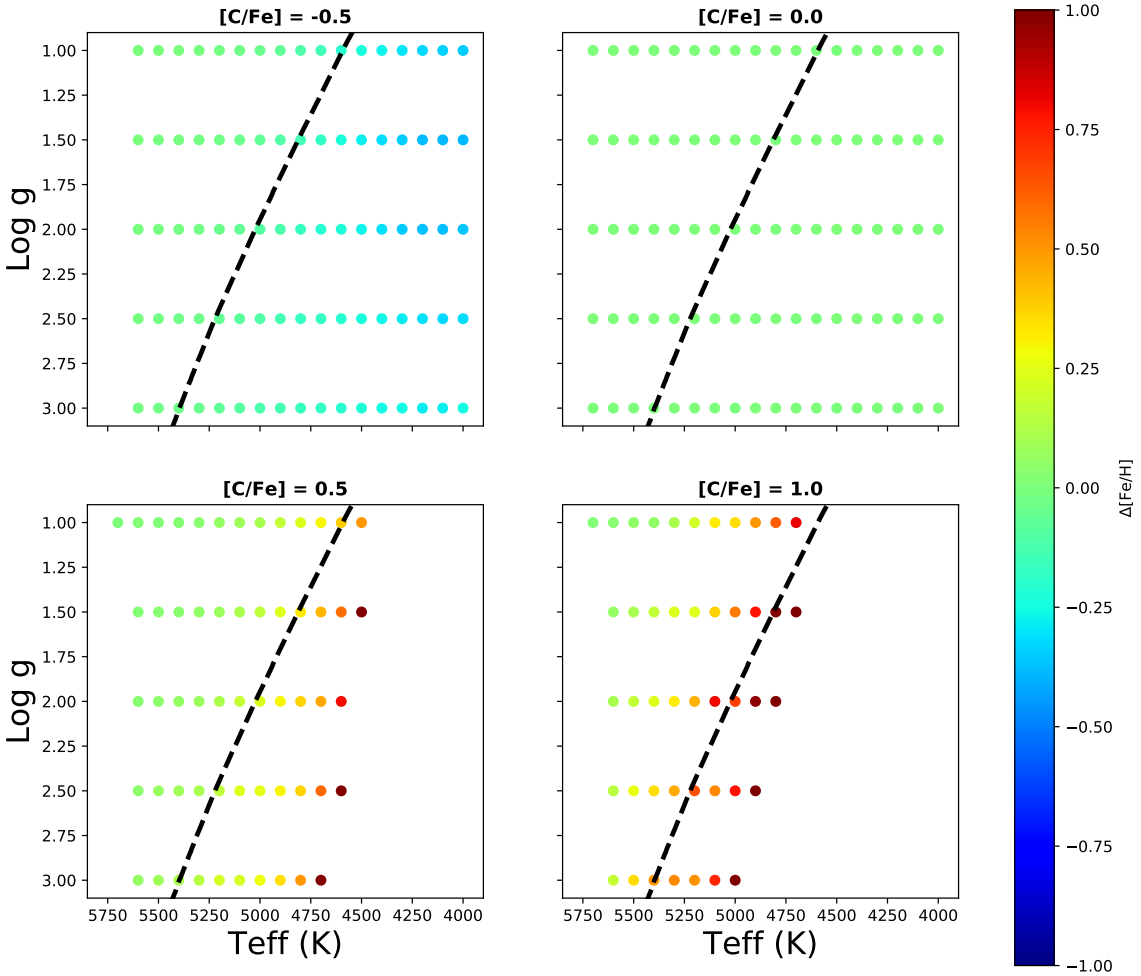

Figure 2-4 Effect of different carbon abundances on the photometric metallicities as a function of surface gravity and effective temperature and a fixed [Fe/H] $= -2.5$. A strong effect occurs towards lower effective temperatures ($\lesssim$4700 K) and with increasing carbon enhancement ([C/Fe] ≥ 0.5) because the strength of the CN feature at $\sim$3870 Å has a significant effect on the flux through the v filter. The dashed line corresponds to the RGB of a [Fe/H] $=-2.5$, 12 Gyr Dartmouth isochrone [10].

The SkyMapper u and v filters can be used to discriminate the surface gravities of stars. These filters bracket the Balmer Jump at 3646 Å which is sensitive to the H^- opacity, which, in turn, is a function of the $\log g$ of the star [e.g., 136]. Similar to

the method outlined in Section 2.4.1 for deriving photometric metallicities, plotting $u-v-0.9\times(g-i)$ vs. $g-i$ can discriminate stellar surface gravities. This behavior is illustrated on the right panels in Figure 2-3, based on the synthetic spectra described in Section 2.3. We then use the same interpolation technique described in Section 2.4.1 to derive photometric surface gravities from the $u-v-0.9\times(g-i)$ contours.

We use the first-pass synthetic metallicities from Section 2.4.1 to choose the corresponding set of $\log g$ contours from which to derive surface gravities. Since we use surface gravities solely to remove foreground main-sequence stars from our sample, we opt not to iteratively re-measure $\log g$ with updated photometric metallicity values.

2.4.3 Dependence of the photometric metallicity measurements on carbon abundance

Since a CN molecular absorption feature is located at $\sim$3870 Å in the bandbass of the SkyMapper v filter (encompassing $\sim$ 3600 Å to $\sim$ 4100 Å), its spectral morphology can become strong enough to systematically affect the flux through the filter. The strength of the CN feature significantly depends on the carbon abundance and effective temperature of the star: A higher carbon abundance and a lower effective temperature leads to a stronger CN absorption feature which, in turn, leads to an artificially higher photometric metallicity. This could systematically skew photometric metallicity results since a significant fraction of metal-poor stars tend to be enhanced in carbon ([C/Fe] $>$ 0.7) and are known as carbon-enhanced metal-poor (CEMP) stars. 80% of stars with [Fe/H] <-4.0 and still 24% of stars with [Fe/H] <-2.5 have [C/Fe] $>$ 0.7 [8]. We thus attempt to quantify these effects to gauge how our photometric metallicities derived from the v filter are influenced by the carbon abundance.

We test the effect of the strength of the CN feature on the flux through the SkyMapper v filter by regenerating our grid of synthetic spectra, as described in Section 2.3. We do so by varying the carbon abundances of the synthetic spectra between [C/Fe] $=-0.5$ and [C/Fe] $=$ 1.0 in intervals of 0.5. We then derived the

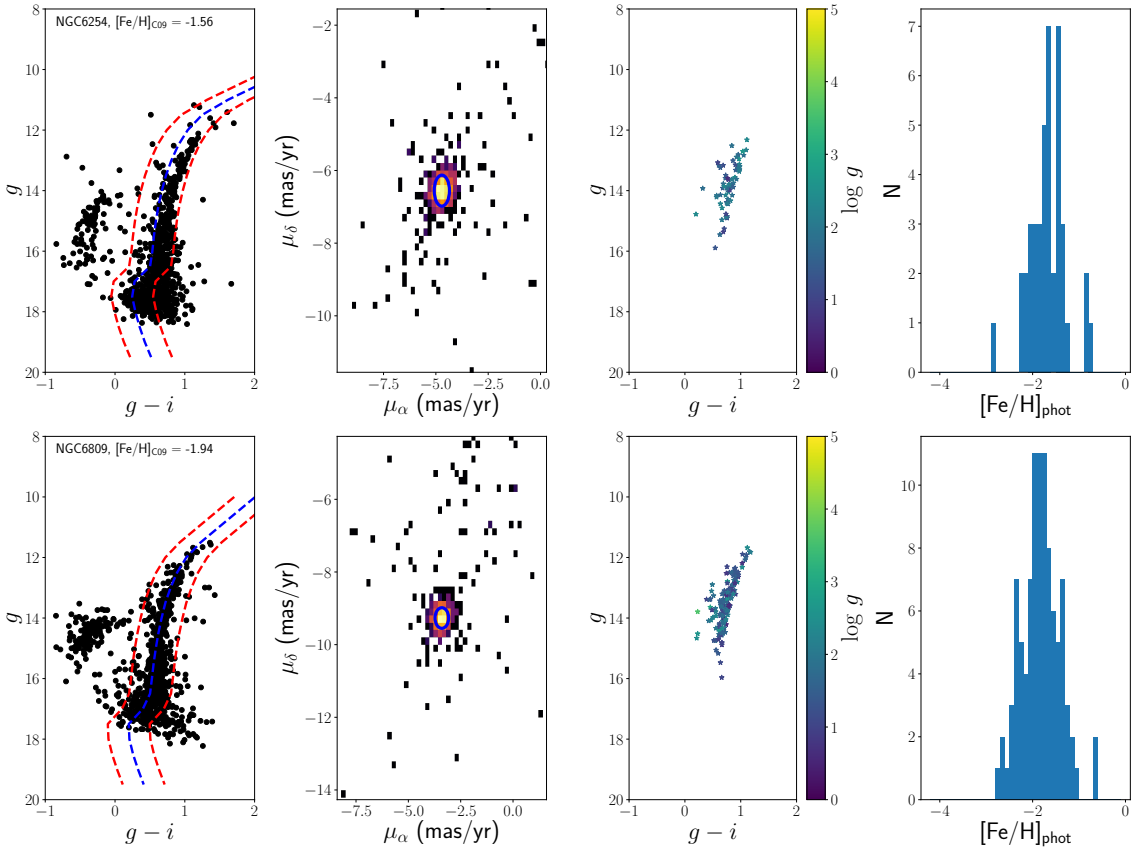

Figure 2-5 Overview of the process of finding likely member stars to derive mean photometric metallicities for NGC6254 (top), a cluster with [Fe/H] = −1.56, and NGC6809 (bottom), a cluster with [Fe/H] = −1.94 [11]. From left to right: selection of candidate members using a Dartmouth isochrone [10]; further selection using *Gaia* proper motion data: a 2d Gaussian (blue) is fitted to a density plot of the proper motion data to select likely members; resulting CMD after only retaining stars with photometric log $g < 3$ and with proper motions in the fitted 2d Gaussian; histogram of photometric metallicities of the stars that passed all selection criteria.

$v - g - 0.9 \times (g - i)$ index and $g - i$ colors for these synthetic spectra and obtained the corresponding photometric metallicities following the procedure described in Section 2.4.1.

In Figure 2-4, we plot the changes in the resulting photometric metallicity, relative to a baseline of [C/Fe] = 0, for four different carbon abundances as a function of surface gravity and effective temperature, corresponding to our RGB grid in Table 2.2. The [C/Fe] = 0 baseline, however, is temperature-dependent as the strength of the CN band is temperature sensitive. Decreasing the carbon abundance by 0.5 dex to

gauge the corresponding effect on the photometric metallicity leads minimal effects of ~ 0.1 dex, as seen in Figure 2-4. But among the cooler stars ($T_{\rm eff} < 4700$ K) with [C/Fe] > 0.5, we find significant changes (the ultimately measured [Fe/H] of a CEMP star gets artificially increased by Δ[Fe/H]~ 0.5). Accordingly, some true CEMP stars may always remain "hidden" in our samples, especially among the cooler stars. No significant effects are apparent otherwise since the CN feature is relatively weak for all these stars, meaning the feature does not influence the overall flux through the v filter. Therefore, our analysis suggests that we would still select moderately cool ($T_{\rm eff} \sim 4700$ K) CEMP stars as very metal-poor candidates. This result is supported by the fact that we can re-identify all three members of Tucana II that are CEMP stars, all of which are warmer than 4600 K [12] but are not greatly enhanced in carbon ([C/Fe] < 1.0 before applying the carbon correction following Placco et al. [8]).

Overall, we conclude that while our derived photometric metallicities are dependent on the carbon abundance and effective temperature of stars, we can select stars with (uncorrected) [C/Fe] $\lesssim 0.5$ that also have [Fe/H] ~ -2.5 and have $T_{\rm eff} \gtrsim 4800$ K with sufficient precision (within $+0.3$ dex). Stars which turn out to have e.g., [C/Fe] ~ 0.35, if on the RGB ($\log g \sim 1.5$), would likely become CEMP stars after applying a correction for the evolutionary status of the star following Placco et al. [8]. Correspondingly, a star with a carbon abundance of up to [C/Fe] ~ 1 and [Fe/H] ~ -2.5 could principally still be identified as a candidate member of a UFD ([Fe/H] $\lesssim -1.5$) when it has $T_{\rm eff} \gtrsim 5000$ K since its photometric metallicity would be shifted by Δ[Fe/H]$\lesssim 1.0$.

CEMP-s stars tend to be the most carbon-enhanced ([C/Fe] $\gtrsim 1.25$ at [Fe/H] $\gtrsim -2.8$) subclass of CEMP stars and would thus systematically have among the strongest CN bands [161] somewhat irrespective of temperature. Consequently, CEMP-s stars would appear as much more metal-rich stars (we estimate by about 1 dex or more) supposing they were on the RGB. Hence, any CEMP-s star with e.g., [Fe/H] $= -2.5$ would be measured as having a metallcity of -1.5 dex or higher. These metallicities tend to be excluded from our selection since we are focused on more metal-poor stars, so our sample could thus be regarded mostly free of CEMP-s stars.

At lower metallicities, the effect of the CN absorption on the measured [Fe/H] is somewhat mitigated. After repeating our procedure for [Fe/H] $= -4.0$, a star with [C/Fe] $= 1.0$ will affect the measured [Fe/H] by ~ 0.3 dex when it has $T_{\rm eff} \gtrsim 4500$ K. When [C/Fe] is increased to 2.0, moderately cool ($T_{\rm eff} \sim 4800$ K) stars will be affected by up to 0.75 dex due to the highly nonlinear growth of the CN feature. Nevertheless, we note that to first order, the CN feature of a star with [Fe/H] $= -5.0$ and [C/Fe] $=$ 2.0 should be similar to that of a star with [Fe/H] $= -4.0$ and [C/Fe] $= 1.0$, assuming similar stellar parameters. This implies that most CEMP stars with [Fe/H] < -4.0 should be identifiable, except for perhaps very extreme cases.

In general, these results suggests that any metallicity distribution function (MDF) derived from SkyMapper photometry will likely be upscattered to some degree. According to our models, the most metal-poor ([Fe/H] ~ -4.0), moderately cool ($T_{\rm eff} \sim$ 4800 K) stars with a significant carbon-enhancement ([C/Fe] ~ 2.0) will be affected by up to 0.75 dex. High-resolution spectroscopic follow-up observations of stars in the SkyMapper dataset can confirm the extent of these CN feature-induced changes.

2.4.4 Comparison to Globular Clusters

Globular clusters are old ($\sim$ 10 Gyr) and metal-poor ([Fe/H] < -1.0) star clusters. The dispersion of the metallicities of their member stars is generally small ($\sigma_{\rm [Fe/H]} \sim 0.05$) as discussed in e.g., Carretta et al. [11]. The stellar population of individual globular clusters therefore provides a useful test of the precision of deriving photometric metallicities, since most of the dispersion in the photometric metallicities of member stars can be ascribed to the uncertainty in our SkyMapper data and broader methodology.

While we did not observe any globular clusters as part of our observing program, a number of globular clusters are located within the footprint of the first data release (DR1.1) of the SkyMapper Southern Survey [9]. Thus, we retrieved SkyMapper u, v, g, and i photometry from the DR1.1 catalog for member stars of all globular clusters in the southern hemisphere with a distance less than 10 kpc. Specifically, we used the Harris [162] catalog of globular clusters, an update to the older Harris [163] catalog,

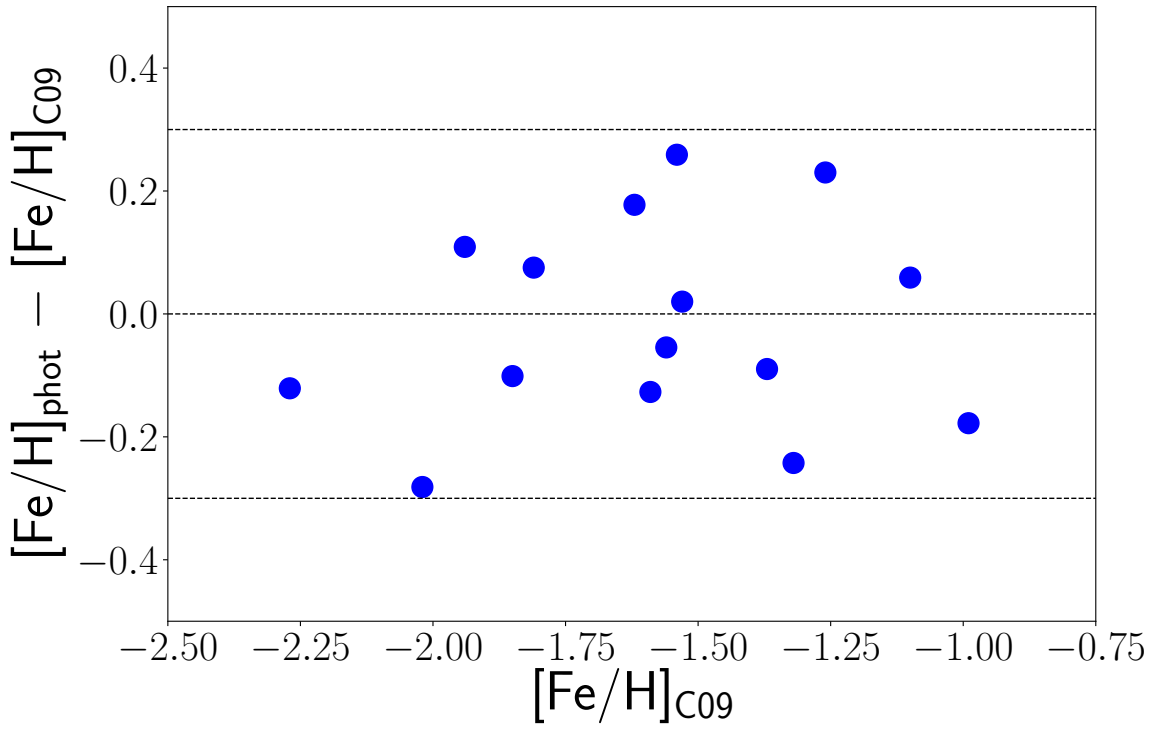

Figure 2-6 Residuals of our photometric metallicities of globular clusters with respect to spectroscopic results from Carretta et al. [11], as a function of their metallicities. These residuals have a standard deviation of 0.16 dex. The standard error in the mean of the residuals is $\sigma_{\Delta[\mathrm{Fe/H}]} = 0.04$.

and retrieved all stars within three times the tidal radius of each globular cluster. This resulted in the retrieval of 17 globular clusters with metallicities ranging from [Fe/H] $= -2.27$ to [Fe/H] $= -0.99$ as measured in Carretta et al. [11].

Upon retrieving SkyMapper u, v, g, i photometry from the public catalog, we selected likely member stars of each globular cluster. We first overlaid 13 Gyr Dartmouth isochrones [10] with metallicities and distance moduli matching those from Carretta et al. [11] and then selected all stars with $g-i$ within 0.3 mag of the isochrone. We then computed photometric metallicities and surface gravities of these candidate members using the methods described in Sections 2.4.1 and 2.4.2.

We used proper motion measurements from the second data release from the *Gaia* mission [DR2; 111, 112, 164] as an additional avenue to exclude non-members since members of a globular cluster should have similar proper motions. To identify the systemic proper motion of each cluster, we generated 2d histograms of the proper motions with a binsize of 0.2 mas/yr in μ_α and μ_δ. We then fitted a 2d elliptical Gaussian to the overdensity in each proper motion histogram and selected all stars enclosed within the 3σ bounds of the Gaussian.

We then chose to only retain stars with photometric surface gravities of $\log g < 3$, as the depth of the public SkyMapper photometry with usable photometric metallicity precision ($g \sim 16$) does not extend to the main sequences in our sample of globular clusters. We also only retained stars with photometric metallicity uncertainties below 0.5 dex and photometric surface gravity uncertainties below 0.75 dex. The determination of the uncertainties is described in Section 2.4.7. Each step of our selection of likely member stars of globular clusters is shown in Figure 2-5. We finally derive an overall metallicity of each globular cluster by taking the average of the photometric metallicities, weighted by the inverse-squared photometric metallicity uncertainties, of each remaining sample of likely member stars. Two histograms of the photometric metallicities of likely member stars for NGC6254 and NGC6809 are shown as examples in Figure 2-5.

For all clusters for which we identify $N > 1$ member stars, we plotted the residuals of our derived cluster metallicities with respect to spectroscopically-derived metallic-

Table 2.3. Photometric metallicities of globular clusters based on SkyMapper DR1.1 data

Name	$(m-M)$	$[\mathrm{Fe/H}]_{\mathrm{C09}}$	$[\mathrm{Fe/H}]_{\mathrm{phot}}$	N
NGC7099	14.54	−2.27	−2.39	10
NGC6397	11.81	−2.02	−2.30	29
NGC6809	13.66	−1.94	−1.83	97
NGC4833	14.10	−1.85	−1.95	3
NGC6541	14.38	−1.81	−1.73	7
NGC6681	14.77	−1.62	−1.44	2
NGC3201	13.45	−1.59	−1.72	23
NGC6254	13.22	−1.56	−1.61	42
NGC6752	13.01	−1.54	−1.28	68
NGC5139	13.58	−1.53	−1.51	185
NGC6218	13.41	−1.37	−1.46	28
NGC288	14.75	−1.32	−1.56	7
NGC362	14.67	−1.26	−1.03	15
NGC6723	14.70	−1.10	−1.04	7
NGC6362	14.40	−0.99	−1.17	4

ities of each cluster from Carretta et al. [11]. We found that applying an offset of 0.06 mags to our synthetic v magnitudes removed a ~ 0.1 dex systematic offset between our metallicities and those in Carretta et al. [11]. Thus, we applied this offset to our contours and re-derived our cluster metallicities. We note that all photometric metallicities and log g values presented in this paper are calculated with this $+0.06$ mags offset in the synthetic v magnitudes.

The final residuals of our cluster metallicities with respect to Carretta et al. [11] are shown in Figure 2-6. A negligible final offset of -0.02 dex is found with a standard deviation is 0.16 dex with respect to the values from Carretta et al. [11]. We thus take 0.16 dex as an estimate of the intrinsic uncertainty from our method as further discussed in Section 2.4.7. Table 2.3 lists our measured photometric metallicities as well as spectroscopic metallicities from Carretta et al. [11].

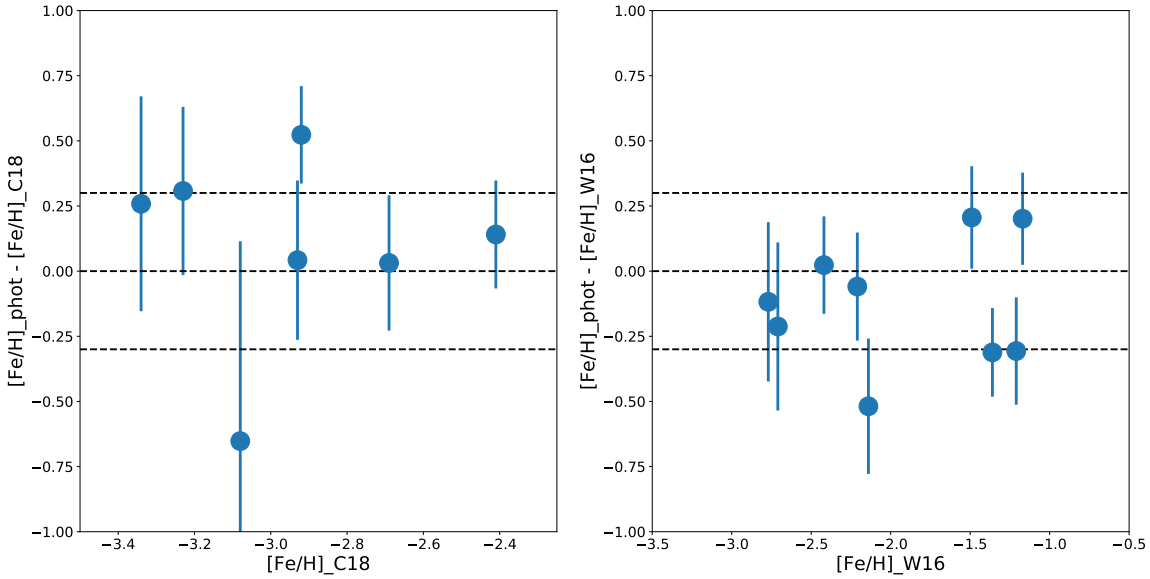

Figure 2-7 Left: Comparison of our photometric metallicities to those derived from high-resolution spectroscopy in Chiti et al. [12]. Right: Comparison of our photometric metallicities to those derived from medium-resolution spectroscopy in Walker et al. [1] for all stars in that paper with metallicity values with an uncertainty less than 0.2 dex and [Fe/H] < -1.0. We note that Walker et al. [1] applied a zero-point offsets of either 0.16 dex or 0.32 dex to their metallicities that may account for the zero-point offset between our measurements and those in Walker et al. [1]. Dashed lines are drawn at $+0.3$ and -0.3 to guide the eye. Error bars correspond to the uncertainty in the photometric metallicities of these stars.

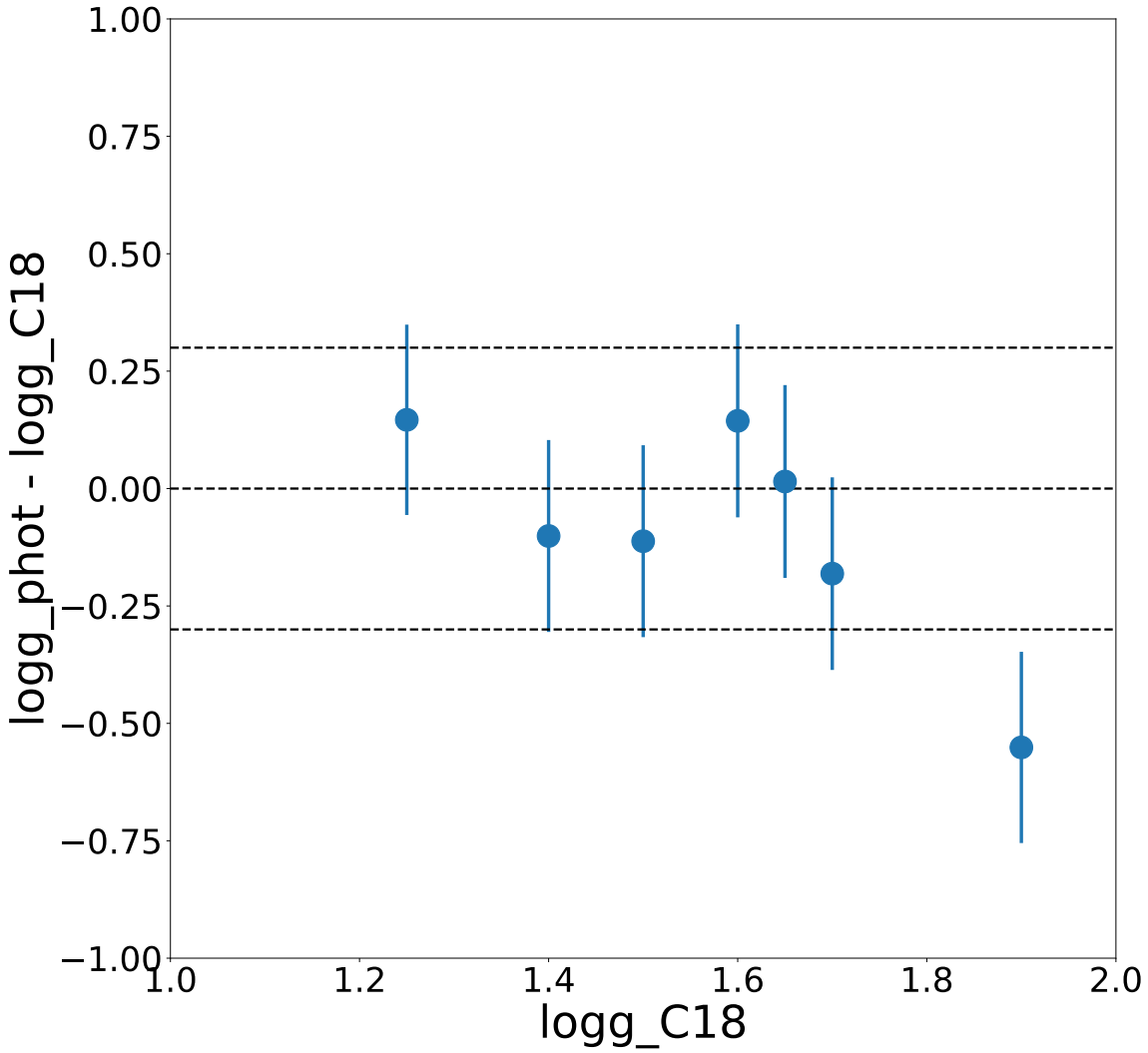

Figure 2-8 Comparison of our photometric $\log g$ values to those derived from high-resolution spectroscopy in Chiti et al. [12]. Dashed lines are drawn at $+0.3$ and -0.3 to guide the eye. Error bars correspond to the uncertainty in the photometric $\log g$ values of these stars.

2.4.5 Comparison to Tuc II high-resolution members

Seven stars in Tucana II have high-resolution spectroscopic metallicities presented in Chiti et al. [12]. We compare our photometric metallicities and surface gravities for those seven stars to the spectrosopically determined values. The results are shown in the left panel of Figure 2-7 and in Figure 2-8.

For the metallicities, we find a mean offset between our values of 0.09 dex (in which we measure a higher [Fe/H]) with a standard deviation of 0.34 dex. This is excellent agreement, given that all but one photometric metallicity is within 1σ agreement of the metallicities derived from high-resolution spectroscopy (see Section 2.4.7 for a discussion of the derivation of these uncertainties). Additionally, the mean carbon abundance of these stars is [C/Fe] = 0.35 and their mean $T_{\rm eff}$ is 4870 K, which, according to Figure 2-4 would suggest that we should overestimate the photometric metallicity by $\sim$0.1 dex.

We also find generally excellent agreement between our photometric $\log g$ values and those in Chiti et al. [12], as shown in Figure 2-8. The mean offset is -0.09 dex, meaning we measure a lower $\log g$ relative to those derived from high-resolution spectroscopy. The standard deviation of the residual between our $\log g$ measurements is 0.22 dex. The standard deviation and mean offset are almost entirely driven by the one outlier, labeled as TucII-078 in Chiti et al. [12], at $\log g \sim 1.9$ in Figure 2-8. Excluding it would change the offset to $+0.02$ dex and the standard deviation to 0.11 dex. However, the presence of this outlier is not entirely surprising, given that Chiti et al. [12] derive a correspondingly large uncertainty of 0.67 dex in the $\log g$ of TucII-078.

2.4.6 Comparison to Walker et al. [1]

We also compare our photometric metallicities to [Fe/H] values from Walker et al. [1], who derived these values from $R \sim 18,000$ and $R \sim 10,000$ spectra of the Mg b region ($\sim$ 5150 Å) for 137 candidate member stars in the vicinity of Tucana II. We chose to only compare with stars in Walker et al. [1] that had metallicity uncertainties $<$

0.20 dex to ensure a high-quality comparison. We further only compared to stars with [Fe/H] < -1.0 in Walker et al. [1], as our grid of synthetic photometry only extends to [Fe/H] $= -0.5$. We find good agreement between our photometric metallicity measurements and those in Walker et al. [1], with a mean offset of -0.12 dex, meaning we measure a lower [Fe/H], and a standard deviation between our measurements of 0.23 dex.

2.4.7 Final [Fe/H] and $\log g$ uncertainties

We assume that the uncertainty in each photometric [Fe/H] value is a combination of 1) intrinsic uncertainty from our methodology and 2) random uncertainty that is propagated from uncertainties in the photometry. The intrinsic uncertainty in our methodology is assumed to be 0.16 dex, which is the standard deviation of the residuals of our photometric metallicities for globular clusters (see Section 2.4.4). We thus take into account that the mean photometric [Fe/H] value for each cluster is usually derived from a large number of stars ($N > 10$), suggesting that the standard error in each of these values is generally small. We therefore assume that the 0.16 dex scatter in the residuals is mostly driven by the intrinsic uncertainty in our method, which we adopt as such when calculating the final uncertainty in our photometric [Fe/H] values. The random uncertainty is derived by adding in quadrature the difference in photometric [Fe/H] obtained after varying each the v, g, and i magnitudes by their 1σ photometric uncertainties and redetermining final values. If the variation of any of the magnitudes by their 1σ photometric uncertainties takes them beyond the bounds of the grid of synthetic photometry, then a conservative uncertainty of 0.75 dex is adopted.

The intrinsic and random uncertainties are then added in quadrature to derive final uncertainties on our photometric [Fe/H] values. Our final photometric metallicity uncertainties appear to be reasonable, as the median of the uncertainty of the photometric metallicities in the left and right panels of Figure 2-7 is 0.31 dex and 0.21 dex, respectively. These uncertainties are similar to the standard deviations of the data points in each of these panels of 0.34 dex and 0.23 dex, respectively. For

another estimate of the precision of our method, we can thus pool together the residuals in Figures 2-6 and 2-7 and compute their standard deviation. Upon doing this, we find that the standard deviation of the residuals is 0.20 dex for data points with [Fe/H] > -2.5 and 0.34 dex for those with [Fe/H] < -2.5.

The uncertainty in the photometric $\log g$ is calculated a similar manner. The random uncertainty is derived by adding in quadrature the difference in photometric $\log g$ after varying the u, v, g, and i magnitudes by their 1σ photometric uncertainties. The intrinsic uncertainty is assumed to be 0.20 dex, since this leads to the median uncertainty of the photometric $\log g$ values in Figure 2-8 to agree with the standard deviation of the residuals.

2.5 Re-discovering the Tucana II dwarf galaxy

In this section, we show that our photometric metallcities and surface gravities, when combined with *Gaia* DR2 proper motion data, provide an extremely efficient means to identify likely member stars (Section 2.5.1) of Tucana II. This principally enables precise studies of the properties of a UFD. We further outline a method using the python `emcee` package to quantify membership probability (Section 2.5.2) to derive a metallicity distribution function (MDF) for the Tucana II UFD (Section 2.5.3). In principle, these techniques could also be used to study other UFDs with incomplete or no spectroscopy of member stars.

2.5.1 Identifying members of Tucana II

We performed several preliminary steps to prepare our source catalog for analysis. We first removed galaxies by cross-matching our sources with those in the DES Y1A1 gold catalog [146]. Following the criteria and procedure described in Desai et al. [165] and Bechtol et al. [37], we excluded all sources from the DES catalog with the parameter `SPREAD_MODEL_I` > 0.003 [165] to retain only stars. We then measured photometric metallicities and surface gravities of every star within the parameters of our grid of synthetic photometry, and compiled their proper motion measurements

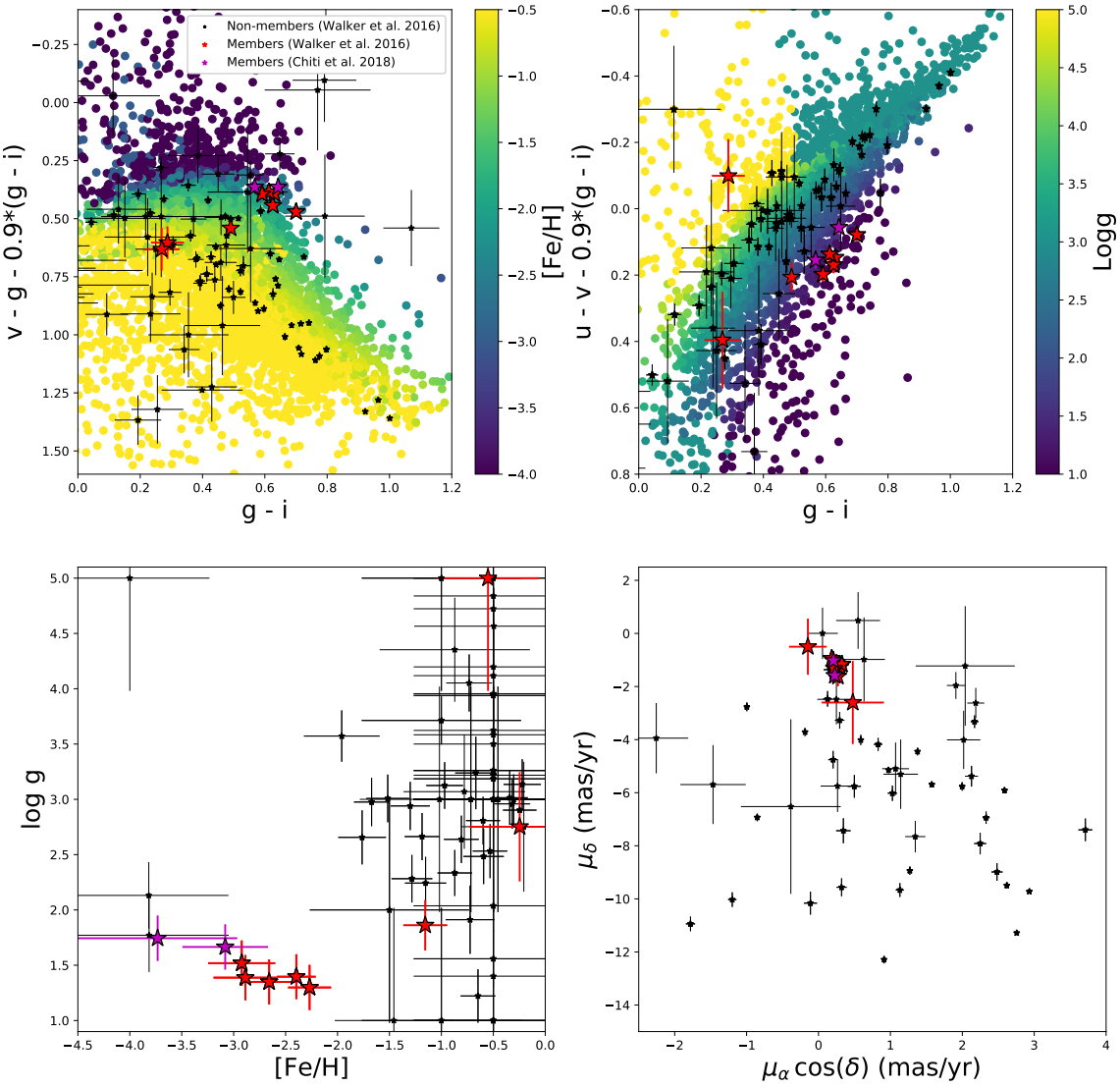

Figure 2-9 Top left: Color-color plot for determining photometric metallicities. All stars selected along an isochrone that matches the Tucana II red giant branch stellar population are colored according to their photometric metallcities. Red star symbols are confirmed members ($p > 0.95$) from Walker et al. [1]; small black star symbols are confirmed non-members from Walker et al. [1]; purple star symbols are confirmed members from high-resolution spectroscopy from Chiti et al. [12]. Top right: Color-color plot for determining photometric $\log g$. As discussed in Section 2.5.2, stars with [Fe/H] > -1.0 and $\log g \geq 3.0$ are excluded when deriving membership probabilities since they are very likely to be foreground contaminants. Bottom left: A plot of photometric $\log g$ vs. photometric [Fe/H] for stars in Walker et al. [1] and Chiti et al. [12]. Note the separation of the majority of confirmed members from foreground stars at high metallicites. Bottom right: *Gaia* DR2 proper motions of stars in Walker et al. [1] and Chiti et al. [12].

from the *Gaia* DR2 catalog [111, 112]. Then, we compiled a list of confirmed member stars of Tucana II from Walker et al. [1] and Chiti et al. [12] and confirmed non-member stars in the vicinity of Tucana II from Walker et al. [1]. Walker et al. [1] derived membership probabilities for 137 stars in the vicinity of the Tucana II UFD. Two new confirmed member stars of Tucana II had already been identified by Chiti et al. [12] from the data presented in this paper.

We consider all stars with a membership probability $> 95\%$ in Walker et al. [1] to be likely members in our subsequent analysis. Of particular interest in this regard is whether likely member stars could be separated from non-member stars using our photometric stellar parameter measurements and *Gaia* proper motion data. In Figure 2-9, we illustrate several tests to qualitatively separate the non-members and likely members from Walker et al. [1] and Chiti et al. [12]. The top two panels demonstrate that the majority of likely members separate from non-members in the color-color plots we employ to measure photometric stellar parameters. The bottom two panels of Figure 2-9 show that when combining metallicity, $\log g$, and proper motion information, the confirmed members are largely distinct from foreground stars. However, three members from Walker et al. [1] do not separate as cleanly. One of these stars is fairly metal-rich ([Fe/H] ~ -1.3), about 1 dex more compared to the other member stars. It is likely a metal-rich, or carbon-enhanced (see Section 2.4.3), member of the UFD, given its separation from the foreground in $\log g$ and proper motion. The other two stars may indeed be non-members, given our measurements of their photometric metallicity ([Fe/H] > -1) and surface gravities ($\log g > 2.5$). Furthermore, the slight separation of these two stars from the other confirmed member stars in proper motion space, as shown in the bottom right panel of Figure 2-9, supports this notion. However, since these two stars are faint ($g > 20$) and their measurements are correspondingly less precise, firm arguments about their membership status cannot be made.

In conclusion, however, we demonstrate that photometric metallicities and surface gravities, especially in the case of high-quality measurements, can clearly separate UFD member stars from foreground stars. Furthermore, the *Gaia* proper motion

data is useful in identifying likely members that may otherwise be metal-rich (i.e., the one star at [Fe/H] ~ -1.3 in the bottom left plot of Figure 2-9).

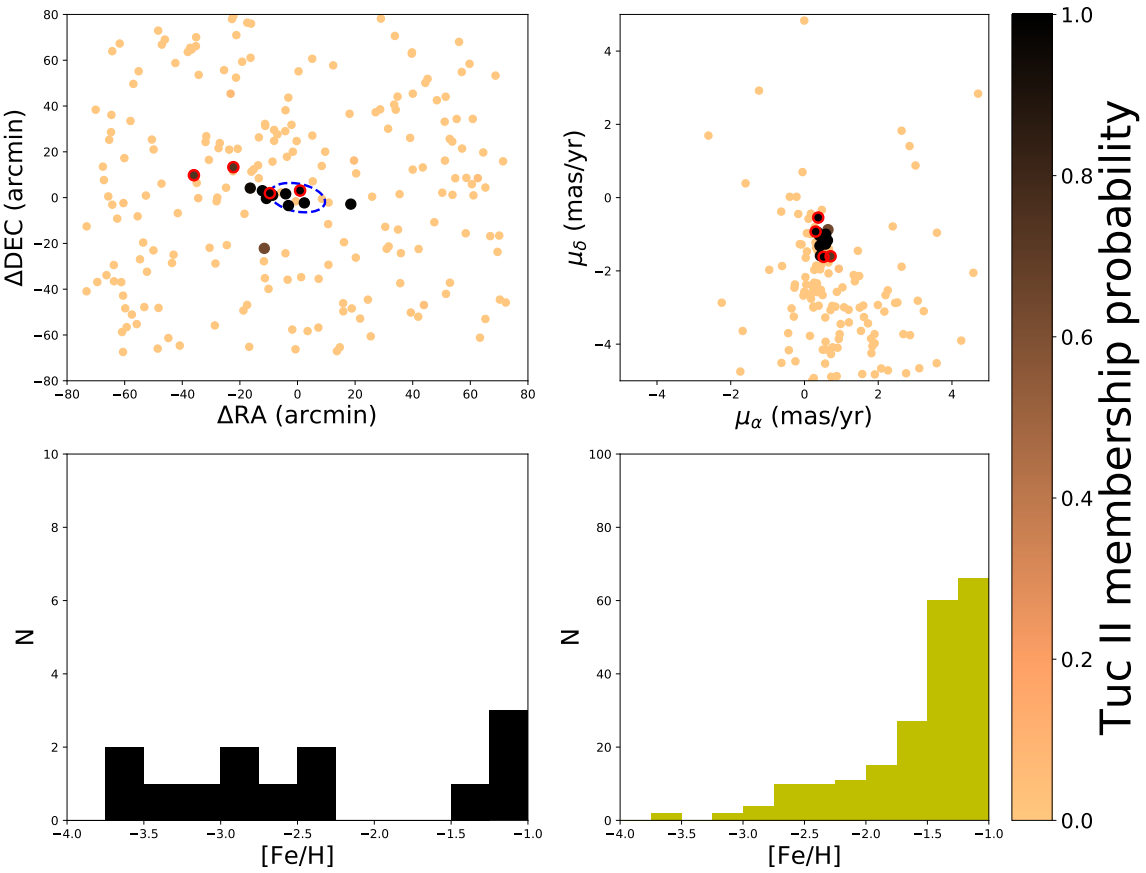

Figure 2-10 Top left: Location of each metal-poor ([Fe/H] < -1.0) giant ($\log g < 3.0$) in our sample of stars, and colored by membership probability. As expected, we identify a number of likely members near the center of the galaxy. The three likely members with photometric [Fe/H] > -1.5 are circled in red. The half-light radius from Koposov et al. [13] is overplotted in blue. Top right: Same as the top left, but plotted in proper-motion space. We find that the likely Tucana II members are tightly clustered in proper-motion space which is unsurprising given the small intrinsic dispersion in the system. Bottom panels: Metallicities of stars with membership probability $p > 0.50$ (left) and $p < 0.50$ (right). Despite not applying an additional metallicity-dependent term in calculating the membership probabilities, beyond the initial sample cut we find that the metallicities of the likely members are on average more metal-poor than the likely non-members. See text for discussion.

2.5.2 Quantifying membership probabilities

In order to quantitatively derive properties (i.e., MDF) of the Tucana II UFD, member stars need to be selected well despite the presence of large numbers of foreground stars. Given that we derive photometric log g and [Fe/H] values, we can immediately remove foreground metal-rich, and main sequence stars from our sample to alleviate the issue of significant foreground contamination. Then, as previously demonstrated in e.g., Pace and Li [124], we use a combination of the spatial location of each star and its *Gaia* DR2 proper motion measurements to derive quantitative membership probabilities for each star. The bottom panels of Figure 2-9 already qualitatively show that using photometric metallicity, $\log g$, and proper motions enable adequate membership identification.

To quantify the membership likelihood of each star, we then proceed with several steps. First, we remove stars that are either metal-rich ([Fe/H] > -1.0), not on the red giant branch ($\log g \geq 3.0$), or fainter than $g = 20$. We apply the brightness cut to ensure that our stars have reliable photometric $\log g$ and [Fe/H] values. We apply the metallicity cut since no metal-rich stars are known as members of UFDs (see i.e., Frebel and Norris 99, Simon 121 for reviews), and we apply the $\log g$ cut as stars in Tucana II down to $g = 20$ are at the base of the red giant branch or higher up.

We model the remaining set of metal-poor giants using a mixture model with the following likelihood function:

$$\begin{aligned}\mathcal{L}_{\rm Total} = f_{\rm mem}\mathcal{L}_{\rm sp,mem}\mathcal{L}_{\rm pm,mem} + \\ (1 - f_{\rm mem})\mathcal{L}_{\rm sp,nonmem}\mathcal{L}_{\rm pm,nonmem}\end{aligned} \tag{2.2}$$

where $f_{\rm mem}$ denotes the fraction of member stars of Tucana II. The spatial distribution of member stars of Tucana II is assumed to follow an exponential profile, following Martin et al. [166] and Longeard et al. [134], with a likelihood function given by:

$$\mathcal{L}_{\rm sp,mem} = \frac{\exp(-\frac{R}{R_e})}{2\pi R_e(1-\epsilon)} \Bigg/ \int_S \frac{\exp(-\frac{R}{R_e})}{2\pi R_e(1-\epsilon)}\, dS \tag{2.3}$$

where ϵ is the ellipticity, R_e is the exponential radius, and R is the elliptical radius, given by:

$$R = ((\frac{1}{1-\epsilon}((x-x_0)\cos\theta - (y-y_0)\sin\theta))^2 \\ +((x-x_0)\sin\theta + (y-y_0)\cos\theta)^2)^{1/2} \tag{2.4}$$

where x_0 and y_0 are the right ascension and declination of the center of Tucana II, as measured in Koposov et al. [13], and θ is the position angle of the elliptical distribution. x and y are the distances from the center of Tucana II along the direction of right ascension and declination, respectively. The spatial distribution of non-members, $\mathcal{L}_{\rm sp,nonmem}$ is assumed to be uniform.

The likelihood functions for the proper motions of members and non-members, $\mathcal{L}_{\rm pm,mem}$ and $\mathcal{L}_{\rm pm,nonmem}$ are assumed to be bivariate Gaussians, following the formalism presented in e.g., Longeard et al. [134]. We use a standard bivariate gaussian to model the foreground stars, but use the following probability density to model the members of Tucana II:

$$p = \frac{(2\pi)^{-1}}{\sigma_{\mu_\alpha}\,\sigma_{\mu_\delta}} \times \\ \exp\left[-\frac{(\mu_\alpha - \langle\mu_\alpha\rangle_{\rm TII})^2}{2\sigma^2_{\mu_\alpha}} - \frac{(\mu_\delta - \langle\mu_\delta\rangle_{\rm TII} - k\,(\mu_\alpha - \langle\mu_\alpha\rangle_{\rm TII}))^2}{2\sigma^2_{\mu_\delta}}\right] \tag{2.5}$$

where μ_α is *Gaia* proper motion in the direction of right ascension, μ_δ is the proper motion is the direction of declination, σ_{μ_α} and σ_{μ_δ} are their corresponding uncertainties, $\langle\mu_\alpha\rangle_{\rm TII}$ and $\langle\mu_\alpha\rangle_{\rm TII}$ denote the systemic proper motion of the Tucana II UFD, and k adds the analog of a position angle to the bivariate gaussian. Identically to Pace and Li [124], we assume that the intrinsic proper motion uncertainties are much smaller than the observational uncertainties in proper motion, and thus the width of the bivariate Gaussian for the UFD members is solely determined by the uncertainties in proper motions.

We sample the likelihood function using the `emcee` package [167], which uses the ensemble sampler from Goodman and Weare [168]. There were 8 free parameters in

our sampling, which were $f_{\rm mem}$, k, $\langle\mu_\alpha\rangle_{\rm TII}$, $\langle\mu_\alpha\rangle_{\rm TII}$, $\langle\mu_\alpha\rangle_{\rm MW}$, $\langle\mu_\alpha\rangle_{\rm MW}$, $\sigma_{\mu_{\alpha,\rm MW}}$, $\sigma_{\mu_{\delta,\rm MW}}$. The parameters R_e, ϵ, θ were fixed to the values provided in Koposov et al. [13]. We initialized the sampler with 200 walkers, with 2000 steps after a burn-in period of 500 steps to ensure a good sampling of the posterior distributions. The membership probability was then simply assumed to be the ratio of the membership terms to the total likelihood in equation 2.2.

In Table 2.4, Figure 2-10, and the top panels of Figure 2-11, we present our final membership probability for each star. As expected, we find a number of likely members near the nominal center of Tucana II. However, interestingly, we also find several stars well separated from the center of the galaxy that also have a likelihood of being members.

To ensure that our identification of likely members is accurate, we investigated whether we recovered the known sample of Tucana II members from Walker et al. [1] and Chiti et al. [12]. We only considered stars with DES $g < 20$ in Walker et al. [1], as this is comparable to the initial magnitude cut for our sample. We consider stars that have membership probability $p > 0.95$ in Walker et al. [1] and the two additional members presented in Chiti et al. [12] to be likely members, and stars with membership probability $p < 0.50$ in Walker et al. [1] to be likely non-members. Results of our comparison are shown in Figure 2-11.

As an additional check, we also compared our catalog of likely members with that of Pace and Li [124], who identified likely members based on *Gaia* DR2 proper motions and DES photometry. We find that we recover their entire sample of 10 likely ($p > 0.50$) members of the red giant branch of Tucana II brighter than $g \sim 19.6$. We additionally identify three likely member stars not found as having membership probability greater than 0.50 in their catalog. We note that two of our likely members that appear to be more metal-rich ([Fe/H] > -1.5) also appear as likely members in Pace and Li [124], further supporting that they are indeed members.

We find that our initial exclusion of stars with photometric [Fe/H] > -1.0 and $\log g > 3.0$ removes all but five likely non-members from Walker et al. [1]. Furthermore, the five remaining likely non-members are identified as likely non-members from

our method, since we derive membership probabilities $p < 0.10$ for all those stars. We re-identify all likely members of the red giant branch from Walker et al. [1] and Chiti et al. [12] as highly likely members in our sample (all $p > 0.99$). The one likely member we are not recovering from Walker et al. [1] is on the horizontal giant branch, since we exclude stars not on the red giant branch from our sample. In addition to re-identifying all the known likely members on the red giant branch, we here identify likely members both in the core of Tucana II and several half-light radii away from it. This result demonstrates that SkyMapper photometry and *Gaia* proper motions very efficiently identify likely member stars of UFDs, and by extension, alleviate the problem of foreground contamination when studying these systems.

We further note that our selection procedure excludes all known non-members in the core of Tucana II. This fact implies that it may be possible to identify members of Tucana II, agnostic of the spatial distribution of stars. Purely as an exercise, we recompute membership probabilities after excluding the spatial terms in Equation 2.2 and present the result in the bottom panels of Figure 2-11. We find, as expected, that we still exclude all known non-members in the core of Tucana II and re-identify the likely members on the red giant branch. We additionally find a number of candidate members that are many half-light radii from the center of the system. In upcoming work, we indeed confirm the membership status of a handful of these distant stars (A. Chiti et al., in prep), which is suggestive of a more spatially extended population of stars, some tidal disturbance, or a need to revisit the structural parameters of the system.

2.5.3 Metallicity distribution of likely Tucana II members

Given the membership probabilities obtained using Equation 2.2 in Section 2.5.2, we can now derive a MDF for Tucana II including spatial priors. We compile the photometric metallicity values and uncertainties derived in Section 2.4, together with our membership probabilities (see Section 2.5.2). We then generate a Gaussian for each star in which the mean is the photometric metallicity, with one σ being equal to the uncertainty in the photometric metallicity, and the amplitude being equal to the

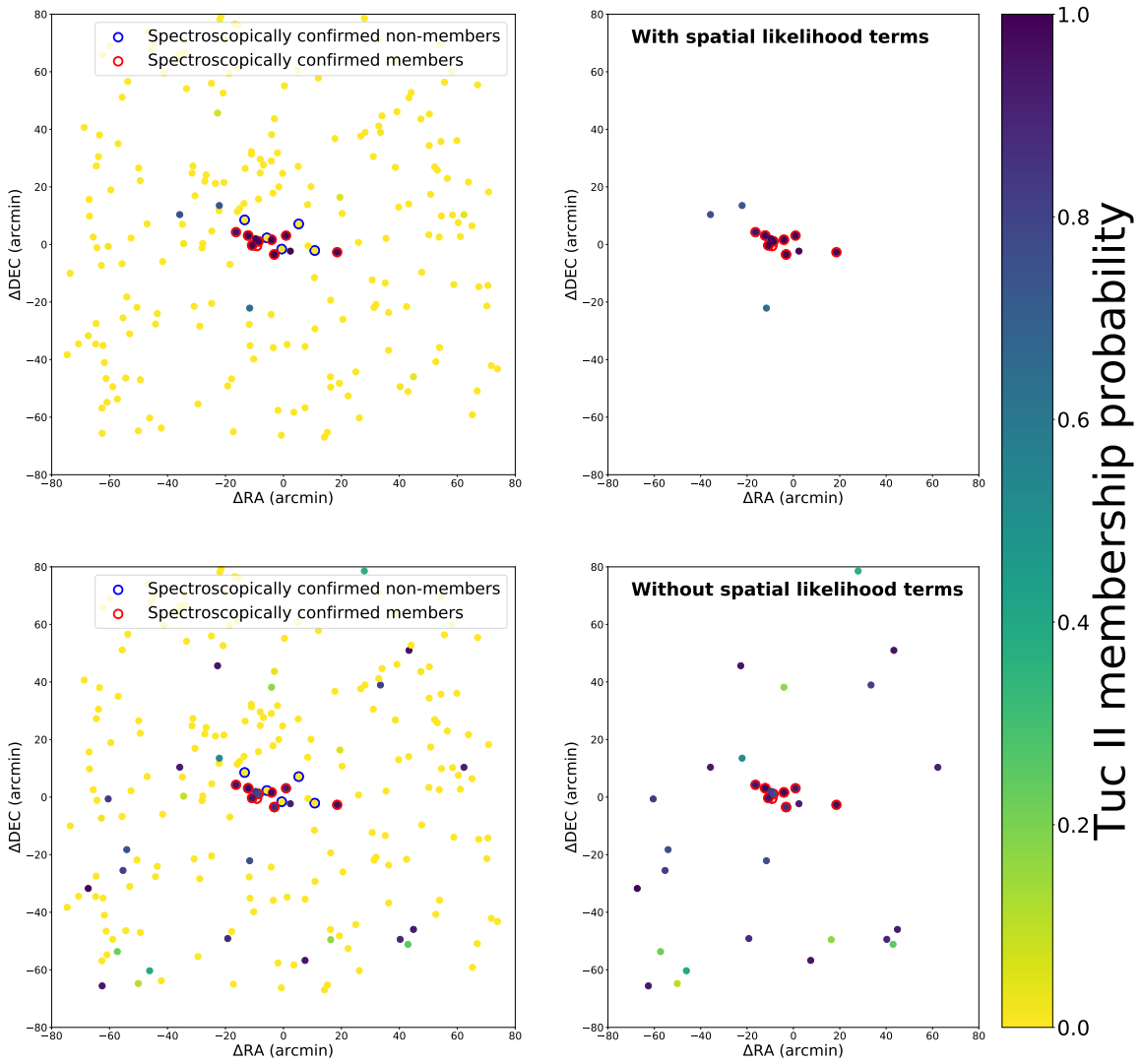

Figure 2-11 Top left: Spatial distribution of stars, colored by their membership probability using the likelihood function in Equation 2.2. Stars with membership probabilities $p > 0.95$ and $g < 20$ in Walker et al. [1], as well as additional confirmed members from Chiti et al. [12], are outlined in red. Stars with membership probabilities $p < 0.50$ and $g < 20$ in Walker et al. [1] are outlined in blue. Top right: Same as left panel, but only including stars with membership probability of $p > 0.10$ from our study. We find that we exclude all known non-members and recover all known members in the literature, except for one horizontal branch star, which naturally would have been excluded by our selection along the red giant branch of an isochrone. Bottom panels: Same as top panels, but membership probabilities are computed excluding the spatial terms in the likelihood function in Equation 2.2. We find several additional candidate member stars in Tucana II that are distant from the center of the system. However, further investigation is needed before these distant stars can be classified as likely members. Note that the color scheme for membership probabilities is different compared to that used in Figure 2-10, to visually aid the identification of marginal members.

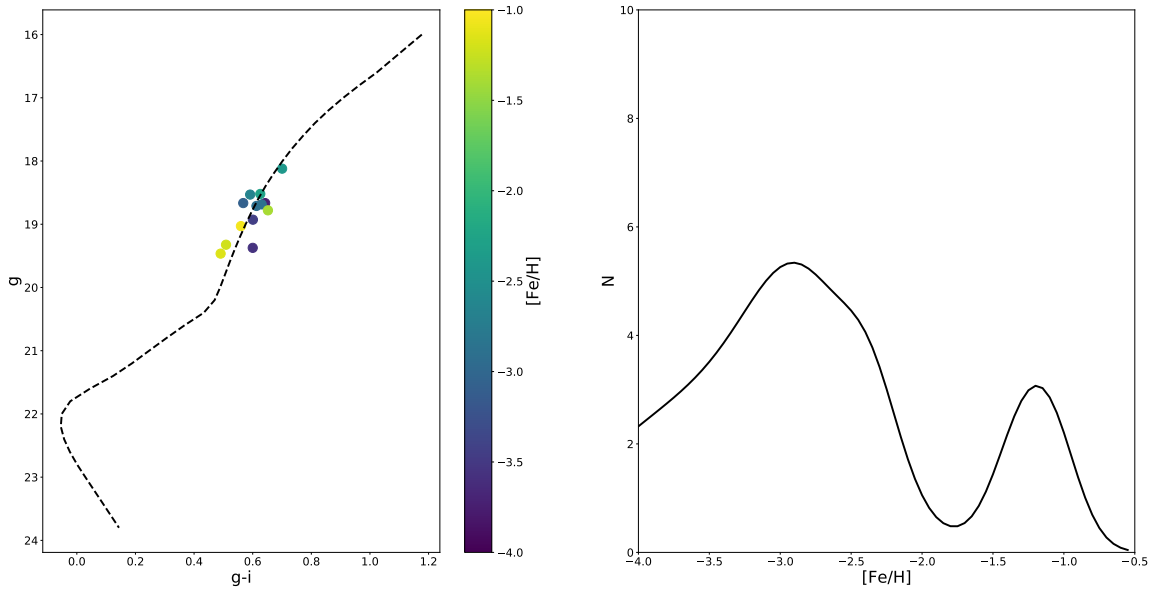

Figure 2-12 Left: color-magnitude diagram of Tucana II with stars that have membership probability $p > 0.50$, based on the methodology presented in this paper. Each star is colored by its photometric metallicity value. A 12 Gyr, [Fe/H] $= -2.5$ MIST isochrone is overplotted for reference [14, 15]. Right: metallicity distribution function (MDF) of the Tucana II UFD based on our membership likelihood analysis. It is largely composed of extremely metal-poor stars with [Fe/H] ~ -3 but we also find a population of stars at photometric [Fe/H]~ -1.25. The latter group is suggestive of additional carbon-enhanced metal-poor giants with overestimated metallicities (see Section 2.4.3 for discussion). We note that all stars with photometric [Fe/H] > -1.0 are removed from our sample, and our grid for deriving metallicities extends down to [Fe/H] $= -4.0$. Thus, our MDF is only populated by stars with metallicities between those values, and extensions above [Fe/H] $= -1.0$ and below [Fe/H] $= -4.0$ are due to uncertainties in the photometric [Fe/H] for individual stars.

membership probability. We then simply sum these Gaussians to generate a MDF. The result is shown in Figure 2-12.

We find a population of extremely metal-poor stars in this distribution which makes Tucana II one of the most metal-poor galaxies, with a MDF peaking at [Fe/H]~ -2.9. This result follows earlier investigations that also yielded overall low metallicities for the system [2, 12]. However, we also find a more metal-rich component around [Fe/H]~ -1.25. If these photometric [Fe/H] values are taken at face value, this higher metallicity component would suggest an extended formation history for the system. Any indications for an extended star formation history might, however, suggest that even more stars at higher metallicity are present in the system. This has not been found by other studies, as all other UFDs have been shown to not contain stars with [Fe/H] > -1.0 [121]. It is thus unlikely that the apparent bump at [Fe/H]~ -1.25 represents a truly metal-rich component. As discussed in detail in Section 2.4.3, the absorption features around the Ca II K line (most importantly the CN feature) artificially increase the measured metallicity of each star in accordance with their carbon abundance. Thus, the high metallicity population may instead be indicative of the presence of strongly carbon-enhanced CEMP stars in Tucana II. Given that the metal-poor halo population contains a significant fraction of CEMP stars [8] and that UFDs have not yielded many strongly enhanced CEMP stars ([C/Fe] > 1.0), this is an interesting option to explore further with spectroscopic followup observations.

2.6 Conclusion

In this paper, we present an application of deep imaging carried out with the SkyMapper telescope to derive stellar parameters for stars. We find that by modeling the predicted fluxes for stars over a wide range of stellar parameters, we can accurately and precisely measure the $\log g$ and metallicities of stars, solely from photometry.

We then apply this technique to the Tucana II UFD. Previous studies of UFDs were hampered by the presence of foreground, metal-rich main-sequence stars. We

Table 2.4. Photometric metallicities of stars with Tucana II membership probabiliy $p_{\rm mem} > 0.50$

RA (deg) (J2000)	DEC (deg) (J2000)	$g_{\rm SM}$	$i_{\rm SM}$	$p_{\rm mem}$	$[{\rm Fe/H}]_{\rm phot}$	$\sigma([{\rm Fe/H}]_{\rm phot})$
342.671075	−58.518976	18.58	17.94	1.00	−2.66	0.26
342.959507	−58.627823	18.17	17.42	1.00	−2.40	0.19
343.136343	−58.608469	19.42	18.77	1.00	−3.56	0.75
342.929412	−58.542702	18.73	18.06	1.00	−2.89	0.31
343.089087	−58.518710	19.51	18.97	1.00	−1.16	0.21
342.753839	−58.537255	19.37	18.81	0.99	−1.21	0.20
342.784619	−58.552258	18.57	17.90	0.99	−2.27	0.21
342.715112	−58.575714	18.76	18.10	0.99	−2.92	0.32
343.652659	−58.616101	18.71	18.10	0.99	−3.08	0.41
342.537105	−58.499739	18.72	18.02	0.96	−3.73	0.75
341.916360	−58.402040	19.09	18.47	0.75	−1.05	0.19
342.352876	−58.346508	18.83	18.13	0.73	−1.39	0.18
342.687905	−58.939023	18.98	18.33	0.64	−3.44	0.75

demonstrate that by leveraging these photometric stellar parameters, we can efficiently identify member stars of these generally metal-poor systems and derive photometric metallicities for these stars. We can also derive quantitative membership probabilities by using *Gaia* DR2 proper motion data, after removing foreground contaminants using our photometric stellar parameters.

Using these membership probabilities, we are able to (1) identify a handful of stars several half-light radii from the center of Tucana II that have high membership probabilities and (2) derive a MDF for the system. We identify additional possible members of the Tucana II UFD upon removing the spatial likelihood terms when computing membership probabilities. Follow-up spectroscopy of several of these stars will be presented in an upcoming paper (A. Chiti et al, in prep), in which we find that a handful of distant stars are indeed members, based on spectroscopic metallicities and radial velocity measurements. The MDF of Tucana II is either suggestive of an extended period of star formation history, or the presence of some very carbon-enhanced metal-poor stars in Tucana II, with the latter option being more likely. Future work will apply this technique to other UFDs to derive spatially complete

MDFs and to investigate whether any other UFDs may host a spatially extended population of stars.

Chapter 3

Chemical abundances of new member stars in the Tucana II dwarf galaxy

The content of this chapter was published in the Astrophysical Journal as [12] on April, 2018.

Abstract

We present chemical abundance measurements for seven stars with metallicities ranging from Fe/H] = −3.3 to [Fe/H] = −2.4 in the Tucana II ultra-faint dwarf galaxy (UFD), based on high-resolution spectra obtained with the MIKE spectrograph on the 6.5 m Magellan-Clay Telescope. For three stars, we present detailed chemical abundances for the first time. Of those, two stars are newly discovered members of Tucana II and were selected as probable members from deep narrow band photometry of the Tucana II UFD taken with the SkyMapper telescope. This result demonstrates the potential for photometrically identifying members of dwarf galaxy systems based on chemical composition. One new star was selected from the membership catalog of Walker et al. [1]. The other four stars in our sample have been re-analyzed, following additional observations. Overall, six stars have chemical abundances that are characteristic of the UFD stellar population. The seventh star shows chemical abundances that are discrepant from the other Tucana II members and an atypical, higher strontium abundance than what is expected for typical UFD stars. While unlikely, its strontium abundance raises the possibility that it may be a foreground metal-poor halo star with the same systemic velocity as Tucana II. If we were to exclude this star, Tucana II would satisfy the criteria to be a surviving first galaxy. Otherwise,

this star implies that Tucana II has likely experienced somewhat extended chemical evolution.

3.1 Introduction

The elements in the atmospheres of metal-poor stars allow us to study the chemical composition of the early universe. The elements in stellar atmospheres reflect the composition of a star's formative gas cloud. Thus, a low surface metal abundance of a metal-poor star indicates its natal gas cloud must have undergone relatively few cycles of chemical enrichments (e.g., from supernovae). This lack of enrichment implies that metal-poor stars generally formed earlier than typical solar-metallicity stars, and that metal-poor stars can be used to probe the composition of the early universe in which they formed.

The iron abundance is typically used as a proxy for the overall metal context (or "metallicity") of a star and metal-poor stars are defined to have an iron abundance of $[\mathrm{Fe/H}] \leq -1$ dex, where $[\mathrm{Fe/H}] = \log_{10}(N_{\mathrm{Fe}}/N_{\mathrm{H}})_{\star} - \log_{10}(N_{\mathrm{Fe}}/N_{\mathrm{H}})_{\odot}$ [99]. Of particular interest are the most metal-poor stars, such as very metal-poor stars (VMP; $[\mathrm{Fe/H}] \leq -2.0$) and extremely metal-poor stars (EMP; $[\mathrm{Fe/H}] \leq -3.0$). The abundance of various elements (i.e., carbon, neutron-capture elements) as a function of overall [Fe/H] for VMP and EMP stars sheds light on the nature of the chemical evolution of the early universe [169, 170, 17, 8]. Stars with $[\mathrm{Fe/H}] \leq -4.0$ can be used to constrain the yields and properties of the very first supernovae [e.g., 102] and by extension, properties of the first stars [171]. Metal-poor stars have also been used to trace old substructure in the Milky Way (e.g., Starkenburg et al. 125), and to address a number of questions related to galaxy formation and cosmology [172, 173, 55, 174, 175, 99].

The simpler formation history of dwarf galaxies makes them an ideal laboratory to use metal-poor stars for studying topics such as chemical evolution, star formation history, and stellar populations [176]. Furthermore, faint dwarf galaxies are thought to be the surviving analogs of the ancient galaxies that were accreted to form the Milky Way halo [20, 177], and are also themselves older and more metal-poor than

some components of the Milky Way such as the disk [178, 179]. Thus, studying the metal-poor stars in these systems provides insights on the nature of the first galaxies and the origins of the of chemical signatures of the VMP and EMP stellar population in the halo [180].

Ultra-faint dwarf galaxies (UFDs), in particular, are among the oldest ($\geq$10 Gyr), most metal-poor (typically a mean [Fe/H]< -2.0), and dark-matter dominated ($M/L_V \gtrsim 100$) [e.g., 109] dwarf galaxy systems. These characteristics make stars in UFDs especially promising targets to study the aforementioned questions. Several surveys over the past decade have detected dozens of UFDs [106, 181, 107, 182, 183, 37, 184, 185, 186, 13, 187, 188, 189, 190, 191], thus greatly increasing the prospect for studying the population of metal-poor stars in their environments.

To investigate the detailed chemical composition of stars, it is necessary to obtain high-resolution spectra. Results already show the utility of detailed studies of the composition of metal-poor stars in UFDs. For instance, the strong over-abundance of neutron-capture elements associated with the r-process in seven stars in the Reticulum II UFD has constrained the dominant astrophysical site of the r-process [82]. However, only 59 stars have been observed with high-resolution spectroscopy in 14 UFD systems [18, 19, 20, 21, 22, 23, 24, 25, 26, 27, 28, 29, 30, 2, 31, 32, 33, 34, 35, 36] since the low stellar mass ($\lesssim 10^4 M_\odot$), distance ($d \gtrsim 30$ kpc), and lack of giant branch stars in UFDs [e.g., 192] strictly limits the stars for which high-resolution spectroscopy can be performed with current technology. Adding to the observational burden, medium-resolution spectroscopy is required to identify which stars in their field are members of these systems before high-resolution observations can be carried out. All of these reasons make the time required to identify and observe member stars of UFDs a bottleneck to progress in the field.

In this paper, we present the chemical abundances of seven stars with [Fe/H] ranging from -2.4 to -3.3 dex in the UFD Tucana II [37, 13] derived from high-resolution spectroscopy. Two stars are new members that were identified from photometry of the Tucana II dwarf galaxy obtained with the filter set on the SkyMapper telescope (Chiti et al. 2018, in prep). The discovery of these stars motivated studying Tucana

Table 3.1. MIKE observations of stars in Tucana II

Name	RA (h:m:s) (J2000)	DEC (d:m:s) (J2000)	Slit size	g (mag)	$t_{\rm exp}$ (min)	S/N[a]	$v_{\rm helio}$ (km/s)
TucII-006	22:51:43.06	−58:32:33.7	1.″0	18.78	206[b]	15, 30	−126.1
TucII-011	22:51:50.28	−58:37:40.2	1.″0	18.27	314[b]	15, 30	−124.6
TucII-033	22:51:08.32	−58:33:08.1	1.″0	18.68	155[b]	17, 32	−126.9
TucII-052	22:50:51.63	−58:34:32.5	1.″0	18.83	155[b]	17, 35	−119.9
TucII-078	22:53:06.67	−58:31:16.0	1.″0	18.62	215	15, 30	−123.8
TucII-203	22:50:08.87	−58:29:59.1	1.″0	18.81	275	16, 37	−126.1
TucII-206	22:54:36.67	−58:36:57.9	1.″0	18.81	385	15, 37	−122.9

[a]S/N per pixel is listed for 4500 Å and 6500 Å

[b]Combined exposure time from Ji et al. [2] and this work

II in more detail. We also observed one new star that was previously confirmed as a member by Walker et al. [1]. To supplement the new observations, we decided to re-analyze the four stars with published measurements from Ji et al. [2], after collecting additional data to improve measurement precision. Since observations suggest that UFDs contain no members with [Fe/H] > -1, selecting metal-poor stars from photometry is a potentially powerful way to identify significant numbers of UFD members for spectroscopic follow-up observations. This has the potential for bypassing the expensive medium-resolution spectroscopy step of the process, and thus accelerating the characterization of UFDs and other dwarf galaxies.

This paper is organized as follows. We outline the target selection procedure and observations in Section 3.2, discuss the abundance analysis in Section 3.3, present the chemical signatures of stars in Tucana II and implications in Sections 3.4, and conclude in Section 3.5.

3.2 Target Selection and Observations

3.2.1 Members from Walker et al. [1]

Ji et al. [2] observed TucII-006, TucII-011, TucII-033, and TucII-052 with the MIKE spectrograph (see Table 3.1). All four stars were selected from the membership catalog of Walker et al. [1]. They observed each star between 100 mins to 4.42 hrs in

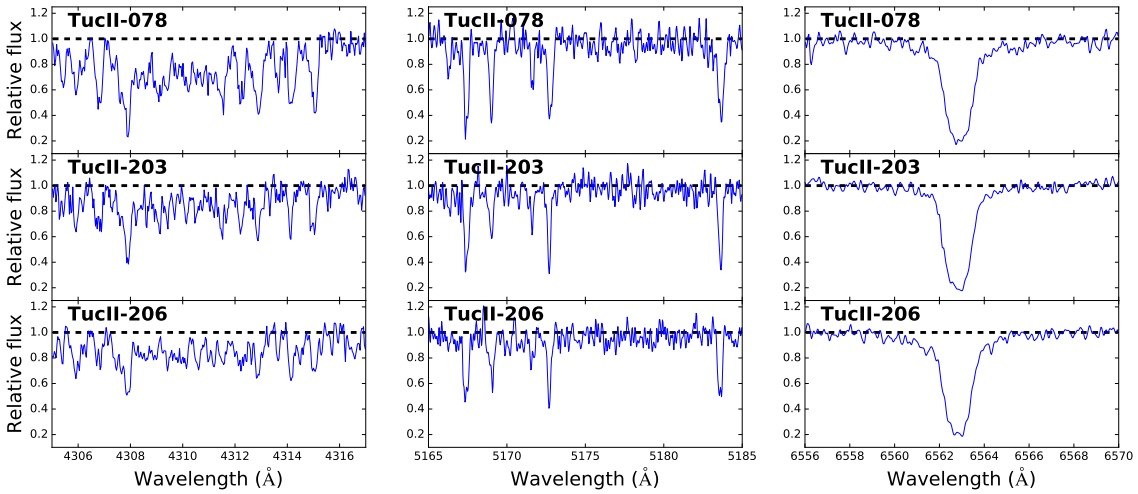

Figure 3-1 Plots of the CH region (left), Mg b line region (center), and Hα feature (right) for each of the Tucana II members with no prior high-resolution chemical abundance measurements available. TucII-078 was spectroscopically identified as member [1], while TucII-203 and TucII-206 were identified based on narrow band photometry.

August 2016 with the MIKE spectrograph on the Magellan-Clay telescope. For the stars with the shortest exposure times (TucII-033 and TucII-052), this precluded the measurement of several elements and led to large uncertainties in the measurement of the abundances of several other elements. Thus, we re-observed each star in [2] for an additional 55 mins to address the aforementioned deficiencies. In addition to re-observing these stars, we observed an additional member (TucII-078) from Walker et al. [1] that had not previously been observed with a high-resolution spectrograph.

3.2.2 Members selected from SkyMapper photometry

Through a P.I. program, we obtained SkyMapper photometry of Tucana II using the 1.3 m telescope at Siding Spring Observatory. In an upcoming paper, we will fully discuss the implementation of the SkyMapper filter-set to determine photometric metallicities (Chiti et al. 2018, in prep) but we briefly discuss the method here. The SkyMapper filter set includes a narrow-band v filter that covers the prominent Ca II K line at 3933.7 Å [135]. Given the strength of this line, the preponderance or lack of metals sufficiently affects the line strength which changes the total flux through this filter. Thus, a metal-poor star with a weak Ca II K line appears brighter in

this filter than more metal-rich stars. To quantify this effect, we generated a grid of flux-calibrated spectra using the Turbospectrum synthesis code [193, 148], the MARCS model atmospheres [149], and a line list derived from the VALD database [150, 151]. The stellar parameters of our grid covered the expected stellar parameters ($4000 < T_{\rm eff}\,[{\rm K}] < 5700; 1 < \log g < 3$) and metallicities ($-4.0 <$ [Fe/H] < -0.5) of RGB stars in dwarf galaxies. We closely followed the methodology of Bessell and Murphy [194] and Casagrande and VandenBerg [159] to generate a library of synthetic photometry through the SkyMapper u, v, g, and i filters for spectra in this grid.

By relating our observed SkyMapper photometry in the v, g, and i filters to the synthetic photometry from our grid, we selected a few metal-poor targets for spectroscopic test observations. Two of these targets (TucII-203 and TucII-206) were confirmed as members of Tucana II since radial velocity measurements from their MIKE spectra were similar to the systemic velocity of Tucana II of $-129.1\,{\rm km/s}$ [1].

3.2.3 High-resolution spectroscopy

The data in this paper were obtained with the Magellan Inamori Kyocera Echelle (MIKE) spectrograph on the Clay telescope at Las Campanas Observatory [195]. The observations were taken between August 14-17 and October 7-11, 2017. Examples of the spectra are shown in Figure 3-1. The location of each star in the color magnitude diagram of Tucana II is shown in Figure 3-2. Targets were observed with 2x2 binning and the $1\farcs0$ slit (R $\sim$ 28,000 on the blue chip and R $\sim$ 22,000 on the red chip) covering $\sim$3500 Å to $\sim$ 9000 Å. The weather was mostly clear on all nights. The spectra were all reduced and wavelength-calibrated with the MIKE CarPy pipeline[1] [196].

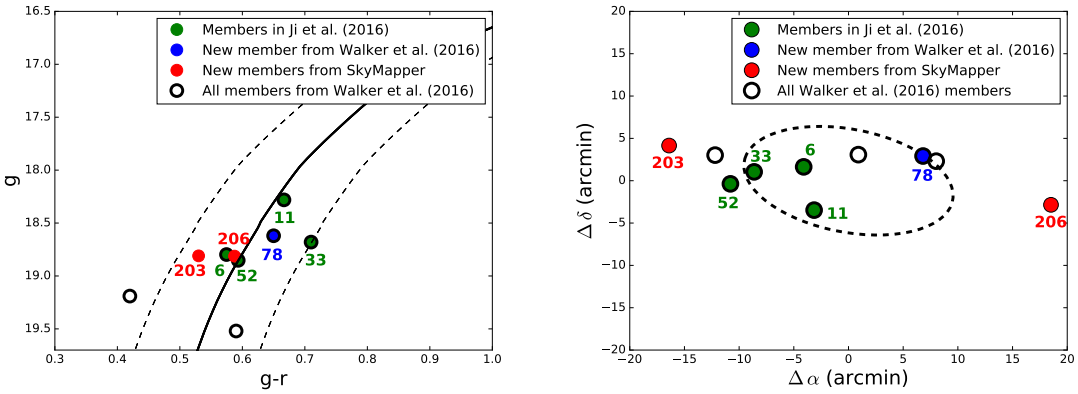

Figure 3-2 Left: Color magnitude diagram of Tuc II stars from this study. A Dartmouth isochrone [10] with an age of 12.5 Gyr, distance modulus of 18.8, and a metallicity of [Fe/H] = −2.5 is overplotted in black along with offsets of (g−r)±0.1 in dashed lines to guide the eye. We denote with different colors the four members previously observed by Ji et al. [2], one member selected from Walker et al. [1], and two selected from our SkyMapper photometry. Open circles indicate confirmed members in Walker et al. [1] with no high-resolution spectroscopic observations. Right: Spatial distribution of Tuc II members centered on the coordinates of Tucana II. The elliptical half-light radius from Koposov et al. [13] is overplotted. In both plots, each star is labeled by its identifier as found Table 3.1.

Table 3.2. Stellar parameters of stars in Tucana II

Name	$T_{\rm eff}$ (K)	Log g (dex)	$v_{\rm micro}$ (km s^{-1})	[Fe/H] (dex)
TucII-006	5017 ± 227	1.50 ± 0.54	1.95 ± 0.24	-2.93 ± 0.27
TucII-011	4693 ± 158	1.25 ± 0.50	1.95 ± 0.21	-2.92 ± 0.16
TucII-033	4828 ± 153	1.40 ± 0.53	1.80 ± 0.21	-2.41 ± 0.12
TucII-052	4819 ± 195	1.70 ± 0.42	1.85 ± 0.23	-3.23 ± 0.20
TucII-078	4954 ± 178	1.90 ± 0.67	2.20 ± 0.23	-2.69 ± 0.20
TucII-203	4882 ± 186	1.60 ± 0.33	2.00 ± 0.22	-3.08 ± 0.19
TucII-206	4900 ± 186	1.65 ± 0.85	1.90 ± 0.26	-3.34 ± 0.28

3.3 Abundance Analysis

3.3.1 Derivation of stellar parameters and chemical abundances

The python-based Spectroscopy Made Hard (SMH) analysis software first described in Casey [197] was used for the majority of our analysis, including normalizing spectra, measuring equivalent widths, and generating synthetic spectra. Our version of this software made use of the 2011 version of MOOG [198], which has an updated treatment of scattering from Sobeck et al. [199]. The spectroscopic stellar parameter adjustment scheme by Frebel et al. [59] is based on this version. We used α-enhanced, 1D plane-parallel stellar model atmospheres from Castelli and Kurucz [200]. The line list in Roederer et al. [17] was used for identifying lines and deriving abundances from equivalent width measurements. For spectral syntheses, we supplemented this line list with those used in Ji et al. [32]. Namely, we incorporated lines from Hill et al. [201], Den Hartog et al. [202], Ivans et al. [203], Lawler et al. [204], Lawler et al. [205], Sneden et al. [206], and Masseron et al. [53]. Our chemical abundances are listed relative to the solar abundances of Asplund et al. [207].

We derived radial velocities by cross-correlating our observed spectra with a template spectrum of HD140283 over the Hβ feature at 4861 Å. Heliocentric velocity corrections were derived using the `rvcorrect` task in `IRAF`. We find evidence that TucII-078 may be in a binary, since our measured velocity is $\sim 12\,\mathrm{km/s}$ greater than the velocity reported in Walker et al. [1].

We determined stellar parameters and chemical abundances following Frebel et al. [59] whose methodology we briefly outline in this paragraph. First, equivalent widths were measured by fitting a Gaussian profile to each line. We generally excluded lines with reduced equivalent width measurements greater than -4.5, since these measurements potentially lie outside the linear regime of the curve of growth. We varied the stellar parameters ($T_{\rm eff}$, $\log g$, $v_{\rm micro}$, and [Fe/H]) until our Fe I abundances showed no trend with both excitation potential and reduced equivalent width. We further constrained $\log g$ by requiring our Fe I and Fe II abundances to match. We

[1] http://code.obs.carnegiescience.edu/mike

then corrected our $T_{\rm eff}$ with the prescription given in Frebel et al. [59], but re-adjusted $\log g$, $v_{\rm micro}$, and [Fe/H] until the above criteria were again satisfied. To determine random uncertainties, stellar parameters were varied to match the 1σ uncertainty in the Fe I abundance trends. These random uncertainties were added in quadrature to the systematic uncertainties, which were assumed to be 150 K for $T_{\rm eff}$, 0.3 dex for $\log g$, and 0.2 km s^{-1} for $v_{\rm micro}$. Final stellar parameter measurements are listed in Table 3.2.

We followed a few prescriptions to determine uncertainties for abundances based on equivalent width measurements. For abundances measured with a large number of lines (N $\geq$ 10), we take the standard deviation of the individual line abundances as the random uncertainty. We adopt the standard deviation as it well represents abundance uncertainties obtained from data with poor signal to noise. For abundances with a small number of lines (1 $<$ N $<$ 10), we derived random uncertainties by multiplying the range covered by the line abundances by the k-statistic following Kenney [208] to obtain a standard deviation. The k-statistic gives measurements with a smaller number of lines an appropriately larger uncertainty. For abundances derived from only one line measurement, we derived the random uncertainty by varying the continuum placement and assuming the resulting abundance variation as the uncertainty. If any resulting random uncertainty was below the standard deviation of the abundances of the iron lines, we nominally adopt as a conservative random uncertainty the standard deviation of the iron abundance (0.12 dex to 0.27 dex). The total uncertainty for each element was then determined by adding the random uncertainty in quadrature with the systematic uncertainties. The systematic uncertainties were assumed to be the difference in the abundances caused by varying each stellar parameter by its 1σ uncertainty.

For abundances measured by spectrum syntheses, we also derived uncertainties by adopting the procedure in the previous paragraph. If an element had only one synthesized line, the random uncertainty was assumed to be the change in abundance that was required to capture the variations of the continuum placement. The systematic uncertainty was obtained by measuring the change in the abundance after

varying each stellar parameter by its 1σ uncertainty. If an element had measured abundances from both spectrum synthesis and equivalent width measurements, we pooled the measurements and derived random uncertainties following the procedure outlined in the previous paragraph. The random uncertainty was then added in quadrature with the systematic uncertainties for each star to derive a total uncertainty. Certain elements (e.g., Al and Si) had absorption features that were detected in our data, but the signal to noise was too poor to derive a meaningful abundance and especially uncertainty. However, we report tentative abundances but mark them with a colon in Table 3.3 to indicate a large uncertainty. Our measurements and uncertainties are listed in Tables 3.3 and 3.4. Our individual equivalent width and synthesis measurements are listed in Table 3.5.

3.3.2 Comparison to Ji et al. [2] and Walker et al. [1]

We compare our results with measurements from Ji et al. [2] and Walker et al. [1] to check consistency with previous studies of Tucana II. We focus on comparisons with Ji et al. [2], with whom we have four stars in common, as they also analyzed high-resolution spectra from the MIKE spectrograph.

We first discuss our measured stellar parameters and chemical abundances of TucII-006, TucII-011, TucII-033, and TucII-052 in comparison to those presented in Ji et al. [2]. For TucII-011 and TucII-052, we find excellent agreement (within 1σ) in stellar parameters and chemical abundances. For TucII-006, we measure a discrepant $\log g$ by 0.4 ± 0.4 dex, a discrepant microturbulence by 0.25 ± 0.26 dex, and a discrepant [Fe/H] by 0.25 ± 0.21 dex, where the uncertainties are from Ji et al. [2]. However, 0.15 dex of the discrepancy in [Fe/H] can be explained by differences in the stellar parameters, and the discrepancy in the stellar parameters can be explained by the lack of Fe II measurements for that star in Ji et al. [2]. We measure three Fe II lines for the same star due to the better S/N of our spectra. This comparison underscores the importance of propagating stellar parameter uncertainties to final abundance uncertainties, particularly in the case of spectra with low S/N and few lines. For TucII-033, we measure a larger microturbulence and [Fe/H], which partially

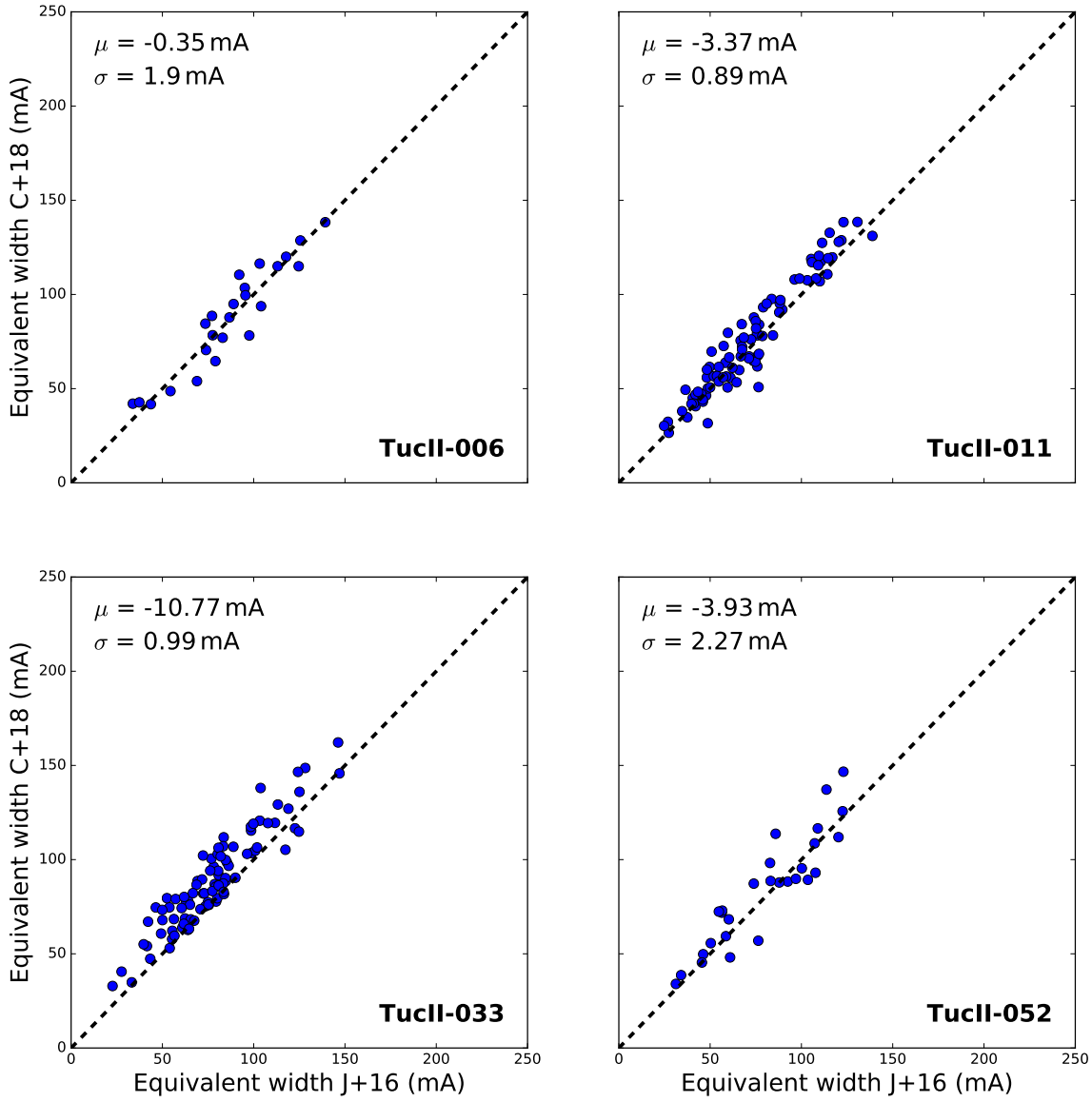

Figure 3-3 Comparison of the equivalent widths of Fe I lines measured on the same spectra using our method and Ji et al. [2]. The mean offset and standard error in the mean between our measurements are listed in each panel.

contributed to large discrepancies in the measurements of the Sr and Ba abundances (see Section 3.4.1). To isolate whether the discrepancies in measurements of TucII-033 were indeed due to the better S/N of our spectra, we performed our analysis on exactly the spectra used in Ji et al. [2]. Furthermore, we chose to analyze the spectra of all four stars in Ji et al. [2] as a check on our method of measuring equivalent widths and deriving stellar parameters.

Applying our methodology to the same spectra that Ji et al. [2] analyzed gives broadly consistent results. We recover their measured $T_{\rm eff}$ within their reported 1σ bounds. We also recover their $\log g$ measurements to within 1σ for all stars. We find general agreement within 2σ between our microturbulence measurements and no obvious systematic effects.

All [Fe/H] measurements agree within 1σ as well, but we measure a larger [Fe/H] by at least 0.15 dex for three stars (TucII-006, TucII-033, and TucII-052). For the star with the largest discrepancy (TucII-033), we thus inspected the equivalent width measurements. After inspecting fits to the individual absorption lines, it became apparent that the discrepancy is likely due to unfortunate continuum placement issues with the automated continuum fitting routine in previous work. We thus inspected and compared equivalent widths of all stars, as shown in Figure 3-3. We find a small (somewhat) statistically significant difference between measurements for TucII-001 and TucII-052 but which are overall on the level of 3-4 m Å, and thus not a source for any significant abundance differences. No offset is found for TucII-006. For TucII-033, there is indeed a significant offset, of ~ 10 m Å, which indeed explains why we measure systematically increased [Fe/H].

We conclude that any abundance discrepancies are consistent with previous uncertainties, but we now have significantly better S/N than before. Thus, differences in our final stellar parameters and abundances between this work and Ji et al. [2] are likely due to the additional observations that we have combined with theirs for a new analysis presented here.

Walker et al. [1] measured metallicities for their Tucana II stars by matching their observed spectra of the Mg b region ($\sim$5150 Å) to a grid of synthetic spectra in the

Segue Stellar Parameters Pipeline [SSPP; 209]. They obtained R ∼18,000 spectra of their brighter targets and R ∼10,000 of their fainter targets. We find that our metallicities are typically much lower (at least ∼0.50 dex) than those in Walker et al. [1] for the five stars in common, including the four stars in Ji et al. [2]. There is no obvious significant systematic difference between other stellar parameters that could explain this offset. We do measure lower $T_{\rm eff}$ values by 70 K on average, but this difference does not explain such a large difference in the metallicities. Neither do we see trends in our measured Mg abundances that could affect the Mg b region, and consequently, the metallicity measurements in Walker et al. [1]. Much of the discrepancy, however, can be attributed to the fact that Walker et al. [1] applied a metallicity offset of 0.32 dex to their measurements based on an offset with respect to the measured metallicity of a solar spectrum, which may not be appropriate in our case, given that the Sun and these dwarf galaxy stars have very different stellar parameters.

3.4 Chemical signatures of the Tucana II stellar population

We first explore the possibility that TucII-033 is a halo interloper in Section 3.4.1. Then, we discuss the trends of element abundances provided, and how they characterize the stellar population of Tucana II in the remainder of this section.

3.4.1 Is TucII-033 a member of Tucana II?

Traditionally, the membership status of stars in dwarf galaxies is derived from a combination of velocity and metallicity measurements. However, the detailed chemical abundances of candidate member stars might also be used to determine membership because UFDs are expected to show distinct chemical signatures (e.g., lower Fe, Sr, Ba) compared to the halo background. Additional evidence for non-membership might be gained if any star has chemical abundances distinct from those of other stars in the sample. The small number of stars currently known in UFDs that do not necessarily yield well-defined abundance trends over large parameter space (e.g., [Fe/H])

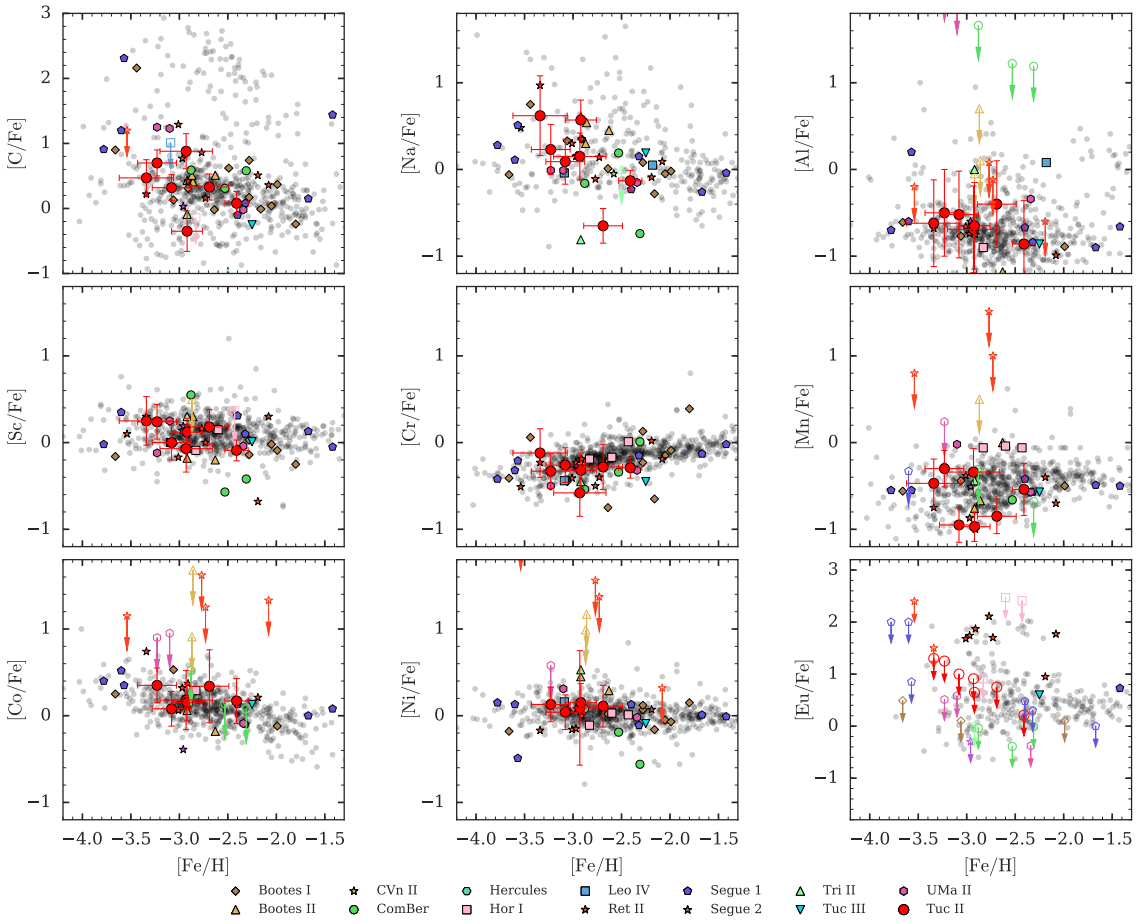

Figure 3-4 [X/Fe] vs. [Fe/H] ratio for the abundances of carbon, the odd-Z elements, the iron-peak elements, and europium. Gray data points correspond to stars in the halo [16, 17]. Colored symbols are UFD stars. Error bars correspond to random uncertainties; see Table 3.4 for total uncertainties. Abundances marked by colons (:) in Table 3.3 are shown with uncertainties of 0.5 dex. The carbon abundances in this plot are not corrected for the evolutionary state of each star following [8]; see Table 3.3 for corrected carbon abundances. In general, the abundances of these elements in Tucana II stars agree with trends in other UFDs and the Milky Way halo. UFD abundances are from Koch et al. [18], Feltzing et al. [19], Frebel et al. [20, 21, 22], Norris et al. [23, 24], Simon et al. [25], Gilmore et al. [26], Koch et al. [27], Ishigaki et al. [28], Koch and Rich [29], Roederer and Kirby [30], Ji et al. [2, 31, 32], Hansen et al. [33], Kirby et al. [34], Venn et al. [35], Nagasawa et al. [36].

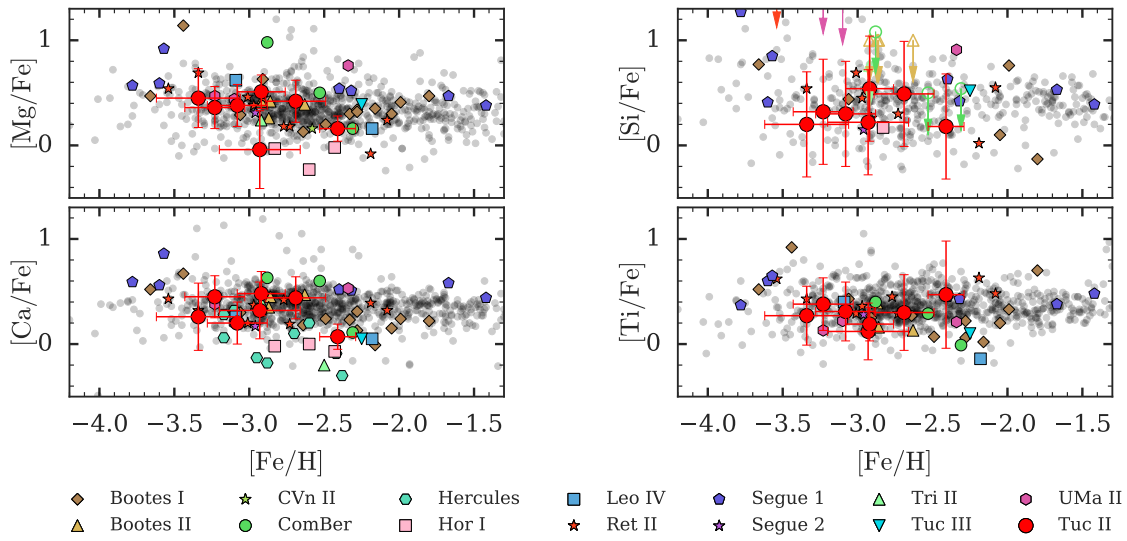

Figure 3-5 [X/Fe] vs. [Fe/H] ratio of abundances of α-element abundances in stars in Tucana II. Gray data points correspond to stars in the halo [16, 17]. Colored symbols are UFD stars. Error bars correspond to random uncertainties; see Table 3.4 for total uncertainties. Abundances marked by colons (:) in Table 3.3 are shown with uncertainties of 0.5 dex. The decrease in the [α/Fe] ratio of the most metal-rich star (TucII-033) would suggest that Tucana II had an extended star formation history, but see Section 3.4.1 for a discussion on the membership of TucII-033.

requires, in particular, that any claim of chemical (non-)membership be investigated thoroughly. In this section, we thus discuss if any stars in our sample have chemical signatures that challenge their radial velocity membership status.

All stars in our sample except one have abundances that are consistent with those of typical UFD stars, as can be seen in Figures 3-4, 3-5, and 3-6. The exception is TucII-033, the most metal-rich ([Fe/H] $= -2.41$) star. It displays a Sr abundance ([Sr/Fe] $= -0.39$, [Sr/H] $= -2.8$) that is in disagreement with that of the typical UFD stars [21, 22], and importantly, with that of the other stars in Tucana II. TucII-033 has a [Sr/H] abundance distinctly different by 1.7 dex (a 50 fold increase) from five of the stars in Tucana II, which have an average [Sr/H] $= -4.46$ (with a standard deviation of only 0.14 dex). The remaining star (TucII-078) is also distinct in that it has a low upper limit on its Sr abundance. The lack of Sr in TucII-078 relative to the other Tucana II members is puzzling, but similar stars are known to exist in other UFDs (e.g., Segue I). TucII-033 has an enhancement in Sr that appears to

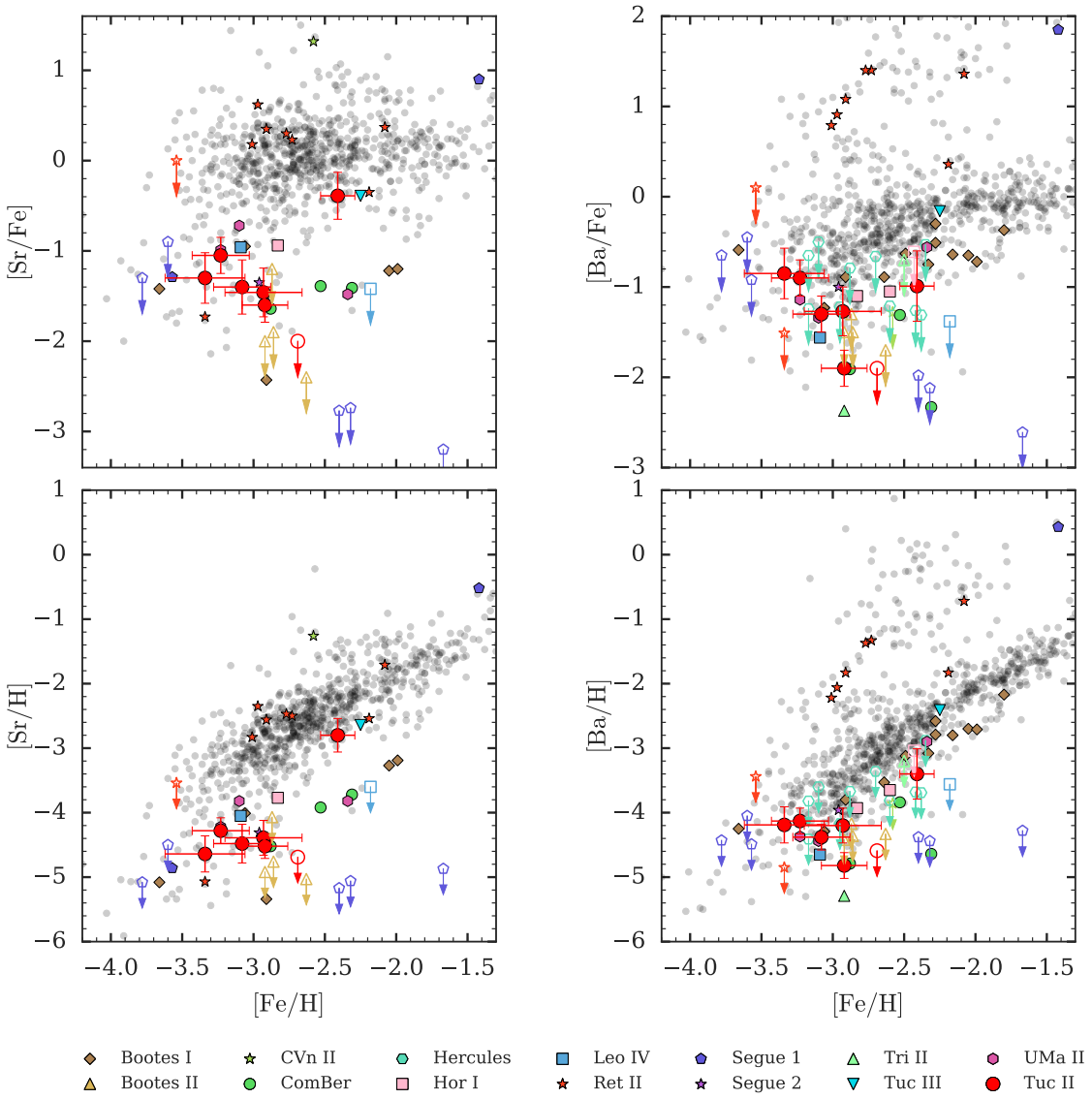

Figure 3-6 [X/Fe] vs. [Fe/H] and [X/H] vs. [Fe/H] ratio of abundances of strontium and barium in stars in Tucana II. Gray data points correspond to stars in the halo [16, 17]. Colored symbols are UFD stars. Error bars correspond to random uncertainties; see Table 3.4 for total uncertainties and Section 3.3.1 for a discussion on deriving uncertainties. The most metal-rich star in Tucana II (TucII-033) has Sr and Ba abundances that are above those typically seen in UFD stars.

agree with the trend for halo stars as shown in Figure 3-6, whereas TucII-078 and the other Tuc II members have Sr abundances far below the halo trend. This comparison raises the possibility that TucII-033 might be an interloping halo star with the same systemic velocity as Tuc II.

To further investigate, we determined whether it was plausible for a halo star to have the same systemic velocity of Tucana II ($v_{\rm sys} = -129.1\,{\rm km/s}$; Walker et al. 1). We retrieved the velocities of halo stars with metallicities of [Fe/H] < -2.0 in the literature [210]. We find that this sample of 799 halo stars has a distribution of velocities that is roughly Gaussian and centered on 15 km/s with a standard deviation of 154 km/s. Using this distribution of velocities, we can calculate the odds of finding an interloping halo star around the mean systemic velocity of Tucana II. We derive a 6% chance of finding a halo star within two times the velocity dispersion (8.6 km/s in Walker et al. 1) around the mean velocity of Tucana II, and a 9% chance if we increase the bounds to three times the velocity dispersion. Thus, it is unlikely but not unreasonable for a metal-poor halo star to have the same systemic velocity as Tucana II. As an aside, we do note that considering exclusion from our sample likely does not affect the status of Tucana II as a dwarf galaxy. Walker et al. [1] measure a mean velocity for Tucana II of $-129^{+3.5}_{-3.5}$ km/s and a velocity dispersion of $8.6^{+4.4}_{-2.7}$ km/s. The velocity measurement of TucII-033 ($v_{\rm helio} = -127.5\,{\rm km/s}$) is close to 1σ of the error on the measured systemic velocity of Tucana II. Thus, it is unlikely that the exclusion of this star would remove any velocity spread that is used to classify Tucana II as a UFD.

While there are also stars in Reticulum II [31], a star in Tucana III [33], and a star in Canes Venatici II [211] that show an enhancement in Sr, we do not consider them to be typical UFD stars. In the case of Reticulum II and Tucana III, this Sr enhancement is reflective of strong and moderate r-process enrichments, respectively. Given that the origin of these enhancements clearly derive from r-process events that occurred in these systems, and that these events are regarded rare, we do not consider them to be typical examples of UFDs. Moreover, TucII-033 is not a r-process enhanced star. It is difficult to judge the significance of the one available Sr abundance ([Sr/Fe]

= 1.32) in Canes Venatici II. This star has a Sr enhancement that could be a result of a weak r-process enrichment event [e.g., 212] and in theory, a similar event may have enhanced TucII-033. However, more data from Canes Venatici II is needed to derive firm conclusions. Thus, around the metallicity of TucII-033 ([Fe/H] ~ -2.5), the typical UFD stellar population either has extremely low upper limits on the Sr abundance (i.e., Segue 1; [Sr/H] $\lesssim -4.0$) or marginal detections (e.g., stars in Coma Berenices, Ursa Major II; Frebel et al. 21, 22).

This high Sr abundance measurement of TucII-033 also naturally raises the question of why the Sr abundance was not recognized as such in the previous study of this galaxy. Upon investigation, we find that we measure a higher Sr abundance than Ji et al. [2] by 0.70 dex. However, their Sr abundance has a large uncertainty (~ 0.6 dex) and somewhat distorted lines due to low S/N at the Sr lines (4077 Å and 4215 Å). Our improved S/N in this region clearly shows that high Sr is required.

We do note that TucII-033 is distinct from halo stars in that it has a markedly lower [α/Fe] ratio ($\sim$0.05 dex) than other halo stars (~ 0.4 dex) as discussed in Section 3.4.3. Using the compilation by Abohalima and Frebel [210], we find that only 8% of halo stars have a lower Ca abundance than TucII-033 and 15% have a lower Mg abundance. These fractions, when viewed in the context that TucII-033 has the same systemic velocity as Tucana II, make it less likely that TucII-033 is an interloping star.

For these reasons, for the remainder of the analysis, we present two lines of argument: one assuming TucII-033 as a member, and one assuming TucII-033 as a non-member. The exclusion of TucII-033 from the interpretation of this galaxy would be meaningful, since its low [α/Fe] abundance would otherwise imply that Tucana II had an extended star formation history and would thus not be a surviving first galaxy (see Sections 3.4.3 and 3.4.5). While the Sr abundance of TucII-033 might suggest that it is a halo interloper, its [α/Fe] and velocity make this scenario less likely.

3.4.2 Carbon

Empirically, a high fraction of EMP stars in the halo ($\sim 42\%$; Placco et al. [8]) are enhanced in carbon ([C/Fe] > 0.7 dex) and are thus classified as carbon-enhanced metal-poor stars. This enhancement in carbon has been used to constrain potential sites of nucleosynthesis that may have dominated early chemical evolution [e.g., 213, 214, 99]. From the paradigm of hierarchical galaxy formation, we might expect that stars in dwarf galaxies also display this enhancement given that accreted analogs perhaps contributed to the metal-poor population of the halo. However, recent studies of the prevalence of carbon-rich stars in dwarf galaxies give differing results [4, 6, 215].

In Tucana II, we find that three stars out of five with [Fe/H] < -2.9 are enhanced in carbon, following the correction in Placco et al. [8]. This fraction is slightly larger than that of the halo, with the caveat of the small size of our sample. One star (TucII-011) appears to be somewhat less enhanced in carbon ([C/Fe]= 0.29 after correction for the evolutionary state of the star). This slight outlier might reflect inhomogeneous mixing of gas in the system or multiple avenues of enrichment that contributed to the chemical evolution of the system.

3.4.3 α-elements

The abundance of α-elements (Mg, Si, Ca, Ti) in stars can be used investigate the integrated population of supernovae (SNe) that chemically enriched the natal gas cloud of the stars. In particular, enrichment by core-collapse SNe results in a flat [α/Fe] ~ 0.4 trend vs. [Fe/H], whereas Type Ia SNe enrichment result in a declining [α/Fe] abundance trend vs. [Fe/H] [e.g. 88, 89]. Typically, this switch from a flat to a declining [α/Fe] vs. [Fe/H] indicates the metallicity at which type Ia SNe started dominating the Fe production. The most metal-rich member of our sample, TucII-033, shows a slight deficiency in its α-element abundance compared to the other stars in our sample. This deficiency suggests that Type Ia SNe contributed to the chemical abundances of at least some stars in this galaxy, which in turn would suggest somewhat extended star formation and chemical enrichment in Tucana II [e.g., 89].

Declining [α/Fe] is seen in most UFDs [216], though Tucana II is one of the least luminous UFDs with available [α/Fe] measurements.

If TucII-033 were a halo interloper (see Section 3.4.1), our sample would instead show a trend consistent with a constant [α/Fe], as produced by core-collapse SNe only. We note, that the lower Mg abundance displayed by TucII-006 is likely due to a distortion in one of the two lines used to measure its abundance, which is reflected in the larger uncertainties on its Mg abundance of 0.46 dex.

3.4.4 Odd-Z, iron-peak and neutron-capture element abundances

We find no significant deviation from the halo trend in the odd-Z elements (Na, Al, Sc) and iron-peak elements (Cr, Mn, Co, Ni). This is also consistent with abundances of other UFD stars in the literature (see Figures 3-4 and 3-5). We do find one star (TucII-078) with a lower Na abundance than typical halo and dwarf galaxy stars.

We find low strontium and barium abundances in six stars that are characteristic of the stellar populations set by other UFD stars (see Figure 3-6). See Section 3.4.1 for a discussion of the neutron-capture element abundances in TucII-033. We do not detect europium or other neutron-capture elements in any stars in our sample.

3.4.5 Tucana II as a surviving first galaxy

Frebel and Bromm [122] predict chemical characteristics of the population of surviving first galaxies:

1. A large spread in [Fe/H] (~ 1 dex),

2. Light element abundance ratios in agreement with a core-collapse supernova enrichment

3. No stars with [α/Fe] systemically lower than the galactic halo abundance of [α/Fe] ~ 0.35, and

4. No signatures of s-process enhancement from AGB stars.

The first prediction is a consequence of inhomogeneous mixing in the first galaxies, and the last two predictions are consequences of the first galaxies being enriched by "one-shot" chemical enrichment events since extended star formation is not thought to have occurred in the first galaxies. The second criterion simply confirms enrichment by supernovae. According to our chemical abundance results, Tucana II largely satisfies the aforementioned first, second and fourth criteria for a surviving first galaxy. The second one would also be satisfied if we exclude TucII-033 when assuming it is a halo interloper (see Section 3.4.1). However, if we include TucII-033 in the interpretation, then its Sr relative enhancement relative to other Tuc II members and [α/Fe] deficiency would imply that Tuc II had undergone some period of chemical evolution, and would thus not be a surviving first galaxy. Given the low luminosity of Tucana II ($\sim 3 \times 10^3\,L_\odot$; Bechtol et al. 37, Koposov et al. 13), it would still be interesting to find that Tucana II has some chemical evolution as opposed to isolated chemical enrichment events.

Together with Segue 1 [22], Tucana II might still be one of the best candidates for a surviving first galaxy, as determined from chemical abundances of six stars in each galaxy. Moreover, these six stars form the majority of known members in Tucana II, and their chemical abundances suggest that most stars in the galaxy are consistent with having formed in an environment similar to a first galaxy. Theoretical modeling of early galaxies such as these two systems could shed further light on this issue. However, detailed abundances of more stars with [Fe/H]$\gtrsim -2.5$ in Tucana II are needed to further investigate the nature and origin of Tucana II, as is the case with other potential first galaxy candidates (i.e., Ursa Major II, Coma Berenices, Leo IV).

3.5 Conclusion

In this paper, we presented the high-resolution chemical abundance measurements of seven stars in the Tucana II dwarf galaxy. Three stars with no previous high-resolution chemical abundance measurements were analyzed. Four other stars had been reanalyzed from the sample in Ji et al. [2] with the addition of new data.

From the detection of new members and the re-analysis of known members, we were able to discuss the chemical signatures of stars in the Tucana II UFD. We raise the possibility that one of the stars (TucII-033) may be an interloping halo star given its high Sr abundance with respect to other known UFD stars, but its velocity and [α/Fe] ratio make this unlikely. Excluding TucII-033 from the interpretation, Tucana II does meet all the criteria to be a surviving first galaxy [122]. Assuming TucII-033 is a member, Tucana II would not meet the one-shot enrichment criterion due to the star's low [α/Fe] and likely somewhat extended chemical evolution.

We confirmed two new members of Tucana II that were pre-selected as probable members from SkyMapper photometry. Given the large field of view of the SkyMapper telescope (5.7 sq. deg.) and the metallicity discriminating "v" filter, we were able to search for metal-poor stars within a large area around Tuc II UFD. As a result, our two new members are ~ 2 half-light radii from the center of Tucana II and may have been missed by traditional spectroscopic follow-up observations (see Figure 3-2). Interestingly, one of these new members is the most metal-poor star discovered in Tucana II thus far ([Fe/H] $= -3.34$). From our small sample, we however cannot claim these new members display systematic differences to stars near the center of Tucana II.

This new photometric metal-poor star identification technique might aid in identifying members for detailed chemical analysis and studying potential correlations with substructure of UFD systems. Combining this photometric selection technique with traditional spectroscopic follow-up would result in more accurate parameters for UFDs (e.g., half-light radii, mass-to-light ratios), supposing the photometry itself could predict membership status. In particular, this highly efficient large-field of view method for finding members would be interesting to apply on systems that show potential elongated tidal features, such as Tucana III [189, 217]. Moreover, the spectroscopic study of more stars in UFDs would have multiple benefits. For instance, detecting more stars with [Fe/H]~ -2.5 in Tuc II would potentially resolve whether the entire galaxy had undergone chemical evolution. This would better inform whether TucII-033 is indeed a halo interloper or rather signaling unusual enrichment events or

some degree of chemical evolution in that UFD. At minimum, future work will extend this selection technique to other UFDs for the purpose of efficiently identifying new members and enabling detailed abundance measurements.

Table 3.3. Detailed chemical abundances of stars in Tucana II

El.	N	$\log\epsilon(\mathrm{X})_\odot$	[X/H]	[X/Fe]	σ[a]	El.	N	$\log\epsilon(\mathrm{X})_\odot$	[X/H]	[X/Fe]	σ[a]
		TucII-006						TucII-011			
CH	2	8.43	−2.05	0.88	0.27	CH	2	8.43	−3.27	−0.35	0.31
CH[b]	2	8.43	−1.69	1.24	0.27	CH[b]	2	8.43	−2.63	0.29	0.31
Na I	2	6.24	−2.78	0.15	0.27	Na I	2	6.24	−2.35	0.57	0.23
Mg I	2	7.60	−2.97	−0.04	0.37	Mg I	5	7.60	−2.41	0.51	0.16
Al I	1	6.45	−3.62:[c]	−0.69:[c]	···	Al I	2	6.45	−3.57:[c]	−0.65:[c]	···
Si I	1	7.51	−2.71:[c]	0.22:[c]	···	Si I	2	7.51	−2.38:[c]	0.54:[c]	···
Ca I	2	6.34	−2.61	0.32	0.27	Ca I	10	6.34	−2.44	0.48	0.21
Sc II	5	3.15	−3.00	−0.07	0.27	Sc II	6	3.15	−2.80	0.12	0.16
Ti II	12	4.95	−2.81	0.12	0.27	Ti I	2	4.95	−2.73	0.19	0.16
Cr I	3	5.64	−3.51	−0.58	0.27	Ti II	17	4.95	−2.60	0.32	0.22
Mn I	3	5.43	−3.27	−0.34	0.27	Cr I	5	5.64	−3.24	−0.32	0.20
Fe I	52	7.50	−2.93	0.00	0.27	Mn I	3	5.43	−3.89	−0.97	0.17
Fe II	3	7.50	−2.93	0.00	0.27	Fe I	99	7.50	−2.92	0.00	0.16
Co I	1	4.99	−2.75	0.18	0.34	Fe II	11	7.50	−2.91	0.01	0.16
Ni I	2	6.22	−2.84	0.09	0.66	Co I	3	4.99	−2.77	0.15	0.21
Sr II	2	2.87	−4.39	−1.46	0.27	Ni I	3	6.22	−2.77	0.15	0.22
Ba II	2	2.18	−4.20	−1.27	0.27	Sr II	2	2.87	−4.52	−1.60	0.19
Eu I	1	0.52	< −2.02	<0.91	···	Ba II	1	2.18	−4.82	−1.90	0.20
						Eu I	1	0.52	< −2.27	<0.65	···
		TucII-033						TucII-052			
CH	2	8.43	−2.33	0.08	0.18	CH	2	8.43	−2.53	0.70	0.20
CH[b]	2	8.43	−1.81	0.60	0.18	CH[b]	2	8.43	−2.33	0.90	0.20
Na I	2	6.24	−2.54	−0.13	0.12	Na I	2	6.24	−3.00	0.23	0.29
Mg I	4	7.60	−2.25	0.16	0.12	Mg I	2	7.60	−2.87	0.36	0.20
Al I	2	6.45	−3.27:[c]	−0.86:[c]	···	Al I	1	6.45	−3.73:[c]	−0.50:[c]	···
Si I	2	7.51	−2.23:[c]	0.18:[c]	···	Si I	2	7.51	−2.91:[c]	0.32:[c]	···
Ca I	8	6.34	−2.34	0.07	0.12	Ca I	4	6.34	−2.78	0.45	0.20
Sc II	5	3.15	−2.50	−0.09	0.12	Sc II	5	3.15	−2.99	0.24	0.20
Ti I	2	4.95	−1.94	0.47	0.51	Ti II	12	4.95	−2.85	0.38	0.25
Ti II	12	4.95	−2.49	−0.08	0.27	Cr I	5	5.64	−3.56	−0.33	0.20
Cr II	1	5.64	−2.42	−0.01	0.32	Mn I	4	5.43	−3.53	−0.30	0.21
Cr I	5	5.64	−2.70	−0.29	0.12	Fe I	56	7.50	−3.23	0.00	0.20
Mn I	3	5.43	−2.95	−0.54	0.30	Fe II	3	7.50	−3.21	0.02	0.20
Fe I	92	7.50	−2.41	0.00	0.12	Co I	3	4.99	−2.88	0.35	0.20
Fe II	12	7.50	−2.39	0.02	0.14	Ni I	2	6.22	−3.10	0.13	0.20
Co I	2	4.99	−2.24	0.17	0.26	Sr II	2	2.87	−4.28	−1.05	0.20
Sr II	2	2.87	−2.80	−0.39	0.26	Ba II	2	2.18	−4.13	−0.90	0.20
Ba II	2	2.18	−3.40	−0.99	0.39	Eu I	1	0.52	< −1.98	<1.25	···
Eu I	1	0.52	< −2.21	<0.20	···						
		TucII-078						TucII-203			
CH	2	8.43	−2.36	0.33	0.20	CH	2	8.43	−2.76	0.32	0.20
CH[b]	2	8.43	−2.26	0.43	0.20	CH[b]	2	8.43	−2.44	0.64	0.20
Na I	2	6.24	−3.34	−0.65	0.20	Na I	2	6.24	−2.99	0.09	0.26
Mg I	5	7.60	−2.27	0.42	0.20	Mg I	2	7.60	−2.70	0.38	0.20
Al I	2	6.45	−3.09:[c]	−0.40:[c]	···	Al I	2	6.45	−3.60:[c]	−0.52:[c]	···
Si I	2	7.51	−2.20:[c]	0.49:[c]	···	Si I	1	7.51	−2.78:[c]	0.30:[c]	···
Ca I	8	6.34	−2.25	0.44	0.20	Ca I	4	6.34	−2.88	0.20	0.20
Sc II	6	3.15	−2.51	0.18	0.20	Sc II	5	3.15	−3.08	0.00	0.20
Ti I	1	4.95	−2.39	0.30	0.36	Ti II	14	4.95	−2.77	0.31	0.28
Ti II	20	4.95	−2.22	0.47	0.25	V II	1	3.93	−1.88	1.20	0.21
Cr I	5	5.64	−2.97	−0.28	0.26	Cr I	3	5.64	−3.34	−0.26	0.20
Mn I	2	5.43	−3.54	−0.85	0.20	Mn I	3	5.43	−4.03	−0.95	0.20
Fe I	83	7.50	−2.69	0.00	0.20	Fe I	59	7.50	−3.08	0.00	0.20
Fe II	9	7.50	−2.69	0.00	0.20	Fe II	4	7.50	−3.07	0.01	0.20
Co I	1	4.99	−2.35	0.34	0.42	Co I	2	4.99	−3.00	0.08	0.20
Ni I	2	6.22	−2.58	0.11	0.24	Ni I	3	6.22	−3.04	0.04	0.20
Sr II	1	2.87	< −4.69	< −2.00	···	Sr II	1	2.87	−4.48	−1.40	0.30
Ba II	1	2.18	< −4.59	< −1.90	···	Ba II	1	2.18	−4.38	−1.30	0.20
Eu I	1	0.52	< −1.94	<0.75	···	Eu I	1	0.52	< −2.08	<1.00	···
		TucII-206									
CH	2	8.43	−2.87	0.47	0.28						
CH[b]	2	8.43	−2.61	0.73	0.28						
Na I	2	6.24	−2.72	0.62	0.46						
Mg I	3	7.60	−2.89	0.45	0.28						
Al I	2	6.45	−3.96:[c]	−0.62:[c]	···						
Si I	1	7.51	−3.14:[c]	0.20:[c]	···						
Ca I	2	6.34	−3.08	0.26	0.32						
Sc II	5	3.15	−3.09	0.25	0.28						
Ti II	9	4.95	−3.07	0.27	0.28						
Cr I	3	5.64	−3.46	−0.12	0.28						
Mn I	3	5.43	−3.81	−0.47	0.28						
Fe I	46	7.50	−3.34	0.00	0.28						
Fe II	3	7.50	−3.33	0.01	0.34						
Sr II	2	2.87	−4.64	−1.30	0.28						
Ba II	1	2.18	−4.19	−0.85	0.28						
Eu I	1	0.52	< −2.04	<1.30	···						

[a]Random uncertainties. See Table 3.4 for total uncertainties.

[b]Corrected for the evolutionary status of the star following Placco et al. [8].

[c]Colons (:) indicate large uncertainties despite the detection of a line feature.

Table 3.4. Chemical abundance uncertainties of stars in Tucana II

El.	N	$\sigma_{\rm rand}$	$\sigma_{\rm sys}$	$\sigma_{\rm tot}$	El.	N	$\sigma_{\rm rand}$	$\sigma_{\rm sys}$	$\sigma_{\rm tot}$
		TucII-006					TucII-011		
CH	2	0.27	0.51	0.58	CH	2	0.31	0.39	0.50
Na I	2	0.27	0.39	0.47	Na I	2	0.23	0.33	0.40
Mg I	2	0.37	0.32	0.49	Mg I	5	0.16	0.24	0.29
Al I	1	...	...	...	Al I	2	...	...	...
Si I	1	...	...	...	Si I	2	...	...	...
Ca I	2	0.27	0.30	0.40	Ca I	10	0.21	0.16	0.26
Sc II	5	0.27	0.28	0.39	Sc II	6	0.16	0.15	0.22
Ti II	12	0.27	0.64	0.69	Ti I	2	0.16	0.20	0.26
Cr I	3	0.27	0.53	0.59	Ti II	17	0.22	0.23	0.32
Mn I	3	0.27	0.29	0.40	Cr I	5	0.20	0.29	0.35
Fe I	52	0.27	0.28	0.39	Mn I	3	0.17	0.22	0.28
Fe II	3	0.27	0.20	0.34	Fe I	99	0.16	0.23	0.28
Co I	1	0.34	0.57	0.67	Fe II	11	0.16	0.20	0.26
Ni I	2	0.66	0.45	0.80	Co I	3	0.21	0.25	0.33
Sr II	2	0.27	0.22	0.35	Ni I	3	0.22	0.29	0.36
Ba II	2	0.27	0.26	0.37	Sr II	2	0.19	0.21	0.28
Eu I	1	...	...	...	Ba II	1	0.20	0.20	0.28
					Eu I	1	...	...	...
		TucII-033					TucII-052		
CH	2	0.18	0.41	0.45	CH	2	0.20	0.43	0.47
Na I	2	0.12	0.27	0.30	Na I	2	0.29	0.27	0.40
Mg I	4	0.12	0.25	0.28	Mg I	2	0.20	0.33	0.39
Al I	2	...	...	...	Al I	1	...	...	...
Si I	2	...	...	...	Si I	2	...	...	...
Ca I	8	0.12	0.14	0.18	Ca I	4	0.20	0.17	0.26
Sc II	5	0.12	0.20	0.23	Sc II	5	0.20	0.16	0.26
Ti I	2	0.51	0.22	0.56	Ti II	12	0.25	0.19	0.31
Ti II	12	0.27	0.21	0.34	Cr I	5	0.20	0.28	0.34
Cr II	1	0.32	0.18	0.36	Mn I	4	0.21	0.22	0.30
Cr I	5	0.12	0.28	0.30	Fe I	56	0.20	0.28	0.34
Mn I	3	0.30	0.31	0.43	Fe II	3	0.20	0.14	0.24
Fe I	92	0.12	0.23	0.26	Co I	3	0.20	0.28	0.34
Fe II	12	0.14	0.18	0.23	Ni I	2	0.20	0.28	0.34
Co I	2	0.26	0.30	0.40	Sr II	2	0.20	0.23	0.30
Sr II	2	0.26	0.19	0.32	Ba II	2	0.20	0.19	0.28
Ba II	2	0.39	0.16	0.42	Eu I	1	0.20	0.16	0.26
Eu I	1	...	...	...					
		TucII-078					TucII-203		
CH	2	0.20	0.39	0.44	CH	2	0.20	0.43	0.47
Na I	2	0.20	0.21	0.29	Na I	2	0.26	0.24	0.35
Mg I	5	0.20	0.25	0.32	Mg I	2	0.20	0.29	0.35
Al I	2	...	...	...	Al I	2	...	...	...
Si I	2	...	...	...	Si I	1	...	...	...
Ca I	8	0.20	0.15	0.25	Ca I	4	0.20	0.19	0.28
Sc II	6	0.20	0.23	0.30	Sc II	5	0.20	0.20	0.28
Ti I	1	0.36	0.25	0.44	Ti II	14	0.28	0.17	0.33
Ti II	20	0.25	0.25	0.35	V II	1	0.21	0.13	0.25
Cr I	5	0.26	0.28	0.38	Cr I	3	0.20	0.29	0.35
Mn I	2	0.20	0.28	0.34	Mn I	3	0.20	0.28	0.34
Fe I	83	0.20	0.23	0.30	Fe I	59	0.20	0.25	0.32
Fe II	9	0.20	0.25	0.32	Fe II	4	0.20	0.13	0.24
Co I	1	0.42	0.29	0.51	Co I	2	0.20	0.25	0.32
Ni I	2	0.24	0.27	0.36	Ni I	3	0.20	0.27	0.34
Sr II	1	...	...	...	Sr II	1	0.30	0.22	0.37
Ba II	1	...	...	...	Ba II	1	0.20	0.18	0.27
Eu I	1	...	...	...	Eu I	1	...	...	...
		TucII-206							
CH	2	0.28	0.51	0.58					
Na I	2	0.46	0.32	0.56					
Mg I	3	0.28	0.31	0.42					
Al I	2	...	...	...					
Si I	1	...	...	...					
Ca I	2	0.32	0.27	0.42					
Sc II	5	0.28	0.26	0.38					
Ti II	9	0.28	0.29	0.40					
Cr I	3	0.28	0.29	0.40					
Mn I	3	0.28	0.24	0.37					
Fe I	46	0.28	0.27	0.39					
Fe II	3	0.34	0.29	0.45					
Sr II	2	0.28	0.25	0.38					
Ba II	1	0.28	0.29	0.40					
Eu I	1	...	...	...					

Table 3.5. Line measurements from spectroscopy of stars in Tucana II

Star name	Rest wavelength (Å)	Species	Excitation potential (eV)	Oscillator strength	Equivalent width (m Å)	$\log \epsilon(\mathrm{X})$
TucII-006	4313.00	CH	syn	syn	syn	6.25
TucII-006	4323.00	CH	syn	syn	syn	6.50
TucII-006	5889.95	Na I	0.00	0.11	146.4	3.61
TucII-006	5895.92	Na I	0.00	−0.19	114.9	3.31
TucII-006	5172.68	Mg I	2.71	−0.45	120.3	4.33
TucII-006	5183.60	Mg I	2.72	−0.24	162.6	4.92
TucII-006	3944.00	Al I	syn	syn	syn	2.83
TucII-006	3905.52	Si I	syn	syn	syn	4.80
TucII-006	4454.78	Ca I	1.90	0.26	73.2	3.77
TucII-006	6122.22	Ca I	1.89	−0.32	42.3	3.69

Note. — Table 3.5 is published in its entirety in the machine-readable format. A portion is shown here for guidance regarding its form and content.

Chapter 4

An Extended Halo around an Ancient Dwarf Galaxy

An amended version of this chapter was published in Nature Astronomy as [218] on February, 2021. The data tables in this chapter can be provided upon request to the author.

Abstract

The Milky Way is surrounded by dozens of ultra-faint ($< 10^5$ solar luminosities) dwarf satellite galaxies[219, 177, 121]. They are the surviving remnants of the earliest galaxies[70], as confirmed by their ancient ($\sim$13 billion years old)[109] and chemically primitive[179, 22] stars. Simulations[110, 220, 221] suggest that these systems formed within extended dark matter halos and experienced early galaxy mergers and supernova feedback. However, the signatures of these events would lie outside their core regions (>2 half-light radii)[222], which are spectroscopically unstudied due to the sparseness of their distant stars[223]. Here we identify members of the Tucana II ultra-faint dwarf galaxy in its outer region (up to 9 half-light radii), demonstrating the system to be dramatically more spatially extended and chemically primitive than previously found. These distant stars are extremely metal-poor (<[Fe/H]>=-3.02; less than $\sim$1/1000th of the solar iron abundance), affirming Tucana II as the most metal-poor known galaxy. We observationally establish, for the first time, an extended dark matter halo surrounding an ultra-faint dwarf galaxy out to one kiloparsec, with a total mass of $> 10^7$ solar masses. This measurement is consistent with the expected $\sim 2\times10^7$ solar masses using a generalized NFW density profile. The extended nature of Tucana II suggests that it may have undergone strong bursty feedback or been the product of an early galactic merger [221, 222]. We demonstrate that spatially extended stellar populations, which other ultra-faint dwarfs hint at hosting as

well[224, 225], are observable in principle and open the possibility for detailed studies of the stellar halos of relic galaxies.

4.1 Primary Text

Tucana II is a typical ultra-faint dwarf galaxy: it is extremely dark-matter-dominated (M/L$\sim$2000[1]), has a low metallicity ($<$[Fe/H]$>$ = $-$2.7[2, 12]), and has a low stellar mass ($\sim$3000 solar masses[37]). As with other similar systems[121], spectroscopy of its member stars remains sparse due to its low stellar density[37, 13]. Previous follow-up spectroscopic studies were largely limited to stars within two half-light radii[1, 2, 12] and identified ten probable members of Tucana II.

To significantly extend the spectroscopic characterization of Tucana II, we obtained wide-field images ($\sim$2 x 2 degrees) with the ANU 1.3 meter SkyMapper telescope[127] and used its unique filter-set to efficiently identify metal-poor red giant stars at large galactocentric distances[39]. This efficiency arises because the filter-set enables the derivation of stellar metallicity and surface gravity solely from photometry. By combining these derived stellar parameters with Gaia DR2 proper motions[112], we identified new candidate member stars in Tucana II in a spatially unbiased manner. We then verified their membership and spectroscopically characterized nine of these stars, nearly doubling the previously known stellar population of this galaxy. These stars were detected out to $\sim$9 times the half-light radius[37] ($\sim$1 kiloparsec) of Tucana II – the first detection of member stars beyond $\sim$4 half-light radii in any ultra-faint dwarf galaxy.

Our follow-up spectroscopic observations of candidate members were performed with the MagE[226] and IMACS[227] instruments on the 6.5 meter Magellan-Baade telescope. These spectra enable measurement of radial velocities with a precision of $\sim$3 km/s and $\sim$1 km/s, respectively, and metallicities with a precision of $\sim$0.2 to $\sim$0.3 dex. Such precisions are sufficient to conclusively determine the membership status of all candidate stars from a joint velocity and metallicity analysis.

The metallicities of the spatially extended members decrease the Tucana II galactic

metallicity to <[Fe/H]>=−2.77, affirming Tucana II as the most metal-poor galaxy known. Metallicities from prior work[2, 12] already show Tucana II to have a low average metallicity of <[Fe/H]>=−2.71. However, we find that the stars beyond two half-light radii are preferentially more metal-poor (<[Fe/H]>=−3.02) than the already studied core population (see Figure 4-1), which has a mean metallicity of (<[Fe/H]>=−2.62). Such metallicity gradients have previously been seen in larger dwarf galaxies and are hypothesized to result from, e.g., chemical evolution, feedback, or mergers [228]. Our finding is the first evidence of such a metallicity gradient in a relic early galaxy, indicating that their formation may have also been shaped by the same processes.

The spatial configuration of Tucana II members – twelve giants within two half-light radii and seven between two and nine half-light radii – suggests that this ultra-faint dwarf galaxy's stellar density profile may differ from one typically assumed for such systems. Under the common assumption of an exponential density profile, we would not statistically expect to see seven giant stars beyond ∼2 half-light radii (∼0.24 kiloparsecs[37]) in a sample of 19 members. However, when assuming a Plummer profile, it is unlikely but still principally plausible (at a 7% level) to identify seven giant stars beyond ∼2 half-light radii in a sample of nineteen members. Conclusive results rest on a precise knowledge of the half-light radius, which is currently not well constrained (see Methods). Deeper photometry and more precise structural parameters of Tucana II would thus enable a more robust determination of these potential density profile differences. Any such discrepancies might cause concern regarding the existence of these distant members in Tucana II, but with the possible exception of the most metal-rich star (see Methods), every distant star is unambiguously a member. We expect no false positive classifications among our most metal-poor distant stars because the systemic velocity (−129.1 km/s) and low mean metallicity (<[Fe/H]> −2.77) of Tucana II are well separated from those of foreground Milky Way stars (see Methods).

Tidal disruption is the most obvious process to displace stars to large radii, but that explanation is inconsistent with the orbital parameters of Tucana II (see meth-

ods). The location of any predicted Tucana II tidal debris, based on its orbit, would be perpendicular to the position of the most distant newly discovered Tucana II member stars (Figure 4-1). Furthermore, tidally disrupted systems should display a velocity gradient[229], which is not observed in Tucana II. For instance, the radial velocity of the farthest star, at 9.3 half-light radii, is only $\sim(1\pm3)$ km/s away from the systemic velocity of Tucana II. Therefore, Tucana II is currently not tidally disrupting.

It follows that the farthest star in Tucana II must be gravitationally bound to the system, given that Tucana II is not tidally disrupting and that the probability of falsely identifying a member is negligible (see methods). To be bound, the farthest star must lie within the tidal radius of Tucana II. Thus, the tidal radius of Tucana II must extend beyond 1 kiloparsec, which requires an enclosed total mass within 1 kiloparsec of at least 1.3×10^7 solar masses (see methods). This mass is a factor of 4 larger than the mass within one half-light radius. Such extended, massive dark matter halos of relic galaxies were predicted[230], but previous mass estimates of ultra-faint dwarf galaxies were limited to those within a few hundred parsecs. Our study confirms that the halo of a relic galaxy contains significant mass out to a large distance ($\sim$1 kiloparsec) for the first time. The majority of this extended mass distribution of at least 1.3×10^7 solar masses must consist of dark matter, given the low stellar mass of Tucana II ($\sim$3000 solar masses[37]).

We estimate the mass for this extended dark matter halo by attempting to directly model Tucana II with a generalized NFW dark matter density profile. This mass enclosed within $\sim$ 9 half-light radii comes to $(2.1{+}3.7/{-}1.2)\times10^7$ solar masses. At face value, this estimate is in excellent agreement with the mass deduced from assuming that the farthest member star is bound and thus adds further evidence that these distant stars are indeed bound to Tucana II. We note that adopting the highest and lowest plausible velocity anisotropy prescriptions only vary this mass at the $\sim$1sigma level (see methods). We show the corresponding enclosed mass and density profiles of Tucana II in Figure 4-2. To test whether masses at large radii can be extrapolated from estimates within the half-light radius, we also calculated the NFW density profile solely from previously known members[1] and extrapolated to $\sim$9 half-light radii.

This extrapolation results in a consistent enclosed mass as inferred from all member stars, and supports the common practice of extrapolating the masses from within one half-light radius to larger radii to, for instance, compare with theoretical models[230]. We also note that our derived mass within 1kpc of $\sim 2\times10^7$ solar masses is consistent with an overall halo mass of $\sim 10^8$ Msun, roughly compatible with constraints on the minimum virial halo mass [231].

We find tentative evidence for a metallicity gradient in Tucana II, as our more distant member stars tend to have lower metallicities than those in the galaxy core. If such gradients are actually pervasive amongst other ultra-faint dwarf galaxies, then the dwarf galaxy metallicities derived only from core populations may be biased high. This bias might affect prior studies that place ultra-faint dwarf galaxies on the dwarf galaxy mass-metallicity relation, a key prediction from galaxy formation simulations that is sensitive to mechanisms including supernova yields, feedback, and gas accretion [232]. For instance, lowering the mean metallicity of the most metal-poor ultra-faint dwarf galaxies may increase the number of plausible feedback prescriptions in simulating these systems [232].

One way to form the extended stellar halo component of Tucana II is by heating the system via galaxy mergers or stellar feedback. The former interpretation implies Tucana II to be the product of an early merger, likely that of two primitive galaxies at high redshift ($z \gtrsim 2$)[110]. Simulations do indeed suggest that a dwarf galaxy with the stellar mass of Tucana II ($\sim$3,000 solar masses[37]) should be assembled by no more than a handful of star forming progenitors[233]. Otherwise, early supernova feedback may have heated the most metal-poor stars, which is plausible since ultra-faint dwarf galaxies may have a bursty star formation history[221].

Our detection of a population of stars out to $\sim$9 half-light radii in Tucana II suggests that other ultra-faint dwarf galaxies could plausibly host member stars at large radii as well. Indeed, the ultra-faint dwarf galaxies Segue 1 and Bootes I presently each have one known member star at $\sim$4 half-light radii[224, 225]. With targeted wide-field photometric searches, it should be feasible to rapidly uncover the distant members of Segue 1, Bootes I, and additional dwarf galaxies to comprehensively es-

tablish the evolution of these early relic systems.

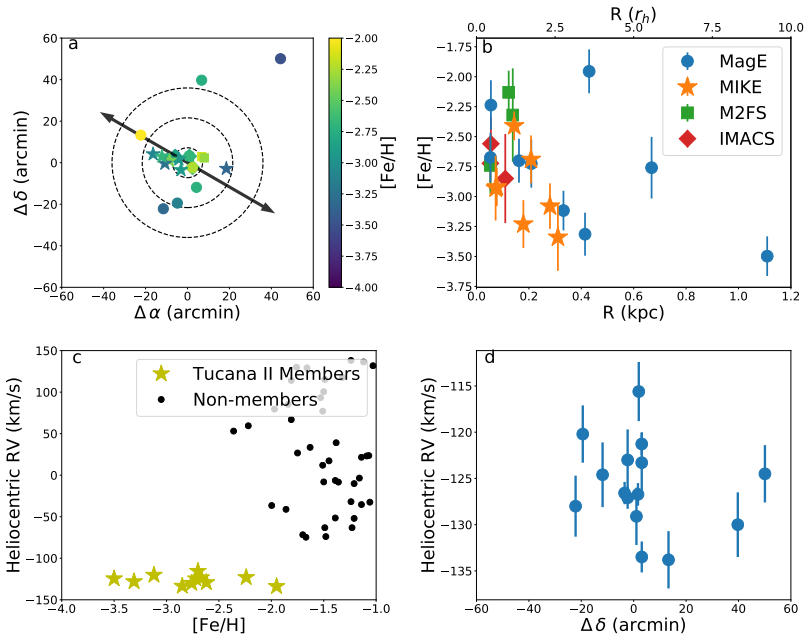

Figure 4-1 a. Spatial distribution of all confirmed member stars of the Tucana II ultra-faint dwarf galaxy, colored by metallicity. The dashed ellipses correspond to one, three, and five half-light radii [37]. Metallicities from MIKE high-resolution spectra are shown as stars[12], those from M2FS spectra are squares[1], and those from MagE and IMACS spectra presented in this work are circles and diamonds, respectively. For Tucana II stars with no high-resolution MIKE results, we plot all our available medium-resolution measurements. Metallicities from M2FS spectra are reduced by 0.32 dex for agreement with high-resolution metallicities (see methods). Contours correspond to 1, 3, and 5 half-light radii. Arrows indicate the direction of predicted Tucana II tidal debris (see methods). Our distant members lie perpendicular to this track, suggesting that their distant location is not due to tidal disruption. b. Metallicities of Tucana II member stars as a function of their geometric radius from the center of the system. There is a general trend towards lower metallicities at larger distances. As for panel (a), metallicities from M2FS spectra are reduced by 0.32 dex. The error bars correspond to 1sigma uncertainties on the metallicity, as derived in the methods section. c. Velocities and metallicities of our IMACS and MagE Tucana II members (yellow stars) compared to non-members in those samples with metallicity measurements and non-members with S/N $>$ 5 observed with M2FS[1] (black points). There is a clear separation in metallicity and velocity space between the two populations. d. Heliocentric radial velocities from MagE and IMACS measurements of Tucana II members as a function of distance (declination) from the center of the system. A velocity gradient would be present in the data if the newly discovered member stars were being dispersed due to tidal stripping. The error bars correspond to 1sigma uncertainties on the velocity measurements, as derived in the methods section.

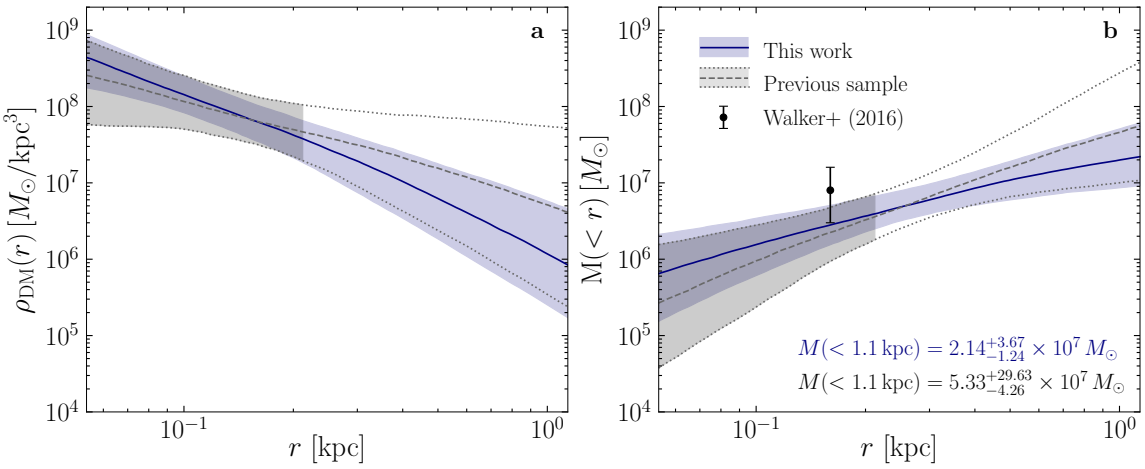

Figure 4-2 a. Density profiles of Tucana II, derived using data from previous spectroscopic work [1] shown in grey, and from including the new stars in blue. The error bounds correspond to 1sigma uncertainties from the posterior density distribution. b. Enclosed mass as a function of distance, derived using data from previous spectroscopic studies[1] shown in grey, and from including the new members, in blue. An enclosed mass measurement within a half-light radius[38] using the velocity dispersion and 1 sigma uncertainty from refWalker et al. [1] is shown as the black data point. The error bounds correspond to 1sigma uncertainties from the posterior mass distribution in our modeling.

4.2 Methods

4.2.1 Selection of Candidate Members

Targets were initially selected using deep narrow-band imaging of the Tucana II ultra-faint dwarf galaxy obtained using the 1.3m SkyMapper Telescope at Siding Springs Observatory[127] between July and December 2015. The SkyMapper filter-set[135] is unique in that the flux through the u, v, g, and i filters can be related to stellar metallicity and surface gravity[234, 39, 235]. Therefore, SkyMapper photometry can directly identify metal-poor red giant stars. These stars are more likely to be members of the Tucana II ultra-faint dwarf galaxy, since the mean metallicity of Tucana II is very low (<[Fe/H]> ~ -2.7[2, 12]) compared to most Milky Way halo stars and based on the distance of Tucana II, all members brighter than g 22 should be red giant stars or blue horizontal branch stars[37, 13].

In previous work[39], we have shown that one can quantitatively determine stel-

lar metallicities and surface gravities from SkyMapper photometry by generating synthetic photometry[193, 148] over a range of stellar parameters and relating observed magnitudes to theoretical magnitudes from this synthetic grid. We applied this method to derive surface gravities and metallicities for every star brighter than g$\sim$19.5 in the field of view of the SkyMapper Telescope ($\sim$2 degrees $\times$ $\sim$2 degrees). We thereby identified many metal-poor ([Fe/H] < -1.0) giant (log g < 3.0) stars as candidate members of Tucana II.

We further refined this sample of likely member stars by making use of Gaia DR2 proper motion data[111, 112]. Since ultra-faint dwarf galaxies are gravitationally bound, their member stars should have proper motions clustered around the systemic proper motion of the galaxy. We narrowed down our sample of candidates by only including stars with proper motions close to the systemic proper motion of Tucana II (pm_ra = 0.936 mas/yr, pm_dec = -1.23 mas/yr [236]). Specifically, we selected stars with proper motions and proper motion uncertainties that are consistent within two sigma of the following bounds: 0.4 mas/yr $<$ pm_ra $<$ 1.2 mas/yr and -1.4 mas/yr $<$ pm_dec < -1.0 mas/yr (see extended data Figure 4-3). These proper motion ranges were chosen to roughly correspond to the proper motions of stars that were previously confirmed to be members of Tucana II[1, 12]. Note that we slightly relaxed this proper motion criterion for one candidate member – it was subsequently found to be a non-member. We then selected a sample of 22 metal-poor red giant stars with proper motions similar to that of Tucana II to observe with the MagE spectrograph. Observing priority was given to stars with photometric [Fe/H] < -1.5, as more metal-poor stars have increased likelihood of being members. Full observational details are given in Extended Data Table 1 below, and the SkyMapper color-color plots from which stars were identified as metal-poor giants are shown in Extended Data Figure 4-4.

Prior to the Gaia DR2 data release and any of our Tucana II SkyMapper photometry studies, we had already taken spectra of 43 stars with the IMACS spectrograph[227] (more details given below). This early target selection was solely based on choosing stars with g$-$r colors within 0.1 mag of a 12 Gyr, [Fe/H] $= -2.5$ isochrone[10] over-

laid at the distance modulus of Tucana II[37, 13] on a g, r color-magnitude diagram of stars within 20 arcmin of the center of the system, along with a few horizontal branch candidates. This color-magnitude diagram had been generated by running the Source Extractor software[237] with default parameters on Dark Energy Survey images of Tucana II obtained from the NOAO public data archive[238, 239].

4.2.2 Spectroscopic Observations

We obtained spectra of 22 candidate members of the Tucana II ultra-faint dwarf galaxy using the MagE spectrograph[226] on the Magellan-Baade Telescope on 3-5 August 2019. Data were obtained using 1x1 on-chip binning and a 0.7" slit which granted a resolving power of R$\sim$6000, and spanning a wavelength range of $\sim$320nm to $\sim$1000nm. The seeing was excellent ($<$0.6") throughout the duration of these observations. The MagE data were reduced using the CarPy reduction pipeline[196]. From a subsequent radial velocity analysis of these spectra (see Radial Velocity Analysis section below), 10 of these 22 candidates were confirmed as members of Tucana II. A Thorium-Argon lamp frame was obtained for wavelength calibration after slewing to each target. Our targets had g magnitudes between 17.5 and 20.5, and each star was observed for at least 10 minutes. For the purposes of more accurate metallicity determinations, the two most metal-poor stars in our sample were observed for more extended periods of time. A full summary of our MagE observations, including total exposure times and signal-to-noise values, is provided in Extended Data Table 1. Examples of our MagE spectra are shown in Extended Data Figure 4-5.

We had also obtained spectra of 43 stars in the field of the Tucana II ultra-faint dwarf galaxy using the IMACS spectrograph[227] on 23-25 July 2015, 25 May 2016, and 5-7 August 2016. These spectra were obtained simultaneously by using the multi-slit mode of the spectrograph with the f/4 camera, which granted a 15.4 arcmin x 15.4 arcmin field of view. A slit size of 0.7" and a 1,200l/mm grating were used for these observations, which resulted in a resolving power of R$\sim$11,000 and a dispersion of 0.19A/pixel over the wavelength range of these spectra ($\sim$750nm to $\sim$900nm). We note that this spectral range was chosen to cover the prominent telluric

absorption feature at ∼760nm and the calcium triplet lines at 849.8nm, 854.2nm, and 866.2nm. Due to the configuration of the multislit mask used for these observations, the actual wavelength range varied from star to star, but slits were placed such that, at minimum, the calcium triplet region was included. Our observing strategy followed that of previous IMACS spectroscopic studies of ultra-faint dwarf galaxy stars[217, 240], except we used a HeNeAr comparison lamp in each of our observations. A total of 14 x 2700s exposures were taken in July 2015 in mediocre seeing conditions (∼1.0" seeing), 4 x 2700s exposures in May 2016 in poor seeing conditions (>1.0"), and 8 x 2700s in generally fair seeing conditions (∼0.9") in August 2016. We reduced our data in the exact manner as outlined in the aforementioned studies, utilizing the Cosmos pipeline[227, 241] and a modified version of the DEEP2 reduction pipeline[242, 243].

4.2.3 Radial Velocity Analysis

We derived radial velocities closely following methods by refs[217, 240] when analyzing our IMACS spectra, and with slight modifications when analyzing our MagE spectra to account for instrumental differences, differences in wavelength range, and resolution. We briefly describe both analyses here.

The velocities from the IMACS spectra were derived by chi-squared fits[91] to a template IMACS spectrum of the bright, metal-poor giant HD 122563[56] observed in the same configuration as the multi-slit observations. The chi-squared fits were performed over the wavelength range 845nm to 868nm, and a velocity of -26.51 km/s was assumed for HD 122563[244]. Velocity corrections for the mis-centering of stars in their slits were computed by performing this same procedure over the telluric A-band region (750nm to 770nm) using a spectrum of the rapidly rotating hot star HR 4781[217]. These velocity corrections from the A-band region showed a systematic dependence on the position of the slit on the chip[217, 240]. Therefore, we fit a linear relation between the velocity correction and the slit position and applied the velocity correction from the A-band following this relation. This had the advantage of being applicable to spectra with A-band regions not covered in the spectral range or with low S/N. Heliocentric corrections were computed using the astropy package[245, 246].

The velocities from the MagE spectra were derived by cross-correlating the observed spectra with a template MagE spectrum of HD 122563 observed in the same configuration. The cross-correlation was performed over a wavelength region encompassing the prominent Mg b absorption feature (490nm to 540nm), and the velocity of HD 122563 was again assumed to be -26.51 km/s. The A-band region of an IMACS spectrum of HR 4781[217] that was smoothed to the resolution of the MagE spectra (R$\sim$6,700) was used to perform any corrections for the mis-centering of the stars in the slit.

The uncertainties on our velocity measurements were derived by adding in quadrature the statistical uncertainty with an estimate of the systematic uncertainty, following previous work[91, 217, 240]. To derive the statistical uncertainty, we first re-added random noise to each spectrum based on its noise level as estimated from its signal-to-noise ratio, re-measured the velocity, and then repeated this procedure 500 times[91]. Then, the statistical uncertainty was defined as the standard deviation of the resulting distribution of velocities, after removing 5 sigma outliers. To derive the systematic uncertainty, we computed velocities and statistical uncertainties for spectra that were obtained from individual exposures. We then derived the systematic uncertainty as the additional uncertainty needed to account for the variation in velocities across exposures for each star. The systematic uncertainty for the IMACS spectra was determined to be 1.2 km/s, which agrees with previous work[217, 240]. The systematic uncertainty for the MagE data was determined to be 2.95 km/s, likely due to the lower resolution (R$\sim$6,700) relative to the IMACS data (R$\sim$11,000).

Final velocities from the IMACS spectra were taken as the weighted average of velocity measurements from stacked spectra from each observing run, where each measurement was weighted by the inverse-square of the uncertainty. We excluded likely binaries from this step, which were identified as stars with at least one two sigma discrepancy in their radial velocities across epochs. Final velocities for the MagE spectra were calculated in the same way, except a weighted average was taken over velocity measurements from stacked spectra for each night of observation. All velocity measurements and uncertainties are listed in Extended Data Table 2.

We derive a systemic velocity for Tucana II of -126.4km/s $\pm$ 2.2km/s and a velocity dispersion of 4.6km/s $+1.5/-1.1$km/s using our sample of MagE and IMACS members. We implemented a maximum likelihood estimate following ref[247] using the emcee python package[248] to derive these values. Our systemic velocity and velocity dispersion are consistent with previous of those quantities for Tucana II[1], but have significantly smaller uncertainties. Our measurements imply that Tucana II has a mass of (2.4 +1.9/-1.2)$\times 10^6$ solar masses within a half-light radius, following ref[38]. We note that performing this analysis for a subsample of only the MagE spectra and another subsample of only the IMACS spectra both return Tucana II systemic velocities apart by 1.3 km/s, which is well within the statistical uncertainty in the systemic velocity. This suggests no significant systematic offset in the velocities derived from each instrument. Excluding the Tucana II star most likely to be a non-member (TucII-309; see Membership Confirmation) lowers our velocity dispersion by only $\sim$5%.

4.2.4 Metallicity analysis

From the MagE spectra, we derived metallicities using the magnesium b absorption feature ($\sim$515nm) and the calcium triplet lines (849.8nm, 854.2nm, and 866.2nm). From the IMACS spectra, we solely used the calcium triplet lines. We used an empirical calibration to derive metallicities from the calcium triplet lines[249], and employed standard spectral synthesis techniques to derive metallicities from the magnesium b region. Our particular implementation of these techniques is comprehensively described in prior work with MagE spectra of dwarf galaxy stars[137], which we summarize here.

Stellar metallicities can be derived from the equivalent widths of the calcium triplet lines in combination with the absolute V magnitude of the star[249]. For our MagE spectra, we measured the equivalent widths of the calcium triplet lines by fitting the Voigt1D model in the astropy.modeling package to each line. The spectra were continuum normalized by iteratively fitting a 3rd order spline after masking absorption features. For fits requiring additional attention due to, e.g., poor estimates

of the stellar continuum, equivalent widths were measured using the splot task in IRAF[250, 251]. The absolute V magnitude was derived for each star using color transformations from the DES photometric system[37] and the distance modulus of Tucana II[37, 13]. Random uncertainties were derived by re-measuring the equivalent widths after varying the continuum level by 1 sigma according to the S/N of each spectrum, and adopting a systematic uncertainty of 0.17dex[249] for the calcium triplet metallicity calibration. For our IMACS spectra, we fit the calcium triplet lines and derive uncertainties following previous studies of dwarf galaxies with IMACS [240]. We find that our IMACS metallicities agree within 1 sigma with literature metallicities for the two stars that have metallicities from previous spectroscopic work of Tucana II[39].

We measured metallicities from the magnesium b region by fitting synthetic spectra of varying abundances to the observed spectrum. The syntheses and fitting were performed with the Spectroscopy Made Hard software[197] using a 2017 version of the MOOG radiative transfer code[198] that has an updated treatment of scattering[199] and the ATLAS9 model atmospheres[200]. The linelist was compiled from various sources[252, 206, 153, 253] using software provided by C. Sneden (priv. comm.). The effective temperature and surface gravity of each star are required as inputs for the spectral synthesis. Initial stellar parameters were derived by matching the g−r colors of the Tucana II stars[254] to those on a [Fe/H] = −2.5, 12 Gyr isochrone[10]. To test this method we also derived stellar parameters in this manner for stars with known stellar parameters[39]. We find on average higher effective temperatures by 120 K and higher log g by 0.33 dex compared to the literature results. We therefore correct our stellar parameter measurements by these values in our analysis. We obtain random uncertainties by noting the variation in [Fe/H] required to encompass most of the noise in the absorption feature. Systematic uncertainties were derived by re-measuring [Fe/H] after varying the effective temperature by 150 K and the surface gravity by 0.3 dex. We note that all of our Tucana II members have metallicity measurements dominated by the systematic uncertainty, due to the relatively high signal-to-noise ratio (S/N > 25) of their spectra. Using these methods, we derive

metallicities that agree with literature values for the standard stars CD 38 245 ([Fe/H] = −3.97; literature [Fe/H] = −4.06[59]), CS 22897-052 ([Fe/H] = −3.11; literature [Fe/H] = −3.08[59]), and HD 122563 ([Fe/H] = −2.57; literature [Fe/H] = −2.64[56]) that were also observed by the MagE spectrograph.

We find that our metallicities from the magnesium b synthesis generally agree well with metallicities from the calcium triplet method. The metallicity differences have a mean value of 0.01 dex and a standard deviation of 0.26 dex, suggesting no systematic offset. We note that one distant star (Tuc2-309) has significantly different calcium triplet ([Fe/H] = −1.77) and magnesium b ([Fe/H] = −2.47) metallicities. Upon inspection of its spectrum, this star appears to be genuinely deficient in magnesium, or unusually enhanced in calcium, rendering its overall metallicity somewhat ambiguous. For consistency with our other measurements, we still report its metallicity as the weighted average of the calcium triplet and magnesium b metallicities. Further investigation of systematic offsets from the few stars in common between our MagE, IMACS, and MIKE datasets shows that they have metallicities consistent within 2 sigma uncertainties. The stars in common between the samples are indicated in extended Data Table 2.

The final metallicity measurements were derived by taking the weighted average of the metallicities from the calcium triplet lines and the magnesium b region (for the MagE spectra), or simply from the calcium triplet lines (for the IMACS spectra). Due to reduction issues (e.g., bad sky subtraction), we estimate the equivalent width of the reddest calcium triplet line for two stars (Tuc2-303 and Tuc2-319) by taking it to be 0.62 times the sum of the equivalent widths of the other two calcium triplet lines. The value of 0.62 is the mean of the corresponding ratio of equivalent widths for the other Tucana II members. As an additional quality criterion, we only report metallicities from IMACS spectra with S/N greater than or equal to 10. All the metallicities and uncertainties of Tucana II members are presented in Extended Data Table 3.

The mean metallicity of Tucana II was calculated as the average of the metallicities of its member stars, weighted by the squared inverse of their metallicity uncertainty. If

available, metallicities from high-resolution MIKE spectra were assumed as the stellar metallicities. Otherwise, metallicities from medium-resolution MagE and IMACS spectra were used. We used metallicities from M2FS spectra[1] for the two stars in that study listed as likely members (membership probability > 0.90) but that were not later re-observed. We reduced these M2FS metallicities by 0.32 dex, which is necessary to undo an artificial offset and bring the metallicities of the entire M2FS sample in agreement with those from high-resolution spectra[39].

We find some tantalizing evidence of a metallicity gradient in Tucana II (see top right panel of Figure 4-1). A linear fit to the stellar metallicities as a function of their distance from the center of Tucana II returns a statistically significant slope of -0.87dex/kpc $\pm$ 0.29dex/kpc. We note that this result rests on the existence of the farthest star in Tucana II; however, given its low metallicity of [Fe/H] $= -3.50$ there is little doubt that this star is not a member. For reference, if we were to exclude it, the resulting slope of -0.73dex/kpc $\pm$ 0.66dex/kpc would no longer be statistically significant. However, excluding the distant star that has the highest probability of being a foreground star, Tuc2-309 (see Section ?Membership confirmation?), results again in a more statistically significant slope of -0.99dex/kpc $\pm$ 0.24dex/kpc. This highlights the need for a larger sample of distant members to further validate the existence of any such gradient. At face value, our derived metallicity gradient for Tucana II is -0.11dex/r_h, assuming the Tucana II half-light radius in ref[37]. This is comparable to other metallicity gradients seen in larger dwarf spheroidal galaxies [89].

4.2.5 Membership confirmation

Members of ultra-faint dwarf galaxies are generally identified through a joint analysis of their metallicities and radial velocities, since ultra-faint dwarf galaxy stars tend to be far more metal-poor than foreground Milky Way stars and have clustered radial velocities. Namely, we identified members as stars with radial velocities within thrice the velocity dispersion of Tucana II around the mean radial velocity of Tucana II (-141 km/s to -110 km/s) and with metallicities [Fe/H] < -2.0. It is unlikely that

we excluded members based on the velocity threshold- no stars had radial velocities just beyond these cutoffs. However, one distant star (Tuc2-309) has a metallicity just above this threshold ([Fe/H] = -1.95), but a radial velocity and proper motion still consistent with membership. We therefore regard it as a likely member. Both the mean metallicity (~ -2.85) and systemic radial velocity (~ -125.6 km/s) of Tucana II are well separated from the corresponding values of the foreground stellar population, granting confidence to this particular scheme of confirming membership status. However, given the distant nature of our newly identified members, we performed an additional check on their membership likelihood.

In extended data Figure 4-6, we show the predicted halo distribution of radial velocities and metallicities for stars in the vicinity of Tucana II from the Besancon stellar population model[49], after replicating our isochrone, [Fe/H], and logg target selection cuts. We find that 0.4% of these stars satisfy our velocity and metallicity criteria for Tucana II membership. By replicating our isochrone, [Fe/H], and logg cuts but relaxing the proper motion cut on our SkyMapper catalog, we estimate that there are 260 foreground metal-poor giant stars within $\sim$9 half-light radii of Tucana II. If 0.4% of these stars satisfy our membership criteria, this would result in $\sim$1 false positive in our sample of Tucana II members. However, we note that the false positive rate drops off rapidly at lower metallicities. Restricting the range of membership metallicities to [Fe/H] < -2.5 results in a rate of 0%. Thus, while one of our more metal-rich Tucana II members could conceivably be a foreground star, there is a negligible chance that the farthest member is falsely classified, given its very low metallicity of [Fe/H] = -3.50. It is also extremely unlikely that any members beyond two half-light radii are falsely classified, given that their metallicities are all below [Fe/H] = -2.5, except for Tuc2-309.

In Extended Data Table 2, we list the membership status of every star in our sample. We identify stars that meet the above radial velocity and metallicity criteria as members. Some stars in our sample have radial velocity measurements that satisfy the velocity criterion, but do not have metallicities as their spectra have S/N < 10. We identify these stars as likely members. We note that all members have proper

motions consistent with the bounds defining the Tucana II stellar membership as listed in Section Selection of Candidate Members

4.2.6 Comparison to Canonical Stellar Density Profiles

We tested whether the spatial distribution of Tucana II member stars is compatible with either an exponential or a Plummer stellar density profile. Specifically, we drew samples of 19 members 10,000 times from each distribution to test the likelihood of observing 12 stars within 2 half-light radii and 7 stars beyond that distance. We find this happens in 7% of cases under a Plummer profile and in 2% of cases under an exponential profile. Excluding our distant member that is most likely to be a foreground star, Tuc2-309, leads to 15% of cases under a Plummer profile fulfilling our criterion. However, we caution that these numbers are very sensitive to the choice of structural parameters for Tucana II.

We assume a half-light radius of 7.2" for Tucana II[37] in this analysis. We opt for this value over others[13, 255] due to better agreement (within 2 sigma) between the structural parameters in ref [37] and those obtained from deeper follow-up photometry[256, 257, 258, 259, 260] of seven other dwarf galaxies with such available data. The structural parameters from refs[13, 255] for these seven systems show more scatter when compared to the deeper imaging studies. For completeness, we note that if we were to assume the half-light radii in refs [13, 255], the distances of the farthest two stars would be 4.1 and 6.8 half-light radii, and 3.6 and 6.0 half-light radii, respectively. These radii would lead to substantially more agreement with a Plummer profile. As a consequence, we cannot claim a discrepancy with these canonical profiles until deeper photometry of Tucana II is obtained.

From our Extended Data Figure 4-3 of candidate members, spectroscopic observations of stars can be regarded as complete down to g$\sim$19.5 within the inner region of the galaxy, but likely incomplete in the outer regions (beyond 3 half-light radii). This implies that additional distant members of the galaxy may be discovered in the future. If more stars were known in the extended halo, the underlying stellar density distribution would stray even further from any canonical density profile.

Finally, we note that there are multiple distance measurements of Tucana II in the literature, with all measurements being consistent within 2 kpc [37, 13, 261]. For consistency with our choice of structural parameters, we adopt a distance of 58 kpc from ref[37] throughout our analysis.

4.2.7 Systemic Proper Motion of Tucana II

We derive the systemic proper motion of Tucana II by taking the weighted average of the Gaia DR2 proper motions[111, 112] of members brighter than g = 20 in Extended Data Table 2. Each weight was taken as the inverse-square of the measurement uncertainty. We derive a systemic pm_ra = 0.955 mas/yr ± 0.047 mas/yr and a systemic pm_dec = -1.212 mas/yr ± 0.058 mas/yr.

4.2.8 Modeling of Tidal Disruption

In order to determine the expected location of tidal debris from Tucana II, we simulate its tidal disruption and subsequent stream formation using the modified Lagrange Cloud stripping technique[262] which has been updated to include the influence of the Large Magellanic Cloud (LMC)[263]. Including the LMC is crucial since it can deflect tidal debris, leading to a significant misalignment between the progenitor's orbit and tidal debris[263, 264]. We use a realistic Milky Way model[265] and the machinery of GALPOT[266] to evaluate accelerations in this potential. Motivated by recent fits to the LMC mass[263], we treat the LMC as a Hernquist profile[267] with a mass of 1.5×10^{11} solar masses and a scale radius of 17.13 kpc. We integrate Tucana II backwards for 5 Gyr starting from its present day distance[13], proper motions[124], and radial velocity from this work. The LMC is similarly integrated backwards starting with its present day observables[268, 269, 270]. We model the progenitor of Tucana II as a Plummer sphere with a conservative mass estimate of 2×10^{6} solar masses[1] and a scale radius of 100 pc. This produces tidal debris which is well aligned with the orbit. This shows that the debris should be aligned with the track shown in Figure 4-1 with a small offset of -2 ± 4 degrees on the sky. We find

that this alignment is not sensitive to the precise choice of the total mass of Tucana II.

We derived the tidal radius of Tucana II using the galpy[271] python library. Specifically, we instantiated an orbit using the orbital parameters of Tucana II[236] and derived a tidal radius using the rtide function[272] under the Milky Way potential MWPotential14. We then derived tidal radii for various masses of Tucana II to determine at what mass the tidal radius encompasses the distance to the farthest member (1.11 kiloparsec). This occurred for a mass of 1.3×10^7 solar masses, which we take as the lower limit on the Tucana II mass. We note that our choice of MWPotential14 is consistent with reporting a lower bound on the Tucana II mass. MWPotential14 is a low estimate for the Milky Way mass, and adopting a heavier Milky Way mass would only increase the Tucana II mass required to bound its farthest member.

We also tested whether the spatially extended members of Tucana II display a velocity gradient, which is a signature of tidally disrupting systems[229]. To do this, we fitted a line to our MagE and IMACS velocities, weighted by the inverse square of their velocity uncertainty, as a function of declination from the center of Tucana II. These velocities as a function of their declination from the center of Tucana II are shown in the bottom right panel of Figure 4-1. We find a slope of 0.06km/s/arcmin $\pm$ 0.16km/s/arcmin, suggesting that our velocities show no strong evidence of a velocity gradient. Our 2sigma upper limit on the velocity gradient would therefore be 0.32km/s/arcmin. The 2sigma upper limit increases to 0.36km/s/arcmin if Tuc2-309, the distant star most likely to be a non-member, is excluded.

4.2.9 Modeling of Dark Matter Density Profile

We model the density profile of the dark matter halo of Tucana II using a Jeans modeling procedure[272, 273, 274]. For completeness, we briefly outline the most important steps here but more details will be reported in Chang and Necib [275].

The three-dimensional distribution of the stars is modeled by a Plummer profile,

$$\nu(r) = \frac{3M}{4\pi a^3}\left(1+\frac{r^2}{a^2}\right)^{-5/2}$$

where L is the total luminosity and a is the scale length of the distribution. Given that the system is observed in projection, we use the surface brightness profile

$$I(R) = \frac{M}{\pi a^2}\left(1+\frac{R^2}{a^2}\right)^{-2}$$

where R is the projected radius, while r is the three dimensional radius from the center of the dwarf. Because the stars contribute negligibly to the gravitational potential, the value of L does not carry physical influence.

We model the density profile of dark matter by a generalized NFW profile[276],

$$\rho_{DM}(r) = \rho_0\left(\frac{r}{r_s}\right)^{-\gamma}\left[1+\left(\frac{r}{r_s}\right)\right]^{-(3-\gamma)}$$

where the free parameters that we fit for are the overall density normalization (ρ_0), the scale radius (r_s), and the slope of the inner profile (γ). We assume that the system is spherical and in equilibrium, and solve the projected Jeans equation

$$\sigma_p^2(R)I(R) = 2\int_R^\infty \left(1-\beta(r)\frac{R^2}{r^2}\right)\frac{\nu(r)\sigma_r^2(r)r}{\sqrt{r^2-R^2}}dr$$

where σ_p is the projected velocity dispersion along the line of sight, σ_r is the radial velocity dispersion in 3 dimensions, and $\beta(r) = 1-(\sigma_\theta^2+\sigma_\phi^2)/(2\sigma_r^2)$ is the velocity anisotropy of the stars. The radial velocity dispersion is the solution to

$$\frac{1}{\nu}\left[\frac{\partial}{\partial r}(\nu\sigma_r^2)+\frac{2\beta(r)}{r}(\nu\sigma_r^2)\right] = -\frac{GM(<r)}{r^2}$$

where G is the gravitational constant, and M(<r) is the enclosed mass within radius r, calculated from the density profile of dark matter.

We use an unbinned likelihood function[277] in order to take into account the in-

dividual velocity uncertainties of each star, first assuming that the system is isotropic ($\beta(r) = 0$). We use a MCMC procedure to find the best fit parameters, assuming uniform priors on Log10(a/kpc) of [-1.2, -0.6], Log10(L/(Lsun)) of [2.0, 4.0], Log10(ρ_0)/(solar masses/kpc^3) of [2.2, 13.0], Log10r_s/kpc of [-3.0, 2.0] γ of [-1, 3], and average velocity $< v >$/(km/s) of [-200,200].

Given the large swaths of literature on the mass anisotropy degeneracy (see ref[273] and references therein), we also rerun the mass modeling assuming the standard Osipkov-Merritt anisotropy[278, 279], defined as

$$\beta(r) = r^2/(r^2 + r_a^2)$$

,

where σ_r, σ_ϕ, and σ_θ are the velocity dispersions in spherical coordinates, and r_a is the anisotropy parameter that we fit for, which describes the transition of the anisotropy from beta = 0 at small radii, to beta = 1 at large radii. We assume a prior on Ln(r_a/kpc) of [-5, 0] to ensure the transition radius occurs before the location of the farthest star. We find that the mass of the system with this anisotropy model increases to (4.1 +6.1/-2.68)$\times$ 10^7 solar masses within 1 kpc, which is within a 1sigma variation of the mass in the isotropic case of (2.1 +3.7/-1.2)$\times 10^7$ solar masses. Furthermore, adopting the most extreme cases of constant velocity anisotropy still only vary our results at the 1 sigma level relative to the mass derived assuming isotropy. Assuming constant radial anisotropy (beta=1) increases our mass estimate to (7.0 +9.0/-3.0)$\times 10^7$ solar masses, while assuming extreme constant tangential anisotropy (beta = -9) still results in a large mass of (1.0 +1.6/-0.5)$\times 10^7$ solar masses within 1 kpc.

As presented in Figure 4-2, we performed the above analysis on two samples to investigate the effect of adding our newly discovered members to the body known members in the literature. The first sample is simply the previously known red giant members in the literature with precise velocity measurements[1]. The second sample is composed of previously known members and our newly discovered members. We

note that the sample of eight red giant members in ref[1] has a systemic velocity (~ -127.3 km/s) similar to the systemic velocity of just our newly discovered members (~ -126.4 km/s), suggesting no statistically meaningful velocity systematics across the two samples.

We note that the theoretically derived mass estimate from this method, and any larger mass estimates, are supported by our observationally derived lower bound of 1.3 $\times 10^7$ solar masses that is required to ensure that the most distant Tucana II member is gravitationally bound to the system.

We also derive the enclosed mass within 1 kpc of a 10^8 solar mass NFW halo to compare our results to recent bounds on the minimum halo mass[231]. We begin this calculation by using the python package Halotools v0.7[280] to initialize a 10^8 solar mass halo with a concentration parameter of 26[281]. We then use the enclosed_mass method to calculate that a mass of 2.5×10^7 solar masses exists within 1 kpc of such a NFW halo, which is comparable to the mass we derive within 1 kpc of Tucana II.

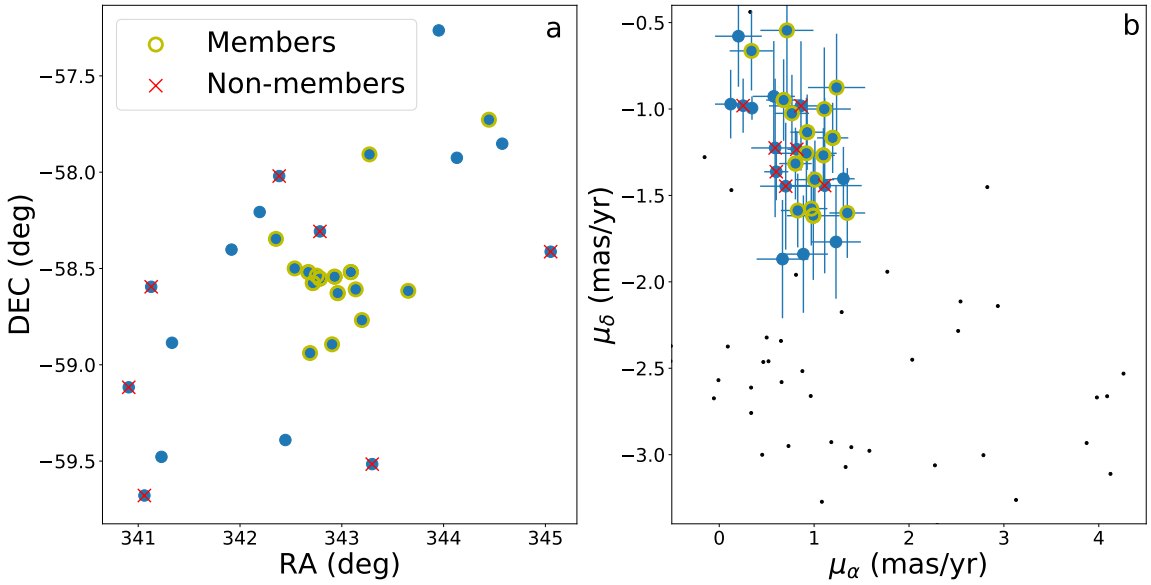

Figure 4-3 a. Locations of candidate members (blue data points) with g $<$ 19.5. Candidates were selected by identifying metal-poor giants with SkyMapper photometry (photometric [Fe/H] $<$ -1.0 and photometric log g $<$ 3.0 [39]), and then only including stars with proper motions around the systemic proper motion of Tucana II (0.2 mas/yr $<$ pm_ra $<$ 1.4 mas/yr and -1.7 mas/yr $<$ pm_dec $<$ -0.5 mas/yr). All stars confirmed as members of Tucana II in this work or prior work [1, 12] are highlighted in yellow. Confirmed non-members of Tucana II that were observed in this work are marked in red. b. Proper motions of candidate members with g $<$ 19.5. The majority of stars with proper motions near the systemic proper motion of Tucana II are members. This results from our exclusion of stars that are not metal-poor giants using log g to cut out foreground stars. Milky Way foreground stars outside our proper motion selection criteria are shown as small black points. The error bars on the proper motions correspond to 1sigma uncertainties in the Gaia DR2 catalog.

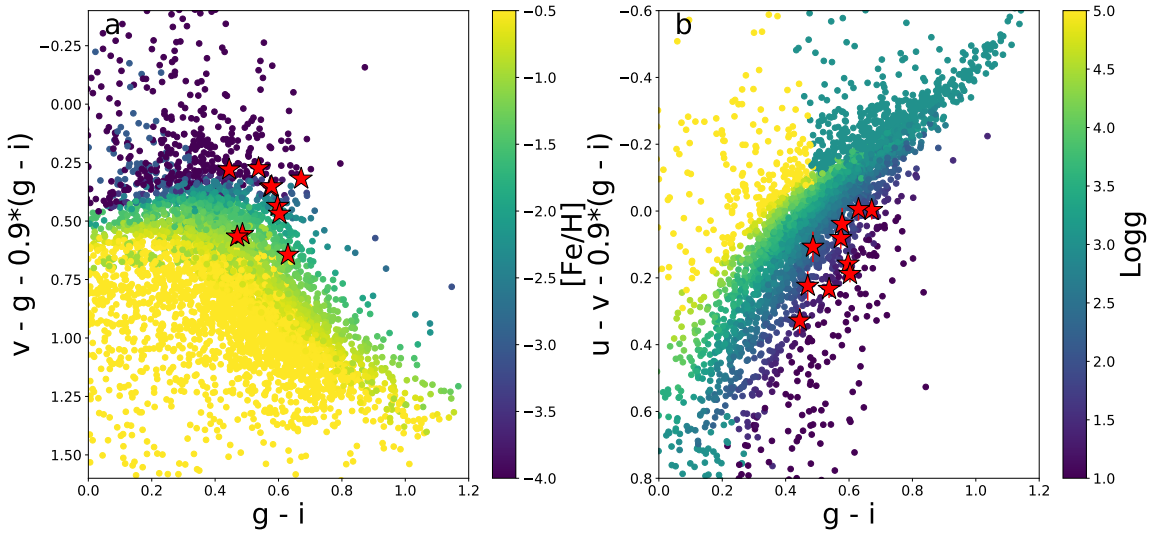

Figure 4-4 a. A metallicity-sensitive SkyMapper color-color plot of every star within a degree of Tucana II. The Tucana II members observed with MagE in this study are shown as purple stars, and all have photometric [Fe/H] < -1.0. Photometric metallicities were derived following ref[39]. b. A surface gravity-sensitive SkyMapper color-color plot of every star within a degree of Tucana II. Similarly to the metallicity-sensitive plot, the Tucana II members observed with MagE separate from the foreground population due to their low surface gravities.

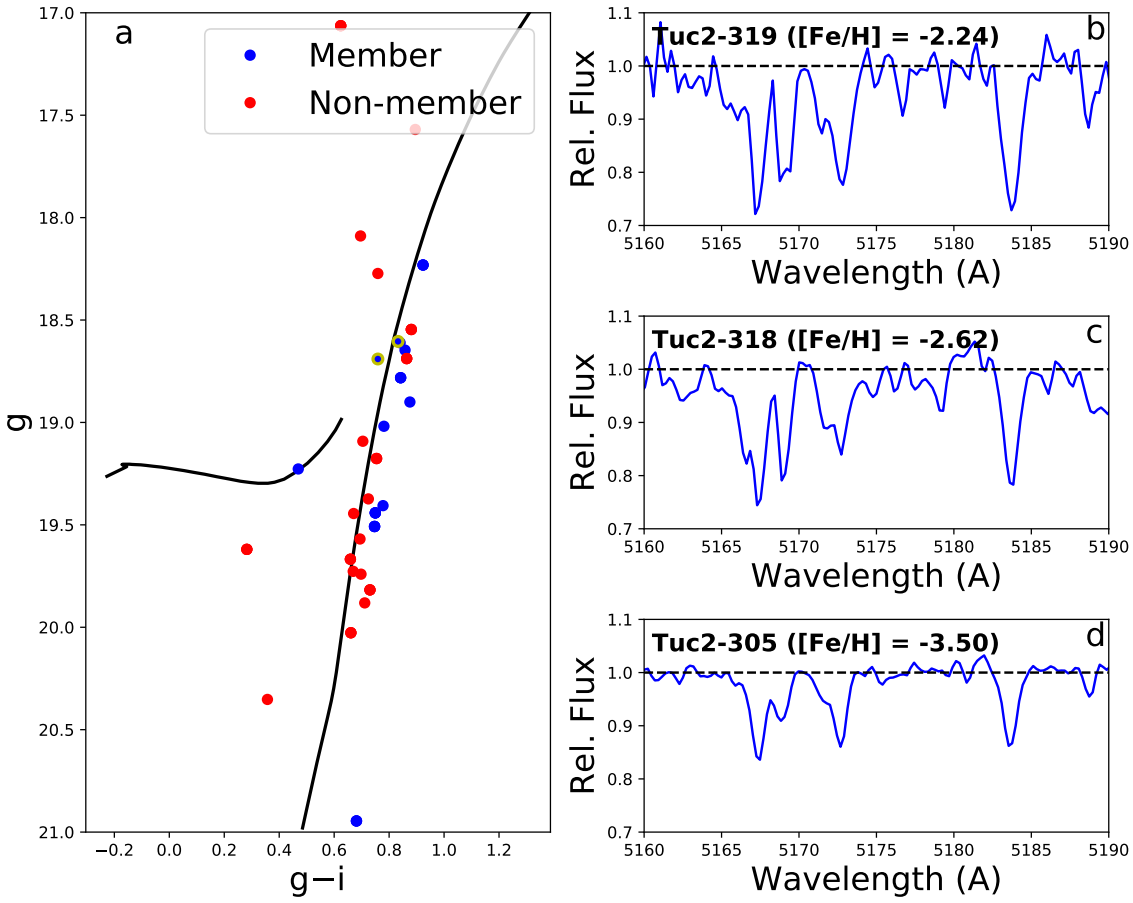

Figure 4-5 a. Color-magnitude diagram of the MagE and IMACS Tucana II members with DES photometry. A 10 Gyr, [Fe/H] = −2.2 MIST isochrone[14, 15, 40, 41, 42] at the distance modulus of Tucana II[37] is overplotted for reference. The horizontal branch from a PARSEC isochrone[43, 44, 45, 46, 47, 48] with the same parameters is also shown. Members and non-members are indicated in blue and red, respectively. The two most distant members are outlined in yellow. b,c,d. MagE spectra of the magnesium region Tuc2-319, Tuc2-318, and Tuc2-305. The absorption lines in the region become noticeably weaker at lower metallicities.

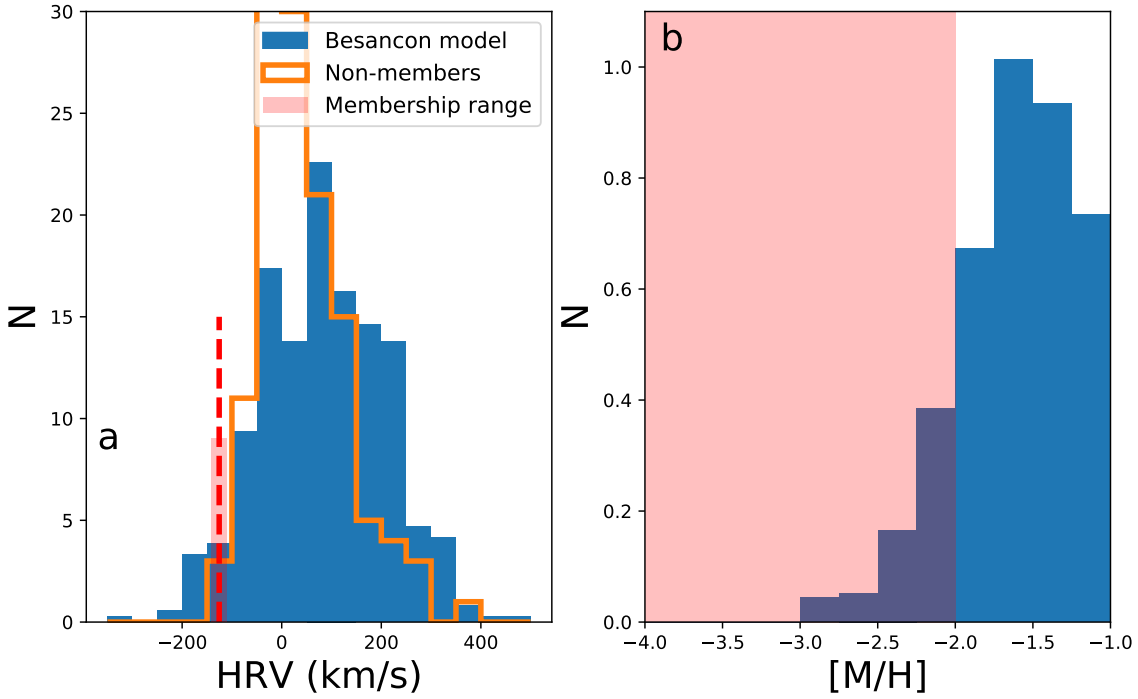

Figure 4-6 a. A histogram of MagE and IMACS radial velocities of stars determined to be non-members of Tucana II is shown in orange. In blue, we plot a scaled histogram of radial velocities of stars in the field of Tucana II, as generated from the Besancon model of stellar populations in the galaxy[49] after replicating our target selection cuts (blue). The vertical red line marks the systemic velocity of Tucana II [1], which is well separated from the foreground velocity distribution. b. Scaled histogram of metallicities of stars generated from the Besancon model following those in panel a. The red shaded region ([Fe/H] < -2.0) corresponds to the metallicities of the newly detected Tucana II members. Only 0.4% of simulated foreground stars satisfy our Tucana II membership criteria (-141 km/s $<$ HRV < -110 km/s; [Fe/H] < -2.0)[1], implying that our newly identified members are extremely unlikely to be false positives.

Chapter 5

Detection of a Population of Carbon-Enhanced Metal-Poor Stars in the Sculptor Dwarf Spheroidal Galaxy

The content of this chapter was published in the Astrophysical Journal as [215] on April, 2018.

Abstract

The study of the chemical abundances of metal-poor stars in dwarf galaxies provides a venue to constrain paradigms of chemical enrichment and galaxy formation. Here we present metallicity and carbon abundance measurements of 100 stars in Sculptor from medium-resolution ($R \sim 2000$) spectra taken with the Magellan/Michigan Fiber System mounted on the Magellan-Clay 6.5m telescope at Las Campanas Observatory. We identify 24 extremely metal-poor star candidates ([Fe/H] < -3.0) and 21 carbon-enhanced metal-poor (CEMP) star candidates. Eight carbon-enhanced stars are classified with at least 2σ confidence and five are confirmed as such with follow-up $R \sim 6000$ observations using the Magellan Echellette Spectrograph on the Magellan-Baade 6.5m telescope. We measure a CEMP fraction of 36% for stars below [Fe/H] $= -3.0$, indicating that the prevalence of carbon-enhanced stars in Sculptor is similar to that of the halo ($\sim 43\%$) after excluding likely CEMP-s and CEMP-r/s stars from our sample. However, we do not detect that any CEMP stars are strongly enhanced in carbon (e.g., [C/Fe] > 1.0). The existence of a large number of CEMP stars both in the halo and in Sculptor suggests that some halo CEMP stars may have originated from accreted early analogs of dwarf galaxies.

5.1 Introduction

The oldest stars in the Milky Way contain trace amounts of elements heavier than helium (or “metals") and measurements of their relative chemical abundances provide key constraints on the early phases of chemical evolution [e.g. 282, 283], galaxy formation [e.g. 284], and the star-formation history (SFH) and initial mass function (IMF) of their birth environment [e.g. 285]. Studying metal-poor (MP) stars ([Fe/H] < -1.0, where [Fe/H] $= \log_{10}(N_{Fe}/N_H)_\star - \log_{10}(N_{Fe}/N_H)_\odot$) and in particular, extremely metal-poor (EMP) stars ([Fe/H] < -3.0) in the Milky Way's dwarf satellite galaxies effectively probes the aforementioned topics due to the simpler dynamical and chemical evolution histories of dwarf galaxy systems (see Tolstoy et al. 176 for a complete review). Furthermore, dwarf galaxies have innate cosmological significance as they are hypothesized to be the surviving analogs of the potential building blocks of larger systems in hierarchical galaxy formation scenarios. Studying the most metal-poor stars in these systems is a promising avenue to explore this intriguing potential connection.

While the specific relationship between dwarf galaxies and their ancient analogs is not entirely understood, detailed abundance studies of the most metal-poor stars in ultra-faint dwarf galaxies and classical dwarf spheroidal (dSph) galaxies have shown some remarkable similarities between the chemical composition of EMP stars in dSphs and EMP stars in the halo of the Milky Way [286, 287, 288, 20, 21, 289, 290, 23, 24, 291, 26, 22, 29, 30, 5, 6, 32]. These results hint, at some level, of universality in early chemical evolution and suggest that some of the most metal-poor stars in the Milky Way halo could have formed in dwarf galaxies. Because of the rarity of EMP stars, further identification and study of these objects in any dwarf galaxy provides key information to further investigate these initial findings.

Chemically characterizing members of the Sculptor dSph galaxy has provided insights on its chemical evolution and formation using high-resolution spectroscopy of red giant stars [292, 293, 294]. Tolstoy et al. [228] found evidence for two stellar components in Sculptor, as also seen in other dSphs. More recently, Kirby et al.

[288] analyzed 388 members of Sculptor to derive the metallicity distribution function (MDF). Later, Kirby et al. [283] used the MDFs of Sculptor (Scl) and other dSphs to investigate chemical evolution models. Additionally, observations of ∼600 probable members in Scl by the DART collaboration [e.g., 295, 296] were used by Romano and Starkenburg [297] to get a more complete picture of the MDF of Scl for modeling chemical evolution. Moreover, observations of a few individual EMP stars in Sculptor provided the first evidence that low-metallicity stars in dSphs are present and have chemical signatures matching those of EMP halo stars [20, 290]. Recently, work by Simon et al. [5] and Jablonka et al. [6] has indicated that EMP stars in Sculptor may have been enriched by just a handful of supernovae from the first generation of stars.

The population of stars with [Fe/H] $<$ –2.5 in the Milky Way halo has long been known to include a large fraction enhanced in carbon [298, 299, 300, 301, 170, 302, 54, 8, 99]. This discovery led to the classification of carbon-enhanced metal-poor (CEMP) stars (metal-poor stars with [C/Fe] > 0.7), within which exist subdivisions contingent on the enhancements of r-process and/or s-process elements. Of those, CEMP-s and CEMP-r/s stars are readily explained as the products of binary mass transfer from an asymptotic giant branch (AGB) companion [303, 304]. However, stars that show [C/Fe] enhancement reflecting the chemical composition of their formative gas cloud, as is thought to be the case for CEMP-r and CEMP-no stars, are the most useful in constraining theories of early chemical evolution. Proposed mechanisms behind this early carbon enhancement include "mixing and fallback" SNe and massive rotating stars with large [C/Fe] yields, as discussed in e.g., Norris et al. [305].

Interestingly, the current sample of stars in Sculptor with [Fe/H] < -2.5 from Starkenburg et al. [306], Simon et al. [5], and Jablonka et al. [6] contains no CEMP stars, contrary to expectations set by the high fraction of CEMP halo stars and earlier results that low-metallicity chemical evolution appears to be universal. Only one CEMP-no star has been previously detected in Sculptor [307], with [Fe/H] = –2.03 and [C/Fe] $\sim$ 0.51, and only three CEMP-s stars are known in the galaxy out of spectroscopic samples of hundreds of stars [308, 309]. Under the assumptions that the ancient analogs of today's dwarf galaxies formed the Milky Way halo, one

would expect that dwarf galaxies should show carbon enhancement in their oldest stellar population as well. Earlier work detected a number of carbon-strong stars in dSph galaxies, including Sculptor, but did not report individual metallicities for stars, precluding the characterization of these detected carbon-strong stars as CEMP stars [310, 311, 312, 313, 314, 315, 316, 317]. More recent searches in dSph galaxies [291, 318, 306, 307, 4, 319] have, however, detected only a handful of any category of CEMP stars.

To investigate this apparent dearth of true CEMP stars, or CEMP-no stars, we surveyed Sculptor with the goal of identifying EMP star candidates and robustly characterizing its metal-poor population (Hansen et al., in prep). We conducted follow-up observations of the most promising of these candidates to establish the low-metallicity tail of the MDF of Sculptor, and constrain the CEMP fraction in the system. In this paper, we present [Fe/H] and [C/Fe] measurements of the stars in our sample. In Section 5.2, we provide an overview of the target selection and observations. In Sections 5.3 and 5.4, we outline our methods of obtaining [Fe/H] and [C/Fe] abundances for our sample. In Section 5.5, we discuss additional measurements and considerations that are useful in analyzing our sample. We present our results, discuss implications, and conclude in Section 5.6.

5.2 Observations and Data Reduction

5.2.1 Target Selection

We first obtained low-resolution ($R \approx 700$) spectroscopy of eight fields in Sculptor using the f/2 camera of the IMACS spectrograph [227] at the Magellan-Baade telescope at Las Campanas Observatory. Each IMACS field spans a diameter of $27.4'$, and the eight fields together produce nearly complete coverage of the upper three magnitudes of Sculptor's red giant branch (RGB) over a $37' \times 39'$ area centered on

the galaxy, which approximately corresponds to a diameter of four times the core radius [320]. The IMACS observations were taken with a narrow-band Ca K filter attached to a 200-lines mm^{-1} grism. With this setup, approximately 900 stars can be observed at a time. IMACS targets were selected from the photometric catalog of Coleman, Da Costa, and Bland-Hawthorn [50] using a broad window surrounding the RGB so as not to exclude stars at the extremes of the metallicity distribution. The selection limits were based on a Padova isochrone [321] passing through the Sculptor RGB, and extended from 0.37 mag bluer than the isochrone to 0.19 mag redder than the isochrone in $V - I$, down to $V = 20$.

We selected Sculptor stars from the IMACS spectra for more extensive spectroscopic follow-up observations. We identified a sample of low-metallicity candidates by searching for stars with the smallest Ca K equivalent widths, adjusting for the color of each star according to the calibration of Beers et al. [52]. The most metal-poor known Sculptor stars from Frebel et al. [20] and Tafelmeyer et al. [290] were independently recovered in this data set, as well as two new [Fe/H] < -3.5 stars [5]. We then obtained $R \sim 4000$ and $R \sim 6000$ optical spectra of 22 of the best candidates, using the MagE spectrograph [226] at the Magellan telescopes. The majority of the observed stars were confirmed as EMP stars, including a number with spectra dominated by carbon features.

5.2.2 M2FS Observations

Having confirmed the utility of the IMACS data for both identifying EMP and carbon-rich candidates in Sculptor, we set out to obtain medium-resolution spectra of a much larger number of EMP candidates. We observed two partially overlapping 29.5′-diameter fields in Sculptor using the Michigan/Magellan Fiber System (M2FS) [322] on the Magellan–Clay telescope. We employed the low-resolution mode of M2FS, producing $R = 2000$ spectra covering $3700 - 5700$ Åfor 256 fibers.

M2FS targets were selected in two categories. First, we chose all of the EMP candidates from the IMACS sample (including those confirmed as low metallicity and/or carbon-rich with MagE spectra). Since these candidates only occupied about

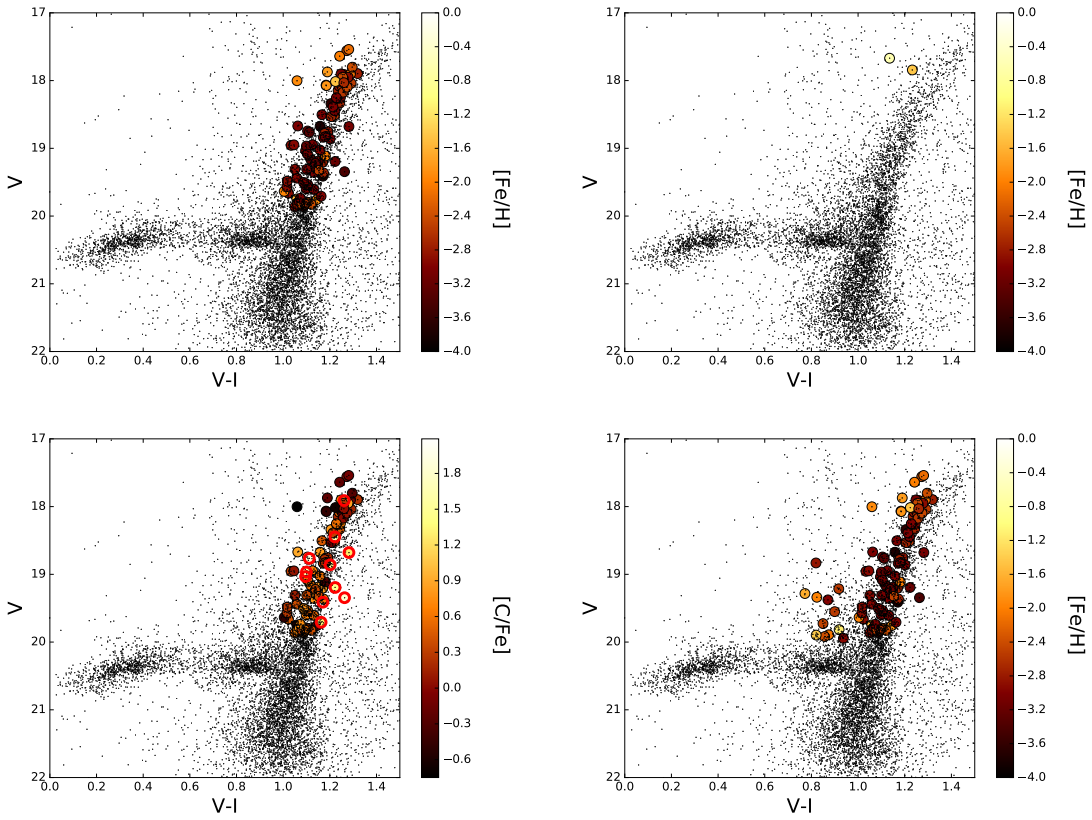

Figure 5-1 Color magnitude diagrams (CMDs) of Sculptor from Coleman et al. [50]. M2FS targets for which [Fe/H] and [C/Fe] are computed are over plotted. Top left: [Fe/H] of stars on the red giant branch of Sculptor that were selected as the most metal-poor candidates. Top right: [Fe/H] of bright stars that were selected to fill available fibers. Much of the bright star sample was excluded from this work (see Section 5.3.3). Bottom left: [C/Fe] of stars on the red giant branch of Sculptor that were selected to be metal-poor. Stars with saturated G-bands are circled in red. Bottom right: [Fe/H] of all stars we observed that were selected to be metal-poor.

half of the M2FS fibers, we then added a magnitude-limited "bright" sample containing all stars along the Sculptor RGB brighter than $V = 18.1$ in field 1 and $V = 18.0$ in field 2 (the difference between the two reflects the number of fibers available and the number of bright stars in each field). This bright sample should be unbiased with respect to metallicity or carbon abundance. About 30 fibers per field were devoted to blank sky positions. A few broken fibers were not used. The first M2FS field, centered at RA (J2000), Dec (J2000) = 00:59:26, −33:45:19, was observed for 5×900 s on the night of 23 November, 2013. The second M2FS field, centered at 01:00:47, −33:48:39 was observed for a total of 6838 s on 14 September, 2014. Figure 5-1 shows the M2FS targets for which [Fe/H] and [C/Fe] were measured in this work on color magnitude diagrams of Sculptor. We note that stars with saturated CH G-bands are circled in red in the bottom left panel of Figure 5-1. While the most carbon-enhanced stars do appear to be biased redward of the Sculptor RGB, they are not excluded from our selection procedure.

M2FS data were reduced using standard reduction techniques [323]. We first bias-subtracted each of the four amplifiers and merged the data. We then extracted 2D spectra of all the fibers by using the spectroscopic flats to trace the location of science spectra on the CCD, flattened the science data, and took the inverse variance weighted average along the cross-dispersion axis of each science spectrum to extract a 1D spectrum.

We computed wavelength solutions using spectra of HgArNeXe and ThAr calibration arc lamps. The typical dispersion of our wavelength solution was ~ 0.10 Å, which we derived by fitting third-degree polynomials to the calibration lamp spectra for the 2013 data. We derived the wavelength solution for the 2014 data by fitting third-degree Legendre polynomials. We performed the sky-subtraction by fitting a fourth-order b-spline to the spectra of ~ 10 sky fibers on the CCD, and fitting a third-order polynomial to the dependence of these spectra on the cross-dispersion direction of the CCD (e.g., the location of the fiber's output on the CCD). We then subtracted the predicted sky model at the location of each science spectrum on the CCD, and extracted final 1D spectra.

5.2.3 Follow-up MagE Observations

Motivated by the number of EMP and CEMP candidates from the M2FS data, we observed an additional ten Sculptor stars using the MagE spectrograph on the Magellan-Baade telescope in September 2016. This brought the total number of Sculptor stars observed with MagE to 31 stars, as one star had already been observed as part of the original 22 star sample (see Section 5.2.1). Five of these ten stars showed strong carbon features in their M2FS spectra. Another five were not seen to be as carbon-enhanced from their M2FS spectra, but we chose to observe them due to their similar stellar parameters to the strongly carbon-enhanced stars. These ten stars were analyzed to corroborate our M2FS carbon measurements. We also observed the halo CEMP-r/s star CS29497-034 for reference purposes. Five stars (four CEMP candidates and CS29497-034) were observed with the $0.7''$ slit ($R \sim 6000$), which granted sufficient resolution to resolve barium lines at 4554 Å, 4934 Å, 5853 Å, 6141 Å, and 6496 Å. The remaining stars were observed with the $1.0''$ slit ($R \sim 4000$). The MagE spectra were reduced using the Carnegie Python pipeline described by Kelson [196]. With these observations, we confirmed the CEMP and regular metal-poor nature of our candidates, as suggested by the M2FS observations.

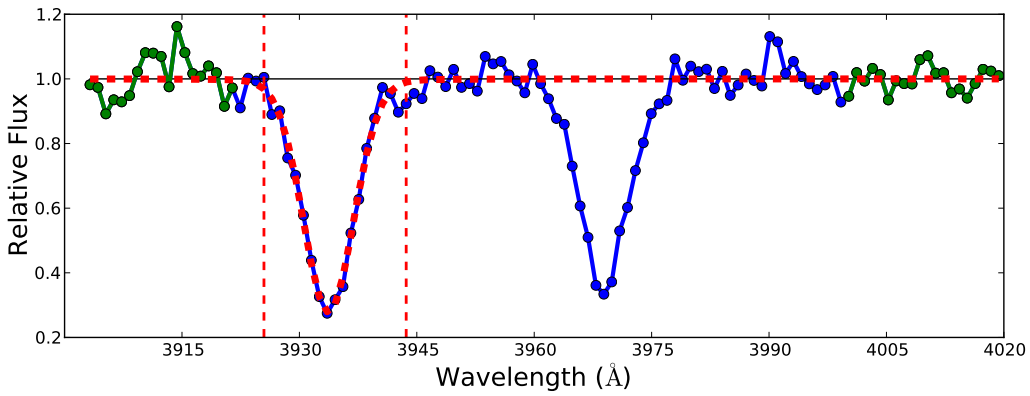

Figure 5-2 Spectral region around the Ca II K line (3933.7 Å) after continuum normalization. The horizontal black dashed line depicts the continuum fit to the blue and red sidebands (green), and the vertical red dashed lines correspond to the range of integration for the KP index. The over-plotted dashed red line corresponds to the best fit Voigt profile.

5.3 Metallicity Measurements

We used established calibrations of two spectral line indices to measure [Fe/H] from the M2FS spectra. The first such index is the KP index, a measure of the equivalent width of the Ca II K line at 3933.7 Å. The second index is the LACF index, a line index derived from applying the autocorrelation function (ACF) to the wavelength range 4000 Å to 4285 Å, which is chosen due to the presence of many weak metal lines. Both line indices, along with the nature of their calibration to [Fe/H] values, are thoroughly discussed by Beers et al. [52] and their implementation in this work is detailed in this subsection.

5.3.1 Membership Selection

We measured radial velocities for each star primarily to exclude non-members of Sculptor. Radial velocities were measured by cross-correlating the spectrum of each star with a rest-frame spectrum of the metal-poor giant HD122563. Wavelength calibration for spectra obtained in 2013 was carried out using a ThAr lamp, resulting in a well calibrated range from 3900 Å to 5500 Å. For the cross-correlation, we used this full range to determine velocities. However, spectra obtained in 2014 had associated HgArNeXe arc lamp frames taken, which provided fewer usable reference lines. It was found that cross-correlating over only the Hβ line (4830 Å to 4890 Å) gave the most precise ($\sim$10 km s^{-1}) velocity measurements for these spectra. Moreover, velocities obtained from the M2FS fiber observations in 2014 had to be adjusted to ensure that the mean velocity of the stars was centered on the velocity of Sculptor. Accordingly, velocities measured based on fiber observations on the red CCD chip were increased by 35 km s^{-1}. Those from the blue CCD chip observations were increased by 31 km s^{-1}. For stars on both the 2013 and 2014 fiber plates, we used the velocity measurement from the 2013 spectrum.

We assumed that stars with velocities within 35 km s^{-1} of the systemic velocity of Sculptor were members. This threshold corresponded to roughly 2.5σ of our distribution of velocities after excluding outliers. We found that applying this membership

criterion recovered known members of Sculptor from Walker et al. [324] and Kirby et al. [288]. Using this criterion, we excluded four stars in our sample that would otherwise have been part of this data set.

5.3.2 Stellar Parameters

We derive initial $B-V$ color, $T_{\rm eff}$, and $\log g$ estimates of stars in our IMACS sample by transforming V and I band photometry from Coleman et al. [50] using a 12 Gyr, [Fe/H] $= -2.0$ Dartmouth isochrone [10]. After a first pass measurement of [Fe/H] with this initial $B-V$ estimate (see Section 5.3), we iteratively update the metallicity of the isochrone and re-derive parameters until convergence. Before any measurement of [Fe/H], the spectrum was shifted so that the Ca II K line was centered at 3933.7 Å. This re-centering was necessary given that the wavelength calibration was not necessarily accurate around the Ca II K feature, since only there was only one line below 4000 Å (a weak Ar II line at 3868.53 Å) in our arc frames.

5.3.3 KP Index

The KP index is a measurement of the pseudo-equivalent width of the Ca II K line at 3933.7 Å. To determine final KP indices, we first compute the K6, K12, and K18 indices using bandwidths of $\Delta\lambda = 6$ Å, 12 Å, and 18 Å, respectively, when calculating the equivalent width of the Ca II K feature [325]. Table 5.1 lists the bands of these indices. The KP index assumes the value of the K6 index when K6 < 2 Å, the K12 index when K6 > 2 Å and K12 < 5 Å, and the K18 index when K12 > 5 Å.

To derive an estimate of the local continuum around the Ca II K feature, we fit a line through the red and blue sidebands listed in Table 5.1. We then visually inspected each continuum placement and applied a manual correction for a small subset of our sample that had an obviously bad fit (e.g., due to low S/N or nearby absorption features). After continuum normalization, we derived estimates of the K6, K12, and K18 indices using two methods. For the first approach, we directly integrated across the line band to estimate the pseudo-equivalent width. For the

Table 5.1. KP line indices (Å)

Line Index	Blue Sideband	Red Sideband	Band
K6	3903−3923	4000−4020	3930.7−3936.7
K12	3903−3923	4000−4020	3927.7−3939.7
K18	3903−3923	4000−4020	3924.7−3942.7

second approach, we integrated over the best-fit Voigt profile to the Ca II K line as illustrated in Figure 5-2. These two methods gave largely similar results, but the KP values from direct integration were adopted to ensure consistency with previous work involving the calibration. We derive [Fe/H] values using the KP index and $B - V$ color as inputs to the Beers et al. [52] calibration.

The KP index calibration from Beers et al. [52] is only valid for stars with $B-V \leq 1.2$, meaning it can only be readily applied to 100 stars in our sample. This population largely excludes the bright-star sample, which is unbiased with respect to metallicity.

5.3.4 LACF Index

The LACF index measures the strength of many weak metal lines between 4000 Å and 4285 Å [326, 52]. It is computed by taking the autocorrelation of a spectrum within the aforementioned wavelength range after excising extraneous line features. The LACF index is then defined as the log of the value of the autocorrelation function (ACF) at $\tau = 0$ as defined in Equation 5.1 over this interval.

To ensure we computed the LACF index in a manner consistent with Beers et al. [52], we closely reproduced their methodology. We first interpolated each spectrum using a cubic spline and re-binned in 0.5 Å increments to match their calibration sample. We then excised the ranges 4091.8 Å to 4111.8 Å and 4166 Å to 4216 Å to remove effects from the Hδ region and CN molecular absorption, respectively. To calculate the continuum, each of the three resulting ranges were independently fit by a fourth-order polynomial, after which outliers 2σ above and 0.3σ below each fit

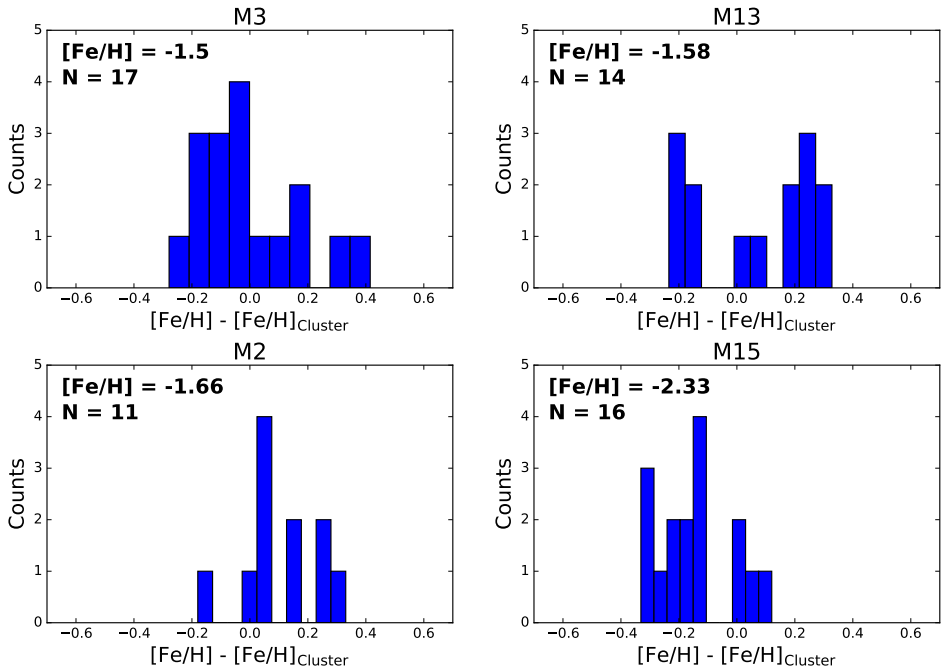

Figure 5-3 Histograms of the difference between our measured metallicity of each globular cluster member and the overall cluster metallicity for globular clusters M3 (top left), M13 (top right), M2 (bottom left), and M15 (bottom right).

were excluded. An acceptable continuum estimate was returned after four iterations of this process.

After normalizing each wavelength segment by its corresponding continuum estimate, we re-stitched the three segments together and computed the power spectrum of the resulting spectrum. We then set the high and low frequency components of the power spectrum to zero in order to remove the effects of high frequency noise and continuum effects, respectively. The inverse Fourier transform of the power spectrum was taken to derive the ACF, which was then divided by the square of the mean counts in the normalized region. We finally computed the LACF index by taking the log of the resulting ACF at $\tau = 0$.

It is important to note that an alternative expression of the autocorrelation function is

$$\mathrm{ACF}(\tau) = \int_{\nu_1}^{\nu_2} f(\lambda + \tau)\bar{f}(\lambda)d\lambda \tag{5.1}$$

where $\bar{f}(\lambda)$ is the complex conjugate of the function $f(\lambda)$. From Equation 5.1, it is clear that computing the LACF index, defined as the log of the value of the ACF at $\tau = 0$, is analogous to integrating the squared spectrum after manipulating Fourier components to remove continuum and noise related effects. This fact motivates the application of an ACF to measure line strength. As with the KP index, the LACF index is only calibrated to [Fe/H] for stars with $B - V \leq 1.2$ (see discussion in Section 5.3.3).

5.3.5 Comparison of Methods and Final [Fe/H] Values

To ensure our measured KP and LACF indices were consistent with the existing [Fe/H] calibration, we measured KP and LACF indices on a subset of the calibration sample in [52]. We found agreement in KP indices, but a gradually increasing scatter in LACF measurements when LACF < 0, which roughly corresponds to very metal-poor stars, stars with high effective temperatures, or stars with spectra that have low signal-to-noise. We thus chose to discard the LACF-based metallicity measurement for stars with LACF < -0.5 or when $[\mathrm{Fe/H}]_{\mathrm{KP}} < -2.5$. Since the LACF works

best at measuring [Fe/H] in the more metal-rich regime where weak metal lines are more prominent, this exclusion seems reasonable. We also chose to discard KP-based metallicity measurements when $[\mathrm{Fe/H}]_{\mathrm{KP}} > -1.0$, motivated by the failure of the KP calibration at high metallicities due to the saturation of the Ca II K line. In the regime where both KP and LACF based metallicities are valid, we take the average of the two measurements weighted by the measurement uncertainty.

The α-element abundance of stars in the Beers et al. [52] calibration is assumed to be $[\alpha/\mathrm{Fe}] = +0.4$ for $[\mathrm{Fe/H}] < -1.5$ and $[\alpha/\mathrm{Fe}] = -0.27\times[\mathrm{Fe/H}]$ for $-1.5 < [\mathrm{Fe/H}] < 0$. Stars in Sculptor display a different trend in $[\alpha/\mathrm{Fe}]$ with [Fe/H]. We account for this discrepancy by first computing an $[\alpha/\mathrm{H}]$ measurement for our stars based on the aforementioned α-element trends used in the Beers calibration for both the KP and LACF derived metallicities. We then fit a line to a Sculptor [Fe/H] vs. $[\alpha/\mathrm{H}]$ trend derived from measurements in Kirby et al. [288], and use this trend to compute an [Fe/H] measurement from our $[\alpha/\mathrm{H}]$ measurement for each of our Sculptor stars. This adjustment is motivated by the fact that the Beers et al. [52] calibrations measure the strength of α-element features and derive metallicities under the assumption of a given $[\alpha/\mathrm{Fe}]$ for halo stars, which is discrepant from the trend in dwarf galaxy stars. This correction typically increased the metallicities of stars in our sample by $\lesssim 0.1$ dex, since it had no effect on stars with $[\mathrm{Fe/H}] < -3.0$ and increased metallicities of stars with $[\mathrm{Fe/H}] = -2.5$ by ~ 0.1 dex.

Initial [Fe/H] uncertainties were assigned following Beers et al. [52]. To account for uncertainties in using an isochrone to transform between $V-I$ and $B-V$ color, we propagated the uncertainty in our original $V-I$ color to the final [Fe/H] measurements and added this effect in quadrature to the other uncertainties. We also propagated uncertainties in the age of the isochrone, which had negligible effects. Finally, we re-measured the metallicities after shifting the continuum by the standard errors of the fluxes in the red and blue continuum regions. The difference between the re-measured metallicities and the original metallities was added in quadrature with the other estimates of uncertainty. Typical uncertainties are ~ 0.25 dex.

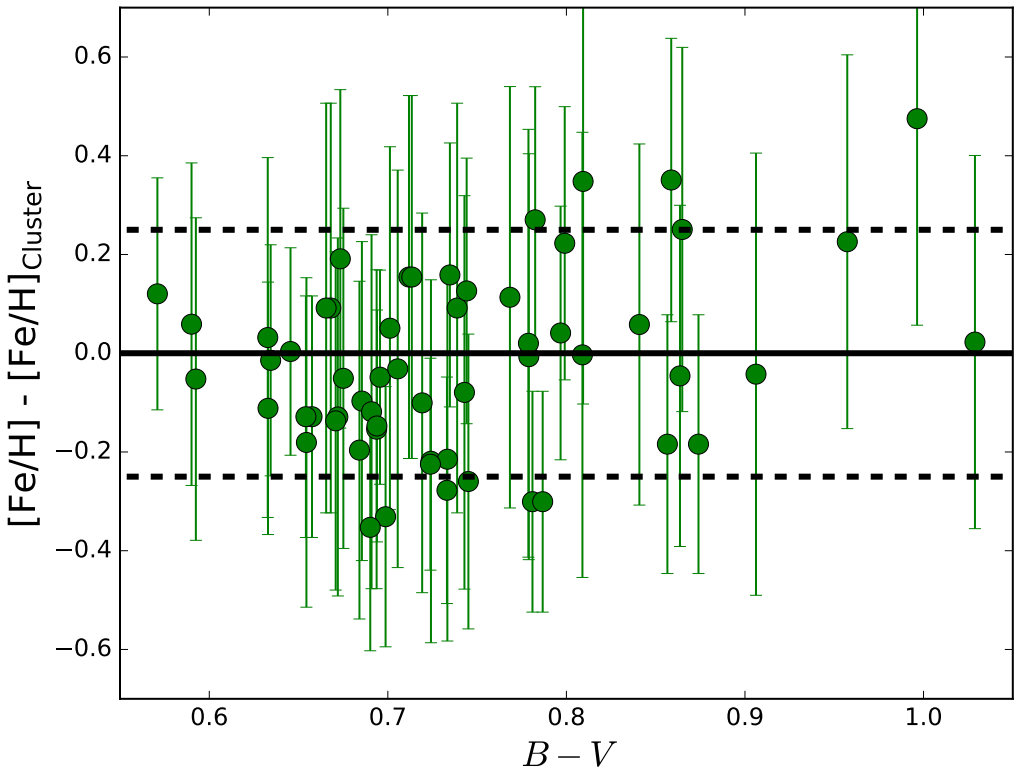

Figure 5-4 Difference between our measured metallicity of each cluster member and the overall cluster metallicity as a function of $B-V$ color. Dashed lines correspond to ± 0.25 dex. The mean of the distribution of residuals is -0.02 and the standard deviation is 0.18.

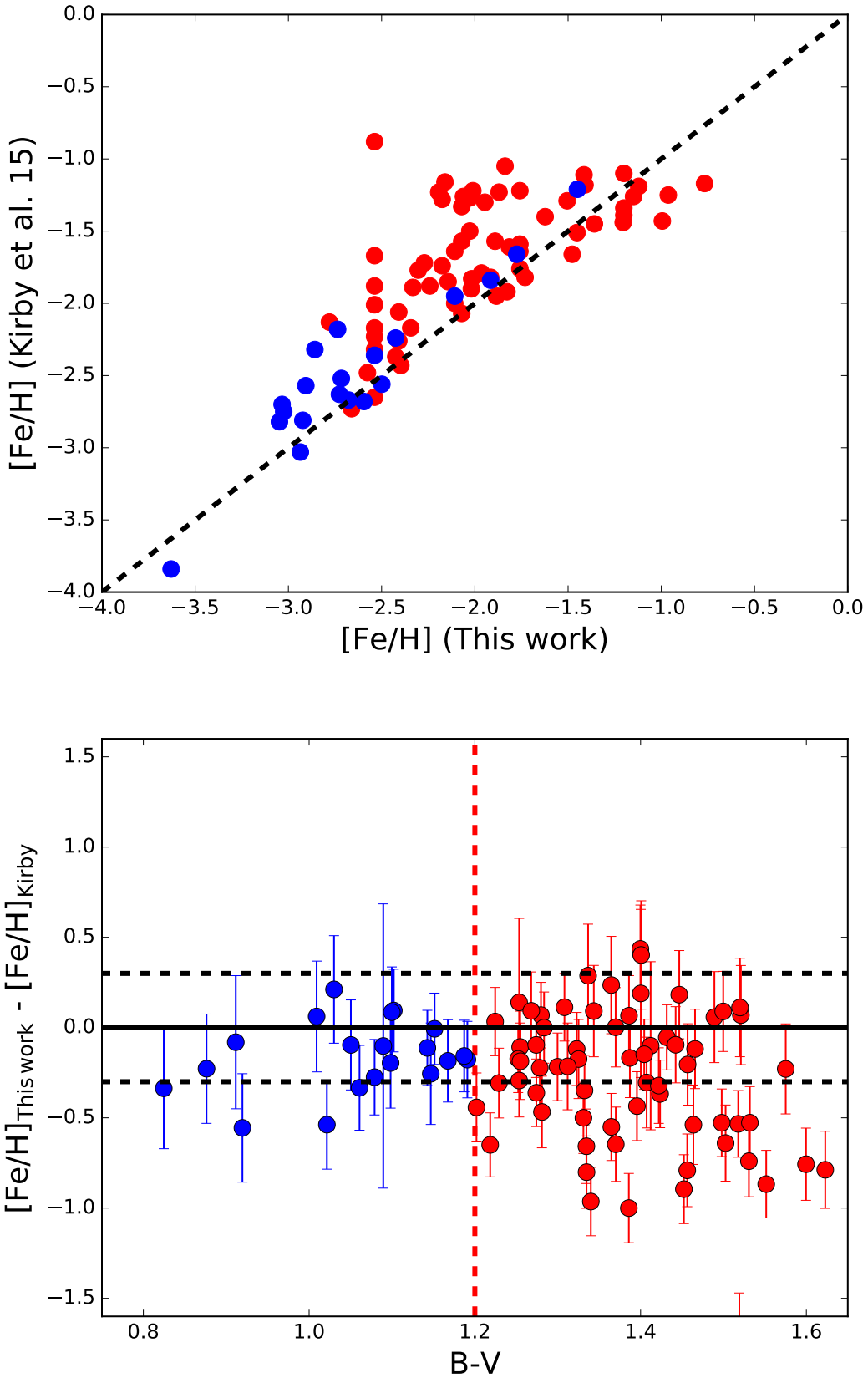

Figure 5-5 Left: Comparison of [Fe/H] measured by Kirby et al. [51] and [Fe/H] measured in this work for the 86 stars in both samples. Blue points correspond to stars with $B-V \leq 1.2$ and red points correspond to stars with $B-V > 1.2$. Right: The difference between [Fe/H] measured in this work and [Fe/H] measured by Kirby

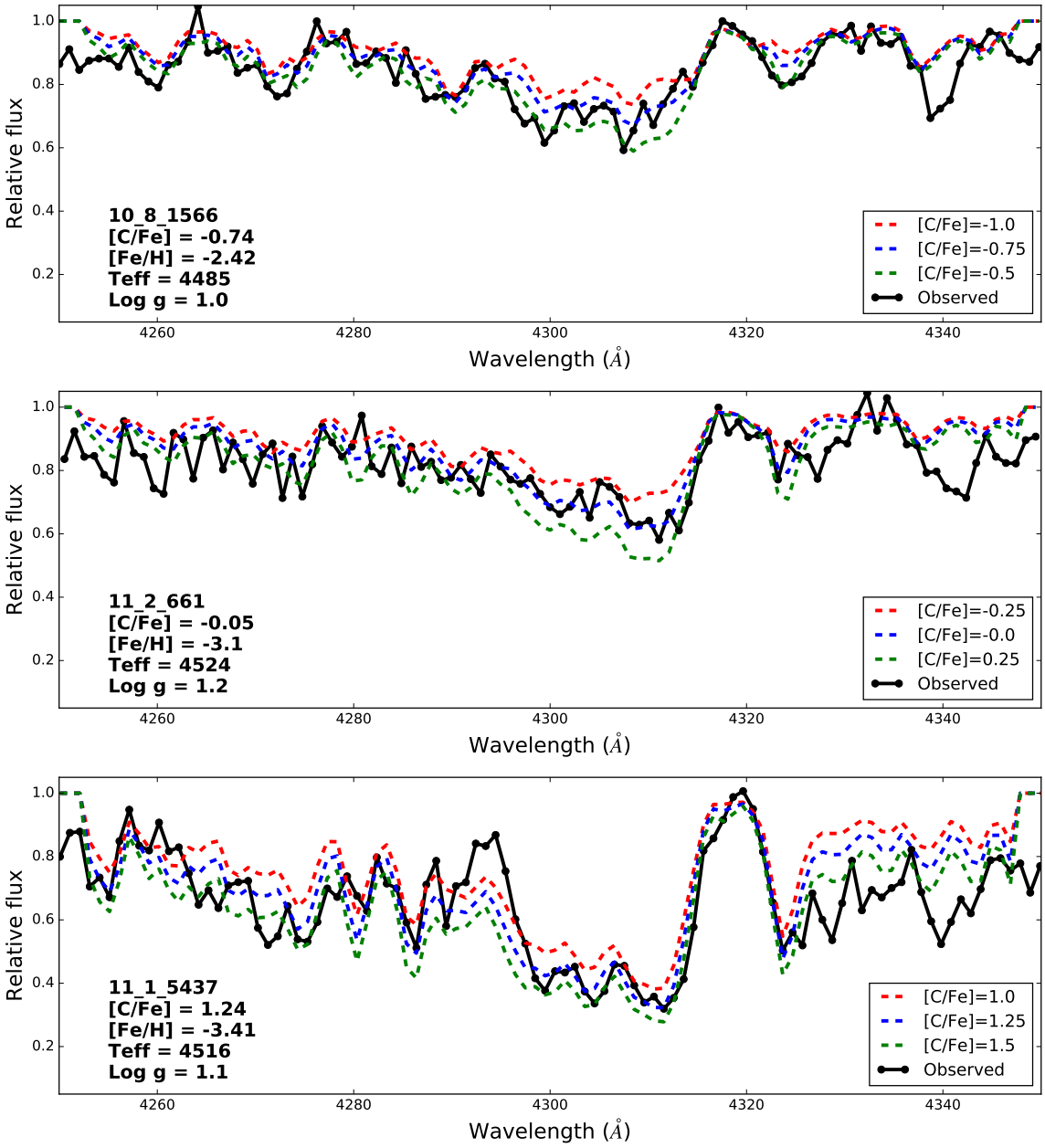

Figure 5-6 Spectral region around the G-band together with best fitting synthetic spectra (blue) for three example observed M2FS spectra (black). Synthetic spectra with [C/Fe] closest to the 1σ upper and lower [C/Fe] measurements are overplotted in red and green, respectively.

Table 5.2. Stellar parameter comparison of stars in the Sculptor dSph

ID	$\log g_{\rm MR}$	$\log g_{\rm HR}$	$T_{\rm eff_{MR}}$ (K)	$T_{\rm eff_{HR}}$ (K)	$[{\rm Fe/H}]_{\rm KP}$	$[{\rm Fe/H}]_{\rm HR}$	Δ[Fe/H]	Ref.
S1020549	1.30	1.25	4610	4702	-3.74 ± 0.21	-3.68	-0.06	S15
Scl 6_6_402	1.67	2.00	4796	4945	-3.91 ± 0.25	-3.53	-0.38	S15
Scl 11_1_4296	1.52	1.45	4716	4770	-3.90 ± 0.21	-3.77	-0.13	S15
Scl 07−50	1.35	1.05	4676	4558	-3.96 ± 0.20	-4.05	$+0.09$	S15
S1020549	1.29	1.25	4581	4702	-3.63 ± 0.21	-3.68	$+0.05$	S15
Scl 11_1_4296	1.55	1.45	4697	4770	-3.33 ± 0.22	-3.77	$+0.44$	S15
Scl 07−50	1.40	1.05	4641	4558	-3.77 ± 0.20	-4.05	$+0.28$	S15
ET0381	1.19	1.17	4532	4540	-2.83 ± 0.19	-2.83	$+0.00$	J15
Scl_03_059	1.10	1.10	4492	4400	-3.00 ± 0.15	-3.20	$+0.20$	J15

Note. — $[{\rm Fe/H}]_{\rm KP}$ is the metallicity measured by applying the KP index calibration. $[{\rm Fe/H}]_{\rm HR}$ is the metallicity measured in the indicated reference paper. Measurements labeled MR are medium-resolution measurements following the methodology of this paper. Top section: Measurements from smoothed high-resolution spectra of stars presented in Simon et al. [5]. Bottom section: Measurements from our medium-resolution M2FS spectra. S15 and J15 refer to Simon et al. [5] and Jablonka et al. [6], respectively. Log g values in this table have been corrected by $+0.39$ dex to account for the measured offset with respect to Kirby et al. [51].

5.3.6 External Validation: Comparison to Globular Cluster Members

As an external check on our metallicity measurements, we determined [Fe/H] values for cool ($T_{\rm eff} < 5500$ K) member stars in four globular clusters (M2, M3, M13, M15) with metallicities ranging from [Fe/H] = -2.33 to -1.5. We retrieved medium-resolution spectra of these stars from the Sloan Digital Sky Survey-III[1] [327, 328]. $V - I$ colors were derived by applying an empirical color transformation following Jordi et al. [329].

The metallicity spread among members of a globular cluster is a fraction of our measurement uncertainties, with the exception of some anomalies in M2 [330]. Thus, we used the offset of our [Fe/H] values of each cluster member from the average metallicity of the globular cluster to gauge the validity of our metallicity calibration. Before measuring metallicities, we recorded the mean [α/Fe] of these globular clusters from Carney [331], Kirby et al. [332], and Yong et al. [330] and corrected them for the discrepant [α/Fe] assumption in our calibrations. As shown in Figures 5-3 and 5-4, our measurements gave largely reasonable results, with an overall [Fe/H] offset of -0.02 dex and scatter of 0.18 dex. This is consistent with our typical derived

[1] `http://dr10.sdss3.org`

uncertainty in [Fe/H] of $\sim$0.25 dex.

5.3.7 External Validation: Comparison to Kirby et al.

Kirby et al. [288, 51, 179] measured the metallicities and α-abundances of a total of 391 stars in Sculptor with medium-resolution spectroscopic data from the Deep Imaging Multi-Object Spectrometer on the Keck II telescope. We found 86 stars in common with our full sample of $\sim$ 250 stars, of which 20 stars have $B-V \leq 1.2$. We compare the stellar parameter measurements between all 86 stars. We find reasonable agreement in our $T_{\rm eff}$ measurements as demonstrated by a mean offset of $\overline{\Delta T_{\rm eff}} = 25\,{\rm K}$ and a standard deviation of $\sigma(\Delta{\rm Teff}) = 137{\rm K}$.

For $\log g$, we correct the significant offset of $+0.39$ dex compared to the Kirby et al. sample. The mean of the differences in $\log g$ then has a standard deviation of 0.17 dex. If we were to only consider stars with $B-V \leq 1.2$, then the standard deviation would be 0.23 dex. This correction also results in agreement with $\log g$ values of stars with high-resolution spectroscopic stellar parameters (see Table 5.2). We note that not applying this gravity correction would artificially increase the carbon abundance correction we apply to take into account the evolutionary state of the star (see Placco et al. 8), and thus the number of CEMP stars in the sample.

We then compare our metallicities for the subset of stars with $B-V \leq 1.2$. We find a mean offset of $[{\rm Fe/H}] - [{\rm Fe/H}]_{\rm K10} \approx -0.11$ dex with a standard deviation of ~ 0.15 dex (excluding two outliers below $B-V = 1.2$ for which we measure a lower metallicity by over ~ 0.5 dex, see Figure 5-5). Including these outliers changes the mean offset to $[{\rm Fe/H}] - [{\rm Fe/H}]_{\rm K10} \approx -0.16$ dex and increases the scatter to ~ 0.19 dex.

Both outliers (10_8_2730 and 10_8_2788) in Figure 5-5 have low reported calcium abundances ([Ca/Fe]=-0.23 ± 0.30 and [Ca/Fe] = 0.05$\pm$0.39) in Kirby et al. [51]. This could lead to a weaker Ca II K line than our assumed [α/Fe] would suggest and would cause an underestimation of the metallicity.

Figure 5-5 also demonstrates the failure of the KP and ACF calibrations for $B-V > 1.2$. Accordingly, we choose to limit this work to the subset of stars in our sample with $B-V \leq 1.2$.

5.3.8 External Validation: Comparison to High-Resolution [Fe/H]

As a final check to ensure the KP calibration holds for extremely metal-poor (EMP) stars, we retrieved high-resolution spectra of four EMP Sculptor members from Simon et al. [5][2]. We smoothed these spectra to match the resolution of our medium-resolution data and degraded the signal-to-noise ratio to $20\,\text{Å}^{-1}$. We then computed KP-derived metallicities of these stars. The results are shown in the top portion of Table 5.2 and demonstrate the accuracy of KP calibration.

We also compared the KP-derived metallicities from our M2FS sample to high-resolution measurements in Simon et al. [5] and Jablonka et al. [6] for five stars in common to both samples. The results are shown in the bottom panel of Table 5.2. We note a marginally higher KP-derived metallicity in most cases for the EMP stars in the M2FS data. The largest residual (11_1_4296) can reasonably be explained due to the presence of noise near the Ca II K line. Interpolating over this noise spike results in a marginally lower disagreement of $+0.34$ dex when compared to the high-resolution [Fe/H] measurement.

5.4 Carbon Abundance Measurements

To derive carbon abundances ([C/Fe]), we matched each observed spectrum to a grid of synthetic spectra closely following the methodology of Kirby et al. [4]. We generated these using the MOOG spectrum synthesis code with an updated treatment of scattering [198, 199], and model atmospheres from ATLAS9 [200]. We independently computed [C/Fe] using regression relations from Rossi et al. [333], but found that fitting to a grid allowed accurate [C/Fe] measurements over a broader range of input parameters.

[2]The spectrum of the fifth star in that paper does not extend blue-ward to the Ca II K feature.

5.4.1 Spectrum Synthesis

Table 5.3 lists the stellar parameters of the generated grid of synthetic spectra. We used a comprehensive line list spanning 4100 Å to 4500 Å compiled by Kirby et al. [4]. The list comprises transitions from the Vienna Atomic Line Database [VALD; 150, 334], the National Institutes of Standards and Technology [NIST; 335], Kurucz [336], and Jorgensen et al. [337]. We assumed an isotope ratio of $^{12}C/^{13}C = 6$ based on the low surface gravity ($\log g \leq 2.0$) of most of our stars. The α-element abundance of the grid was chosen to be +0.2 dex, which is the mean expected value for this sample of Sculptor members, as gleaned from measurements by Kirby et al. [288]. Each synthetic spectrum was degraded to match the resolution of medium-resolution M2FS spectra. This grid was then used for measuring the carbon abundances reported in this paper. It should have similar inputs (e.g., line lists, model atmospheres) to previous works on the CEMP fraction in dwarf galaxies [e.g., 4] and other studies of halo stars. This enables a fair comparison of our results with literature values.

To appropriately compare our [C/Fe] measurements with nearly all values in the literature, we generated two smaller test grids based on model atmospheres and line lists different from those in the primary grid used in our analysis. The first test grid was generated using the Turbospectrum synthesis code [193, 148], MARCS model atmospheres [149], and a line list comprised of atomic data from VALD, CH data from Masseron et al. [53], and CN data from Brooke et al. [152] and Sneden et al. [153]. The second test grid had the same inputs as the first test grid, but was generated using MOOG to compare differences between just the two synthesis codes. Both test grids spanned 4500 to 4800 K in effective temperature, 1.0 to 2.0 dex in $\log g$, and −4.0 to −2.5 dex in [Fe/H], which roughly covers the stellar parameters of the more metal-poor stars in our sample.

5.4.2 Fitting to the Grid

Since synthetic spectra computed by MOOG are generated as normalized spectra, we normalized each spectrum. We found that iteratively fitting a cubic spline to the

observed data from 4100 Å to 4500 Å, excluding points 5σ above and 0.1σ below in each iteration, reproduced the continuum well. After dividing the observed spectrum by our continuum estimate, we found the best fitting synthetic spectrum by varying [C/Fe].

We then implemented a χ^2 minimizer to match the region spanning the CH G-band (4260 Å to 4325 Å) to the synthetic grid. We measured [C/Fe] by setting the three parameters $T_{\rm eff}$, log g, and [Fe/H] equal to the values determined from our medium-resolution M2FS measurements and letting [C/Fe] vary as a free parameter. We then interpolated between the five [C/Fe] measurements around the best [C/Fe] value with the lowest χ^2 values to determine a final carbon abundance. Sample fits are shown in Figure 5-6. Each [C/Fe] measurement was corrected to account for the depletion of carbon for stars on the upper red giant branch [8]. After this correction, we find no statistically significant trend in the [C/Fe] abundances with respect to measured Log g values.

To determine the uncertainty in our carbon abundance measurements, we re-measured [C/Fe] 100 times for each spectrum after varying the stellar parameters each time. For each measurement of [C/Fe], we drew values of $T_{\rm eff}$, log g, [Fe/H] from gaussian distributions parametrized by the medium-resolution measurements and uncertainties of those parameters. We adopted stellar parameter uncertainties of ± 150 K for $T_{\rm eff}$ and ± 0.15 dex for log g. Before each measurement, the continuum was multiplied by a number drawn from a gaussian distribution centered on one with $\sigma = 0.01$ to capture the uncertainty in continuum placement. The standard deviation of the resulting [C/Fe] measurements was taken as the total uncertainty in our measurement.

5.4.2.1 External Validation: Comparison to SkyMapper Sample from Jacobson et al. [3]

We applied our framework to measure [C/Fe] values to a sample of high-resolution Magellan/MIKE spectra of metal-poor halo stars selected from the SkyMapper survey. These spectra were degraded to match the resolution of our medium-resolution

Table 5.3. Stellar parameter range of grid of synthetic spectra

Parameter	Minimum	Maximum	Step
λ	4250 Å	4350 Å	3930.7−3936.7
log g	0.0	4.0	0.5
[Fe/H]	−4.0	+0.2	0.2
[C/Fe]	−2.00	2.00	0.25

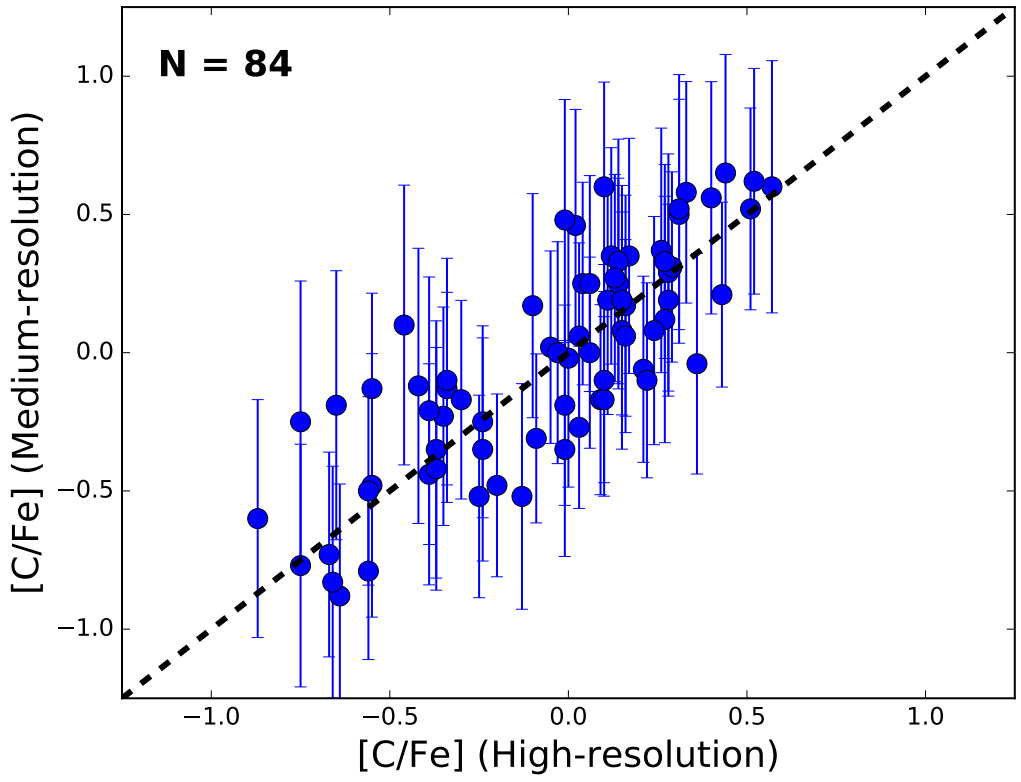

Figure 5-7 Carbon abundance measurements of metal-poor stars from Jacobson et al. [3] after spectra were degraded to the same resolution as the Sculptor M2FS spectra versus high-resolution [C/Fe] measurements of the same stars. The median offset between medium-resolution and high-resolution [C/Fe] measurements is 0.03 dex and the observed scatter is 0.22 dex.

Table 5.4. [C/Fe] comparison with literature

ID	$[C/Fe]_{This\ work}$ (dex)	$[C/Fe]_{ref}$ (dex)	Δ[C/Fe] (dex)	Ref.
S1020549	< 0.25	< 0.20	–	S15
Scl11_1_4296	0.25 ± 0.32	0.34 ± 0.34	-0.09	S15
Scl07-50	< 0.34	-0.28 ± 0.34	–	S15
1008832	-1.14 ± 0.27	-0.88 ± 0.10	-0.26	K15
1007034	-1.01 ± 0.37	-1.11 ± 0.10	$+0.10$	K15
1007391	$+0.55 \pm 0.38$	-0.05 ± 0.13	$+0.60$	K15
1009538	-0.78 ± 0.61	-0.80 ± 0.11	$+0.02$	K15
1010633	-0.84 ± 0.31	-0.84 ± 0.10	0.00	K15
1013035	< 0.00	< -1.24	–	K15
1013808	< 0.22	-1.05 ± 0.27	–	K15
1016486	-0.26 ± 0.36	-0.65 ± 0.12	$+0.39$	K15
ET0381	-0.18 ± 0.34	$-1.00 \pm 0.15^{\dagger}$	$+0.82^{\ddagger}$	J15
scl_03_059	-0.39 ± 0.40	$-1.20 \pm 0.40\dagger$	$+0.81^{\ddagger}$	J15

Note. — S15, K15, and J15 refer to Simon et al. [5], Kirby et al. [4], and [6], respectively.
† Jablonka et al. [6] present asymmetric uncertainties. These are the average of their asymmetric uncertainties.
‡ See Section 5.4.4 for a discussion of the potential causes of these discrepancies.

spectra and were injected with gaussian noise to bring the S/N down to 20 $\mathrm{\AA}^{-1}$. High-resolution [C/Fe] abundances computed by Jacobson et al. [3] were used as reference values.

Analyzing a sample of 84 stars, we find that our [C/Fe] values differ from the high-resolution values [C/Fe] by a median value of 0.03 dex with $\sigma(\Delta[C/Fe]) = 0.22$ dex (see Figure 5-7). We regard this agreement as excellent, since different normalization routines tend to produce different [C/Fe] measurements, given the difficulty of normalizing the G-band due to ubiquitous absorption features. Furthermore, the average offset is dwarfed by the typical measurement uncertainty of ~ 0.35 dex. Raising the continuum placement by 2% increases [C/Fe] by ~ 0.1 dex in this sample.

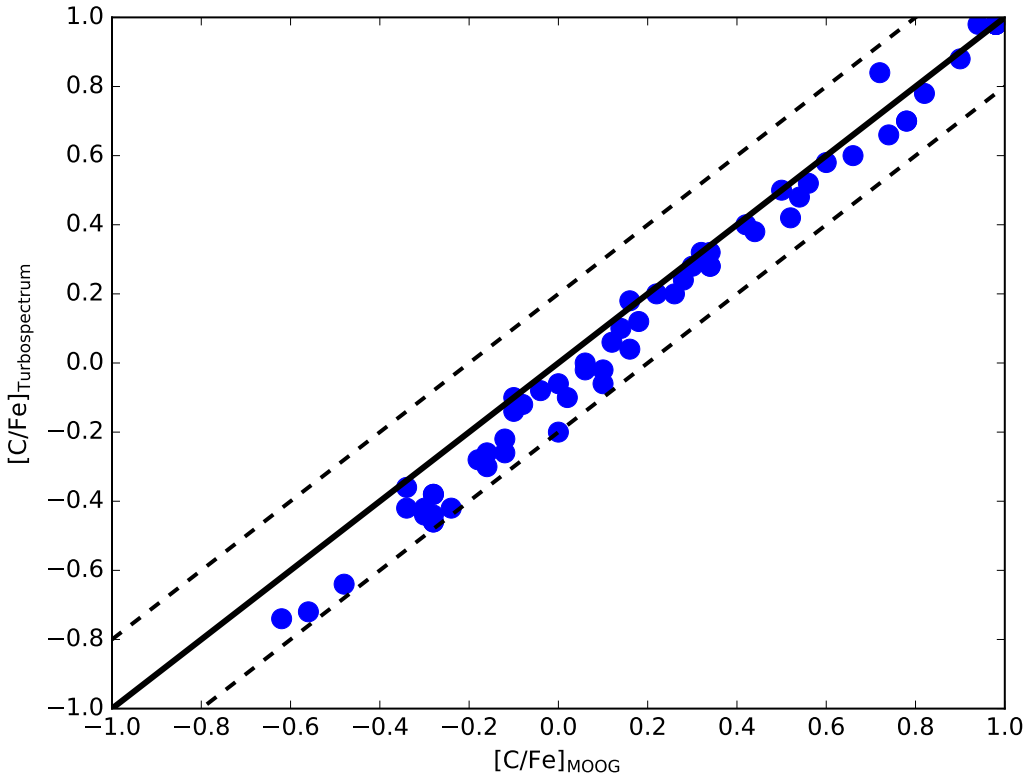

Figure 5-8 [C/Fe] measured with Turbospectrum, the MARCS model atmospheres, and the Masseron et al. [53] line list vs. [C/Fe] measured with MOOG and the same inputs. Dashed lines indicate ±0.2 dex offsets to guide the eye.

5.4.3 External Validation: Comparison to Kirby et al. [4] and Simon et al. [5]

Three stars in our sample have high-resolution [C/Fe] measurements in Simon et al. [5] with which we find agreement, as shown in Table 5.4. Eight stars in our sample have medium-resolution [C/Fe] measurements in Kirby et al. [4]. We find good agreement with their measurements, except for one star for which we measure a higher [C/Fe] by 0.6 dex. If we adopt the stellar parameters provided by Kirby et al. [4], then the discrepancy reduces to 0.33 dex. This resulting discrepancy appears to be reasonable given the reported uncertainty in our [C/Fe] measurements of ~ 0.35 dex and the low S/N of the M2FS spectrum of the star.

5.4.4 External Validation: Comparison to Jablonka et al. [6]

Two stars in our sample have high-resolution [C/Fe] measurements in Jablonka et al. [6]. We do not find agreement in [C/Fe] measurements, as our measurements are at least ~ 0.8 dex higher (see Table 5.4). We note that Jablonka et al. [6] adopted $\log \epsilon(\mathrm{C})_{\odot} = 8.55$ [338, 339], which is discrepant with the $\log \epsilon(\mathrm{C})_{\odot} = 8.43$ assumed in MOOG [207]. This can account for 0.12 dex of the total [C/Fe] offset between the measurements.

To explore whether the rest of this discrepancy could reasonably be explained by differences in the spectrum synthesis codes, model atmospheres, or line lists, we first attempted to reproduce the synthesis shown in Jablonka et al. [6] for star ET0381. We were able to reproduce their synthesis using Turbospectrum, the MARCS model atmosphere, and the Masseron line list, but noticed a consistent offset of $\sim$0.5 dex if we attempted to reproduce the synthesis with our adopted line list and MOOG. This total observed discrepancy between our two approaches reasonably accounts for most of the observed offset between [C/Fe] measurements, and about half of this observed ~ 0.5 dex discrepancy can be ascribed to differences in the line lists and adopted solar abundances.

To ensure that our CEMP detections were not susceptible to differences in synthesis codes, line lists, and model atmospheres, we replicated our analysis for our CEMP stars using the two test grids discussed in Section 5.4.1. We measured [C/Fe] for the subset of stars falling within the grid. As shown in Figure 5-8, the discrepancies in [C/Fe] between the two synthesis codes are largely within 0.2 dex, but grow larger for carbon-poor stars. Different model atmospheres and input line lists cause up to another $\sim$ 0.1 to 0.2 dex difference. Referring to Figure 5-8, we note that a star such as ET0381 with a measurement of [C/Fe]~ -0.20 in MOOG tends to have an abundance lower by ~ 0.15 dex in Turbospectrum. If we apply additional offsets accounting for differences in line lists and adopted solar abundances, we recover the aforementioned offset of ~ 0.50 dex. However, the classification of carbon-enhanced stars appears to be largely robust to different synthesis codes, model atmospheres,

and input line lists.

5.4.5 Confirmation of [C/Fe] with MagE spectra and further classification

Motivated by the high number of CEMP stars in the M2FS sample, we conducted follow-up observations of ten Sculptor stars with the MagE spectrograph as outlined in Section 5.2.3. This sample included five strong CEMP candidates, and five stars that were not as carbon-enhanced but had similar stellar parameters to the five CEMP candidates. We also observed one halo CEMP-r/s star, CS29497-034, as a comparison.

The purpose of these observations was to apply an independent check on our overall classification scheme, and to potentially derive the barium abundance of the stars to further classify them. Large Ba abundances in carbon-rich metal-poor stars are a strong indicator of the stars belonging to the CEMP-s and CEMP-r/s classes that are generally explained as being caused by accretion from a binary companion [304]. The more metal-rich analogs are the CH-strong and Ba-strong stars [340]. Any of these stars have to be excluded when computing a CEMP fraction, as their carbon enhancement does not reflect the abundance pattern in their birth environment. We indeed verified the carbon-rich nature of the five stars in our sample, but found four of them to be more metal-rich stars of potentially either the CH-strong or Ba-strong class (see Section 5.5.1). The other star was observed with the $1''$ slit, which does not provide sufficient resolution to measure barium features. M2FS spectra of a few strong carbon-enhanced stars are shown in Figure 5-9.

5.4.6 Identifying accreting binary carbon-rich stars in our M2FS sample

It is necessary to exclude carbon-rich stars whose source of enhancement is extrinsic (e.g. accretion from a binary companion) from our calculation of the CEMP fraction. Generally, members of this class of carbon-rich binary stars can be identified by radial velocity monitoring or by detecting a combined enhancement in s-process elements (e.g. Ba) together with carbon that would have been produced in a companion

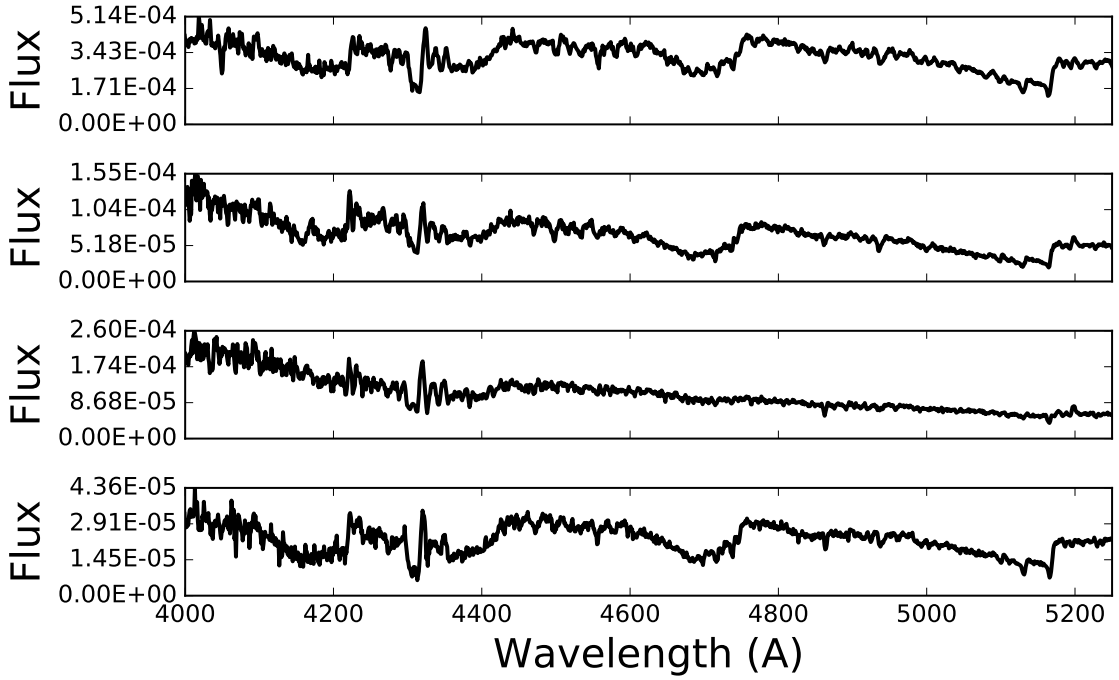

Figure 5-9 M2FS spectra of 4 stars (from top: 10_7_486, 10_8_3963, 11_1_4121, and 11_1_6440) that have saturated G-bands (~ 4315 Å). We measure their carbon abundance using the C2 band head at 5165 Å in their corresponding MagE spectra.

asymptotic giant branch star. But recent work by Yoon et al. [161] suggests that stars with sufficiently high absolute carbon abundance (A(C)) can already be identified as CEMP-s stars just based on the [Fe/H] and A(C) measurements, as shown in Figure 5-10.

We can readily apply the Yoon et al. criterion to both our M2FS and MagE samples. However, for the four most carbon-enhanced stars in our MagE sample there is a discrepancy in our carbon abundance measurements. The A(C) values derived from the MagE data suggests these stars to be clearly s-process rich stars, while the M2FS A(C) measurements place them on the boundary according to the Yoon et al. criterion.

The higher resolution of the MagE spectra better resolves the G-band and the C_2 band head and suggests that these four stars are more carbon-enhanced than inferred from the lower resolution M2FS spectra. In addition, renewed inspection of the Ca II

K line reveals the same trend; these four stars are actually more metal-rich than the KP index measurement from the M2FS data had indicated. Overall, these revisions strongly suggest that the four stars could be either CEMP-s stars (if they indeed have [Fe/H] $\lesssim -1.5$), or belong to the class of even more metal-rich CH-strong or Ba-strong stars.

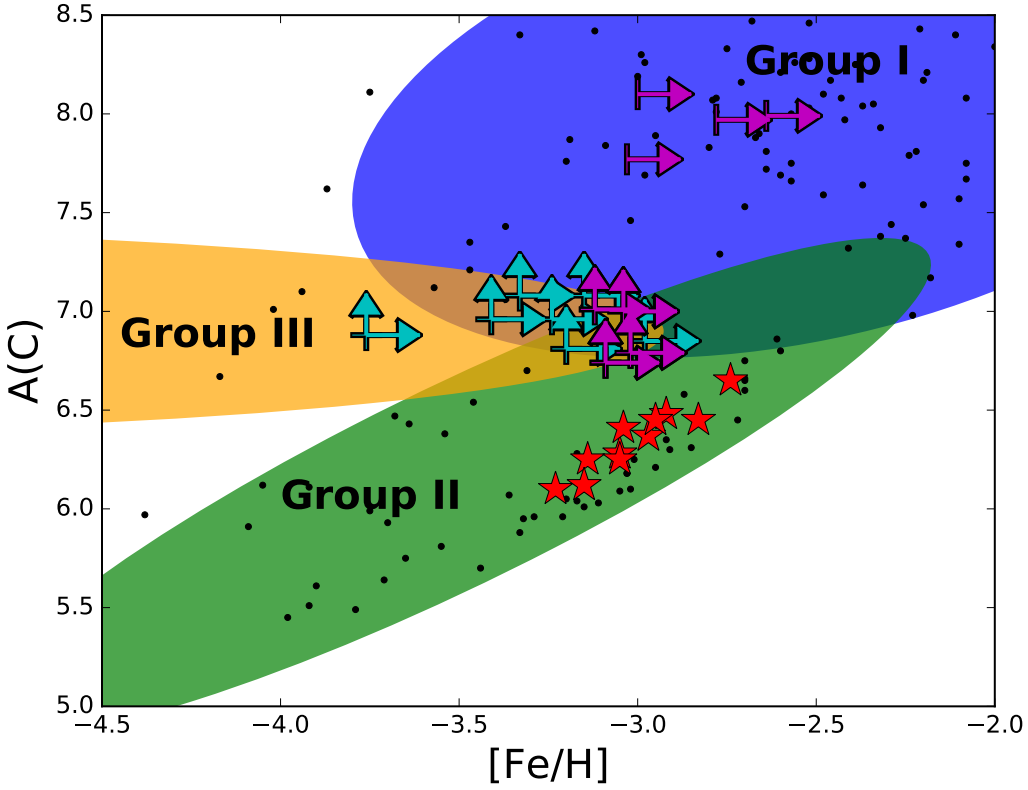

Figure 5-10 Yoon et al. plot with the original sample of halo stars in black and our Sculptor CEMP candidates overlaid in red, cyan, and magenta points. Groups I, II, and III are represented by blue, green, and orange ellipses, respectively. Cyan points correspond to M2FS measurements of stars with saturated G-bands and lower limits on their carbon abundances and metallicities, magenta points correspond to M2FS measurements of stars with saturated G-bands but accompanying MagE carbon abundance measurements, and magenta points in Group I are MagE measurements of those stars with saturated G-bands. The majority of Group I stars are CEMP-s stars, and the majority of Group II and III stars are CEMP-no stars

Regarding the carbon abundance discrepancy, we note that when high carbon abundances lead to strong spectral absorption features (especially in cool stars), there

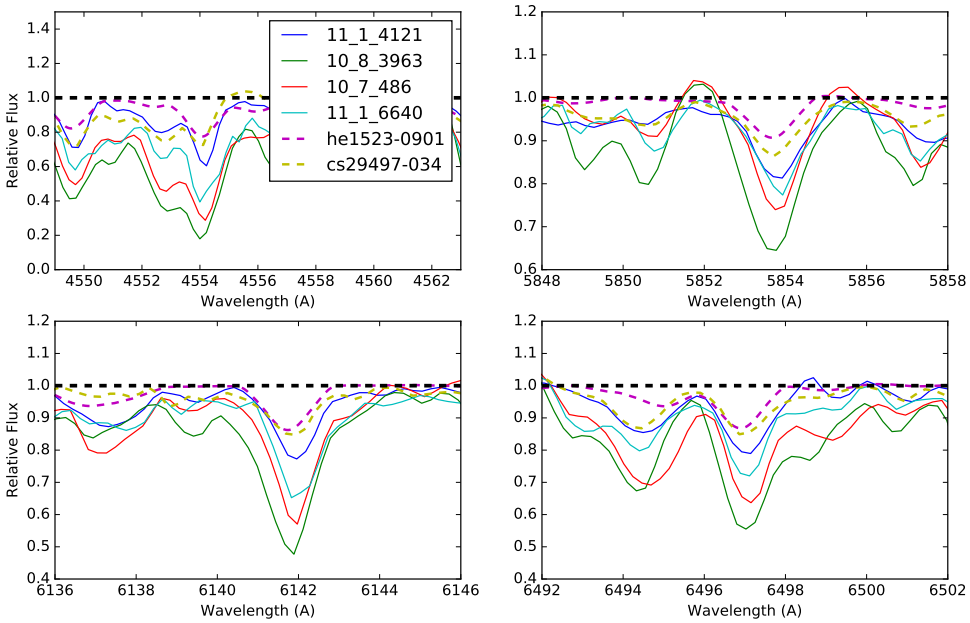

Figure 5-11 Plots of barium lines at 4554 Å, 5853 Å, 6141 Å, and 6496 Å in MagE $R \sim 6000$ spectra for 4 Sculptor CEMP stars (solid lines). The MagE ($R \sim 6000$) spectrum of CS29497-034 ([Ba/Fe] = 2.23 from Aoki et al. 54), a halo CEMP-r/s star, and a high-resolution MIKE spectrum of HE1523-0901 ([Ba/Fe] $\sim$ 1.1 from Frebel et al. 55), an r-process enhanced star, smoothed to $R \sim 6000$ are over plotted for comparison.

is no region in the vicinity of the G-band (4250 Å to 4350 Å) to place the true continuum value in M2FS spectra. Thus, even accounting for this effect can still easily lead to systematically underestimating the continuum, and thus the carbon abundance. These four stars all had $[\mathrm{C/Fe}]_{\mathrm{M2FS}} \gtrsim 1$. We thus speculate that the G-band in M2FS spectra begins to saturate around $[\mathrm{C/Fe}]_{\mathrm{M2FS}} \sim 1$.

We note that the G-band in the higher-resolution MagE spectra also begins to saturate for those four stars. This is illustrated by our inability to use the G-band to recover the literature [C/Fe] measurement of CS29497-034, a star with similar G-band depth in the MagE spectra as our Sculptor members with high [C/Fe]. Motivated by the near-saturation of the G-band for these stars, we instead determined the carbon abundances of CS29497-034 using the C_2 band head at 5165 Å. We used a line list

compiled from Sneden et al. [206, 253] and Masseron et al. [53] and the MOOG synthesis code. We measure [C/Fe] = 2.6±0.1 for CS29497-034, consistent with the literature value of [C/Fe] = 2.72 [341]. We thus use the C_2 band head to measure carbon abundances for the stars observed with MagE that have a near saturated G-band.

We find 11 stars with $[C/Fe]_{M2FS} > 1.0$ and showing the presence of a C_2 band head and a very strong G-band, which we suspect to have underestimated carbon abundances. If the A(C) value of these stars were revised upwards by ∼1 dex (following the results for CS29497-034 and the four stars also observed with MagE), they would clearly be members of the class of s-process rich stars, based on the Yoon et al. plot (see Figure 5-10). We thus consider these stars as s-process rich candidates, and list our derived carbon abundances strictly as lower limits in Table 5.6 and Figure 5-12. Table 5.5 has a final list of the iron and carbon abundances computed for the subset of all 31 MagE spectra with $B - V < 1.2$. Given the ambiguity in the metallicities of the carbon-rich stars observed with MagE, we cautiously only list A(C) measurements for those stars.

5.5 Chemical signatures of the metal-poor stellar population of Sculptor

5.5.1 [Ba/Fe] estimates from MagE spectra & exclusion from CEMP-no classification

In our follow-up MagE observations (Section 5.2.3) of ten stars, we observed four of the five very carbon-enhanced candidates with the 0.″7 slit to obtain sufficient resolution ($R \sim 6000$) to also resolve barium lines at 4554 Å, 4934 Å, 5853 Å, and 6141 Å. We used a line list from Sneden et al. [206, 253] and the MOOG synthesis code to synthesize these lines and constrain [Ba/Fe].

At $R \sim 6000$, these four lines can be blended, e.g., with praseodymium at 5853 Å, when neutron-capture element abundances are high as in s-process-rich stars. We are

able to reproduce the literature [Ba/Fe] = 2.2 measurement of CS29497-034 when considering the depth of the centroid of the line and neglecting fitting the entire line profile. This suggests that the blending features do not significantly affect the centroid of the barium lines. In Figure 5-11, the barium lines of the stars are over-plotted with the resolution-degraded MIKE spectrum of the halo r-process star HE 1523−0901 [55], which has similar stellar parameters to the four Sculptor stars. The barium features of the Sculptor stars are stronger than those in the reference stars CS29497-034 ([Ba/Fe] = 2.2) and HE 1523−0901 ([Ba/Fe] = 1.1), suggesting that they are s-process enhanced stars with [Ba/Fe] > 1.0. The centroid measurements for these stars yield high [Ba/H] values of 0.36, 0.8, −0.53, and −0.18. Taking our KP-based Fe measurements at face value, these abundances translate to [Ba/Fe] = 3.00, 3.80, 2.50, and 2.60. However, these stars show strong CH features in the vicinity of the Ca II K line in their spectra. This prevents an accurate [Fe/H] measurement (see Section 5.5.2). Even if the [Fe/H] values of these stars were underestimated by up to 1.5 dex, these stars would still be considered s-process rich stars due to their high barium abundance. In addition, just based on the A(C) criteria described in Yoon et al. [161], and as shown in Figure 5-10, these stars could independently be classified as s-process rich stars.

5.5.2 Sample bias assessment

Our M2FS sample is composed of the most metal-poor members of Sculptor as selected from measurements of the Ca II K line in lower-resolution IMACS spectra. Our initial metallicity cut based on the IMACS data attempted to include all stars with [Fe/H] < −2.9. The majority of stars are cool red giants. There is a potential for CEMP stars to be preferentially included or excluded from the M2FS sample if their metallicity measurements are systematically biased because of strong C absorption. At face value, we expect CH absorption features to depress the continuum blueward of the Ca II K line in the lower-resolution IMACS spectra, causing a lower measurement of the equivalent width of the Ca II K line and thus a faulty selection. This would mean that carbon-rich stars may be preferentially selected into our M2FS sample

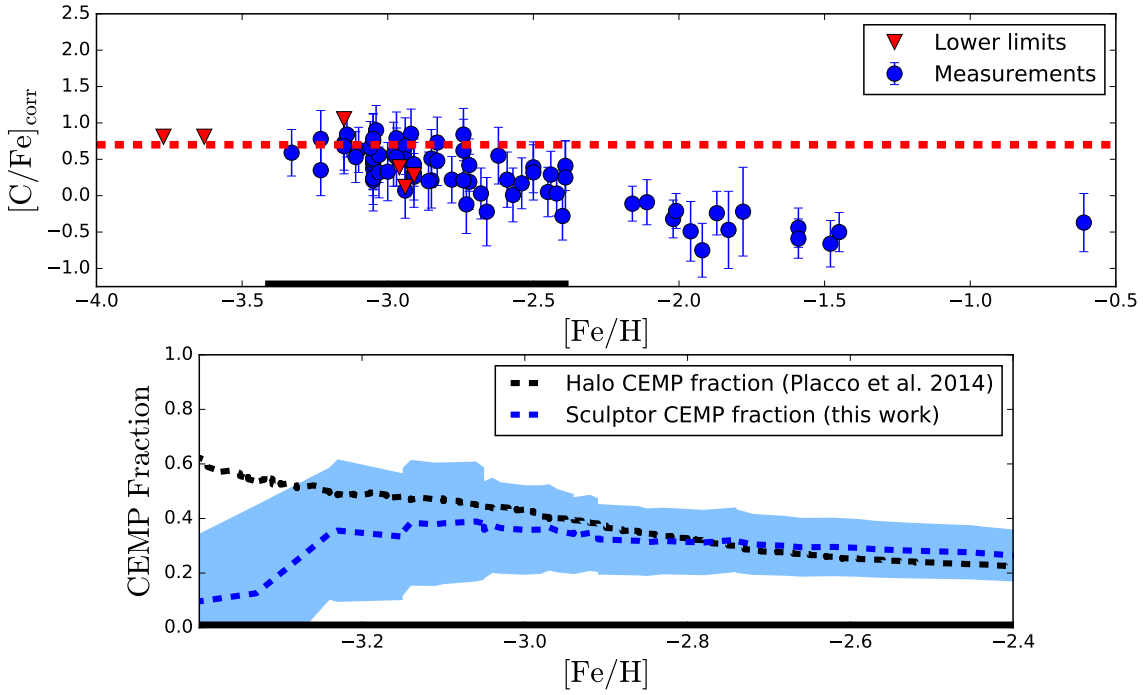

Figure 5-12 Top: [C/Fe] as a function of [Fe/H] for RGB stars in our M2FS Sculptor sample. CH strong, Ba strong, and CEMP-s candidates are not displayed in the upper panel of the plot. The displayed [C/Fe] measurements have been corrected for the evolutionary state of each star following Placco et al. [8]. The dashed red line marks the cutoff for a star to be considered a CEMP star ([C/Fe] > 0.7). Red downward-facing triangles are upper limits on [C/Fe] from non-detections of the G-band. Bottom: Measured cumulative CEMP fraction as a function of [Fe/H] for our Sculptor sample (blue) and the Milky Way halo from Placco et al. [8] (black). The shaded blue region corresponds to the 95% confidence interval of our measured CEMP fraction.

because they may appear to be extremely metal poor stars.

Stars whose carbon-enhancement is driven by accretion across a binary system, such as CEMP-s, Ba-strong, and CH-strong stars, have the highest A(C) values and would thus be the most likely to be preferentially selected into our sample. Indeed, we find 4 more metal-rich CEMP-s, Ba-strong, or CH-strong stars in our M2FS sample based on follow-up observations with MagE (see Section 5.4.6). All of these stars were initially found to have [Fe/H]~ -3.0 based on measurements of the strength of the Ca II K line. But these stars must actually be much more metal-rich as a simple comparison of the magnesium triplet region ($\sim 5175\,$Å) of these stars to that of the

halo CEMP-r/s star CS29497-034 ([Fe/H] = −2.9) shows (see Figure 5-13). Given this comparison, we also chose to investigate the magnesium triplet region of stars without extreme A(C) values to determine whether their metallicity measurements were biased.

For each star in Table 5.5, we derived a Mg abundance from the 5172.7 Å and 5183.6 Å lines if the S/N was sufficiently high. Then, we compared the derived [Mg/Fe] ratio of these stars to the expected [Mg/Fe] ratio for dwarf galaxy stars in their metallicity regime. We would expect to see systematically higher [Mg/Fe] values if the Ca II K based metallicities were biased lower, such as in the case of stars with high A(C) values.

We consider two examples: stars 10_7_442 and 10_8_1226 have carbon abundances close to the CEMP threshold and Mg line equivalent widths in the linear regime of the curve of growth (reduced equivalent widths $\lesssim -4.45$). For these two stars, we measure [Mg/Fe] values of 0.23 and 0.17, respectively. These [Mg/Fe] ratios are roughly at the lower end of the regime of what is expected for dwarf galaxy stars at these metallicities. This suggests that we are not strongly underestimating our [Fe/H] measurements for stars that are near the CEMP threshold.

If we include stars from Table 5.5 with Mg line equivalent width measurements in the non-linear regime of the curve of growth at face value and adopt the M2FS metallicities and carbon abundances when available, the average [Mg/Fe] of stars with [C/Fe] > 0.50 is 0.43. This [Mg/Fe] ratio is also in the regime of expected values. As mentioned, if the metallicities were substantially underestimated, we would expect to get much larger [Mg/Fe] values. For comparison, all the CEMP-s candidates have [Mg/Fe] $\gtrsim 1.0$ if we take the KP-based [Fe/H] measurements at face value. While these Mg abundance estimates may have large uncertainties (up to ~ 0.4 dex, as is expected for data of this quality), they suggest we are not strongly biased in our metallicity estimates for stars without copious carbon-enhancement.

We also compared our observed MagE spectra to MIKE spectra of CS22892-52 ([Fe/H] = −3.16; $T_{\rm eff} = 4690$ K) and HD122563 ([Fe/H] = −2.93; $T_{\rm eff} = 4500$ K) that had been degraded to match the resolution of the MagE data. Measurements of these

standard stars are from Roederer et al. [17]. We find that the strengths of the Mg b lines observed with MagE appear to be roughly consistent with what is expected from our Ca II K derived metallicities.

Thus, only stars with very strong carbon enhancement are incorrectl selected into our M2FS sample. These stars are overwhelmingly likely to have their carbon abundance elevated by accretion from a binary companion (see Figure 5-10), and should already be excluded in a calculation of the CEMP fraction. This confirms that our selection is not biased in favor of CEMP-no stars.

Below a fiducial metallicity of [Fe/H] ~ -3.0 and after excluding CEMP-s, Ba-strong, and CH-strong stars, we can reasonably assume that there is not a strong bias toward high carbon enhancement in our EMP sample in Sculptor.

5.5.3 Measurement of the CEMP fraction in Sculptor

In a measurement of the CEMP fraction, we must exclude stars whose carbon enhancement is extrinsic (e.g. driven by accretion from a binary companion). We identify such stars in our M2FS sample by applying the Yoon et al. criterion (see Figure 5-10), as discussed in Section 5.4.6 and Section 5.5.1. We then excluded 90% of those stars, which is the probability of correct classification according to Yoon et al., from our calculation of the CEMP fraction.

We note that there is a group of stars that sits blueward of the Sculptor RGB by up to $\sim$0.25 mag (see Figure 5-1). Despite detailed investigation, the evolutionary status and hence the nature of these stars remains somewhat ambiguous. While they are generally bluer than would be expected for Sculptor RGB stars, they do tend to have velocities similar to Sculptor. Due to this uncertainty, we thus cautiously exclude these stars from our calculation of the CEMP fraction and we list them separately in Table 5.6. Since they comprise only a small portion of the sample, the CEMP fraction is largely unchanged by their exclusion.

We determined the CEMP fraction by accounting for the probability that any individual star in our sample is carbon enhanced ([C/Fe] > 0.7). We assigned a probability that each star is carbon enhanced based on its [C/Fe] measurement and

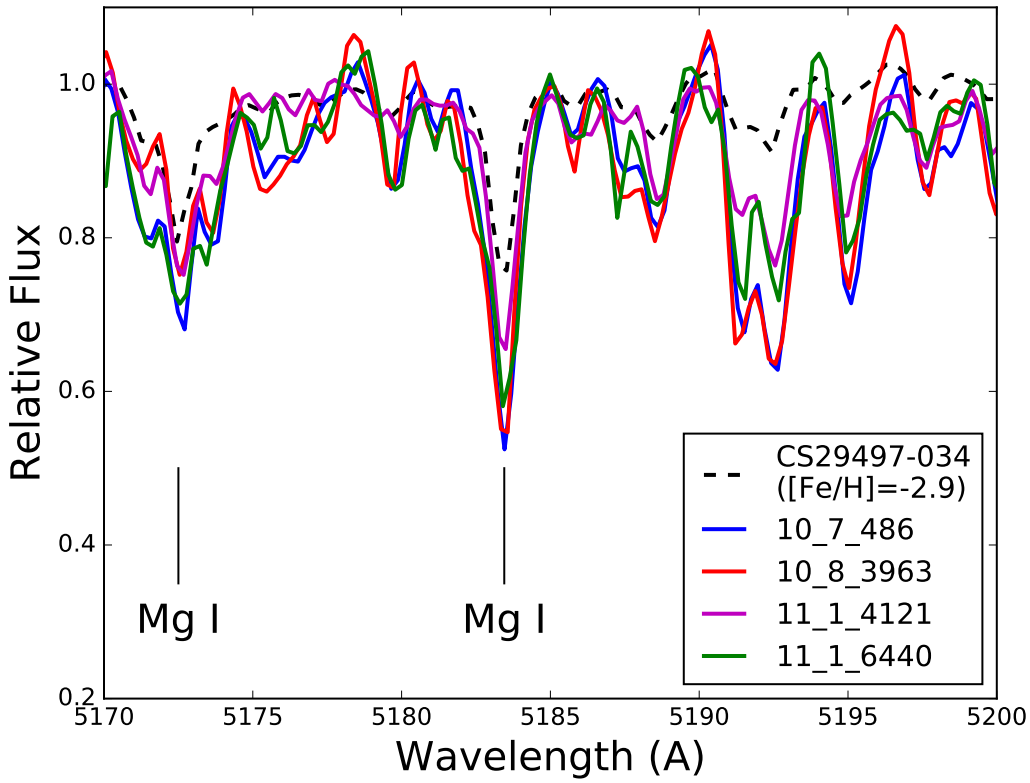

Figure 5-13 Plot of the Mg region of the MagE spectra of CS29497-034 ([Fe/H] = −2.9) and four other more metal-rich Sculptor members. These stars were classified as [Fe/H]∼ −3.0 from measurements of the Ca II K line. It appears that the strong carbon-enhancement of these Sculptor members biased the Ca II K metallicities in lower-resolution spectra (see Section 5.5.2).

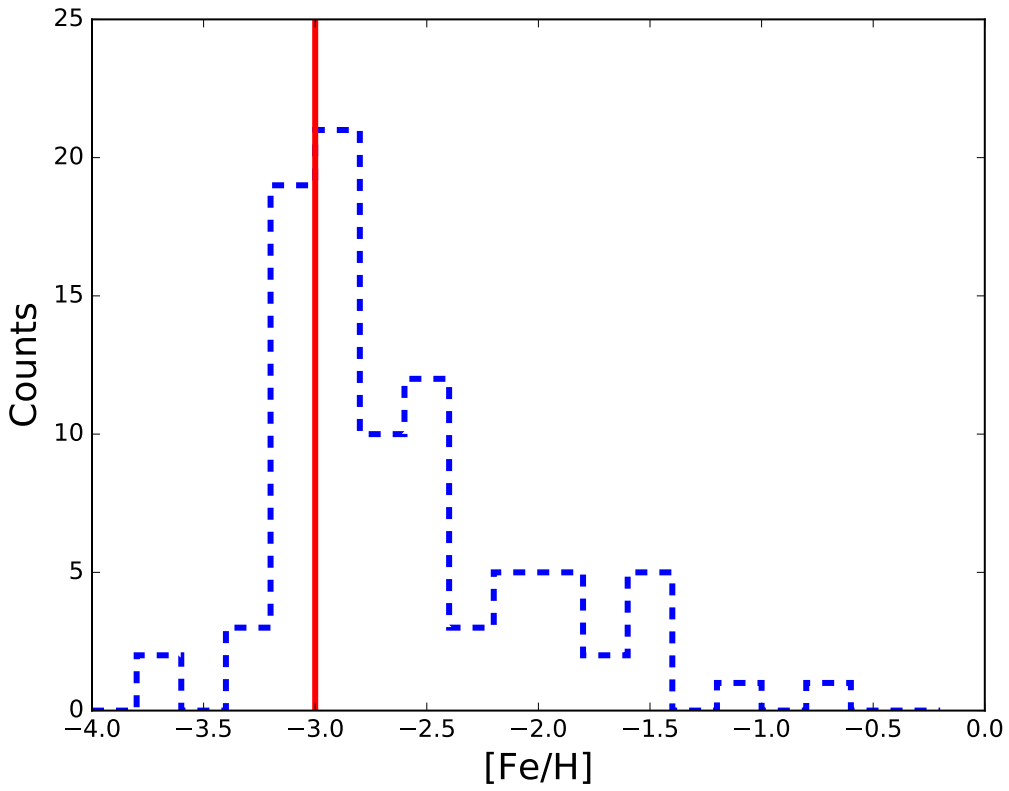

Figure 5-14 Histogram of the metallicities measured for 89 stars. Star with lower limits on metallicities are not included. The vertical red line indicates the cutoff for extremely metal-poor stars ([Fe/H]< -3.0). After excluding lower limits on [Fe/H], we detect 24 extremely metal-poor star candidates.

assuming that the uncertainty on [C/Fe] is normally distributed. Finally, we computed a cumulative CEMP fraction for each metallicity range by finding the expected number of CEMP stars in that subset based on the probabilities of each member being carbon enhanced. We then divided the expected number of CEMP stars by the total number of stars in the subset. This approach enables us to accurately constrain the overall population of such stars even though we are not able to identify individual CEMP stars with high (p>0.95) confidence.

To derive an uncertainty on this CEMP fraction, we modeled the CEMP classification as a random walk where p_i is the probability of a given star being a CEMP star. This formulation yields an uncertainty on the CEMP fraction of $\Sigma_i \sqrt{p_i \times (1-p_i)/N}$. This uncertainty matches the uncertainty derived from Monte Carlo simulations of the

CEMP fraction. We can then measure the observed cumulative CEMP fraction, and an uncertainty on the fraction, as a function of [Fe/H]. While abundance uncertainties in [C/Fe] for our sample are almost certainly non-Gaussian as the distributions of $T_{\rm eff}$ and $\log g$ residuals with respect to Kirby et al. [179] are asymmetric, this method allows us to place a rough uncertainty on the observed CEMP fraction. The results of this analysis are shown in Figure 5-12.

We measure a CEMP fraction of 0.36 ± 0.08 for stars below [Fe/H] $= -3.0$ in Sculptor. If we instead take the simpler approach of dividing the number of CEMP stars by the total number of stars after excluding 10 of the 11 probable CEMP-s stars, we derive a CEMP fraction of 0.24 (6/25) for stars below [Fe/H] $= -3.0$. The latter fraction is likely lower because our carbon abundances have large uncertainties ($\sim$ 0.35 dex) and a number of stars lie right below the cutoff of the CEMP classification. Exactly this fact has been taken into account by the method described in the previous paragraph, so we adopt the former measurement.

5.6 Discussion and Conclusion

The overall aim of this study has been to establish the early chemical evolution of Sculptor by studying a sample of metal-poor stars in this galaxy. In particular, we obtained metallicity ([Fe/H]) and carbon abundance ([C/Fe]) measurements for 100 metal-poor stars in Sculptor using medium-resolution M2FS spectroscopy. We identify 21 carbon-enhanced metal-poor star candidates (CEMP; [C/Fe] > 0.7, [Fe/H] < -1.0), and 24 extremely metal-poor candidates (EMP; [Fe/H] < -3.0). The MDF of our sample is shown in Figure 5-14. Note that this sample is selected to have [Fe/H] ~ -3 and is not representative of the galaxy as a whole.

We also observed 31 stars with the MagE spectrograph of which 26 had $B - V < 1.2$. For ten, their carbon-enhanced nature was confirmed, enabling further insight into the origin of their carbon enhancement.

From these observations, we determine that many of our carbon-rich stars may be CEMP-s, CH-strong, or Ba-strong stars (see Sections 5.4.6 and 5.5.1) but such

Table 5.5. Stellar parameters and abundances of Sculptor stars from MagE spectra

Names	Slit (arcsec)	Log (g) (dex)	Teff (K)	$[Fe/H]_{KP}$ (dex)	A(C) (dex)	[C/Fe] (dex)	$[C/Fe]_{corr}$ (dex)	$[C/Fe]_{final}$ (dex)	[Ba/H] (dex)
CS29497−034[†]	0.7	1.50	4900	-2.90 ± 0.27	8.25 ± 0.29	2.60 ± 0.10	0.09	2.69 ± 0.10	−0.70:[‡]
10_8_3963	0.7	1.08	4513	> -3.00	8.10 ± 0.15	...	...	...	0.80:[‡]
10_7_486	0.7	1.05	4523	> -2.64	7.96 ± 0.15	...	...	...	0.36:[‡]
11_1_6440	0.7	1.29	4605	> -2.78	7.82 ± 0.15	...	...	...	−0.18:[‡]
11_1_4121	0.7	1.24	4579	> -3.03	7.52 ± 0.10	...	...	...	−0.53:[‡]
11_1_4422	1.0	1.75	4810	-2.85 ± 0.23	6.80 ± 0.34	1.10 ± 0.25	0.16	1.26 ± 0.25	...
6_5_1598	1.0	1.08	4516	-2.83 ± 0.16	6.02 ± 0.26	0.30 ± 0.20	0.65	0.95 ± 0.20	...
11_2_661	1.0	1.16	4550	-2.93 ± 0.17	5.67 ± 0.23	0.05 ± 0.15	0.67	0.72 ± 0.15	...
10_8_1566	1.0	1.53	4659	-2.11 ± 0.34	5.84 ± 0.40	-0.60 ± 0.20	0.47	-0.13 ± 0.20	...
7_4_2408	1.0	1.06	4524	-2.64 ± 0.16	5.51 ± 0.26	-0.40 ± 0.20	0.72	0.32 ± 0.20	...
11_1_4673	1.0	1.21	4570	-2.94 ± 0.18	5.31 ± 0.27	-0.30 ± 0.20	0.65	0.35 ± 0.20	...
10_8_3804	1.0	1.62	4752	> -2.78	8.24 ± 0.22	...	...	...	...
11_1_3334[†]	1.0	1.62	4721	...	7.88 ± 0.15	...	...	...	...
6_5_505[†]	1.0	1.57	4706	...	7.52 ± 0.15	...	...	...	...
11_2_556	1.0	2.04	4939	> -3.27	7.48 ± 0.20	...	...	...	...
7_4_3280	0.7	3.59	5518	-2.41 ± 0.25	< 6.84	< 0.70	0.00	< 0.70	...
10_8_2714	1.0	3.02	5328	-2.96 ± 0.38	< 6.59	< 1.00	0.01	< 1.01	...
10_8_3810	1.0	2.69	5199	-3.10 ± 0.33	< 6.15	< 0.70	0.01	< 0.71	...
6_5_1035	0.7	1.27	4589	-2.86 ± 0.20	5.69 ± 0.28	0.00 ± 0.20	0.61	0.61 ± 0.20	...
10_8_1226	1.0	1.47	4685	-3.05 ± 0.21	5.68 ± 0.33	0.18 ± 0.25	0.44	0.62 ± 0.25	...
10_7_442	1.0	1.61	4752	-3.33 ± 0.22	5.67 ± 0.30	0.45 ± 0.20	0.29	0.74 ± 0.20	...
7_4_1992	1.0	1.66	4769	-3.14 ± 0.22	5.60 ± 0.33	0.19 ± 0.25	0.23	0.42 ± 0.25	...
11_1_4296	1.0	1.52	4720	-3.99 ± 0.22	< 5.56	< 1.00	0.36	< 1.36	...
11_1_6015	1.0	1.87	4824	-2.42 ± 0.30	5.53 ± 0.36	-0.60 ± 0.20	0.12	-0.48 ± 0.20	...
10_7_790	0.7	1.23	4574	-3.03 ± 0.17	5.47 ± 0.34	-0.05 ± 0.30	0.63	0.58 ± 0.30	...
6_6_402	1.0	1.68	4802	-3.91 ± 0.25	< 5.44	< 0.80	0.17	< 0.97	...
10_7_923	1.0	1.39	4666	-3.87 ± 0.20	< 4.88	< 0.20	0.49	< 0.69	...

Note. — Stellar parameters and [Fe/H] for CS29497−034 are from Aoki et al. [54]. Stars in the top portion were observed as a follow-up to M2FS observations to confirm [C/Fe] measurements, and stars in the bottom portion were observed immediately after the initial IMACS observations as EMP candidates.

[†]The S/N over the Ca II K feature was too low to estimate a [Fe/H] from the KP index. The M2FS [Fe/H] was assumed when calculating [C/Fe] (See Table 5.6)

[‡]The colon (:) indicates large and uncertain error bars

stars should be excluded in an estimate of the CEMP fraction. Excluding 90% of these stars, which is an approximation of their recovery rate, suggests a true CEMP fraction of 36% (see Section 5.5.3) for EMP stars in Sculptor (see Figure 5-12).

Prior to this study, only four CEMP stars had been identified in Sculptor [307, 308, 309]. Of those, only one was a CEMP-no star, resulting in an apparent disagreement between the CEMP fraction of Sculptor and the CEMP fraction of the Milky Way halo ($\sim$ 42%). This discrepancy, if true, would have hinted at a divergence of the earliest phases of chemical evolution, as reflected in the most metal-poor stars in the halo and in Sculptor. However, our CEMP fraction of $\sim$ 36% for EMP stars in Sculptor is in agreement with the CEMP fraction of $\sim$ 42% for EMP stars in the Milky Way halo, posing no such challenges.

In fact, our results show that Sculptor may have a similar cumulative CEMP fraction as the halo for stars with [Fe/H] < -3.0 (see Figure 5-12), using the compilation of metal-poor halo stars from Placco et al. [8] for comparison. At face value, Figure 5-12 suggests that Sculptor and the halo have the same CEMP fraction at all metallicities below [Fe/H] $= -2.5$. However, the large number of stars in our sample with [Fe/H] ~ -2.8 biases the measurement of the cumulative CEMP fraction towards the value at metallicities lower than that number. Contrary to previous work, this suggests that a high CEMP star fraction may be a defining characteristic of the low metallicity Sculptor population after all, and also suggests that in Sculptor, early chemical evolution was driven by high [C/Fe] producing objects such as fallback supernovae with large [C/Fe] yields and/or massive rotating stars with large CNO yields [342, 343, 344, 345, 346, 102, 347, 348].

This result indicates that the earliest stars in Sculptor and, perhaps, more generally in all classical dSphs, may have undergone similar processes of early chemical enrichment as the birthplaces of halo stars did. This has already been suggested for the ultra-faint dwarf galaxies [21]. Furthermore, because of the similar CEMP fractions, the origin of CEMP stars in the halo may also lie within early analogs of the surviving dwarf galaxies.

However, we do find that none of our CEMP stars have [C/Fe] > 1.0, whereas

32% of stars in the halo with [Fe/H] < -3.0 have [C/Fe] > 1.0 [8]. This discrepancy implies that the distribution and magnitude of carbon-enhancement of CEMP stars in the halo may be different from that in Sculptor. Thus, while our result does indicate some level of similarity in early chemical enrichment among Sculptor and the Milky Way halo in terms of the CEMP fraction, there may be a level of inhomogeneity in producing the most carbon-enhanced stars. More observations of Sculptor will further confirm or refute our findings and shed more light on the enrichment history of this galaxy.

Finally, it is interesting to note that the vast majority of CEMP stars in the Milky Way halo with [Fe/H] < -3.0 are CEMP-no stars, which are stars that display no enhancement in neutron-capture elements. If our population of CEMP-s candidates have [Fe/H] < -2.90, this sample might suggest a discrepancy between the halo and Sculptor in the occurrence rate of CEMP-s stars at low metallicities. However, all of the CEMP-s candidates have only lower limits on their metallicities since strong carbon features blue-ward of the Ca II K line preclude an accurate metallicity measurement. Additional observations with higher resolution spectrographs are needed to verify whether any of our CEMP-s candidates may be EMP stars, although it is unlikely.

Given that most of our CEMP-no candidates have [Fe/H] < -2.8, the previous scarcity of CEMP stars in Sculptor can likely be explained by the overall rarity of EMP stars in Sculptor and the correspondingly small stellar samples at the lowest metallicities with available [Fe/H] and [C/Fe] measurements. The previously known sample with simultaneous [Fe/H] and [C/Fe] abundances includes 198 medium-resolution measurements from Kirby et al. [4], 94 medium-resolution measurements from Lardo et al. [308], and 28 stars with high-resolution measurements [292, 294, 20, 290, 349, 306, 307, 6, 5]. Thirteen of these stars have [Fe/H] < -2.8, one of which is potentially a CEMP-no star (Scl11_1_4296 in Simon et al. [5]). This difference (i.e., a low CEMP fraction), is likely the result of samples that did not target EMP stars systematically as was done in our IMACS survey or potentially unaccounted for sample biases. Regardless, our sample demonstrates the existence of

a substantial population of CEMP stars with [Fe/H]< -2.8 in Sculptor.

In summary, we identified EMP stars in an IMACS survey (Hansen et al. in prep) and based on M2FS follow-up observations, increased the number of known metal-poor stars in Sculptor with available [Fe/H] and [C/Fe] measurements. As a result, we provide the first meaningful sample of EMP stars from which to determine CEMP fractions to learn about early chemical enrichment and evolution. Given the similarity to the halo, perhaps all dwarf galaxies share certain properties of early chemical evolution. Follow-up spectroscopy of additional EMP candidates from our IMACS survey will likely lead to even more EMP and CEMP star discoveries in other dwarf galaxies in the future.

Table 5.6. M2FS measurements of all observed stars in the Sculptor dSph

Names	α (J2000)	δ (J2000)	Log (g) (dex)	Teff (K)	[Fe/H] (dex)	$[Fe/H]_{err}$ (dex)	[C/Fe] (dex)	$[C/Fe]_{err}$ (dex)	$[C/Fe]_{correction}$ (dex)	$[C/Fe]_{final}$ (dex)
					RGB members					
7_4_3266	00:58:38.77	−33:35:02.28	0.98	4461	−2.40	0.15	−1.07	0.33	0.79	−0.28
11_2_956	00:58:39.65	−33:55:34.76	1.02	4477	−2.16	0.18	−0.86	0.24	0.75	−0.11
7_4_3182	00:58:49.80	−33:37:19.10	1.61	4719	−3.05	0.26	0.07	0.37	0.3	0.37
11_1_6533	00:58:57.88	−33:41:50.34	1.43	4635	−2.98	0.22	0.09	0.44	0.48	0.57
11_1_6443	00:59:00.28	−33:43:14.64	1.03	4484	−2.45	0.17	−0.72	0.34	0.77	0.05
11_1_6267	00:59:04.05	−33:40:31.48	1.08	4503	−2.57	0.18	−0.74	0.37	0.75	0.01
11_1_6192	00:59:06.14	−33:44:11.39	1.37	4552	−2.02	0.22	−0.89	0.26	0.57	−0.32
7_4_2750	00:59:17.20	−33:38:06.68	1.36	4606	−3.05	0.2	−0.34	0.42	0.55	0.21
11_2_661	00:59:25.63	−33:58:21.42	1.18	4524	−3.10	0.16	−0.05	0.31	0.68	0.63
11_1_5047	00:59:26.68	−33:40:22.43	1.49	4662	−3.23	0.2	−0.01	0.35	0.36	0.35
7_4_2408	00:59:30.43	−33:36:05.23	1.07	4500	−2.68	0.16	−0.72	0.35	0.75	0.03
11_1_4824	00:59:30.49	−33:39:04.16	1.09	4508	−2.66	0.24	−0.97	0.47	0.75	−0.22
11_1_4673	00:59:33.63	−33:49:10.10	1.23	4546	−3.11	0.17	−0.11	0.35	0.64	0.53
11_1_4422	00:59:36.61	−33:40:38.51	1.76	4783	−3.04	0.25	0.74	0.34	0.16	0.90
11_1_4277	00:59:38.42	−33:40:11.57	1.81	4805	−2.94	0.25	< 0.00	...	0.12	< 0.12
11_1_4296	00:59:38.75	−33:46:14.58	1.55	4697	−3.33	0.22	0.25	0.32	0.34	0.59
11_1_4122	00:59:41.24	−33:48:03.56	1.2	4467	−2.01	0.2	−0.88	0.24	0.67	−0.21
11_1_3738	00:59:45.30	−33:43:53.83	1.79	4756	−1.92	0.35	−1.01	0.37	0.26	−0.75
11_1_3743	00:59:45.37	−33:45:34.19	1.66	4740	−2.97	0.23	0.53	0.36	0.26	0.79
11_1_3646	00:59:46.67	−33:47:19.71	1.72	4764	−3.05	0.24	0.55	0.38	0.2	0.75
11_1_3513	00:59:48.19	−33:46:50.01	1.59	4724	−2.62	0.27	0.18	0.39	0.37	0.55
11_2_425	00:59:50.64	−33:58:07.10	1.6	4715	−3.15	0.22	0.39	0.37	0.33	0.72
7_3_243	00:59:50.78	−33:31:47.06	1.25	4491	−1.48	0.27	−1.32	0.32	0.66	−0.66
11_1_3246	00:59:51.19	−33:44:51.82	1.36	4546	−1.83	0.58	−1.05	0.53	0.58	−0.47
10_8_4250	00:59:51.51	−33:44:02.67	1.29	4573	−2.73	0.22	−0.75	0.40	0.63	−0.12
7_4_1514	00:59:54.47	−33:37:53.50	1.23	4479	−1.45	0.26	−1.14	0.27	0.64	−0.50
10_8_4020	00:59:55.22	−33:42:11.34	1.4	4624	−3.05	0.21	−0.07	0.36	0.51	0.44
11_1_2583	00:59:57.59	−33:38:32.54	1.35	4539	−1.78	0.78	−0.78	0.61	0.56	−0.22
6_5_1598	00:59:59.09	−33:36:44.90	1.09	4492	−2.92	0.16	0.18	0.34	0.67	0.85
10_8_3751	00:59:59.33	−33:44:24.34	1.6	4711	−3.05	0.24	0.18	0.39	0.3	0.48
10_8_3709	00:59:59.95	−33:47:02.03	1.67	4742	−2.85	0.24	0.26	0.40	0.25	0.51
10_8_3698	01:00:00.04	−33:45:28.81	1.18	4546	−2.59	0.21	−0.47	0.38	0.69	0.22
10_7_923	01:00:01.12	−33:59:21.38	1.4	4641	−3.77	0.20	< 0.34	0.36	0.47	< 0.81
10_8_3625	01:00:01.44	−33:51:16.74	1.0	4469	−2.11	0.17	−0.84	0.31	0.75	−0.09
10_8_3520	01:00:03.27	−33:47:44.44	1.33	4591	−2.85	0.21	−0.38	0.38	0.59	0.21
10_8_3315	01:00:05.93	−33:45:56.39	0.99	4465	−2.54	0.18	−0.59	0.35	0.76	0.17
...	...	...	...	...	...	...	...	...	...	...

Note. — A partial version of this Table is shown to illustrate its content. A full version is available in the published version of this article, or can be provided by the author upon request.

† These stars are classified as likely CH-strong, Ba-strong, or CEMP-s stars due to the presence of saturated carbon features (see Sections 5.4.6 and 5.5.1).

Chapter 6

Four Metal-poor Stars in the Sagittarius Dwarf Spheroidal Galaxy

The content of this chapter was published in the Astrophysical Journal as [137] on April, 2019.

Abstract

We present the metallicities and carbon abundances of four newly discovered metal-poor stars with $-2.2 < [\mathrm{Fe/H}] < -1.6$ in the Sagittarius dwarf spheroidal galaxy. These stars were selected as metal-poor member candidates using a combination of public photometry from the SkyMapper Southern Sky Survey and proper motion data from the second data release from the *Gaia* mission. The SkyMapper filters include a metallicity-sensitive narrow-band v filter centered on the Ca II K line, which we use to identify metal-poor candidates. In tandem, we use proper motion data to remove metal-poor stars that are not velocity members of the Sagittarius dwarf spheroidal galaxy. We find that these two datasets allow for efficient identification of metal-poor members of the Sagittarius dwarf galaxy to follow-up with further spectroscopic study. Two of the stars we present have $[\mathrm{Fe/H}] < -2.0$, which adds to the few other such stars currently identified in the Sagittarius dwarf galaxy that are likely not associated with the globular cluster M54, which resides in the nucleus of the system. Our results confirm that there exists a very metal-poor stellar population in the Sagittarius dwarf galaxy. We find that none of our stars can be classified as carbon-enhanced metal-poor stars. Efficiently identifying members of this population will be helpful to further our understanding of the early chemical evolution of the system.

6.1 Introduction

Studying the detailed chemical abundances of metal-poor stars[1] in our own galaxy, the Milky Way, allows us to probe the physical processes that governed element formation in the early universe. For instance, the most metal-poor stars can be used to study the yields of early nucleosynthesis events [i.e., 343, 350, 102, 351]. Studying these enrichment events helps constrain the properties (e.g., initial mass function) of the First Stars [e.g., 103]. Additionally, comparing the detailed chemical abundance patterns of metal-poor stars in the Milky Way halo to those in other environments such as dwarf galaxies can help constrain paradigms of galaxy formation and environment-related dependencies in star formation and chemical enrichment [reviewed in 352, 99]. The efficient identification of metal-poor stars in a variety of environments is a necessary prerequisite for the aforementioned studies.

Early work on the detection of metal-poor halo stars relied on measuring the strength of the Ca II K absorption line at 3933.7 Å in large samples of low-resolution and medium-resolution stellar spectra [353, 298]. Then, more detailed spectroscopic follow-up of the most promising candidates would be performed. This technique of selecting metal-poor candidates from samples of low-resolution or medium-resolution spectra, and then conducting follow-up observations, has been replicated in a number of large surveys such as the Hamburg-ESO Survey [354, 355], the Sloan Extension for Galactic Understanding and Exploration [SEGUE; 356, 357, 358, 359], the Radial Velocity Experiment [RAVE; 360], and survey work with the LAMOST telescope [361, 362]. The success of these surveys has led to the discovery of more than 500 extremely metal-poor (EMP) stars, which are defined as having [Fe/H] < -3.0 [363, and references therein].

Recently, narrow-band photometry has been used to identify metal-poor candidates [i.e., 127, 125, 364]. This involves using a narrow-band v-filter encompassing the region of the Ca II K line as the flux through the narrow-band filter is strongly related to the strength of the Ca II K line. Hence the flux can be related to the

[1]Defined as [Fe/H] ≤ -1 dex, where [Fe/H] $= \log_{10}(N_{\rm Fe}/N_{\rm H})_{\star} - \log_{10}(N_{\rm Fe}/N_{\rm H})_{\odot}$ [170, 99].

overall metallicity of the star, in particular for metal-poor stars. The gain from this technique over spectroscopic identification is that photometry requires less observing time than spectroscopy, and the ability to simultaneously derive metallicity information on all stars to a given magnitude. So far, the application of this technique in the SkyMapper Southern Sky Survey has led to the discovery of over 100 EMP stars [e.g., 3] and a star with an upper limit on the iron abundance of [Fe/H] < -6.5 [129, 365]. Recent work by the Pristine Survey with a more finely tuned narrow-band v-filter has led to the discovery of a star with [Fe/H] $= -4.7$ [132], among others.

A natural venue in which to apply this selection techniques are dwarf spheroidal galaxies (dSphs). Only in the past decade have stars with [Fe/H] < -3.0 been discovered in dwarf galaxies [51, 20] which are simpler systems than the Milky Way due to their smaller size and limited star formation history. Their localized context facilitates interpretation when relating the chemical abundances of metal-poor stars to properties of the galaxy (i.e., star formation history, chemical enrichment events). Certainly, the chemical abundances of EMP stars in dSphs appear to show many similarities to the Milky Way halo population, in accordance with current paradigms of hierarchical galaxy formation (see Frebel and Norris 99 for a review). Further work on efficiently identifying the most metal-poor stars in any dwarf galaxy would thus be useful in probing these similarities across as many systems as possible.

In this paper, we choose to use a combination of SkyMapper [9] and *Gaia* public data [111, 112] to implement an efficient technique to identify metal-poor stars in the Sagittarius dSph [366]. Early work on the chemical abundances of stars in the Sagittarius dSph focused primarily on stars with [Fe/H] > -1.6 [367, 368, 369, 370, 371, 372, 373, 374]. Bellazzini et al. [371] found four stars with [Fe/H] < -2.0 in the nucleus of the Sagittarius dSph, one of which was recovered in the sample of Mucciarelli et al. [375]. However, the proximity of these stars to the globular cluster M54, which also lies in the nucleus of the Sagittarius dSph, make their association with the main body of the Sagittarius dSph slightly less clear. Recently, Hansen et al. [57] published detailed chemical abundances for three more stars with [Fe/H] < -2.0 in the Sagittarius dSph that are beyond the tidal radius of M54 and are thus

Table 6.1. Observations of stars in the Sagittarius dSph

Name	RA (h:m:s) (J2000)	DEC (d:m:s) (J2000)	Slit size	g (mag)	$t_{\rm exp}$ (min)	S/N[a]	$v_{\rm helio}$ (km/s)
Sgr-2	19:01:39.16	−32:56:44.1	$1\farcs0$	16.83	15	22, 35	142.7
Sgr-7	18:50:32.63	−32:35:34.0	$1\farcs0$	16.81	20	30, 60	169.8
Sgr-9	18:55:51.59	−30:39:45.4	$1\farcs0$	17.10	15	25, 45	142.6
Sgr-10	18:50:23.40	−31:09:00.1	$1\farcs0$	15.96	6	20, 40	173.0

[a]S/N per pixel is listed for 4500 Å and 8500 Å

associated with the main body of the Sagittarius dSph. The chemical abundances of these stars show some similarities to stars with [Fe/H] < -2.0 in the Milky Way halo, and have disputed the nature of the Sagittarius dSph having a top-light initial mass function as argued from the more metal-rich population [e.g., 374]. By adding to the population of the most metal-poor stars known in the Sagittarius dwarf galaxy, we aim to probe its early chemical and assembly history. Here we report the discovery of four photometrically-selected metal-poor stars in the Sagittarius dSph. We present spectroscopic measurements of the [Fe/H] and carbon abundance of these stars, of which two have [Fe/H] < -2.0.

The paper is organized as follows. In Section 6.2, we outline our target selection procedure and observations; in Section 6.3, we present our analysis in deriving the chemical abundances of these stars; in Section 6.4, we discuss the chemical abundance signatures of these stars, the efficiency of our target selection procedure, and overall findings regarding the early history of the Sagittarius dSph; in Section 6.5, we provide summarize our results.

6.2 Target Selection & Observations

Traditionally, candidate stellar members of a dwarf galaxy are identified in a color-magnitude diagram along an isochrone. Then, spectra are obtained for these stars to determine their membership status based on metallicity and velocity measurements. With our new technique, we increased the efficiency of the target-selection procedure by leveraging publicly available data to select metal-poor star candidates that appear to have similar proper motions and thus might be associated with a common dwarf

galaxy system.

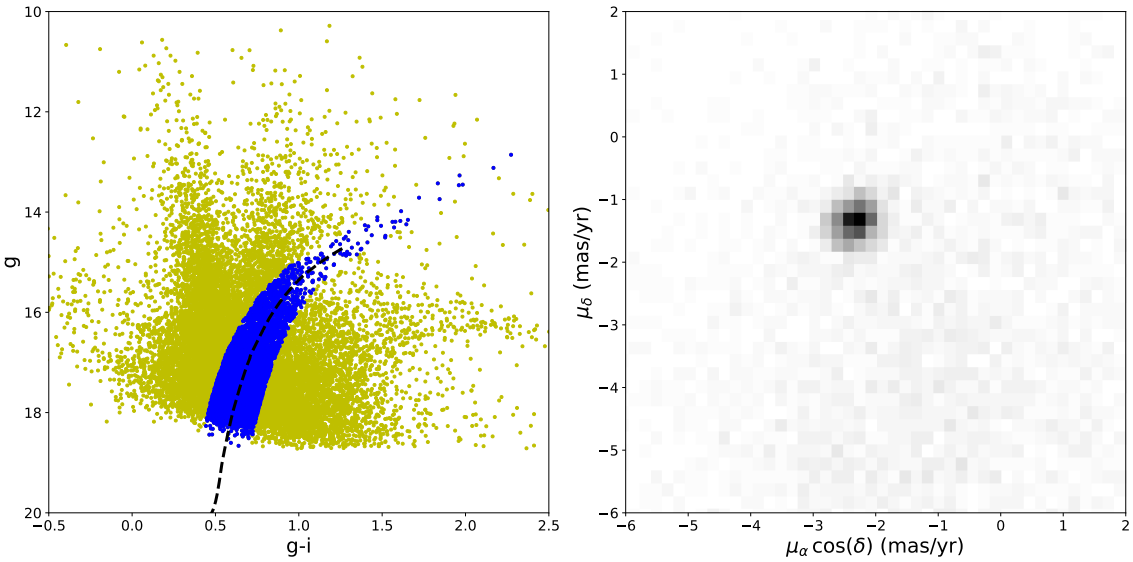

Figure 6-1 Left: Color-magnitude diagram of all sources within 60′of the center of the Sgr dSph. A 10 Gyr, [Fe/H] = −2.0 Dartmouth isochrone is overlaid [10], and points within $g - i \pm 0.15$ are marked in blue. Right: *Gaia* DR2 proper motions of the blue data points in the left panel. An over-density in proper motion space is centered on $\mu_\alpha \cos(\delta) = -2.33\,\mathrm{mas/yr}, \mu_\delta = -1.36\,\mathrm{mas/yr}$, indicating the systemic proper motion of the Sgr dSph members.

6.2.1 Target Selection

We queried the SkyMapper DR1.1 catalog [9] to retrieve photometric information on all sources within 2.85° of the center of the Sagittarius dSph (α_{J2000} = 18h55m19.5s, $\delta_{\mathrm{J2000}} = -30$d32m43s). We opted to use petrosian magnitudes, denoted in the source catalog by the *_petro* flag, for all subsequent analysis. The photometry was de-reddened following the prescription in Wolf et al. [9] using reddening maps from Schlegel et al. [63]. To remove sources that are likely not stars, we chose to exclude all sources with the catalog flag *class_star* < 0.9.

From the resulting catalog, we used $g - i$ colors and g magnitudes to construct a color-magnitude diagram (CMD) to use for a first-pass selection of candidate members of the Sagittarius dSph. A 10 Gyr, [Fe/H] = −2.0 isochrone from the Dartmouth Stellar Evolution Database [10] was overlaid on the CMD at the distance modulus of

the Sgr dSph [16.97; 376]. All stars within $(g-i) \pm 0.15$ of the isochrone were kept as candidate members. The result of this procedure is shown in the leftmost panel of Figure 6-1.

We then retrieved proper motion data from the *Gaia* DR2 catalog [111, 112, 164] for all stars within $(g-i) \pm 0.15$ of the isochrone. Upon plotting each star in proper motion space, we found an over-density centered on $\mu_\alpha \cos(\delta) = -2.33\,\mathrm{mas/yr}, \mu_\delta = -1.36\,\mathrm{mas/yr}$ as shown in the right panel in Figure 6-1. Since this over-density is clearly distinct from the foreground population and since stellar members of a dSph should have similar velocities, it therefore likely corresponds to stellar members of the Sagittarius dSph. Furthermore, the location of this over-density agrees well with the proper motion measurement of the Sagittarius dSph derived using *Gaia* DR2 data in Gaia Collaboration et al. [377]. We then conservatively narrowed our selection of candidate members to all stars with proper motion measurements $-2.75\,\mathrm{mas/yr} < \mu_\alpha \cos(\delta) < -1.90\,\mathrm{mas/yr}$, and $-1.75\,\mathrm{mas/yr} < \mu_\delta < -1.0\,\mathrm{mas/yr}$.

To select the most metal-poor of these stars, we leveraged the v-band photometry in the SkyMapper DR1.1 catalog. The SkyMapper narrow-band v-filter is sensitive to stellar metallicities because much of the bandpass of the filter is encompassed by the prominent Ca II K line [135]. We plotted our candidate members in $v-g-0.9\times(g-i)$ vs. $g-i$ space, since metal-poor stars tend to have lower $v-g-0.9\times(g-i)$ values for a given $g-i$. This argument is based on work presented in Keller et al. [378], who used an index of $v-g-2\times(g-i)$. Since this differs from our index, we had to verify whether the most metal-poor stars will also lie at lower $v-g-0.9\times(g-i)$ indices. We therefore applied this selection process to several globular clusters in the footprint of the SkyMapper survey to test whether their member stars were identifiable as more metal-poor than foreground stars.

We performed the same CMD and proper motion selection procedure on four globular clusters: NGC6752 [[Fe/H] $= -1.43$; 379], NGC6397 [[Fe/H] $= -2.10$; 380], M68 [[Fe/H] $= -2.23$; 11], M30 [[Fe/H] $= -2.27$; 11]. Since all member stars of a globular cluster have a similar metallicity, their members should form a distinct contour in $v-g-0.9\times(g-i)$ vs. $g-i$ space. In Figure 6-2, we see a clear separation in

$v - g - 0.9 \times (g - i)$ vs. $g - i$ space between foreground halo stars and members of the globular clusters NGC6397, M68, and M30. The separation is visible, but less prominent, for the member stars of NGC6752, since they do not separate as clearly from the foreground. This result implies that stars with metallicities below [Fe/H] $= -1.43$, which is the metallicity of NGC6752, should begin to separate from the halo foreground in our metallicity selection. Of note, we also found that SkyMapper DR.1.1 v band photometry for stars fainter than $g \sim 16$ appears to have insufficient precision to clearly separate members from the foreground. Thus, having demonstrated the utility of selecting metal-poor candidates using this technique, we followed this procedure to pick metal-poor candidate stars in the Sagittarius dSph. Following Hansen et al. [57], we observed stars outside the tidal radius of the nearby globular cluster, M54 [7.′5; 381] to ensure our targets were not members of that system.

6.2.2 Observations & Data Reduction

We used the Magellan Echellette (MagE) Spectrograph [226] on the Magellan-Baade telescope at Las Campanas Observatory to obtain medium-resolution spectra of six metal-poor candidate member stars in the Sagittarius dSph. These stars were selected since their $v - g - 0.9 \times (g - i)$ indices were among the lowest in the sample. Targets were observed with the 1.″0 slit and 1x1 binning, which grants sufficient resolution ($R \sim 4000$) and wavelength coverage (3200 Å $-$ 10000 Å) to derive abundances from the Ca II K line ($\sim$ 3933 Å), the CH G band ($\sim$ 4300 Å), the Mg b region ($\sim$ 5150 Å), and the calcium triplet lines ($\sim$ 8500 Å). We observed these stars for the first $\sim$1.5 hours of the night of July 17th, 2018, during which the weather was partially cloudy.

Our spectra were reduced using the Carnegie Python pipeline [196][2] using standard calibration procedures. To account for potential effects from instrument stability on the wavelength calibration, a ThAr calibration arc lamp spectrum was collected after slewing to each target. Spectra of each target were then reduced using the corresponding arc lamp spectrum. Four of the six observed stars were later determined to be members of the Sagittarius dSph. Details of their observations are shown in

[2]https://code.obs.carnegiescience.edu/mage-pipeline

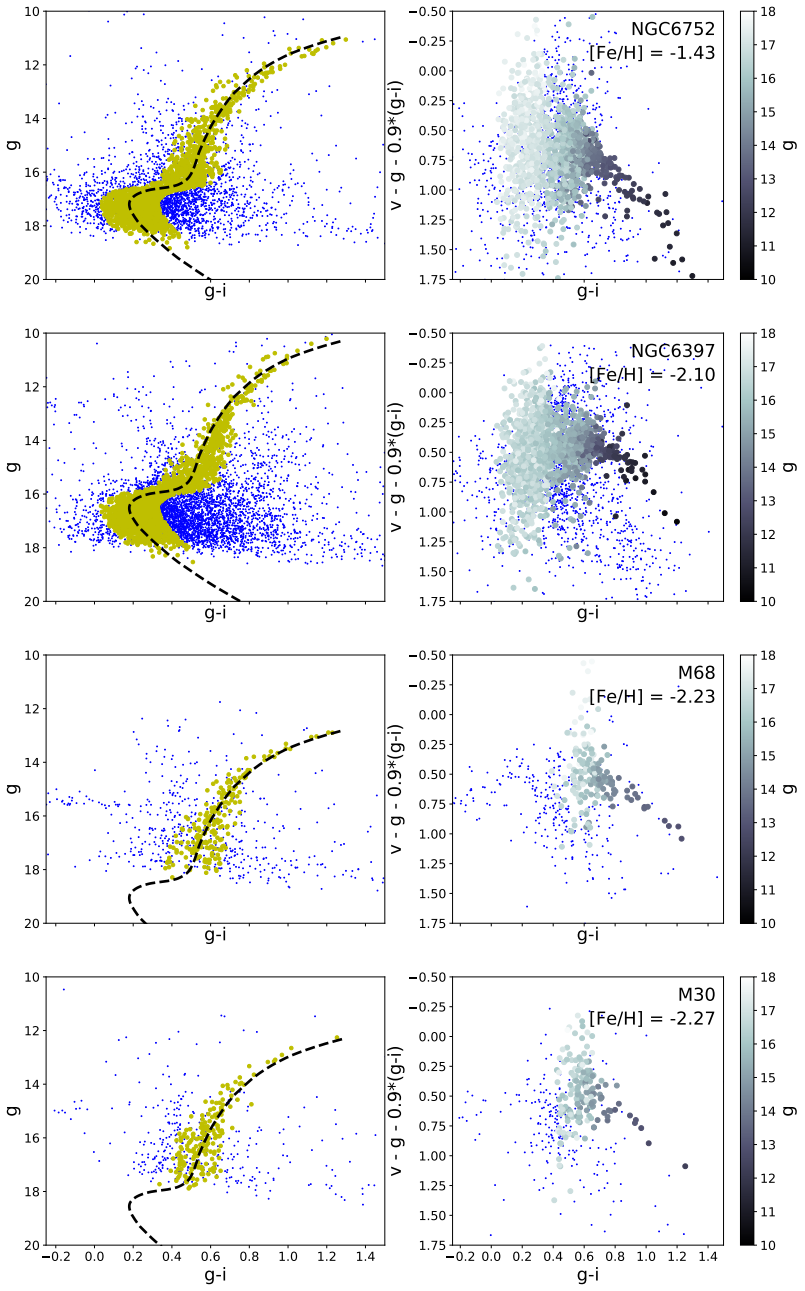

Figure 6-2 Left: Color-magnitude diagrams of NGC6752, NGC6397, M68, and M30, from top to bottom of stars within 15′ from their centers. Dartmouth isochrones of 10 Gyr, [Fe/H] = −2.0 are overlaid. Right: Metallicity-sensitive color-color plots using SkyMapper photometry of the corresponding globular clusters, with the magnitudes of the data points along the isochrone color-coded by magnitude. As noted in Section 6.2.1, the measurements appear to start being less sensitive to metallicity at a magnitude $g \sim 16$, due to a lack of photometric precision.

Table 6.1.

6.3 Analysis

Here we present our methods for deriving the stellar parameters ($T_{\rm eff}$, $\log g$), metallicities, and carbon abundances of the stars we observed. The $T_{\rm eff}$ and $\log g$ values were derived by matching public photometry from SkyMapper DR1.1 to isochrones from the Dartmouth Stellar Evolution Database [10]. The metallicity was derived based on measurements of the strengths of the Ca II K line ($\sim$ 3933.7 Å), Mg b region ($\sim$ 5150 Å), and calcium triplet lines ($\sim$ 8500 Å). The carbon abundance was derived from the CH G band ($\sim$ 4300 Å).

In subsequent analysis, we assume the stars in our sample are members of the red giant branch. There exists a chance that some are instead asymptotic giant branch (AGB) stars, due to the proximity of the AGB track to the red giant branch. However, the timescale of stars existing on the AGB track is short compared to the timescale that stars exist on the red giant branch, which makes it unlikely that any stars in our sample of only four stars are AGB stars.

6.3.1 Radial Velocity Measurements & Deriving Stellar Parameters

As a preliminary step, it was necessary to measure the radial velocity of each star to verify it as a member of the Sagittarius dSph. To derive radial velocities, we cross-correlated each spectrum with a template spectrum of the metal-poor giant HD122563 in the Spectroscopy Made Hard (SMH) analysis software [197]. Heliocentric velocity corrections were derived using the task `rvcorrect` in `IRAF`. We found that the four stars in Table 6.1 have velocities consistent with the systemic velocity of the bulge of the Sagittarius dSph of $\sim$ 141 kms $\pm$ 9.6 kms [371]. While this comparison may not be strictly applicable to Sgr-2, Sgr-7, and Sgr-10 since they are over one degree from the center of the Sagittarius dSph, we note that their velocities are comparable to the velocities of the population of metal-poor members of the Sagittarius dSph presented in Hansen et al. [57], which range from 127.4 km/s to 167.2 km/s. The other two stars

that we observed had radial velocities $\sim 180\,\mathrm{km/s}$ below the systemic velocity of the bulge of the Sagittarius dSph, and we thus concluded that they were not members of the system.

The stellar parameters, T_{eff} and $\log g$, were derived by matching SkyMapper g and i photometry to a 10 Gyr, [Fe/H] $= -2.0$ isochrone from the Dartmouth Stellar Evolution Database. To validate this method of measuring stellar parameters, we performed the same procedure on the seven metal-poor and very metal-poor Sagittarius dSph stars with stellar parameter measurements in Hansen et al. [57] that also had publicly available SkyMapper photometry. Hansen et al. [57] derived T_{eff} and $\log g$ from high-resolution spectra by removing trends in excitation potential with abundance and satisfying ionization equilibrium. For these seven stars, we derive T_{eff} values that are consistent with the measurements in Hansen et al. [57]. We measure a marginally higher T_{eff} of 24 K on average and the residuals have a standard deviation of 176 K. For the $\log g$ values, our measurements are larger than those in Hansen et al. [57] by 0.3 dex on average and the residuals have a standard deviation of 0.7 dex.

To further test the validity of our stellar parameter measurements, we compared our T_{eff} values to those predicted from a color-T_{eff}-[Fe/H] relation. We converted the SkyMapper photometry to the SDSS photometric system by first converting to the Pan-STARRS photometric system (described in paragraph 2 of Section 6.3.2.1) and then the SDSS photometric system using the color transformations in Tonry et al. [382]. Then, we applied the IRFM temperature estimator[3], which is an additional photometric T_{eff} calibration that was added to the original SEGUE Stellar Parameter Pipeline [383]. The IRFM temperature estimator gives largely reasonable T_{eff} values that are offset from our original T_{eff} values by -300 K (Sgr-2), 40 K (Sgr-7), and -71 K (Sgr-10). For Sgr-9, the estimator gives a T_{eff} value that is 590 K lower than our original measurement. We choose to adopt our original T_{eff} value of 4767 K for Sgr-9, since a visual comparison of the Balmer lines in its spectrum to the Balmer lines in the spectra of the other Sagittarius dSph members suggests that all have similar T_{eff} values.

[3]https://www.sdss.org/dr14/spectro/sspp_irfm/

We also compared our $\log g$ values to those derived from an estimate of the absolute magnitude of each of our stars by assuming each star has a distance modulus equal to that of the Sagittarius dSph [16.97; 376]. We then derive $\log g$ values using the canonical equation presented in Hansen et al. [57], assuming a mass of $0.7 M_{\odot}$ and the $T_{\rm eff}$ values in Table 6.2. We find our $\log g$ values are 0.4 dex on average below those derived by the above method, with a standard deviation of the differences in $\log g$ values between the two methods of 0.15 dex.

6.3.2 Deriving Chemical Abundances

We derived the metallicity ([Fe/H]) of each star in our sample from the equivalent widths of the Ca II K line (3933.7 Å) and the calcium triplet lines (8498 Å, 8542 Å, and 8662 Å). We used these measurements to derive metallicities by applying calibrations detailed in Beers et al. [52] and Carrera et al. [249], respectively. Their application is further described in Sections 6.3.2.1 and 6.3.2.2. By using spectral synthesis techniques, we also independently derived the metallicity using the Mg b region ($\sim$ 5150 Å). We derived a carbon abundance ([C/Fe]) for each star using the CH G band ($\sim$ 4300 Å). Details of methodology are provided in Sections 6.3.2.3 and 6.3.2.4.

We took the weighted average of the three iron abundances from the methods described in Sections 6.3.2.1, 6.3.2.2, and 6.3.2.3 to derive final [Fe/H] values. Examples of our spectra covering the three wavelength regions used to derive [Fe/H] are presented in Figure 6-3. All chemical abundance measurements are presented in Table 6.2 and are listed relative to solar abundances from Asplund et al. [207].

6.3.2.1 Ca II K Line

Beers et al. [52] presented a calibration that related a star's $B - V$ color and the strength its Ca II K line at 3933.7 Å to metallicity. The calibration used the KP index, a measurement of the pseudo-equivalent width of the Ca II K line, to quantify line strength. A full discussion of deriving the KP index, which involves measur-

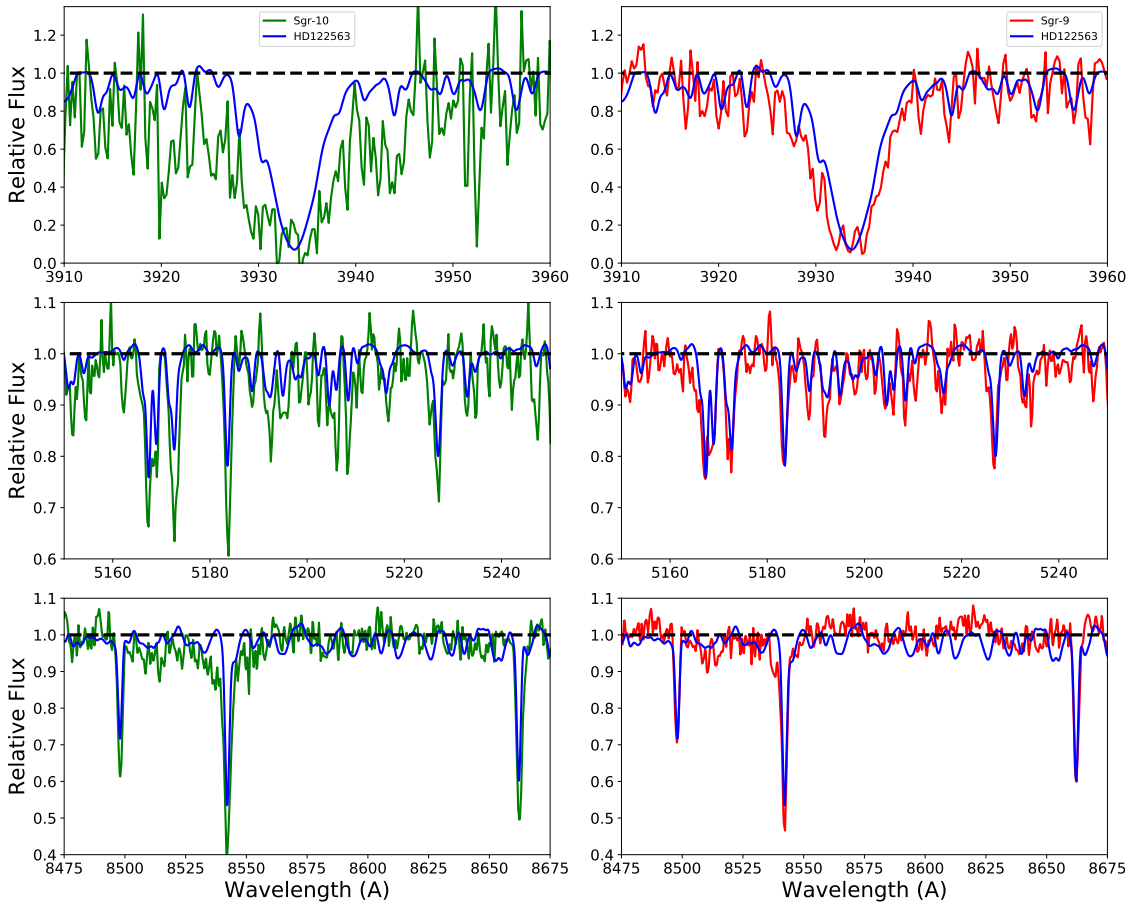

Figure 6-3 Sample spectra of the Ca II K line (top), Mg b region (middle), and the calcium triplet region (bottom). Spectra for Sgr-10 ([Fe/H] $= -1.70$) are shown in green on the left, and those for Sgr-9 ([Fe/H] $= -2.3$) on the right. In all plots, a MIKE spectrum of HD122563 [[Fe/H] $= -2.64$; 56] smoothed to $R \sim 4000$ is overplotted.

ing separate line indices known as K6, K12, and K18, is presented in Beers et al. [52]. We exactly followed their implementation. For continuum normalization, we fit a line through the blue and red sidebands of the Ca II K line located between 3903 Å−3923 Å and 4000 Å−4020 Å, respectively. We then directly integrated over the bandpasses presented in Beers et al. [52] to measure the K6, K12, and K18 line indices, and adopted a final KP index following their prescription. The uncertainty on the KP index was derived by shifting the continuum placement based on the signal-to-noise of the spectrum.

To obtain $B-V$ colors for each of our stars, we first derived a conversion between SkyMapper g and r photometry and the Pan-STARRS photometric system using data for K, G, and F type stars on the SkyMapper Southern Sky Survey website[4] based on the spectral library from Pickles [384]. We then converted the Pan-STARRS g and r photometry to $B-V$ colors using color transformations provided in Tonry et al. [382]. The resulting uncertainties on the $B-V$ colors from these transformations ranged from 0.04 mag and 0.08 mag.

Additionally, we note that Beers et al. [52] assumes [Ca/Fe] = 0.4 when [Fe/H] < -1.5, which holds true for stars in the Milky Way halo. Results from Mucciarelli et al. [375] and Hansen et al. [57] suggest general agreement between the [Ca/Fe] values of Milky Way halo stars and Sagittarius dSph stars for metal-poor stars. Thus, we apply no further correction to our [Fe/H] values derived from the calibration.

The uncertainty on the [Fe/H] from this method was derived by adding in quadrature the model uncertainties from the Beers et al. [52] calibration and the shifts in [Fe/H] by varying the KP index and $B-V$ colors by their uncertainties.

6.3.2.2 Ca Triplet Lines

The equivalent widths of the calcium triplet lines at 8498 Å, 8542 Å, and 8662 Å can also be related to the overall metallicity of the star, as detailed in Carrera et al. [249]. We measured the equivalent width of each of these lines in our spectra using the `splot` function in `iraf`. The uncertainty on each of these equivalent width measurements

[4] http://skymapper.anu.edu.au/filter-transformations

was determined by varying the continuum placement. We note that for Sgr-2, fringing near the calcium triplet lines in its spectrum led to higher uncertainties.

We opted to use the form of the calibration in Carrera et al. [249] that requires an absolute V magnitude measurement. To derive this value, we followed the same steps outlined in the second paragraph of Section 6.3.2.1 to convert SkyMapper photometry to the Pan-STARRS photometric system. We then applied transformations from Tonry et al. [382] to derive V magnitudes. Then, we derived an absolute V magnitude by subtracting the distance modulus of the Sagittarius dSph [16.97; 376].

The uncertainty on the [Fe/H] was derived by propagating the model uncertainties in Carrera et al. [249] calibration, and adding them in quadrature to the shifts in [Fe/H] by varying the equivalent widths and V by their respective uncertainties.

6.3.2.3 Mg b Region

We fit synthetic spectra to the Mg b region (5150 Å− 5220 Å) to derive metallicities. All syntheses and fitting were performed with the SMH software using the 2017 version of the 1D LTE radiative transfer code MOOG [198][5] with an updated treatment of scattering [199][6] and the Kurucz model atmospheres [385]. The line list was compiled using software provided by C. Sneden. The software retrieved data from the Kurucz [252] database and added measurements from references in Sneden et al. [206, 153, 253]. The $T_{\rm eff}$ and $\log g$ values derived in Section 6.3.1 were used as stellar parameters when synthesizing spectra. A microturbulence of $\rm v_{micro} = 2.0$ was assumed in all syntheses.

We generated synthetic spectra with different [Fe/H] until there was agreement with the observed spectra. The [Mg/Fe] ratio was fixed to 0.4, following from a general agreement in [α/Fe] values between Milky Way halo stars and metal-poor Sagittarius dSph stars [375, 57].

To derive the uncertainty on our values, we added random and systematic sources of uncertainty in quadrature. The random uncertainty was derived by noting the

[5]https://www.as.utexas.edu/ chris/moog.html
[6]https://github.com/alexji/moog17scat

Table 6.2. Stellar parameters and chemical abundances of stars in the Sagittarius dSph

Name	$T_{\rm eff}$ (K)	$\log g$ (dex)	[Fe/H]$_{\rm Mg}$ (dex)	[Fe/H]$_{\rm CaT}$ (dex)	[Fe/H]$_{\rm Ca2k}$ (dex)	[Fe/H]$_{\rm final}$ (dex)	[C/Fe] (dex)	[C/Fe]$_{\rm corrected}$ [a] (dex)
Sgr-2	4836	1.71	-2.20 ± 0.33	-1.82 ± 0.43	-2.25 ± 0.41	-2.11 ± 0.18	0.02 ± 0.36	0.34 ± 0.36
Sgr-7	4610	1.25	-1.95 ± 0.34	-1.69 ± 0.30	-1.49 ± 0.46	-1.74 ± 0.17	-0.52 ± 0.33	0.04 ± 0.33
Sgr-9	4767	1.56	-2.47 ± 0.36	-2.10 ± 0.17	-2.34 ± 0.39	-2.19 ± 0.15	-0.66 ± 0.44	-0.25 ± 0.44
Sgr-10	4610	1.25	-1.84 ± 0.32	-1.57 ± 0.27	-1.54 ± 0.48	-1.66 ± 0.13	-0.37 ± 0.35	0.17 ± 0.35

[a]Corrected for the evolutionary state of the star following Placco et al. [8].

variation in [Fe/H] required to encapsulate the noise in each spectrum. This procedure led to random uncertainties between 0.20 dex and 0.25 dex. The systematic sources of uncertainty were from uncertainties in the stellar parameter measurements. We find that uncertainties of $\sim$150 K in $T_{\rm eff}$ and $\sim$0.3 in $\log g$ arise when propagating the SkyMapper photometric uncertainties through our method of deriving stellar parameters. We thus vary each stellar parameter by its uncertainty, re-derive [Fe/H], and note the discrepancy from the original [Fe/H] as a systematic uncertainty. We then add all systematic uncertainties and the random uncertainty in quadrature to derive a final uncertainty. Final derived values and uncertainties are presented in Table 6.2.

6.3.2.4 G Band

We fit synthetic spectra to the CH G band between 4260 Å and 4320 Å to derive carbon abundances. The same procedure was followed as in Section 6.3.2.3 with the exception of the following details. First, the line list was compiled with the same sources as in Section 6.3.2.3, but CH data were added from Masseron et al. [53]. Second, the [Fe/H] value in the synthetic spectra was fixed to the final [Fe/H] presented in Table 6.2, and the [C/Fe] value was allowed to vary. Third, when calculating the uncertainties, we include the uncertainty in [Fe/H] from Table 6.2 as a source of systematic uncertainty in [C/Fe]. Finally, the derived carbon abundances were corrected for the evolutionary state of the star following Placco et al. [8]. The final carbon abundance values are presented in Table 6.2.

6.4 Results

In Section 6.4.1, we discuss the relatively low carbon abundances of the stars in our sample, and in Section 6.4.2, we discuss in more detail the implementation of our technique for identifying metal-poor stars in the Sagittarius dSph. Since our sample of four is small and biased toward metal-poor stars, further interpretation is difficult in the context of the overall metallicity distribution of stars in the system. However, we confirm that the metallicity distribution function reaches below [Fe/H] $= -2.0$. Our fairly efficient detection of two very metal-poor stars builds on the previous detection of such stars in the system [371, 375, 57], and bolsters the argument that Sagittarius dSph should host a population of very metal-poor stars. Our results suggest that this population can be identified for further study by using efficient target selection techniques, thus facilitating a more complete understanding of the early chemical evolution of the system.

6.4.1 The Signature of Carbon in the Sagittarius dSph

Carbon is an important element for studying early chemical evolution, partly because the fraction of stars that are enhanced in carbon increases as metallicity decreases [386, 8]. This observation has led to the identification of carbon-enhanced metal-poor (CEMP) stars ([C/Fe] > 0.7, [Fe/H] < -1.0) as a separate subclass of metal-poor stars [170, 54]. Placco et al. [8] measured the fraction of CEMP stars to be $\sim 20\%$ for stars with [Fe/H] < -2.0. However, CEMP stars are not found in all environments. For instance, only a few s-process rich CEMP stars have been detected in the direction of the Milky Way bulge [387, 388] and studies generally tend to find a lower fraction of CEMP stars in dSphs [4, 6, 215], but a small number have been detected in the ultrafaint dwarf galaxies [99].

We find that none of the stars in our sample meet the threshold to be considered CEMP stars. However, this is not surprising given our small sample size. For instance, Placco et al. [8] find that CEMP stars compose 20% of the Milky Way halo population below [Fe/H] $= -2.0$ and our sample only has two stars with [Fe/H] < -2.0 which

makes a null CEMP detection reasonable. Moreover, a strong CN absorption feature exists at $\sim 3880\,\mathring{\mathrm{A}}$, which is covered by the bandpass of the SkyMapper v filter. The presence of this absorption feature means that the most carbon enhanced stars are likely to be identified as more metal-rich than their true metallicity, and thus might be excluded from our target selection procedure as suggested in e.g., Jacobson et al. [3]. However, Hansen et al. [57] also found no CEMP stars in their three stars with [Fe/H] < -2.0. If we were to assume that the Sagittarius dSph has the same CEMP fraction as the halo, the probability of finding five stars below [Fe/H] $= -2.0$ that are not carbon-enhanced is $\sim$32%. While this calculation ignores sampling biases, it does suggest that a conclusive claim that CEMP stars are under-abundant in the Sagittarius dSph is difficult to argue given the small sample size.

Placco et al. [8] find that the median corrected [C/Fe] is 0.14 for stars in the Milky Way halo with $-2.25 <$ [Fe/H] < -2.0. This value is roughly in agreement with the [C/Fe] values in our sample. In contrast, Hansen et al. [57] and Hasselquist et al. [374] find that, over a broad metallicity range, stars in the Sagittarius dSph tend to be under-abundant in carbon relative to stars in the Milky Way halo. This difference suggests a spread in the carbon abundances of stars at low metallicities. Overall, results suggesting a low carbon abundance over all metallicities and a putative lack of CEMP stars suggest that early nucleosynthetic events in the Sagittarius dSph may not have been dominated by sites hypothesized to have produced CEMP stars, such as e.g., faint supernovae [e.g., 389].

6.4.2 Searching for Metal-poor Stars using SkyMapper Photometry

We observed six candidates selected as metal-poor Sagittarius dSph candidate members from SkyMapper photometry and *Gaia* proper motion data (see Section 6.2.1). Of these six stars, four were confirmed as members by follow-up spectroscopy. Given our success rate and the fact that only a handful of stars were found with [Fe/H] < -2.0 before this study [371, 375, 57] in either M54 or the main body of the Sagittarius dSph, we consider our target selection procedure for metal-poor stars fairly successful.

However, it is worth inquiring into why two of our candidates were not members. Both candidates have proper motions consistent with that of the Sagittarius dSph. Additionally, assuming similar $T_{\rm eff}$ values, both stars appear to have metallicities similar to Sgr-10 ([Fe/H] ~ -1.7) based on visually comparing the strengths of their Ca II K lines, Mg b region, and calcium triplet lines to those in the spectra of the Sagittarius dSph members. Thus, it is likely that the non-members were simply metal-poor halo stars in the vicinity of Sagittarius dSph.

Discriminating stars at very low metallicities ([Fe/H] < -2.0) from simple metal-poor stars ($-2.0 <$ [Fe/H] < -1.0) would likely remove some contamination from the metal-poor halo population. Based on our spectroscopic measurements, we had mixed success at recovering only very metal-poor stars, likely because we opted to observe stars fainter then $g \sim 16$. At these magnitudes, the public SkyMapper photometric uncertainties make a quantitative metallicity prediction unreasonable. This fact is illustrated in Figure 6-2. Despite this fact, we still show a reasonable success rate in identifying metal-poor and very metal-poor stars at these magnitudes, likely because we chose to observe stars that were already predicted to have very low metallicities. For the purposes of future work, we chose to investigate whether it would be possible to quantitatively predict metallicities for stars with sufficient precision in the public SkyMapper DR1.1 catalog.

To quantitatively relate the photometric metallicities to the overall stellar metallicities as a function of photometric precision, we generated synthetic photometry for stars with various stellar parameters. First, we used the Turbospectrum code [193, 148], the MARCS model atmospheres [149], and a line list compiled from the VALD database [150, 151] to generate a grid of flux-calibrated synthetic spectra. The stellar parameters of our grid were the following: $4000 < T_{\rm eff}\,[{\rm K}] < 5700; 1 < \log\, g < 3$; $-4.0 <$ [Fe/H] < -0.5. We then retrieved the bandpass of the SkyMapper v, g, and i filters from the Filter Profile Service[7], which used bandpass data from Bessell et al. [135]. Then, we generated a library of synthetic v,g,i photometry based on the methods presented in Bessell and Murphy [194] and Casagrande and VandenBerg

[7] http://svo2.cab.inta-csic.es/svo/theory/fps3/

[159].

In Figure 6-4, we have overlaid these synthetic contours on the results from the globular cluster SkyMapper photometry. We find that the bright stars in NGC6397, M30, and M68 lie largely between the [Fe/H] = −2.0 and −2.5 contours as expected since their metallicities are [Fe/H] = −2.10, −2.23 and −2.27, respectively. As expected, fainter stars tend to fall outside these contours due to worse photometric precision. This agreement between the synthetic contours and the globular cluster photometry suggests that future work could pre-select stars of specific metallicities for further spectroscopic study. We note that only the most metal-poor stars in Hansen et al. [57] have v-band SkyMapper photometry. This is not surprising because more metal-rich stars appear fainter in the v filter. Thus, the more metal-rich stars in Hansen et al. [57] are likely below the threshold for detection in the SkyMapper survey data. When overlying our observed stars and those in Hansen et al. [57] with v photometry in SkyMapper, we find that all but one star is likely metal-poor, but the photometric uncertainties are sufficiently large that it is unclear which photometric metallicity contour they lie on. Thus, this illustrates the need for precise SkyMapper photometry for target selection or solely choosing brighter stars for future candidate selection.

6.5 Summary

We present a technique for identifying metal-poor stars in dwarf galaxies using public SkyMapper photometry and *Gaia* proper motion data. We obtained spectra of six stars, of which four turned out to be metal-poor members of the Sagittarius dSph. Of the four, two have [Fe/H] < −2.0 and none are enhanced in carbon. This sample builds onto the four known stars in Sgr with a metallicity below [Fe/H] = −2.0, showing that public proper motion and photometric data may be effectively leveraged to identify the most metal-poor stars in dwarf galaxies. Future work will continue to implement SkyMapper photometry in tandem with *Gaia* proper motion data to study dwarf galaxies, both with public survey data and deep imaging of dwarf galaxies using

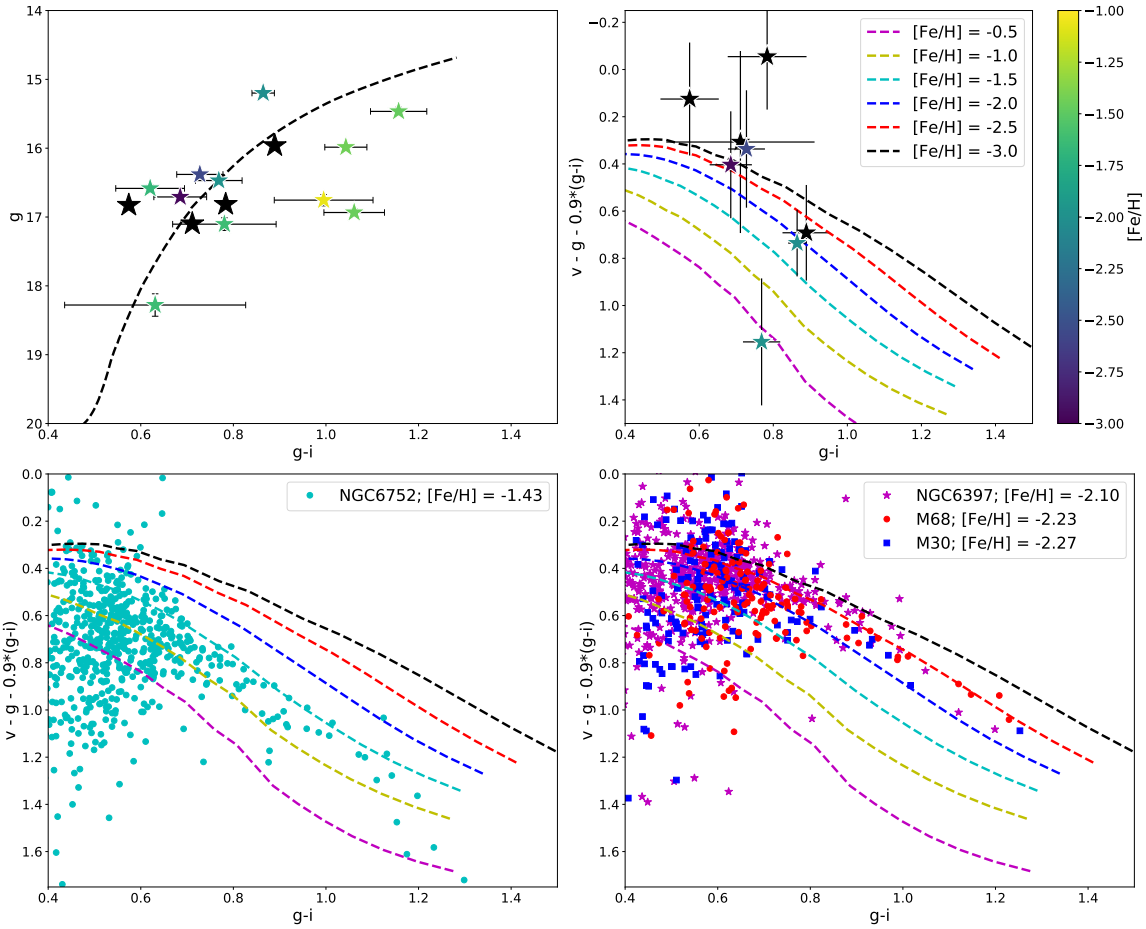

Figure 6-4 Top left: Color-magnitude diagram of stars within 2.85° of the center of the Sgr dSph. Green data points are within $g-i\pm0.15$ along the overlaid Dartmouth isochrone of age 10 Gyr, [Fe/H] $= -2.0$. Black stars are stars with measurements from this study. Colored stars have measurements in Hansen et al. [57], and their metallicities are color-coded by the colorbar on the right. Top right: Metallicity-sensitive color-color plots using SkyMapper photometry with synthetic photometric contours and sources from the top left color-magnitude diagram. The stars in Hansen et al. [57] with v photometry available in the public SkyMapper catalog are also overlaid. Bottom left: Metallicity-sensitive color-color plots using SkyMapper photometry with synthetic photometric contours and the metal-poor globular cluster (NGC 6752) in Figure 6-2 overlaid. Bottom right: Metallicity-sensitive color-color plots using SkyMapper photometry with synthetic photometric contours and the three very metal-poor globular clusters (NGC 6397, M68, M30) from Figure 6-2 overlaid.

the metallicity-sensitive SkyMapper v-filter (A. Chiti et al., in prep).

Chapter 7

Discovery of 18 stars with $-3.10 <$ [Fe/H] < -1.45 in the Sagittarius dwarf galaxy

The content of this chapter was published in the Astrophysical Journal as [390] in October 2020.

Abstract

Studies of the early chemical evolution of some larger dwarf galaxies ($> 10^7\,M_\odot$) are limited by the small number of stars known at low metallicities in these systems. Here we present metallicities and carbon abundances for eighteen stars with metallicities between $-3.08 \leq$ [Fe/H] ≤ -1.47 in the Sagittarius dwarf spheroidal galaxy, using medium-resolution spectra from the MagE spectrograph on the Magellan-Baade Telescope. This sample more than doubles the number of known very metal-poor stars ([Fe/H] ≤ -2.0) in the Sagittarius dwarf galaxy, and identifies the first known extremely metal-poor star ([Fe/H] ≤ -3.0) in the system. These stars were identified as likely metal-poor members of Sagittarius using public, metallicity-sensitive photometry from SkyMapper DR1.1 and proper motion data from *Gaia* DR2, demonstrating that this dearth of metal-poor stars in some dwarf galaxies can be addressed with targeted searches using public data. We find that none of the stars in our sample are enhanced in carbon, in contrast to the relative prevalence of such stars in the Milky Way halo. Subsequent high-resolution spectroscopy of these stars would be key in detailing the early chemical evolution of the system.

7.1 Introduction

The Milky Way's metal-poor stars[1] are a nearby window to the high-redshift universe. The natal chemical composition of these ancient stars is generally preserved in their stellar atmospheres. Accordingly, their chemical abundances trace the formation of the first heavy elements (see review Frebel and Norris 99) and can be used to infer the properties (e.g., initial mass function, explosion energy, chemical yields) of the First Stars and supernovae that drove early nucleosynthesis [102, 103]. The chemical abundances of metal-poor stars also reflect the early evolution of their host galaxies, since an interplay of several galactic properties, including star formation efficiency, accretion, and feedback, drives chemical evolution [352, 297, 179].

In this context, the Milky Way's satellite dwarf galaxies are prime environments to identify and chemically characterize metal-poor stars to learn about early galactic environments. These systems span a range of masses ($\sim 10^5\,\mathrm{M}_\odot$ to $\sim 10^{11}\,\mathrm{M}_\odot$; e.g., Walker et al. 1, Simon 121, Erkal et al. 263) and thus allow the investigation of early chemical evolution in a variety of self-contained environments. Furthermore, analogs of these surviving satellite dwarf galaxies may have been accreted onto the Milky Way to form the old stellar halo. Accordingly, diversity in the chemical abundances of very metal-poor ([Fe/H < -2.0) stars in the Milky Way halo may be explained by its assembly from smaller galaxies [391, 392]. To fully test this claim, and then consequently isolate the environments that produce the chemical signatures we observe in the oldest, most metal-poor stars, it is necessary to identify large samples of similarly metal-poor stars in the Milky Way's satellite dwarf galaxies.

However, the most metal-poor population ([Fe/H] $\lesssim -2.5$) of the most massive Milky Way dwarf spheroidal (dSph) galaxies ($> 10^7\,\mathrm{M}_\odot$) remains sparsely characterized, as galaxies with larger masses have much higher average metallicities [179]. Only 55 stars with [Fe/H] < -2.5 known across all dSphs have detailed chemical abundance measurements available [393, 394, 395, 396, 286, 287, 20, 290, 349, 118, 397, 5, 6, 57, 398], with the majority in just two systems: the Sculptor and Sextans

[1]Defined as [Fe/H] ≤ -1 dex, where [Fe/H] $= \log_{10}(N_{\mathrm{Fe}}/N_{\mathrm{H}})_\star - \log_{10}(N_{\mathrm{Fe}}/N_{\mathrm{H}})_\odot$ [170, 99].

dSphs. Identifying more such metal-poor stars across all dSphs is informative when addressing the aforementioned questions, especially since these larger dwarf galaxies are thought to have contributed the most stars to the Milky Way halo [391].

Here we present the results of a targeted search for very metal-poor stars in the Sagittarius dSph [366, 399]. Sagittarius is the most massive known satellite dwarf spheroidal galaxy of the Milky Way [$\sim 4 \times 10^8\,M_\odot$; 400]. It has only a handful of known very metal-poor stars [371, 375, 57, 137], due to a prominent metal-rich ($\langle$[Fe/H]$\rangle \sim -0.5$) component of its stellar population [375]. A detailed abundance analysis of just three of these very metal-poor stars in Hansen et al. [57] already hinted at some similarities to the chemical abundances of very metal-poor stars in the Milky Way halo. It also challenged claims of a top-light initial mass function as suggested by its more metal-rich population [e.g., 373]. To further investigate the early evolution of this system, we present metallicities and carbon abundances for eighteen red giant metal-poor stars in the Sagittarius dSph that were identified using metallicity-sensitive SkyMapper photometry [127, 9] and Gaia DR2 proper motions [111, 112] following Chiti and Frebel [137]. Notably, we identify nine stars with [Fe/H] ≤ -2.0, one of which is the first known extremely metal-poor star ([Fe/H] < -3.0) in the system.

This paper is organized as follows. In Section 7.2, we provide an overview of our observations; in Section 7.3, we outline our methodology in deriving stellar parameters and chemical abundances. We discuss the implications of our results on the early evolution of the Sagittarius dSph in Section 7.4, and summarize our work in Section 7.4.

7.2 Target Selection & Observations

We identified metal-poor candidate members of the Sagittarius dwarf spheroidal galaxy (dSph) following the criteria in Chiti and Frebel [137], which we briefly outline here. We retrieved photometric data from the SkyMapper DR1.1 catalog [9] on all sources within three degrees of the center of the Sagittarius dSph. This dataset

Table 7.1. Additional observations of stars in the Sagittarius dSph

Name	RA (h:m:s) (J2000)	DEC (d:m:s) (J2000)	g [mag]	$t_{\rm exp}$ [s]	S/N[a]	$v_{\rm helio}$ [km s^{-1}]
Sgr-300	18:44:26.84	−29:37:56.09	15.82	480	40,85	132
Sgr-265	18:44:56.86	−31:12:01.84	16.09	480	40,75	165
Sgr-180	18:48:43.24	−31:46:26.82	15.66	420	25,55	152
Sgr-157	18:48:51.47	−31:35:21.58	17.30	1200	30,40	133
Sgr-298	18:49:32.88	−32:44:26.81	17.46	1200	30,40	165
Sgr-91	18:51:44.32	−29:30:38.85	16.17	540	40,65	125
Sgr-69	18:52:48.45	−29:32:23.42	15.56	480	45,95	129
Sgr-48	18:56:26.25	−31:21:23.61	15.83	480	45,85	142
Sgr-81	18:56:52.64	−31:43:07.51	17.39	900	25,40	138
Sgr-38	18:57:27.66	−31:07:39.87	16.26	540	40,65	150
Sgr-139	18:57:50.62	−29:00:29.93	17.35	1200	40,50	119
Sgr-198	18:57:51.93	−28:37:08.95	15.95	480	25,70	138
Sgr-141	18:59:07.78	−29:08:15.52	16.31	540	35,60	118
Sgr-62	18:59:13.41	−31:12:39.45	16.16	480	35,60	157
Sgr-182	19:00:50.31	−29:04:53.46	17.41	1200	35,50	117
Sgr-136	19:00:53.93	−29:28:38.09	15.68	480	45,90	155
Sgr-162	19:02:12.05	−31:29:37.94	17.40	1200	40,60	156
Sgr-215	19:04:30.07	−29:56:14.05	16.26	540	45,55	130
Sgr-225	19:05:06.80	−30:19:22.89	16.00	480	45,75	120
Sgr-333	19:07:29.65	−29:58:01.35	16.08	480	40,70	126

[a]S/N per pixel is listed both for 4500 Å and 8500 Å

includes photometric data obtained through the metallicity-sensitive SkyMapper v filter [135, 234], which is also sensitive to surface gravity when compared to photometry from the SkyMapper u filter [235]. We thereby derived metallicities and surface gravities for all of these sources using the methods described in Chiti et al. [39] and identified likely metal-poor giants ([Fe/H] < -2.0 and $\log g < 3.0$) for observations. We note that the photometric metallicities for these stars had large uncertainties (~ 0.75 dex) due to the large uncertainties on the SkyMapper u and v photometry at the magnitudes ($g \sim 15.5$ to $g \sim 17.5$) of these stars. As a result, we regarded these metallicity and surface gravity cuts effectively qualitative selection criteria.

To increase the likelihood of membership, we selected the subset of these metal-poor giants with *Gaia* DR2 proper motions [111, 112] near the systemic proper motion of the Sagittarius dSph. The proper motion ranges of $-4.2\,\mathrm{mas/yr} < \mu_\alpha < -1.90\,\mathrm{mas/yr}$ and $-2.15\,\mathrm{mas/yr} < \mu_\delta < -0.85\,\mathrm{mas/yr}$ were used to select likely members for the first night of observations. These criteria were narrowed to $-3.6\,\mathrm{mas/yr} < \mu_\alpha < -2.70\,\mathrm{mas/yr}$ and $-1.6\,\mathrm{mas/yr} < \mu_\delta < -1.2\,\mathrm{mas/yr}$ on subsequent nights to ensure a purer sample of members, since a number of non-members were observed near the bounds of our original proper motion cut. We then generated a color-magnitude diagram of these remaining candidates using SkyMapper g and i photometry. We chose to observe candidates that were within $(g-i) \pm 0.30$ of a 10 Gyr, [Fe/H] $= -2.0$ isochrone from the Dartmouth Stellar Evolution Database [10] placed at the distance modulus of the Sagittarius dSph (16.97; Kunder and Chaboyer 376). A color-magnitude diagram of stars fulfilling these selection criteria is shown in Figure 7-1.

We obtained spectra of 37 of these metal-poor candidate members using the Magellan Echellette (MagE) Spectrograph [226] on the Magellan-Baade telescope during the nights of August 3-5, 2019. Targets were observed with the $0\farcs7$ slit and 1x1 binning, granting a resolution of $R \sim 6700$ over a broad wavelength range of 3200 Å to 10000 Å. The seeing was excellent ($\sim 0\farcs6$) throughout these observations. A spectrum of a ThAr calibration arc lamp was obtained after slewing to each target for wavelength calibration purposes. Our observations were reduced using the Carnegie

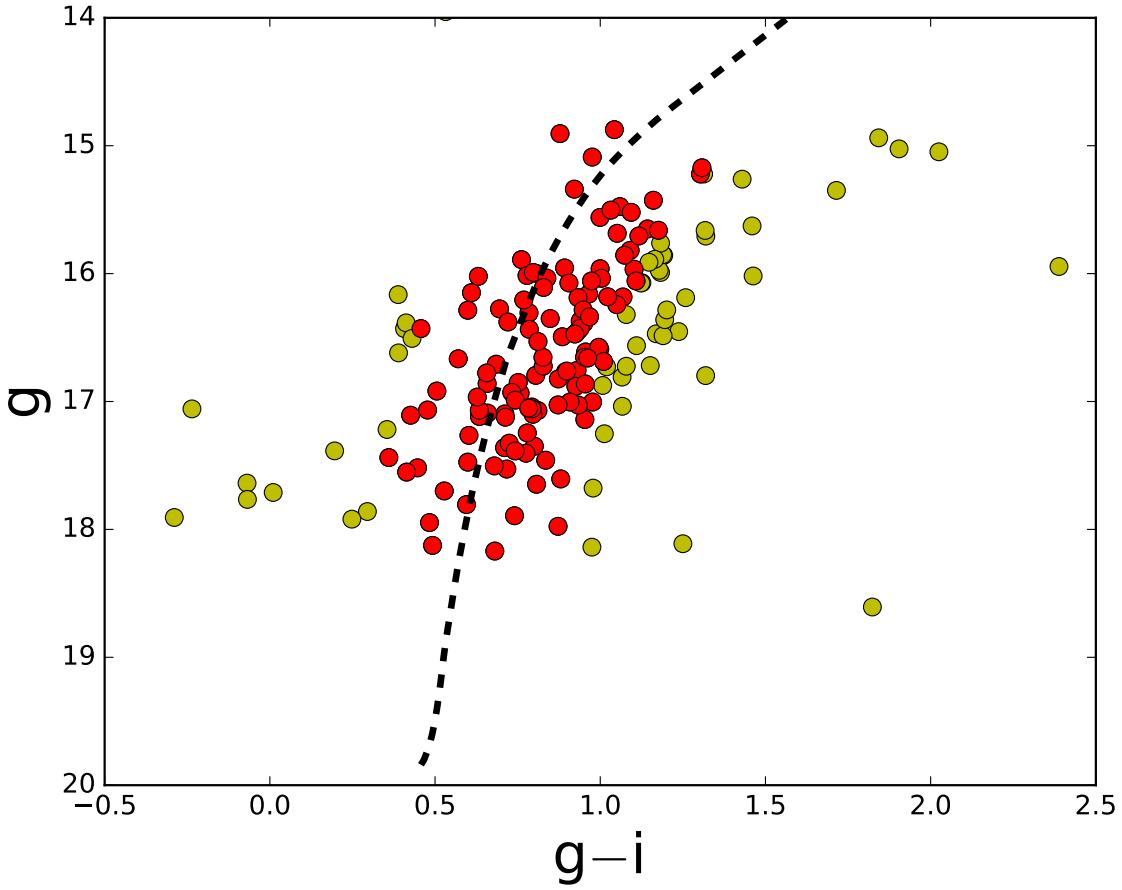

Figure 7-1 A color-magnitude diagram of all stars within three degrees of the center of the Sagittarius dSph that pass the photometric metallicity, surface gravity, and proper motions criteria listed in Section 7.2. A 10 Gyr, [Fe/H] $= -2.0$ isochrone from the Dartmouth Stellar Evolution Database [10] is over plotted for reference. Stars in red are within $(g - i) \pm 0.30$ of the isochrone, and stars in yellow are outside those bounds.

Python pipeline [196][2].

Twenty-one stars that we observed were determined to be members of the Sagittarius dSph (see Section 7.3.1). Of these members, we excluded the following from further analysis: one spectroscopic binary system and two stars with distorted Hα absorption lines. This resulted in 18 members for which we derived chemical abundances. Details of the observations of these 18 members are provided in Table 7.1.

7.3 Analysis

7.3.1 Radial Velocity Measurements

We derived radial velocities by cross-correlating our spectra with a template spectrum of the metal-poor giant HD122563 that was obtained on the second night of data collection. The rest velocity of HD122563 was assumed to be $-26.51\,\mathrm{km\,s^{-1}}$ [244], and the cross-correlation was performed over the Mg b absorption region (4900 Å to 5400 Å). We further performed a cross-correlation over the Telluric A-band absorption region (7590 Å to 7710 Å) between our spectra and a template spectrum of the hot, rapidly rotating giant HR4781 to correct for any slit mis-centering. We note that this template spectrum of HR4781 was obtained with the IMACS instrument [217], but was then smoothed to the resolution of our MagE spectra ($R \sim 6700$). We calculate heliocentric velocity corrections using the SkyCoord function in the Astropy package [139]. These methods resulted in a systematic velocity uncertainty of $\sim 3\,\mathrm{km\,s^{-1}}$, as determined by repeat observations of other dwarf galaxy stars in this observing mode (Chiti et al. 2020, subm.). Table 7.1 lists our final velocity measurements.

We used these radial velocity measurements to determine whether the stars in our sample were members of the Sagittarius dSph. The known stars in the bulge of the Sagittarius dSph display a systemic velocity of $141\,\mathrm{km\,s^{-1}}$ and a velocity dispersion of $9.6\,\mathrm{km\,s^{-1}}$ [371]. We find that the majority of our targets indeed lie within three times the velocity dispersion of this systemic velocity ($111\,\mathrm{km\,s^{-1}}$ to $171\,\mathrm{km\,s^{-1}}$). We

[2]https://code.obs.carnegiescience.edu/mage-pipeline

identify those stars as members and classify the rest as nonmembers (see Figure 7-2). The uncertainties in our velocity measurements are roughly equal to the systematic uncertainty ($\sim 3\,\mathrm{km\,s^{-1}}$), which is small relative to the velocity dispersion assumed for the Sagittarius dSph.

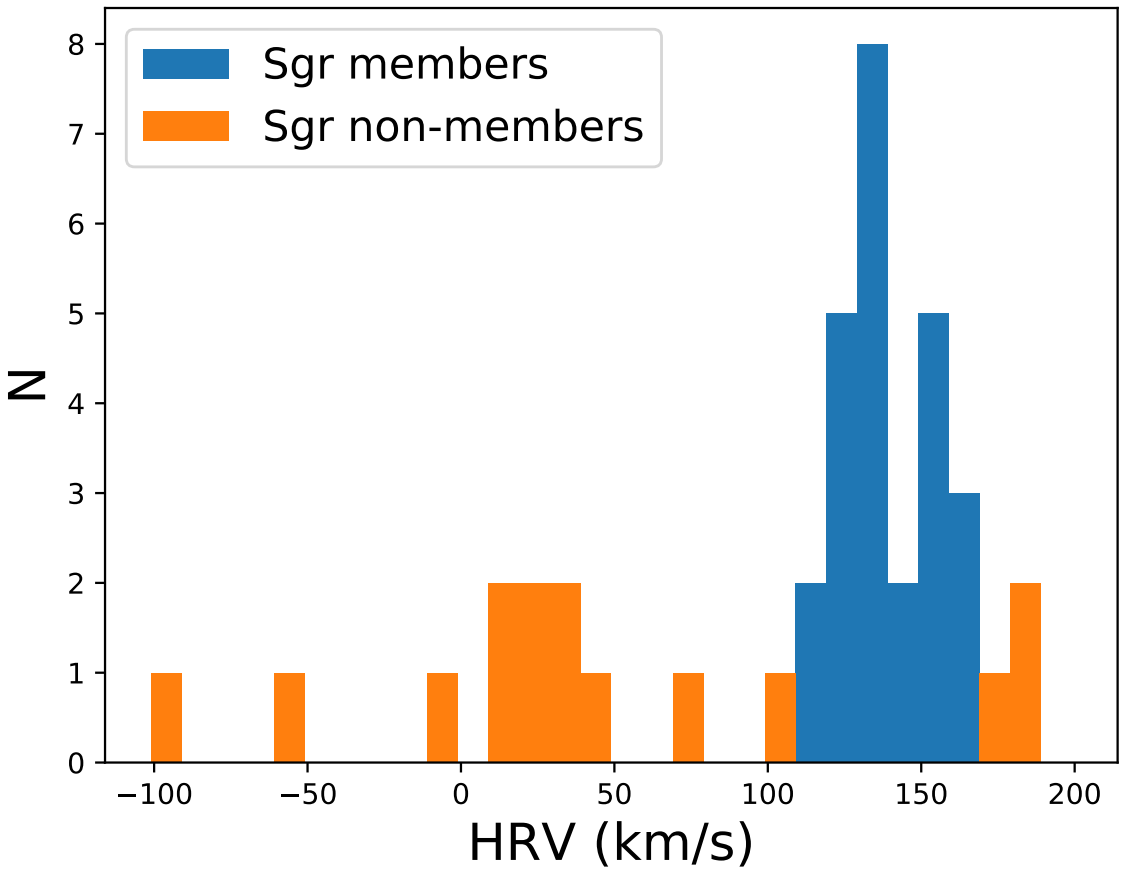

Figure 7-2 Histogram of the heliocentric radial velocities of stars in our sample. The blue portion of the histogram represents the stars that we classify as members of the Sagittarius dSph, as determined by restricting radial velocity values between $111\,\mathrm{km\,s^{-1}}$ and $171\,\mathrm{km\,s^{-1}}$.

7.3.2 Stellar Parameters

We closely follow the methodology presented in Chiti and Frebel [137] to derive the stellar parameters (T_{eff}, $\log g$) of the stars in our sample. Namely, we matched the SkyMapper $g - i$ colors of our stars to those colors in a 10 Gyr, [Fe/H] $= -2.0$ isochrone from the MESA Isochrones & Stellar Tracks database [14, 15, 40, 41, 42, 60]

and retrieved the corresponding stellar parameters. These colors were de-reddened following Wolf et al. [9] using maps from Schlegel et al. [63]. As reported in Chiti and Frebel [137], applying this method on the sample of metal-poor Sagittarius dSph stars with already known stellar parameters derived from high-resolution spectroscopy in Hansen et al. [57] results in stellar parameters that are in good agreement with those spectroscopic stellar parameters and thus validates this approach. With our particular choice of isochrone, this method, on average, leads to a marginally larger $T_{\rm eff}$ of 47 K and $\log g$ of 0.4 dex than those reported in Hansen et al. [57]. We note that these stellar parameter estimates are relatively insensitive to the assumed metallicity of the isochrone. Increasing metallicity of the isochrone by 0.5 dex decreases the derived $T_{\rm eff}$ by only ~ 40 K.

The standard deviation of the $T_{\rm eff}$ residuals with respect to Hansen et al. [57] is 170 K. We adopt this value, subtracted in quadrature by the $T_{\rm eff}$ measurement uncertainty of 50 K in Hansen et al. [57], as our systematic uncertainty in $T_{\rm eff}$. Propagating this systematic uncertainty to $\log g$ results in a $\log g$ systematic uncertainty of 0.25 dex. Random uncertainties were derived by propagating photometric uncertainties in the public SkyMapper photometry to these stellar parameter derivations. The total uncertainty was taken as the quadrature sum of the systematic and random uncertainties.

7.3.3 Metallicity Analysis

We derived metallicities for the stars in our sample using independently the Ca II K absorption feature ($\sim$3933.7 Å), the Mg b absorption region ($\sim$5180 Å), and the calcium triplet absorption features ($\sim$ 8500 Å). The methods for deriving each of these metallicities are described below. The metallicities we derive are shown in Table 7.2, and sample spectra are shown in Figure 7-3. A histogram of our final metallicities is shown in Figure 7-5.

7.3.3.1 Ca II K line

We follow the calibration of Beers et al. [52] to derive metallicities from the Ca II K absorption line at ~ 3933.7 Å. This calibration requires $B-V$ colors and a measure of the strength of the Ca II line known as the KP index, which is an estimate of the pseudo-equivalent width of the feature. We derive the KP index following exactly the procedures presented in Beers et al. [52]. The $B-V$ colors of these stars were derived by first transforming SkyMapper g and r photometry to the Pan-STARRS system using a sample photometry of F, G, and K stellar type stars from the SkyMapper website [384]. We then used the transformations in Tonry et al. [382] to convert from Pan-STARRS g and r photometry to $B-V$ colors.

We note that we excluded Ca II K metallicity estimates if the procedure returned a value of [Fe/H] > -1.5. This is the metallicity regime where the Ca II K line saturates (see top left panel of Figure 7-3) and no longer produces accurate metallicity estimates. This led to removal of metallicities of three stars: Sgr-62, Sgr-136, and Sgr-141. Finally, we note that the Beers et al. [52] calibration assumes a [Ca/Fe] $= 0.4$ when [Fe/H], given that this is a calibration for Milky Way halo stars. We assume the same for these Sagittarius dSph stars, given the general agreement in the [Ca/Fe] values between halo stars and Sagittarius dSph metal-poor stars found by Hansen et al. [57]. Uncertainties in the metallicities of these stars were derived as the quadrature sum of the systematic uncertainty provided in Beers et al. [52], and the random uncertainties propagated by shifting the continuum and from propagating the uncertainty in the $B-V$ color.

7.3.3.2 Mg b line triplet lines

Metallicities were derived from the Mg b line region (5150 Åto 5190 Å) via standard spectral synthesis techniques, following Chiti and Frebel [137]. We do note that several previous studies have used the Mg b region to derive metallicities of stars in dwarf galaxies [401, 402, 1]. Specifically, synthetic spectra were generated using the 2017 version of the MOOG 1D LTE radiative transfer code [198, 199], the Kurucz

model atmospheres [200], and a linelist combining data from Kurucz [252] and Sneden et al. [206, 153, 253]. The [Mg/Fe] in these syntheses was set as [Mg/Fe] = 0.3, matching the general [α/Fe] trend for metal-poor stars in Sagittarius [57]. These syntheses were performed within the SMH software [197], which enabled the visual identification of the synthetic spectrum that best matched each observed spectrum. The [Fe/H] of the best matching synthetic spectrum was taken as the [Fe/H] of the observed spectrum.

The random uncertainty from the fitting procedure was assumed to be the difference in [Fe/H] when requiring to encompass the noise in the observed spectrum with synthetic spectra. The systematic uncertainty was determined by re-deriving metallicities after shifting the $T_{\rm eff}$ and $\log g$ values by their 1σ uncertainties. The total uncertainty was assumed as the quadrature sum of the random and systematic uncertainties. We note that additional uncertainty from variations in the [Mg/Fe] is likely far less than our total uncertainties (~ 0.35 dex). Sagittarius stars with [Fe/H] < -1.5 in Hansen et al. [57] have a scatter of ~ 0.15 dex in their [Ca/Fe]. Since Mg, like Ca, is an α-element, this suggests a similarly low scatter in the Mg abundances relative to our uncertainties.

7.3.3.3 Calcium triplet lines

We derived metallicities from the calcium triplet lines using the calibration of Carrera et al. [249]. This calibration relates the metallicity of a star to its absolute V magnitude and the sum of the equivalent widths of the three calcium triplet lines at 8498 Å, 8542 Å, and 8662 Å. We calculated these equivalent widths by fitting the Voigt1D model in the python astropy package [139] to each line. Absolute V magnitudes were derived following the color transformations described in Section 7.3.3.1, along with an updated distance modulus of the Sagittarius dSph (17.10, Ferguson and Strigari 61). Random uncertainties were determined by re-deriving the metallicity after varying the continuum by 1σ, as determined by the signal-to-noise of the spectrum. Systematic uncertainties were assumed to be 0.17 dex following Carrera et al. [249]. Total uncertainties were derived as the quadrature sum of the random

and systematic uncertainties.

7.3.3.4 Final metallicity values & validation

We derived final metallicity values by taking the average of the three metallicity estimators (see Sections 7.3.3.1 to 7.3.3.3), weighted by the inverse square of their uncertainties. The final uncertainty was taken as the uncertainty in the weighted average. Final metallicities and uncertainties are presented in Table 7.2.

To validate our metallicities, we also derived metallicities for four metal-poor giant stars (HD21581, HD216143, HD122563, and CS22892-052) that we observed with the same MagE observational setup. We obtained metallicities for these stars following the aforementioned methods, and obtained the following values: [Fe/H] = -1.60 ± 0.15 for HD21581, [Fe/H] = -2.25 ± 0.15 for HD216143, [Fe/H] = -2.67 ± 0.13 for HD122563, and [Fe/H] = -3.01 ± 0.14 for CS22892-052. These metallicities all agree within 1σ of the literature metallicities of these stars, which are [Fe/H] = -1.70 for HD21581 [17], [Fe/H] = -2.15 for HD216143 [58], [Fe/H] = -2.79 for HD122563 [59], and [Fe/H] = -3.08 for CS22892-052 [59].

In Figure 7-3, we provide a visual comparison of the spectra of three of these metal-poor giants to selected Sagittarius members with similar stellar parameters and metallicities. As can be seen, the absorption lines of HD21581 and CS22892-052 are slightly weaker than Sgr-136 and Sgr-180, respectively, despite their similar metallicities. This is due to HD21581 and CS22892-052 being on average $\sim 300\,\mathrm{K}$ warmer than the two Sagittarius members. HD216143 and Sgr-333 have nearly identical absorption features and effective temperatures (4600 K vs. 4546 K), validating our derivation of similar metallicities ([Fe/H] = -2.24 vs. [Fe/H] = -2.10) for both stars.

7.3.4 Carbon Abundances

We also derived a carbon abundance ([C/Fe]) for each of our red giants from the CH G bandhead region (4275 Åto 4320 Å) using standard spectral synthesis techniques,

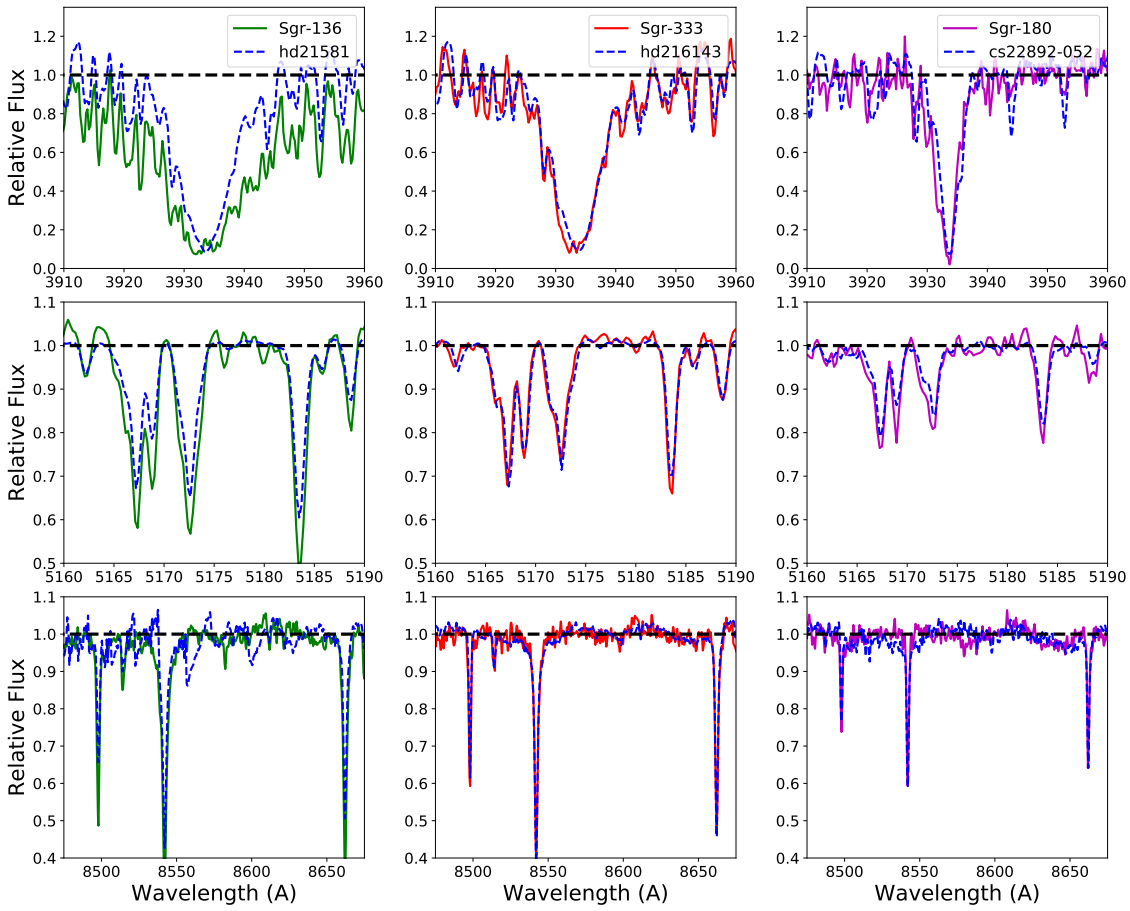

Figure 7-3 Sample spectra over the Ca II K line at 3933.7 Å(top panels), the Mg b line region at $\sim$ 5150 Å(middle panels), and the calcium triplet lines around $\sim$8550 Å(bottom panels). MagE spectra of Sgr-136 ([Fe/H] = -1.69) and HD21581 ([Fe/H] = -1.56; Roederer et al. 17) are shown on the left panels, Sgr-333 ([Fe/H] = -2.10) and HD216143 ([Fe/H] = -2.24; Boeche and Grebel 58) on the middle panels, and Sgr-180 ([Fe/H] = -3.08) and CS22892-052 ([Fe/H] = -3.08; Frebel et al. 59) on the right panels. HD21581 and CS22892-052 have slightly weaker absorption features than Sgr-136 and Sgr-180 due to their higher ($\sim$ 300 K) effective temperatures. HD216143 and Sgr-333 have absorption features of similar strengths, due to their proximate metallicities and effective temperatures.

analogous to our derivation of metallicities from the Mg b line region in Section 7.3.3.2. The line list for these syntheses included CH molecular line data from Masseron et al. [53] in addition to the sources listed in Section 7.3.3.2. The [C/Fe] was varied to find the best fitting synthetic spectrum while the [Fe/H] was set to each star's final metallicity value. The random uncertainty in [C/Fe] was taken as the variation in [C/Fe] needed to encompass the noise in the G band region. The systematic uncertainties were determined by re-deriving [C/Fe] after varying $T_{\rm eff}$, $\log g$, and the metallicity of each star by their 1σ uncertainties. All these sources of uncertainty were added in quadrature to derive a total uncertainty. Examples of our carbon syntheses are shown in Figure 7-4. In Table 7.2, we present our derived carbon abundances in addition to corrected carbon abundances that account for the depletion of the surface carbon abundance as stars ascend the red giant branch [8].

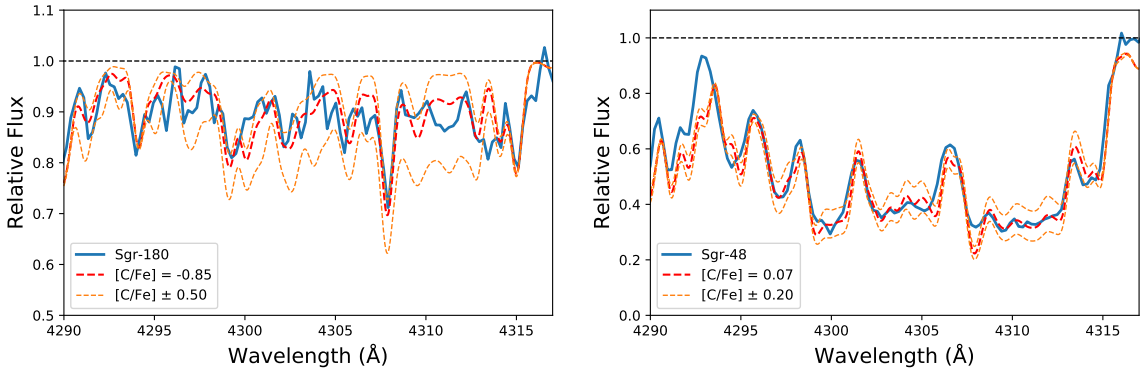

Figure 7-4 Left: The CH G bandhead region of our most metal-poor star, Sgr-180 (blue), compared to its best-matching synthetic spectra (red). Synthetic spectra with carbon abundances offset by ±0.50 are shown as dashed orange lines, and the continuum is marked as a dashed black line to guide the eye. Right: The same plot but with our most carbon-enhanced star, Sgr-48, shown in blue. The best matching synthetic spectrum is again shown in red, and synthetic spectra with carbon abundances offset by ±0.20 are shown as dashed orange lines.

7.4 Results and Conclusions

We present the metallicities and carbon abundances of eighteen red giant stars in the Sagittarius dSph that were identified as metal-poor candidates with publicly available,

Table 7.2. Additional stellar parameters and chemical abundances of stars in the Sagittarius dSph

Name	$T_{\rm eff}$ (K)	$\log g$ (dex)	[Fe/H]$_{\rm Mg}$ (dex)	[Fe/H]$_{\rm CaT}$ (dex)	[Fe/H]$_{\rm CaIIK}$ (dex)	[Fe/H]$_{\rm final}$ (dex)	[C/Fe] (dex)	[C/Fe]$_{\rm corrected}$ [a] (dex)
Sgr-62	4530 ± 170	1.11 ± 0.30	-1.40 ± 0.36	-1.49 ± 0.22	···	-1.47 ± 0.19	-0.53 ± 0.31	0.01 ± 0.31
Sgr-136	4400 ± 160	0.88 ± 0.25	-1.61 ± 0.37	-1.71 ± 0.17	···	-1.69 ± 0.15	-0.73 ± 0.30	-0.08 ± 0.30
Sgr-141	4630 ± 160	1.30 ± 0.25	-1.89 ± 0.33	-1.74 ± 0.18	···	-1.77 ± 0.16	-0.51 ± 0.33	0.04 ± 0.33
Sgr-157	5110 ± 180	2.26 ± 0.30	-2.00 ± 0.39	-1.80 ± 0.20	-1.64 ± 0.43	-1.81 ± 0.16	-0.37 ± 0.34	-0.36 ± 0.34
Sgr-162	4660 ± 200	1.37 ± 0.35	-1.96 ± 0.41	-1.79 ± 0.24	-1.66 ± 0.59	-1.81 ± 0.20	-0.36 ± 0.39	0.13 ± 0.39
Sgr-265	4450 ± 160	0.97 ± 0.25	-1.88 ± 0.37	-1.73 ± 0.20	-2.05 ± 0.32	-1.83 ± 0.15	-0.63 ± 0.31	0.02 ± 0.31
Sgr-225	4520 ± 160	1.09 ± 0.25	-2.02 ± 0.35	-1.85 ± 0.18	-1.52 ± 0.43	-1.84 ± 0.15	-0.72 ± 0.29	-0.08 ± 0.29
Sgr-48	4310 ± 160	0.69 ± 0.25	-2.02 ± 0.37	-1.81 ± 0.18	-2.09 ± 0.25	-1.92 ± 0.14	0.07 ± 0.21	0.56 ± 0.21
Sgr-182	5140 ± 170	2.33 ± 0.25	-2.14 ± 0.35	-1.95 ± 0.23	-1.76 ± 0.37	-1.95 ± 0.17	-0.44 ± 0.38	-0.43 ± 0.38
Sgr-91	4680 ± 160	1.40 ± 0.25	-2.12 ± 0.35	-1.98 ± 0.19	-1.94 ± 0.43	-2.00 ± 0.16	-0.41 ± 0.31	0.12 ± 0.31
Sgr-298	5170 ± 190	2.40 ± 0.30	-2.15 ± 0.33	-2.03 ± 0.20	-1.96 ± 0.36	-2.04 ± 0.15	-0.18 ± 0.40	-0.17 ± 0.40
Sgr-333	4550 ± 160	1.16 ± 0.25	-2.30 ± 0.31	-2.08 ± 0.18	-1.85 ± 0.44	-2.10 ± 0.15	-0.93 ± 0.34	-0.25 ± 0.34
Sgr-300	4440 ± 160	0.95 ± 0.25	-2.17 ± 0.35	-2.12 ± 0.18	-2.33 ± 0.20	-2.21 ± 0.12	-0.65 ± 0.30	0.11 ± 0.30
Sgr-81	4870 ± 170	1.77 ± 0.25	-2.53 ± 0.34	-2.18 ± 0.23	-2.57 ± 0.29	-2.37 ± 0.16	0.26 ± 0.29	0.48 ± 0.29
Sgr-198	4450 ± 160	0.97 ± 0.25	-2.45 ± 0.32	-2.40 ± 0.21	-2.59 ± 0.26	-2.47 ± 0.15	-0.98 ± 0.33	-0.20 ± 0.33
Sgr-69	4380 ± 160	0.83 ± 0.25	-2.79 ± 0.39	-2.43 ± 0.20	-2.64 ± 0.17	-2.58 ± 0.12	-0.73 ± 0.33	0.04 ± 0.33
Sgr-38	4680 ± 160	1.40 ± 0.25	-2.77 ± 0.36	-2.76 ± 0.20	-2.95 ± 0.27	-2.82 ± 0.15	-0.30 ± 0.43	0.23 ± 0.43
Sgr-180	4540 ± 160	1.14 ± 0.25	-2.98 ± 0.37	-3.07 ± 0.21	-3.13 ± 0.22	-3.08 ± 0.14	-0.85 ± 0.47	-0.11 ± 0.47
HD21581	4940[b]	2.10[b]	-1.85 ± 0.32	-1.55 ± 0.18	···	-1.60 ± 0.15	···	···
HD216143	4530[c]	1.10[c]	-2.42 ± 0.32	-2.22 ± 0.19	-2.14 ± 0.36	-2.25 ± 0.15	···	···
HD122563	4612[d]	0.85[d]	-2.70 ± 0.34	-2.60 ± 0.18	-2.78 ± 0.25	-2.67 ± 0.13	···	···
CS22892-052	4828[d]	1.35[d]	-3.11 ± 0.37	-2.91 ± 0.19	-3.12 ± 0.23	-3.01 ± 0.14	···	···

[a]Corrected for the evolutionary state of the star following Placco et al. [8].

[b]Taken from Roederer et al. [17].

[c]Taken from Boeche and Grebel [58].

[d]Taken from Frebel et al. [59].

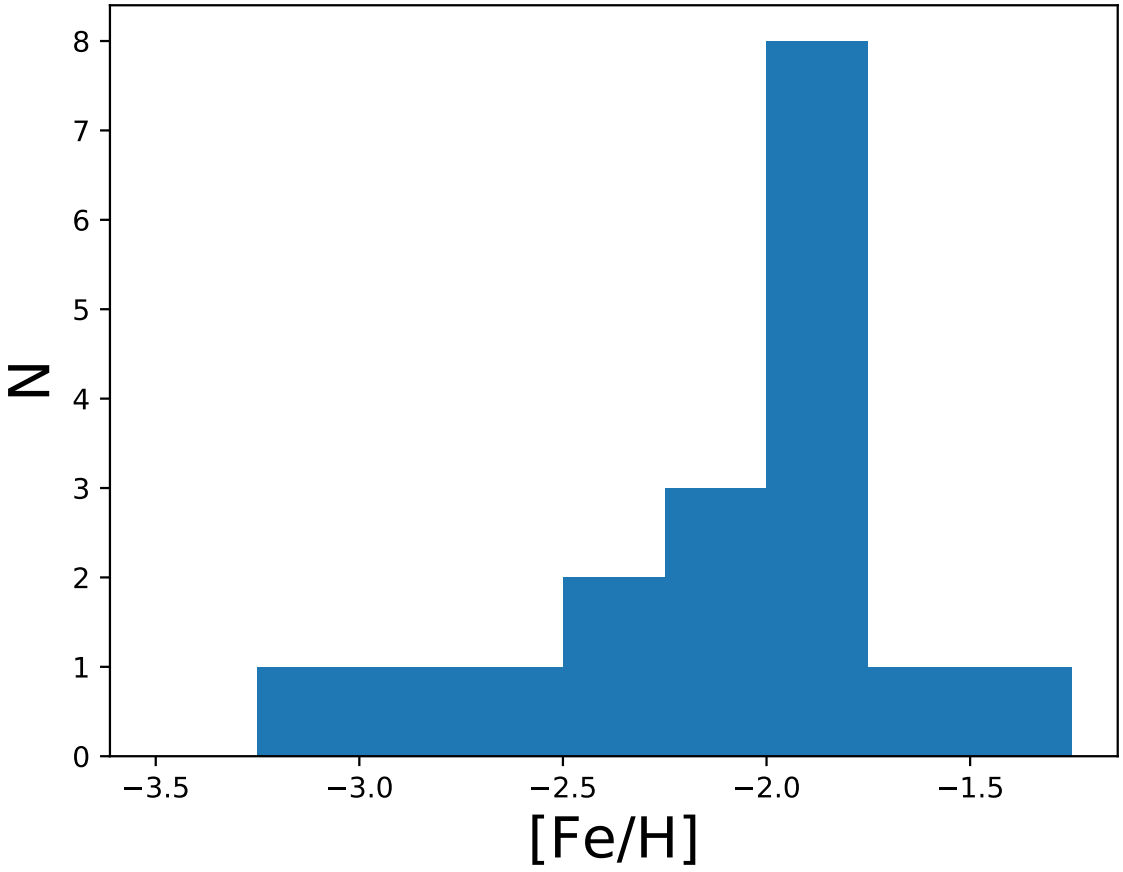

Figure 7-5 Histogram of the metallicities of our sample of 18 our newly discovered members red giant stars. The distribution peaks just above the very metal-poor regime ([Fe/H] = −2.0) with a tail extending to extremely metal-poor ([Fe/H] = −3.0) metallicities.

metallicity-sensitive photometry from SkyMapper DR1.1 [9]. Notably, eight of these stars are very metal-poor ($-3.0 < [\mathrm{Fe/H}] \leq -2.0$) and one is extremely metal-poor ($[\mathrm{Fe/H}] \leq -3.0$), more than doubling the known ~ 5 very metal-poor stars in the system (e.g., Hansen et al. 57, Chiti and Frebel 137) and identifying the first known extremely metal-poor star in the Sagittarius dSph. This result conclusively shows that even the most massive satellite dwarf spheroidal galaxy, Sagittarius, has a metallicity distribution function extending to the extremely metal-poor regime as is also seen in other, less massive dwarf spheroidal galaxies (e.g., Frebel et al. 20, Theler et al. 398).

Our detection of these very metal-poor stars in the Sagittarius dSph aligns with theoretical expectations that all galaxies should plausibly host chemically primitive stellar populations. These stars would likely be remnants from early generations of star formation (e.g., de Boer et al. 403), or could plausibly originate from smaller, more chemically primitive dwarf galaxies that were accreted onto the system, both of which are processes that should occur in the formation of larger dwarf spheroidal systems. The previous scarcity of known stars with $[\mathrm{Fe/H}] < -2.0$ in the Sagittarius dSph was then likely caused by its dominant stellar population having a peak metallicity of $[\mathrm{Fe/H}] \sim -0.5$ [375], which would render very metal-poor stars in the system relatively rare. With our newly discovered sample of very metal-poor stars, we can now investigate the early chemical evolution of this system and compare it with other galaxies.

One curious observed signature of our sample is that none of the stars can be classified as carbon-enhanced metal-poor (CEMP; $[\mathrm{C/Fe}] > 0.7$) stars (see Figure 7-6). In contrast, one prominent signature among old metal-poor stars in the Milky Way's halo is the increase of relative carbon enhancement with decreasing metallicity. Around 20% of stars in the halo are classified as CEMP stars when $[\mathrm{Fe/H}] < -2.0$, and 43% of stars are CEMP when $[\mathrm{Fe/H}] < -3.0$ [8]. Combining our sample with the sample in Hansen et al. [57] and Chiti and Frebel [137] results in 14 stars with $[\mathrm{Fe/H}] \leq -2.0$ in the Sagittarius dSph, none of which are CEMP stars. There is a 4% probability of observing no CEMP stars in a sample of 14 with $[\mathrm{Fe/H}] \leq -2.0$, if the Sagittarius dSph had the same CEMP fraction as the halo. This probability hints

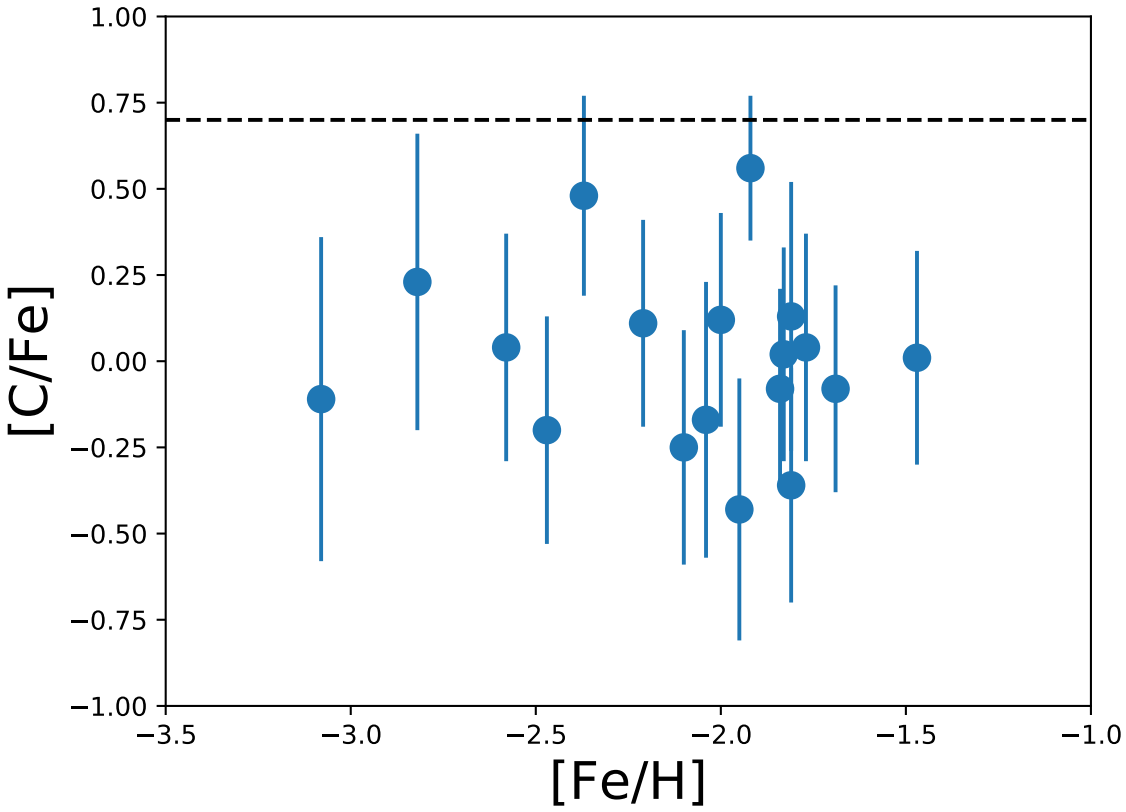

Figure 7-6 Carbon abundances as a function of [Fe/H] for stars in our sample. The plotted carbon abundances have been corrected for the evolutionary state of the star following Placco et al. [8]. The dashed line indicates a carbon enhancement of [C/Fe] = 0.7, above which value stars are defined as carbon-enhanced metal-poor (CEMP) stars.

that the Sagittarius dSph may have a lower CEMP fraction than the Milky Way halo in the very metal-poor regime.

This possible discrepancy between the CEMP fractions in the Sagittarius dSph and the Milky Way halo may hint at some dependence of early chemical evolution on the environment in which stars form. The CEMP fraction in other dwarf spheroidal galaxies also appears to be lower than the halo CEMP fraction when [Fe/H] ≤ -2.0 (e.g., Carina, Draco, Sculptor; Venn et al. 118, Kirby et al. 4), although it may again increase when [Fe/H] ≤ -3.0 (e.g., Chiti et al. 215). Further targeted studies of extremely metal-poor stars would be helpful in further investigating this trend. A similar lack of CEMP stars is observed in the Galactic bulge (e.g., Howes et al. 387, 404), also suggesting that early chemical evolution may not be universal. However,

these discrepancies do not invalidate the Milky Way halo being assembled from the accretion of smaller galaxies, as the spread in carbon abundances of stars in the Milky Way halo may originate from a variety of galaxies that assembled to form the halo.

We note for completion that metallicities derived from the SkyMapper v filter are biased high for carbon-enhanced stars, which can lead to them being excluded from our sample and thus artificially decrease any CEMP fraction [234, 39]. However, we emphasize that this selection effect should be negligible for our sample discussed here. Due to the weakening precision of the v band photometry in SkyMapper DR1.1 at the magnitudes of these stars ($g \sim 15$ to $g \sim 17.5$), our photometric metallicities had large (~ 0.75 dex) uncertainties. Any bias in the photometric metallicities of stars at the CEMP threshold of [C/Fe] = 0.7, after carbon-correction following Placco et al. 8,would have been lower than these uncertainties [39]. Accordingly, the large uncertainties in the photometric metallicities in our selection procedure would supercede much of the bias against CEMP stars. We also note that the metallicity distribution of our observed stars peaks above [Fe/H] $= -2.0$, suggesting that our selection function does select stars at higher metallicities than [Fe/H] $= -2.0$. Accordingly, this suggests that stars with [Fe/H] < -2.0 with slightly artificially higher photometric metallicities due to carbon enhancement would still have been selected for our sample. As a result, our lack of detected CEMP stars is likely independent of our target selection procedure.

At a broader level, we demonstrate that dedicated, wide-field searches for the most metal-poor stars in large dwarf galaxies are feasible using public metallicity-sensitive photometry. As shown in Figure 7-7, all of our observed Sagittarius dSph stars are notably distant from the nucleus of the system ($r_h = 0.43' \pm 0.08'$; Bellazzini et al. 371), but lie within its main body ($r_c = 224' \pm 12'$; Majewski et al. 405). Searches for the most metal-poor stars in the outskirts of dwarf spheroidal galaxies could be particularly productive, since at least some of these systems are known to have metallicity gradients (e.g., Tolstoy et al. 406). At face value, we unfortunately cannot interpret the spatial distribution of our Sagittarius dSph stars further to investigate, for instance, a metallicity gradient, given our relatively small sample of stars and

qualitative selection function. However, such work and more precise targeting of the most metal-poor stars will be possible with the improved photometric precision in future SkyMapper data releases (e.g., Onken et al. 407). At minimum, future high-resolution spectroscopy of these stars will derive their detailed chemical abundance patterns. Such work will enable comprehensive studies of the early chemical evolution and formation history of the massive systems that were accreted to form Milky Way halo.

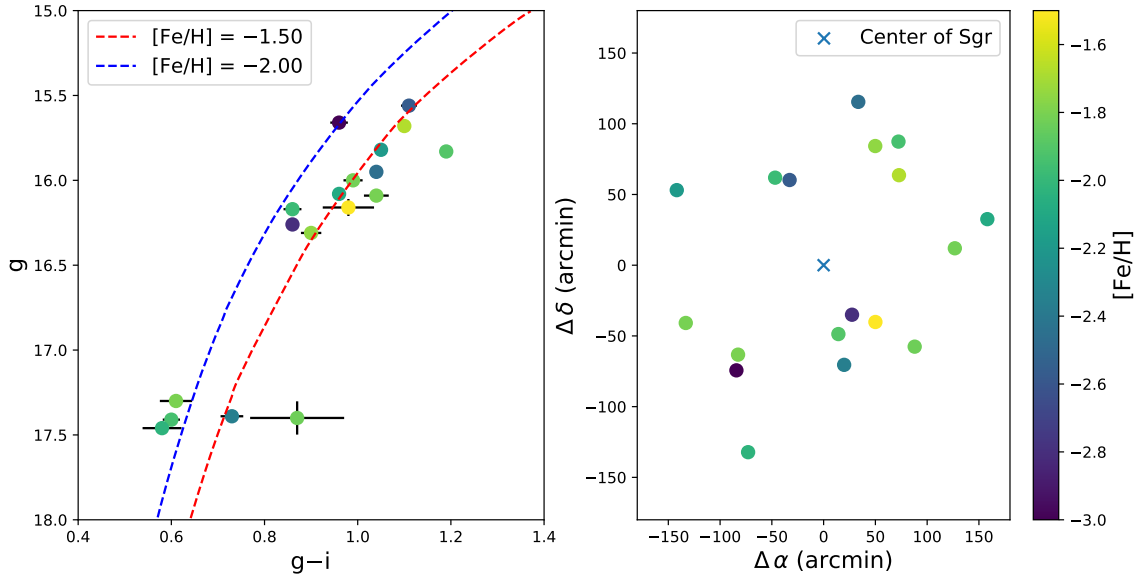

Figure 7-7 Left: Color-magnitude diagram of our observed Sagittarius stars colored by their metallicities. Two 12 Gyr isochrones with [Fe/H] = −2.0 and [Fe/H] = −1.5 from the MESA Isochrones & Stellar Tracks database [14, 15, 40, 41, 42, 60] database are overlaid at the distance modulus of the Sagittarius dSph (17.10, Ferguson and Strigari 61). Right: Position of our Sagittarius members with respect to the center of the Sagittarius dSph, which is marked with a blue cross.

Table 7.3. Velocities of objects omitted from metallicity analysis

Name	RA (h:m:s) (J2000)	DEC (d:m:s) (J2000)	g [mag]	$v_{\rm helio}$ [km s^{-1}]	Comments
Sgr-317	18:43:33.8001	−31:14:41.5383	16.02	−1	
Sgr-105	18:49:00.7118	−30:55:59.5389	15.52	181	
Sgr-87	18:49:38.4731	−30:17:13.1231	14.96	135	Has Balmer emission lines
Sgr-68	18:50:11.9385	−30:50:06.6329	16.08	10	
Sgr-134	18:50:35.179	−31:47:22.3161	15.89	33	
Sgr-179	18:51:11.3552	−28:54:55.0119	16.60	−132	
Sgr-186	18:51:57.8331	−32:18:49.8092	15.79	74	
Sgr-349	18:52:21.1407	−27:51:24.9048	16.46	−58	
Sgr-127	18:55:53.378	−32:02:01.2355	15.93	25	
Sgr-205	18:56:20.4976	−28:31:17.5376	16.18	−92	
Sgr-177	18:58:29.6478	−28:50:05.0311	15.86	29	
Sgr-249	19:01:22.094	−32:24:52.5733	17.67	177	
Sgr-148	19:01:29.765	−31:36:43.6175	17.26	45	
Sgr-7	19:01:43.3463	−29:08:25.4097	14.98	32	
Sgr-115	19:01:48.7458	−30:54:30.8118	15.96	101	
Sgr-170	19:03:29.5049	−31:01:38.7417	16.38	10	
Sgr-228	19:05:16.2722	−30:11:05.3032	15.97	132	Distorted Balmer lines
Sgr-312	19:05:55.7122	−31:48:48.3383	18.04	126	Spectroscopic binary
Sgr-335	19:07:20.3496	−29:46:41.0352	16.15	188	

Part II

Mapping the Ancient Milky Way

Chapter 8

Stellar Metallicities from SkyMapper Photometry II: Precise photometric metallicities of $\sim$280,000 giant stars with [Fe/H] < -0.75 in the Milky Way

The content of this chapter was submitted for publication in the Astrophysical Journal on October 2020.

Abstract

The Milky Way's metal-poor stars are nearby ancient objects that are used to study early chemical evolution and the assembly and structure of the Milky Way. Here we present reliable metallicities of $\sim 280,000$ stars with $-3.75 \lesssim$ [Fe/H] $\lesssim -0.75$ down to $g = 17$ derived using metallicity-sensitive photometry from the second data release (DR2) of the SkyMapper Southern Survey. We use the dependency of the flux through the SkyMapper v filter on the strength of the Ca II K absorption features, in tandem with SkyMapper u, g, i photometry, to derive photometric metallicities for these stars. We find that metallicities derived in this way compare well to metallicities derived in large-scale spectroscopic surveys, and use such comparisons to calibrate and quantify systematics as a function of location, reddening, and color. We find good agreement with metallicities from the APOGEE, LAMOST, and GALAH surveys, based on a

standard deviation of $\sigma \sim 0.25$ dex of the residuals of our photometric metallicities with respect to metallicities from those surveys. We also compare our derived photometric metallicities to metallicities presented in a number of high-resolution spectroscopic studies to validate the low metallicity end ([Fe/H] < -2.5) of our photometric metallicity determinations. In such comparisons, we find the metallicities of stars with photometric [Fe/H] < -2.5 in our catalog show no significant offset and a scatter of $\sigma \sim 0.31$ dex level relative to those in high-resolution work when considering the cooler stars ($g - i > 0.65$) in our sample. We also present an expanded catalog containing photometric metallicities of $\sim 720,000$ stars as a data table for further exploration of the metal-poor Milky Way.

8.1 Introduction

Metal-poor stars in the Milky Way and their role in exploring the early universe have been studied in great detail for several decades [353, 298, 354, 355, 408, 125, 362]. It has long been known that finding the most metal deficient ([Fe/H] < -3.0) of these stars is a challenge because of their extremely rare occurrence rate [409]. As one illustration, these stars are more likely to be found as part of the Milky Way halo component, but the halo-to-disk star ratio is $\sim 10^{-3}$ in the solar neighborhood [410]. More broadly, the number of stars roughly decreases by a factor of $\sim$10 or more for each dex decrease in metallicity [411]. For the solar neighborhood, this translates to expectations that one star with [Fe/H] $= -3.0$ may be found among every 65,000 stars, and one star with [Fe/H] $= -3.5$ among 200,000 stars. Efficient selection techniques are thus required to make large-scale progress of understanding the old halo component with sufficient statistics.

Early searches for metal-poor halo stars were based on kinematics (i.e., high proper motions) and were the first systemic discoveries of tens of stars with [Fe/H] < -3.0 [e.g., 412]. Then came the era of low resolution (R$\sim$ 400) objective-prism spectroscopic surveys of large portions of the sky based on calibrated measurements of the Ca II K line to obtain metallicities for millions of stars. The Southern HK Survey [298] and the Hamburg/ESO Survey [413, 355] resulted in thousands of candidates with [Fe/H] < -3.0. However, these candidates required medium-resolution (R$\sim 2,000$) follow-up spectra to confirm the metallicity before investing in high-resolution spec-

troscopic observations to obtain a detailed chemical abundance analysis. Beers and Christlieb [170] provide a detailed account of all these efforts, including the more recent Northern Sloan Digital Sky Survey (SDSS)[1] and the subsequent SEGUE medium-resolution spectroscopic surveys that extended the reach to fainter stars [414, 327]. For additional details on search and analysis techniques, and how the most metal-poor stars in the halo and dwarf galaxies are utilized to reconstruct the conditions of the early Galaxy, we also refer the reader to Frebel and Norris [99].

Promising recent searches for metal-poor stars are based on custom photometric filters designed to facilitate metallicity measurements of millions of stars as part of large sky surveys. A metallicity sensitive imaging filter centered near the Ca II K line that enabled metallicity measurements in the very and even extremely metal-poor regime [135] was developed for the SkyMapper Telescope and a targeted search for metal-poor stars in the Southern Sky [127]. The Southern Sky Survey has recently provided shallow data of the entire Southern sky (data release DR1.1, Wolf et al. 9), following data collection in the commissioning phase. A number of impressive findings have been achieved, including identification of the most iron-poor stars known in the halo [129, 130], large samples of metal-poor stars analyzed with medium [234] and high-resolution spectroscopy [3, 64], and a kinematic analysis [415]. In addition, exploration of the bulge revealed a population of extremely metal-poor stars [387], and spatial maps of the Southern sky as a function of metallicity (down to [Fe/H] ~ -2.0) were produced [145, 416].

A modified and tuned metallicity-sensitive filter was used to carry out the Pristine survey [125] in the Northern hemisphere with the Canada-France-Hawai'i Telescope. Samples of very and extremely metal-poor stars have also been identified in great numbers and followed-up with medium and high-resolution spectroscopy in the halo [132] and the bulge [417], in addition to the discovery of an ultra metal-poor ([Fe/H] < -4.0) star [132]. The large number of stars with photometric metallicities was also able to probe the extremely metal-poor regime of the metallicity distribution function of the Milky Way [418]. In addition to these targeted surveys for metal-poor stars,

[1] http://www.sdss.org

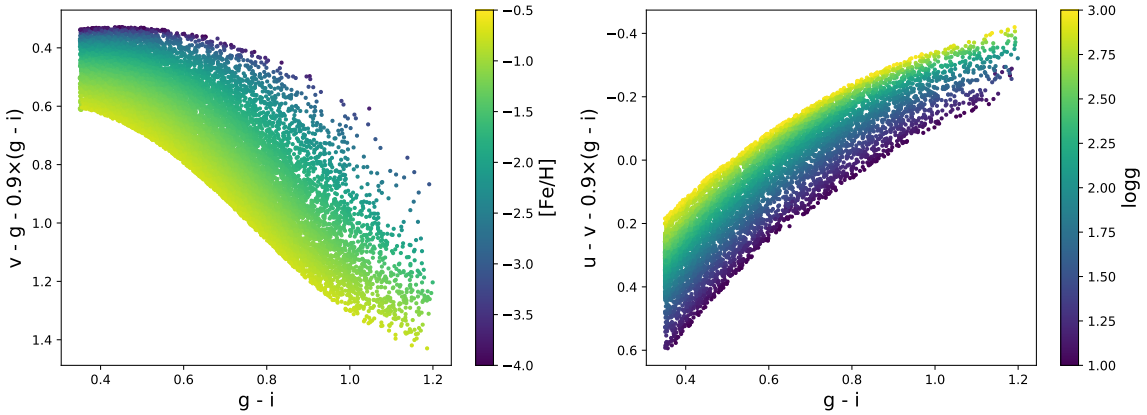

Figure 8-1 Left: Metallicity-sensitive color-color plot that was used to derive photometric metallicities (see Section 8.2.2), where each point corresponds to a star in SkyMapper DR2. Right: Surface gravity-sensitive color-color plot, where each point also corresponds to a star in SkyMapper DR2.

stellar photometric metallicities have also been determined from broadband SDSS data of the Northern hemisphere [419, 420].

Recently, Data Release 2 (DR2) of the SkyMapper Southern Sky Survey was released [113], containing $\sim$ 500 million astrophysical sources and increasing the imaging depth significantly compared to the earlier data release (DR1.1). Chiti et al. (ApJL accepted) presented a metallicity map of the Southern sky with a metallicity resolution down to [Fe/H] ~ -3.3, based on sample of $\sim$111,000 stars with photometric metallicities determined by applying techniques in Chiti et al. [39] on SkyMapper DR2 data. Here we present the full catalog of metallicities of stars from SkyMapper DR2 from which that sample was selected, composed of giant stars with $g < 17$ and $-3.75 <$ [Fe/H] < -0.75 for which we achieved metallicities with uncertainty $\lesssim 0.75$ dex. Our full catalog contains $\sim 720,000$ stars, of which $\sim 280,000$ have reliable metallicities after applying checks on the evolutionary status and metallicities of these stars using *Gaia* EDR3 data [111, 114].

8.2 Methods

Here we outline the steps involved in deriving and compiling photometric metallicities of stars in the second data release (DR2) of the SkyMapper Southern Sky Survey [407].

We first describe how we compiled the SkyMapper photometric catalog, and then we outline our derivation of photometric metallicities.

8.2.1 Compilation of photometric catalog

We queried the entire SkyMapper catalog to retrieve photometry of all sources brighter than $g = 17$ using the Virtual Observatory Access (TAP) protocol[23] with the `TapPlus` class in the `astroquery` python package [421]. To ease computing, individual queries were performed on 15° by 15° regions that, when combined, tiled the full southern hemisphere. The photometry was then de-reddened using maps from Schlegel et al. [63] with bandpass absorption coefficients listed on the SkyMapper website[4]. In all analysis, we used the petrosian magnitudes, which were denoted in the catalog by e.g., `g_petro`. We also only retained objects with the keys `flags=0` and `class_star>0.9` in the SkyMapper DR2 catalog. This initial cut ensured that our sample was composed of stars with no obvious issues e.g., blending affecting their photometry.

8.2.2 Initial derivation of photometric metallicities and stellar parameters

The photometric metallicities of our stars were derived using the methods in Chiti et al. [39], which we briefly outline here. First, we generated a grid of flux calibrated synthetic spectra over a range of stellar parameters (see Table 8.1) using the Turbospectrum software [193, 148], MARCS model atmospheres [149], and a linelist from VALD database [150, 151] supplemented by carbon molecular lines from Brooke et al. [154, 152], Masseron et al. [53], Ram et al. [155], Sneden et al. [153]. The [α/Fe] values was set to match the "standard" MARCS model atmospheres, in which [α/Fe] = 0.4 when [Fe/H] < -1.0, [α/Fe] = 0 when [Fe/H] = 0, and [α/Fe] decreases linearly between the two values when $-1 <$ [Fe/H] < 0. This behavior matches the general [α/Fe] trend in the Milky Way halo. Then, we derived a grid of synthetic photometry

[2]http://skymapper.anu.edu.au/how-to-access/
[3]http://api.skymapper.nci.org.au/public/tap/
[4]http://skymapper.anu.edu.au/filter-transformations/

Table 8.1. Stellar parameters of grid of synthetic spectra

Parameter	Minimum	Maximum	Step
λ	3000 Å	9000 Å	0.01 Å
$T_{\rm eff}$	4000 K	5700 K	100 K
$\log g$	1.0	3.0	0.5
[Fe/H]	−4.0	−0.5	0.5

by calculating the expected flux that each of our synthetic spectra would produce through each of the SkyMapper filters [135].

To derive photometric metallicities, we then matched the magnitudes in SkyMapper DR2 photometry to those in our grid of synthetic photometry and found the associated metallicity. Specifically, stars with distinct metallicities separate in a well-behaved manner in the color-color plot $v - g \times 0.9\,(g - i)$ vs $g - i$ (see Figure 8-1). Consequently, we overlaid our synthetic photometry on this plot and interpolated between the contours of constant metallicity using the `scipy.interpolate.griddata` to map each location in that plot to a metallicity. Then, simply by overlaying the observed SkyMapper photometry onto this plot, we were able to determine metallicities.

We note that the metallicity contours in the color-color plot $v - g \times 0.9\,(g - i)$ vs $g - i$ are dependent on surface gravity (see Figure 3 in Chiti et al. 39), so we iteratively determined photometric metallicities to account for this fact. As such, we first derived photometric metallicities assuming $\log g = 2.0$. Then, we derived photometric surface gravities using the fact that stars with distinct surface gravities separate in a well-behaved manner in the color-color plot $u - v \times 0.9\,(g - i)$ vs $g - i$ (see Figure 8-1). As such, we could simply replicate the procedure described for photometric metallicities to derive photometric surface gravities, using the first-pass metallicity estimates as inputs to generate contours for each star. Then, we used these photometric surface gravity measurements as inputs to adjust the photometric metallicity contours and derive updated, final photometric metallicities.

We note that stars may have stellar parameters or metallicities beyond our grid of synthetic spectra, and we outline how we account for those situations here. In the case of metallicity, stars with SkyMapper photometry consistent with [Fe/H] > -0.5 or [Fe/H] < -4.0 would be beyond the edge of our grid. To avoid the spurious presence of such stars in our catalog, we exclude stars with photometric [Fe/H] > -0.75 or photometric [Fe/H] < -3.75. We exclude all stars with $\log g$ beyond the upper edge of our grid ($\log g = 3.0$), but do retain stars with $\log g$ below the lower range of our grid ($\log g = 1.0$) as the effect on the photometric metallicity contours from $\log g$ is not hugely significant below that value. Finally, we account for stars with $T_{\rm eff}$ beyond the range of our grid by excluding stars with $g - i < 0.35$ and $g - i > 1.2$.

We derived uncertainties on our photometric metallicities by adding sources of random uncertainty and an estimate of the systematic uncertainty in quadrature. We derived random uncertainties by varying the $v - g \times 0.9\,(g - i)$ and $g - i$ colors for each star by propagating the photometric uncertainties in SkyMapper DR2. After each term was varied, photometric metallicities were re-derived and the differences between the re-derived metallicity and the original metallicity were added in quadrature to derive the total random uncertainty. The intrinsic systematic uncertainty from this method was taken as 0.16 dex, following Chiti et al. [39]. The random and systematic uncertainties were then added in quadrature for each star to derive a final uncertainty on the photometric metallicity.

8.2.3 Refinement of stellar metallicities through comparison to large-scale sky surveys

Due to the large size and broad spatial coverage of the SkyMapper catalog, it was necessary to test for systematic effects in our metallicities as a function of sky location, color, and reddening. To accomplish this, we compared our photometric metallicities to metallicities derived in three large spectroscopic surveys: APOGEE DR16 [327, 422, 423], GALAH DR3 [424], and LAMOST DR6 [425, 426, 427]. A full description of the cross-matching procedure and quality criteria that were applied to compile a

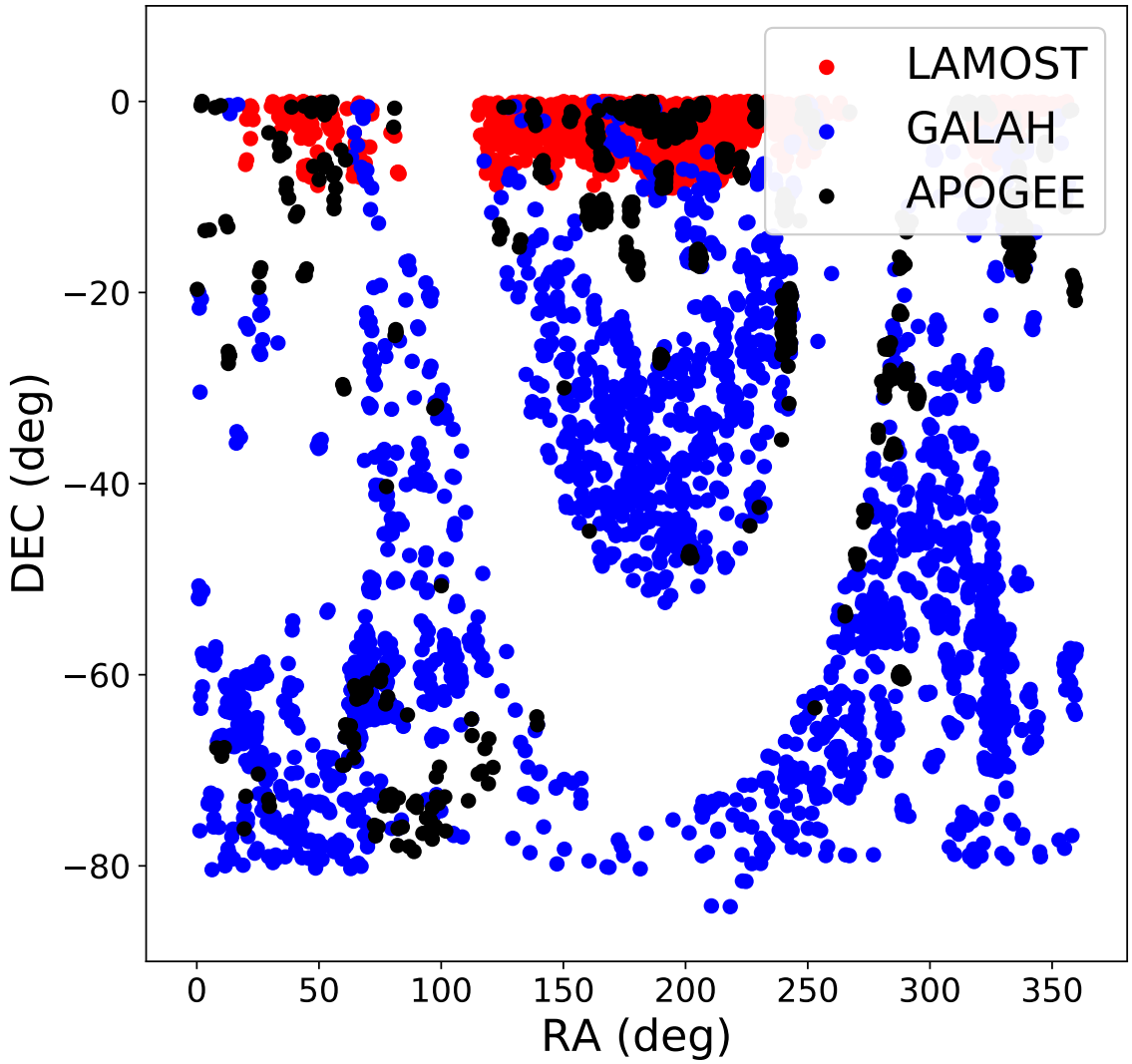

Figure 8-2 Spatial location of stars with SkyMapper photometric metallicities that also have high-quality metallicities (see Section 8.3.1 for a description) from LAMOST DR6 (red), GALAH DR3 (blue), and APOGEE DR16 (black).

comparison sample from these large spectroscopic surveys is detailed in Section 8.3.1. For the investigations in this section, we only included stars from those surveys in the metallicity range of our sample ($-3.75 <$[Fe/H] < -0.75) to ensure a consistent comparison sample.

We first checked for any trends in the residuals of our photometric metallicities with respect to the metallicities from GALAH DR3 as a function of right ascension, declination, galactic longitude (l), and galactic latitude (b). The GALAH survey

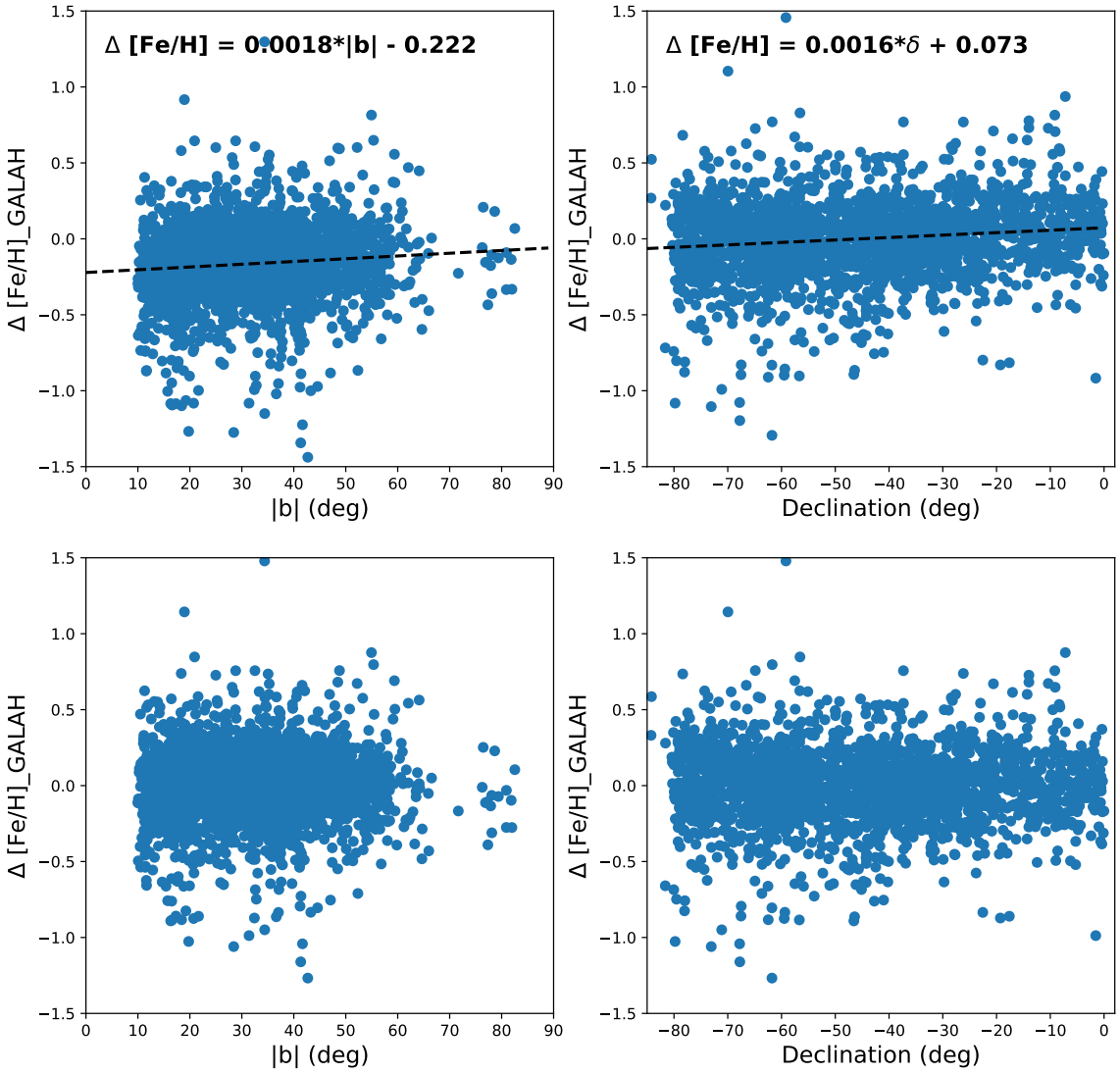

Figure 8-3 Top left: Residuals of the initial photometric metallicities derived in Section 8.2.2 with respect to metallicities of stars in GALAH DR3 as a function of galactic latitude. A line is fit to the residuals and the trend is subtracted from the initial photometric metallicity determination to account for the spatial variation of the metallicity. Top right: Same as top left, but shown as a function of declination. Bottom left: Residuals of the photometric metallicities after removing the trend as a function of galactic latitude. No further trends are apparent. Bottom right: Same as bottom left, but shown as a function of declination.

was chosen for the comparison sample due to its broad overlap in spatial coverage and magnitude range with our catalog of photometric metallicities (see Figure 8-2). We find no trends with respect to right ascension and galactic longitude, but find statistically significant trends as a function of declination and galactic latitude (see

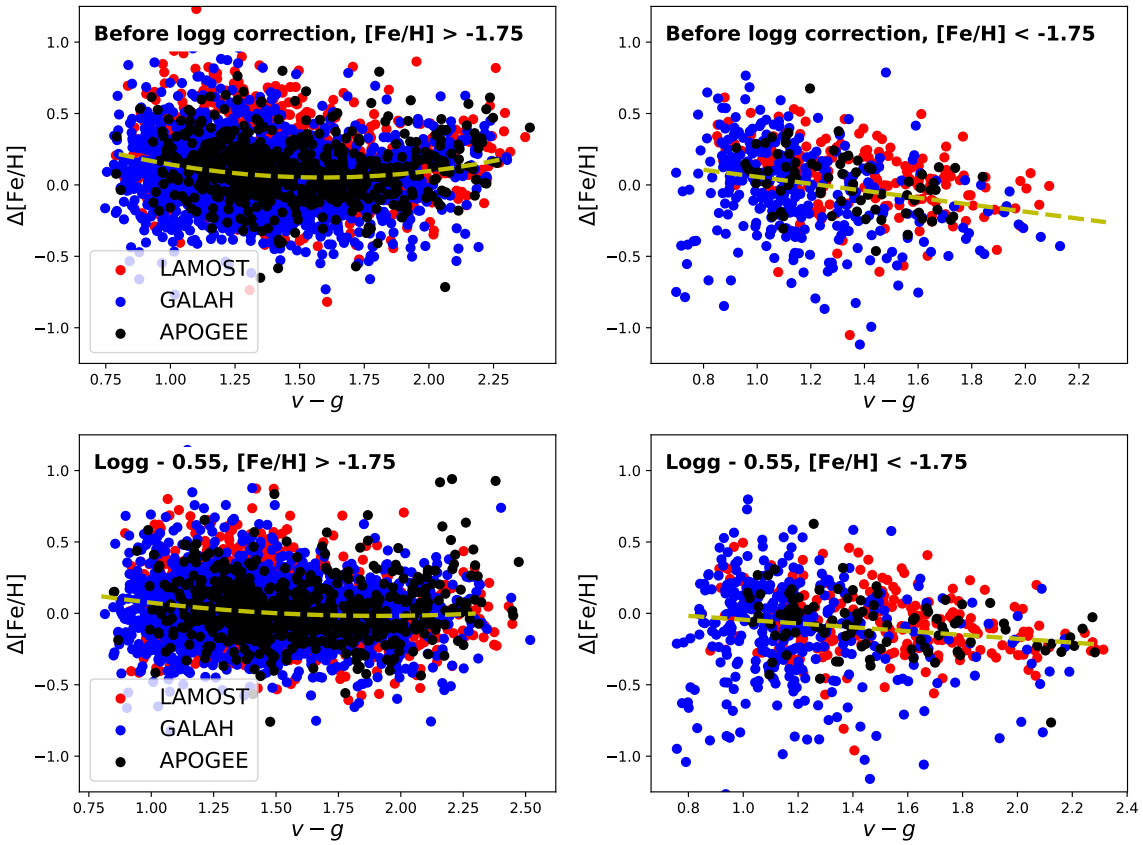

Figure 8-4 Top left: Residuals of our initial photometric metallicities derived in Section 8.2.2 with respect to high-quality (see Section 8.3.1 for a full description) metallicities of stars in LAMOST DR6 (red), GALAH DR3 (blue), and APOGEE DR16 (black) as a function of the $v-g$ color for stars with photometric metallicities [Fe/H] > -1.75. A clear quadratic trend is apparently in the residuals. Note that the residuals with respect to each survey have been slightly adjusted to account for zero-point offsets in metallicities. Top right: Same as left, but residuals are shown for stars with photometric [Fe/H] < -1.75 for which a slightly different trend is apparent. Bottom left and right: Same as top panels, but using photometric metallicities that were calculated after decreasing the photometric log g by 0.55 dex to bring our surface gravity scale in agreement with that in Ezzeddine et al. [62] and Ou et al., in prep. Only negligible trends in the residual metallicities exist after the surface gravity correction.

Figure 8-3). The trend with respect to declination likely arises from residual effects on the photometry from the airmass. Similarly, the trend with respect to galactic latitude likely arises from residual effects of reddening on the photometry, which would become more notable at lower galactic latitudes. We fit the trends in the top panels of Figure 8-3 with the displayed linear equations and subtracted the trends from our metallicities to account for these systematic effects.

We then investigated the behavior of the metallicity residuals as a function of the metallicity-sensitive color $v - g$ to calibrate for possible imperfections in our grid of synthetic photometry. We used LAMOST, GALAH, and APOGEE metallicities as comparison samples to investigate such effects. We find that the residuals of the photometric metallicities with respect to metallicities in those surveys show systematic trends with respect to the $v - g$ color (see Figure 8-4), suggesting slight imperfections in our method of deriving metallicities. We alleviated this imperfection by reducing our photometric surface gravities by 0.55 dex before deriving final photometric metallicities. This adjustment to the surface gravities reduces these systematic trends (see bottom panels of Figure 8-4) and also brings our surface gravity scale in agreement to that used in large high-resolution spectroscopic studies of metal-poor stars (e.g., Ezzeddine et al. 62).

We further find no strong systematics in the residuals of our photometric metallicities with respect to metallicities from GALAH DR3 as a function of reddening values from Schlegel et al. [63] out to E(B−V) ~ 0.35. This is shown in Figure 8-5.

8.2.4 Distance-based pruning using *Gaia* EDR3

We performed additional tests using *Gaia* EDR3 data [111, 114] to flag two cases of contaminants in our catalog. First, while we aim for our catalog to be limited to giant stars by limiting to photometric surface gravities $\log g < 3.0$, there may still be main-sequence interlopers due to e.g., stars with high uncertainties on their $\log g$ values. Second, given the large number of stars in the Milky Way in the metallicity regime right above our sample ($-0.75 <$ [Fe/H] < 0.0), it is possible for some stars in that metallicity regime to contaminate the more metal-rich end ([Fe/H] $\gtrsim -1.25$) of our sample. We thus performed two checks to identify such stars in our catalog.

We first cross-matched our sample with Bailer-Jones et al. [115] to compile their photogeometric distances. We then derived a distance modulus and absolute magnitude for each star from these distances to generate a color-magnitude diagram of our entire sample of stars. We identified stars that had a 84% percentile value in their distance posterior that led to absolute SkyMapper g magnitude < 5.0 as plau-

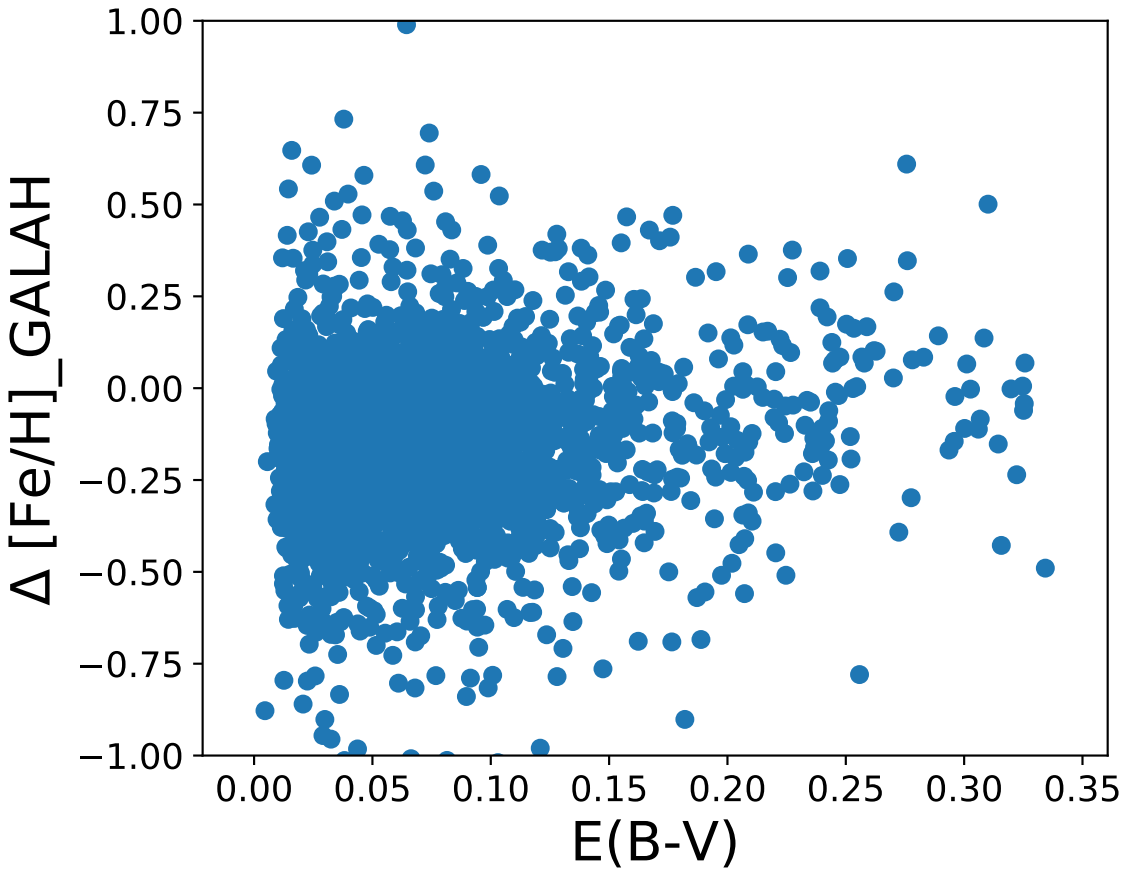

Figure 8-5 Residuals of the final photometric metallicities with respect to metallicities from GALAH DR3 shown as a function of the reddening values from Schlegel et al. [63]. No strong systematics appear as a function of reddening value out to E(B−V) ~ 0.35, beyond an offset with metallicities in GALAH DR3.

sible main sequence interlopers, since such magnitudes easily exclude stars from the giant branch (see Figure 8-6). Further, we then overlaid a Dartmouth isochrone [10] with [Fe/H] $= -0.75$, 10 Gyr on our color-magnitude diagram to identify plausible metal-rich stars in our catalog. We identified stars that had a 84% percentile in their distance posterior that placed them red-ward of the isochrone and that had photometric [Fe/H] > -2.0 as plausible metal-rich interlopers. Stars that satisfy either of these criteria have `flag_msmr = 1` in our catalog (see Table 8.2).

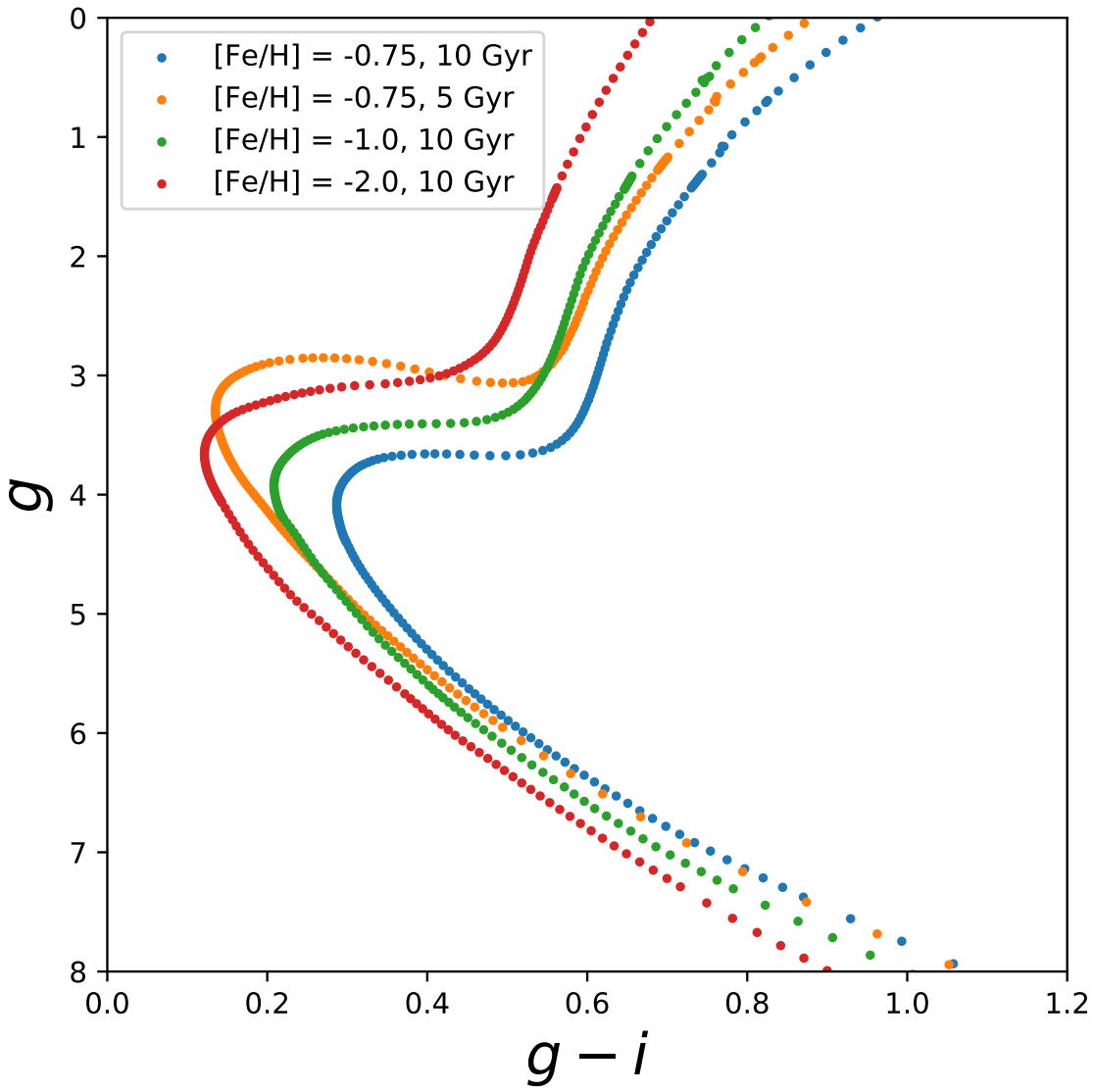

Figure 8-6 Dartmouth isochrones of [Fe/H] $= -0.75, -1.0$, and -2.0 plotted with SkyMapper $g - i$ color and absolute g magnitude. We flag stars in our sample that have absolute SkyMapper $g > 5.0$ or that are redward of the [Fe/H] $= -0.5$, 10 Gyr isochrone as plausible main-sequence or metal-rich contaminants in our sample (see Section 8.2.4). We show the [Fe/H] $= -0.75$ isochrone with two ages for illustrative purposes.

8.2.5 Description of final metallicity catalog

Our full catalog of photometric metallicities is composed of 728,712 stars, after the implementation of a number of cuts for quality control purposes that we briefly describe here. First, we applied an initial photometric quality cut, as outlined in Section 8.2.1.

Table 8.2. Photometric metallicities of stars in SkyMapper DR2

RA (deg) (J2000)	DEC (deg) (J2000)	g [mag]	i [mag]	[Fe/H] [dex]	$\sigma_{\rm [Fe/H]}$ [dex]	*Gaia* DR2 source ID	$\rm flag_{msmr}$
10.46886	−12.648856	10.35	9.55	−1.05	0.22	2376821329509745152	1.0
11.33971	−13.854287	10.38	9.60	−1.30	0.25	2375707631605778560	0.0
12.850476	−10.422958	10.38	9.63	−1.12	0.19	2473618420505263232	1.0
12.709095	−13.133477	10.73	9.97	−1.39	0.26	2376214300308134784	0.0
12.501912	−13.469329	10.83	10.32	−0.97	0.42	2372823990562608256	1.0

Note. — Table 8.2 is published in its entirety in the machine-readable format. A portion is shown here for guidance regarding its form and content.

Second, to ensure a basic quality of our compiled photometric metallicities, we excluded stars with a random uncertainty in their photometric metallicity (e.g., the propagated uncertainty from the photometry) of ≥ 0.75 dex. Third, we applied cuts discussed in Section 8.2.2 to avoid keeping stars with stellar parameters near the edge of our grid of photometry. Fourth, we excluded stars at galactic latitudes $|b| < 10^{\circ}$ or with E(B−V) > 0.35 to excise regions of extreme reddening. This ultimately resulted in our final sample of stars, which we refer to as our catalog in the following discussions. The distribution of magnitudes and metallicity uncertainties of our catalog are shown in Figure 8-7. Our catalog is shown in Table 8.2, which is published in its entirety in machine-readable format. Of the 728,712 stars in our catalog, 282,351 stars pass the checks in Section 8.2.4.

8.3 Validation

8.3.1 Comparison to Large Spectroscopic surveys

Due to the large size of our dataset and sky coverage, there is significant overlap with several large spectroscopic surveys. To test the validity of our metallicities, for stars in common, we compared our photometric metallicities with metallicities presented in LAMOST DR6 [425, 426, 427], GALAH DR3 [424], and APOGEE DR16

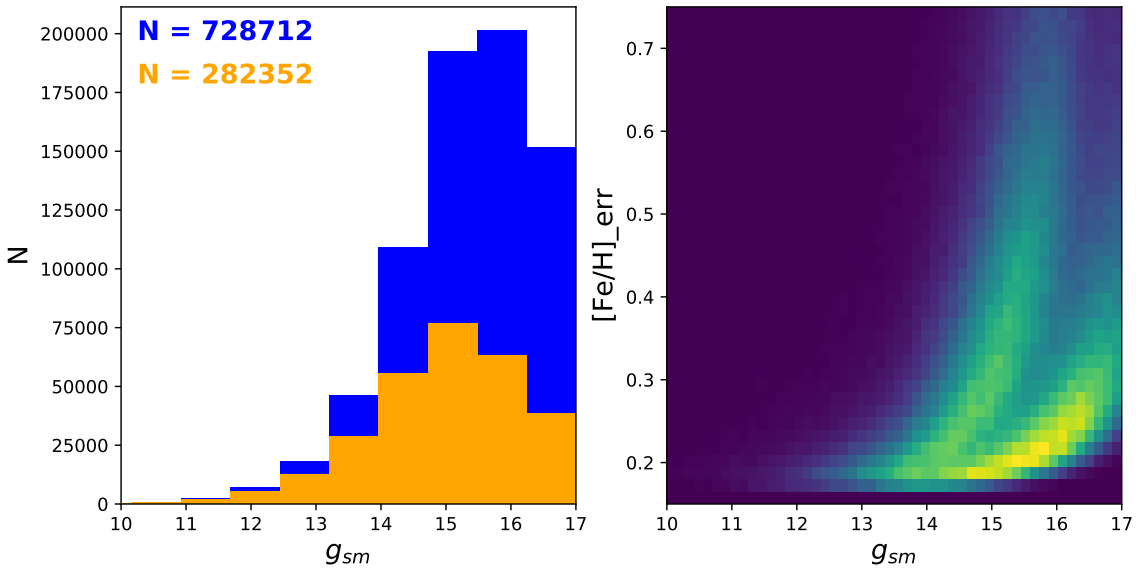

Figure 8-7 Left: Histogram of the magnitudes of all stars in our catalog (blue) and those passing the flags in Section 8.2.4 (orange). Right: Uncertainties on the photometric metallicities of the stars in our sample as a function of magnitude.

[327, 422, 423]. Data from these surveys were downloaded[5,6,7] and cross-matched to our catalog using the `TOPCAT` software [428]. The results of these comparisons are presented in Figure 8-8, and are discussed further in this section.

We find 6,409 stars in our catalog that have stellar parameters in LAMOST DR6. We applied several cuts to the LAMOST catalog ($\log g < 3.0$, and $4000 < T_{\rm eff} < 5700$) to ensure the stellar parameters of stars in the LAMOST sample were comparable to those of stars in our catalog. Then, we excluded stars in LAMOST and our catalog that have metallicity uncertainties greater than 0.3 dex, and stars in LAMOST with $\log g$ uncertainties > 0.30 to compare stars with high-quality stellar parameters. This resulted in a sample of 2,262 stars, which are plotted in the leftmost panel of Figure 8-8 as hollow squares. Of those stars, 1,835 pass the *Gaia*-based quality checks in Section 8.2.4 and are plotted as solid squares. We find that our metallicities that pass the quality checks are on average 0.05 dex lower than the LAMOST metallicities, and the standard deviation of the residuals between metallicities is 0.24 dex. This is

[5]http://dr6.lamost.org
[6]https://docs.datacentral.org.au/galah/
[7]https://www.sdss.org/dr16/irspec/spectro_data

great agreement, given typical best metallicity precisions achievable with medium-resolution spectroscopy are ~ 0.15 dex, and the systematic floor on the metallicity precision from our photometric method is $\sim$0.16 dex.

There are 14,362 stars in our catalog that have stellar parameters in GALAH DR3. We applied the same cuts to the GALAH catalog that we applied to the LAMOST sample to ensure a high quality stellar parameter comparison. We also applied some cuts using flags in the GALAH catalog (`flag_sp = 0, flag_fe_h == 0`) to further increase the quality of the comparison sample. This resulted in a sample of 6,957 stars, of which 4,312 passed all the checks outlined in Section 8.2.4. The comparison between the metallicities is plotted in the middle panel of Figure 8-8. We find that these metallicities are on average 0.24 dex lower than those metallicities presented in GALAH and the standard deviation of the residuals between our metallicities is 0.25 dex.

The same cuts were applied to the APOGEE DR16 catalog as for the previous catalogs to ensure a high quality reference sample. Additionally, we only retained APOGEE stars with `ASCAPFLAG = 0` which indicated no warnings or errors were raised by the APOGEE stellar parameter pipeline [429]. This led a sample of 1,307 stars in total and 959 stars passing the checks in Section 8.2.4, all of which are plotted in the right panel of Figure 8-8. Our photometric metallicities that pass the quality checks are on average 0.11 dex lower than the APOGEE metallicities, and the residuals of metallicities between the two datasets have a standard deviation of 0.23 dex.

8.3.2 Comparison to high-resolution spectroscopic samples

There are a number of stars in our catalog that have metallicities previously determined by high-resolution spectroscopic studies. Metallicity comparisons are particularly useful to test the behavior of our photometric values in the very low metallicity regime ($-3.5 <$[Fe/H]< -2.5). We thus compared our metallicities to those derived by the high-resolution studies of Barklem et al. [65], Jacobson et al. [3], Marino et al. [64], and Ezzeddine et al. [62] that are within the metallicity range of our grid ([Fe/H]

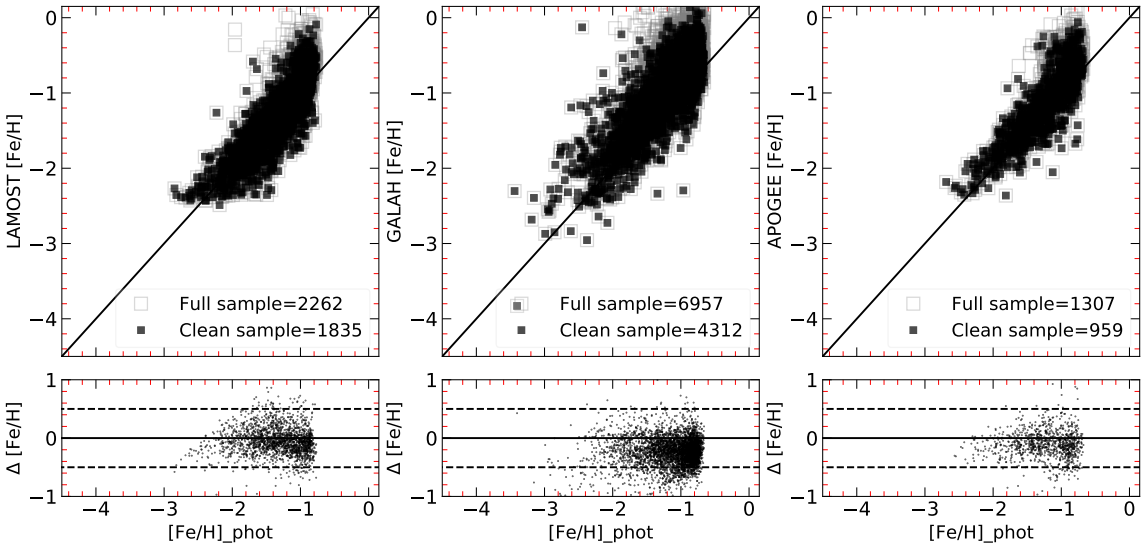

Figure 8-8 Our SkyMapper photometric metallicities, compared to metallicities from LAMOST DR6 (left panels), GALAH DR3 (middle panels), and APOGEE DR16 (right panels) for stars with photometric metallicity uncertainties lower than 0.30 dex. The filled black squares correspond to stars that passed the flags in Section 8.2.4, and the open squares correspond to the entire sample. The Lower panels show the residuals between our photometric metallicities and those presented in the above surveys. Dashed lines indicate ±0.50 to guide the eye. The agreement between our metallicities and those in presented in these surveys is good, as indicated by the relatively low standard deviation of the residuals in the bottom panel ($\sim$ 0.25 dex) despite slight offsets with each survey.

> -4.0), as well as a sample of stars that was specifically observed for comparison purposes with the high-resolution MIKE spectrograph [195] on the Magellan/Clay Telescope in January, October, and December 2020. Detailed results will be presented in Ou et al., in prep. but we compare to their derived metallicities here. For completeness, we refer the reader to Section 3 of Ezzeddine et al. [62] which comprehensively details the methodology (e.g., linelist, analysis software) used in Ou et al., in prep for deriving stellar metallicities.

Results of the various metallicity comparisons are shown in Figure 8-9. The top left panel displays the comparisons to both Ou et al., (in prep) and Marino et al. [64]. The following panels, in clockwise order, show the comparisons to Barklem et al. [65], Ezzeddine et al. [62], and Jacobson et al. [3], respectively. The orange data points in the panels correspond to the warmer stars in our sample ($g - i < 0.65$) and the black data points correspond to the cooler stars ($g - i > 0.65$). For reference, $g - i = 0.65$ corresponds to an effective temperature of $\sim 5000\,\mathrm{K}$.

The agreement of photometric metallicities for all 55 stars in common with those of the combined sample of Marino et al. [64] and Ou et al. (in prep) is excellent. Our metallicities are marginally higher (0.15 dex) on average but the standard deviation of the residuals is 0.29 dex. Note that in the Figure 8-9 we list a slightly different standard deviation that refers to stars with $g - i > 0.65$.

We find worse agreement (mean offset of 0.24 dex with a standard deviation of 0.45 dex) for the metallicities of our stars in common with the three other studies [65, 3, 62] combined but there are hints that this is the case because our photometric metallicities are biased high when $g - i < 0.65$. If we only include the 87 cooler stars with $g - i > 0.65$, the average offset drastically reduces to 0.08 dex, and the standard deviation of the residuals reduces to 0.36 dex. Finally, combining all five high-resolution samples and restricting the comparison to $-4.0 <$ [Fe/H] < -2.5 (as measured on our metallicity scale), metallicities agree reasonably well mean offset of 0.03 dex with a standard deviation of 0.30 dex), with roughly similar scatter when $g - i > 0.65$ (mean offset on 0.02 dex with a standard deviation of 0.31 dex).

To further gauge precision in the lowest metallicity regime ($-3.5 \lesssim$ [Fe/H] $\lesssim$

-2.5), we investigated the contamination rate of stars with [Fe/H] < -4.0 in our catalog by cross-matching our catalog to the sample of ultra metal-poor stars listed in Ezzeddine et al. [104]. We recover only three of their sixteen stars: CD -38° 245, HE 2139−5432, and SMSSJ0313−6708, suggesting a negligible presence of stars below [Fe/H] < -4.0 in our catalog. Furthermore, the presence of HE 2139−5431 and SMSSJ0313-6708 in our catalog is not altogether surprising, given their extremely large relative carbon abundances ([C/Fe] = 2.59; Yong et al. 430 and [C/Fe] > 4.8; Keller et al. 129, respectively) which significantly up-scatters their photometric metallicities (see Section 8.3.3). Our recovery of CD -38° 245 ([Fe/H] $= -4.12 \pm 0.10$; Ezzeddine et al. 62) cannot be explained this way as it has no strong overabundance of [C/Fe], but we note a [Fe/H] $= -3.05 \pm 0.48$ for this star in our catalog. In general, anomalously high or low [α/Fe] values, unresolved interstellar Ca absorption, significant CH absorption or other issues may mask as stellar Ca, and are known to result in systematic overestimates for stars when the signal from the Ca II K line has become incredibly weak (e.g., when [Fe/H] $\lesssim -3.5$). This highlights the difficulty in extending this technique to derive precise metallicities at the very lowest [Fe/H] regime (e.g, ultra metal-poor stars).

This comparison exercise with results from high-resolution spectroscopy principally validates our analysis technique and confirms that our photometric metallicities are reliable down to [Fe/H] ~ -3.3 for the cooler subsample of our catalog ($g - i > 0.65$). It also suggests that the photometric metallicities presented in this catalog could feasibly be used for targeted searches for the most metal-poor stars in our galaxy, especially among the cooler stars. The use of metallicities of warmer stars with $g-i < 0.65$ is less accurate due to some evidence of systematic metallicity offsets when compared to Barklem et al. [65], Jacobson et al. [3], and Ezzeddine et al. [62], but we still report their metallicities because (1) of the overall good agreement with the Ou et al. (in prep) and Marino et al. [64] studies, and (2) even if these metallicities were somewhat biased high, they would still be useful for targeted spectroscopic follow-up campaigns for low metallicity stars.

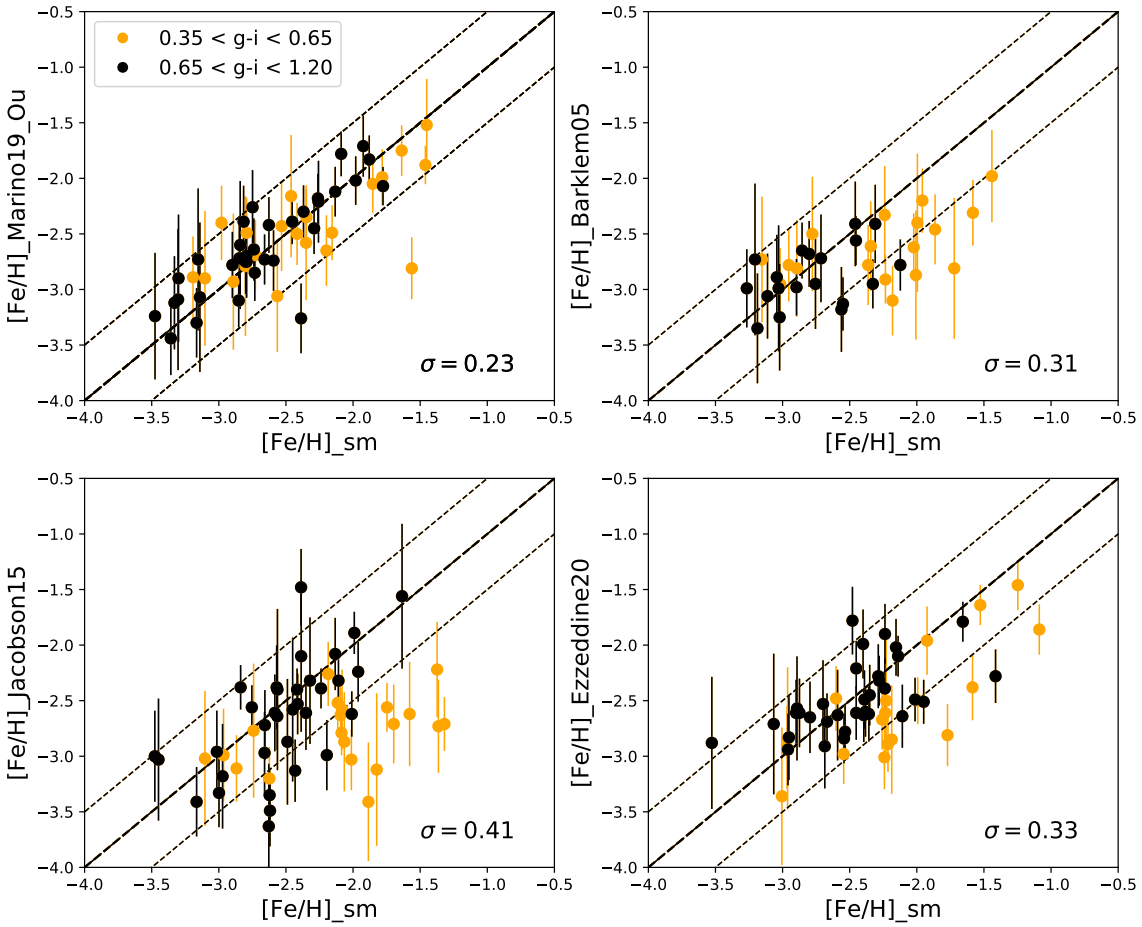

Figure 8-9 Top left: A comparison between the photometric metallicities of stars presented in our catalog and metallicities from high-resolution spectroscopy of Marino et al. [64] and X. Ou et al. (in prep). Top right: Same comparison but with the high-resolution spectroscopy results of Barklem et al. [65]. Bottom right: Same comparison but with the high-resolution spectroscopy results of Ezzeddine et al. [62]. Bottom left: Same comparison but with the high-resolution spectroscopy results of Jacobson et al. [3]. The black data points correspond to cooler stars in our sample ($g-i > 0.65$) and orange data points to warmer stars ($g-i < 0.65$). There is some evidence that our photometric metallicities are biased high with respect to three of the studies when $g-i < 0.65$. Lines are drawn at ± 0.5 dex to guide the eye. The σ in each panel corresponds to the standard deviation of the metallicity residuals between our catalog and the corresponding study for stars with $g-i > 0.65$.

8.3.3 Effect of carbon abundance

As extensively discussed in e.g., Da Costa et al. [234] and Chiti et al. [39], stars with a prominent CN spectral feature at $\sim$3870 Å may have photometric metallicities from SkyMapper photometry that are biased high. This is because that absorption feature is located within the wavelength region covered by the SkyMapper v filter and thus affects the observed flux and will make the star appear more metal-rich. Such an effect could be particularly pronounced at lower metallicities where carbon-rich stars become more frequent.

At face value, this effect implies that carbon-enhanced metal-poor (CEMP) stars in this catalog will appear to have higher metallicities than their true metallicity. For reference, a star with $T_{\rm eff} = 4700\,{\rm K}$, [Fe/H] $= -2.5$, and [C/Fe] $= 0.50$ will have a metallicity biased upward by $\sim 0.40\,{\rm dex}$ compared with a similar star with [C/Fe] $=$ 0 [39]. This means that for the majority of stars in our catalog, this effect will be below that $\sim 0.40\,{\rm dex}$ level since most stars with $-3.0 <$ [Fe/H]< -1.0 do not reach that level of carbon enhancement (Figure 2 in Placco et al. 8). Obvious exceptions to this would be e.g., CEMP-s stars (typically with [Fe/H] $\gtrsim -2.5$,) that display extreme carbon enhancements due to mass transfer from a binary companion but those numbers are expected to be comparably small. We also emphasize that if variations in the carbon abundance were greatly influencing our metallicity determinations for a bulk of stars in this catalog, this effect would have manifested as a much larger scatter in our comparisons to the metallicities obtained by the LAMOST, GALAH, and APOGEE surveys (see also Section 8.3.1) which is not observed. Hence, for the bulk of stars in this catalog, we regard the effect of the carbon abundance on the metallicity as likely not significant.

8.3.4 Selection Effects on the Metallicity Distribution

We also attempt to quantify the extent to which our catalog is biased in selecting or de-selecting stars as a function of metallicity. We test for any such effect among stars with $-2.0 <$ [Fe/H] < -1.0 by deriving the fraction of stars that we recover in the

southern hemisphere coverage of the LAMOST DR6, GALAH DR3 and APOGEE DR16 catalogs with comparable stellar parameters ($\log g < 3.0$, $-2.50 <$[Fe/H]< -0.75, $4000\,\mathrm{K} < T_{\mathrm{eff}} < 5700\,\mathrm{K}$, and $\sigma_{\mathrm{[Fe/H]}} < 0.3$) and spatial distribution ($|b| > 10°$), over a magnitude range $11 \lesssim g \lesssim 16.5$.

We note that our recovery rate with respect to the combined sample of LAMOST, GALAH, and APOGEE stars is between 40 % and 50,%, but this apparently low value is largely driven by our initial photometric quality cut on the SkyMapper DR2 catalog (`flags = 0`). After that initial cut, a significantly higher 70 % of stars in the LAMOST, GALAH, and APOGEE catalogs are retained in our photometric metallicity catalog, suggesting that the majority of the loss is driven by photometric quality and not anything particular to our subsequent analysis technique. However, we still present the recovery fraction below including the loss of stars in our catalog due to photometric quality, in order to test whether such losses could plausibly have an effect on the metallicity selection. Since SkyMapper imaging covers the entire southern sky, we note that our catalog includes a significant number of stars that are in neither the LAMOST, GALAH, or APOGEE catalogs.

We determined that for $-1.5 <$[Fe/H]< -1.0, 42 % of stars were retained in our catalog. For $-2.0 <$[Fe/H]< -1.5, 47 % were retained. At face value, this suggests that we are slightly more sensitive to accurately selecting stars with $-2.0 <$[Fe/H]< -1.5 than $-1.5 <$[Fe/H]< -1.0. This difference in recovered stars is robust given the large sample size of 8270 reference stars from LAMOST, GALAH and APOGEE.

To test whether any potential selection effects extend into the [Fe/H] < -2.0 regime, we performed the same exercise, except this time using the combined sample of stars from Barklem et al. [65], Jacobson et al. [3], Marino et al. [64], Ezzeddine et al. [62], and X. Ou et al. (in prep) as references, as they extend to lower metallicities than the APOGEE/LAMOST/*GALAH* comparison. In this case, we find no strong dependency of the recovery fraction with metallicity, with recovery fractions of 58 %, 51 %, 45%, and 25 % for the respective 0.5 dex increments ranging from [Fe/H] $= -1.5$ to [Fe/H] $= -3.5$. Unfortunately, the smaller sample size of 417 stars in this combined sample is too small to resolve differences below a ~ 7 % level (set by

Poisson statistics) in each of these bins. For that reason, it is particularly difficult to asses the completeness in the extremely metal-poor regime with [Fe/H] < -3.0 at this time, although indications suggest that our catalog is preferentially incomplete in that regime. This is not surprising, as the selection is likely to decrease due to a loss of metallicity precision since the color-color separation between stars of different metallicities significantly narrows in this regime (see Figure 8-1). We note that including/excluding stars that fail the quality checks in Section 8.2.4 negligibly changes these recovery fractions.

8.4 Summary and Conclusion

In this paper, we have presented a new catalog of $\sim 720,000$ stars in the Southern hemisphere for which we have obtained photometric metallicities using metallicity-sensitive photometry from the second data release (DR2) of the SkyMapper Southern Survey. We identify $\sim 280,000$ of these stars as having reliable metallicities, after excluding main-sequence and more metal-rich ([Fe/H] > -0.75) contaminants using *Gaia* EDR3 data. This sample of giants with $T_{\rm eff} \lesssim 5600\,$K, $\log g < 3.0$, and $-3.75 <$ [Fe/H] < -0.75 reaches down to $g = 17$, and stretches throughout the inner halo to a scale height of $|Z| \sim 7\,$kpc (Chiti et al. ApJL accepted). We find that our photometric metallicities compare well (average offsets $\sim 0.15\,$dex with standard deviation $\sigma \sim 0.25\,$dex) to those obtained in large-scale surveys (e.g., LAMOST, GALAH, APOGEE), suggesting that our analysis techniques produce accurate metallicities for the bulk of the stars in our sample. Overall, this validates our general approach of deriving photometric metallicities.

To test the performance of our catalog in the [Fe/H] < -2.5 regime, we compared our photometric metallicities to metallicities derived in several high-resolution spectroscopic studies of very and extremely metal-poor stars in Barklem et al. [65], Jacobson et al. [3], Marino et al. [64], Ezzeddine et al. [62], and X. Ou et al. (in prep). We find some evidence that warmer stars in our catalog ($g - i < 0.65$) have systematically higher photometric metallicities. However, we find good agreement

(mean offset = 0.02 dex with standard deviation $\sigma = 0.31$ dex) between the photometric metallicities of cooler stars with $g - i > 0.65$ with [Fe/H] < -2.5 and their metallicities from high-resolution studies.

We highlight that several systematic effects could bias our photometric metallicities. First, as noted before, warmer stars with $g - i < 0.65$ may have metallicities biased high, at least when compared to several high-resolution studies of very and extremely metal-poor stars. Secondly, carbon-enhanced metal-poor (CEMP) stars will systematically have artificially higher photometric metallicities due to the presence of a CN absorption feature in the bandpass of the SkyMapper v filter. However, the latter effect likely does not affect the bulk of stars in our sample as evidenced by the good agreement of our photometric metallicities to metallicities presented in APOGEE and LAMOST.

In Chiti et al. (ApJL accepted), we use a subset of this catalog to explore the metallicity distribution function (MDF) of the Milky Way and create spatial metallicity maps of our galaxy. We recover well-known features in the MDF, such as a peak at [Fe/H] ~ -1.5 when considering stars distant from the disk plane ($|Z| > 5$ kpc) [419]. We also find that the metallicity distribution function steepens below [Fe/H] $= -2.3$, confirming the significant challenge in searching for the most metal-poor stars, and we identify of order 1000 giants with quality photometric metallicities (random uncertainties < 0.50 dex) and colors ($g - i > 0.65$) that have [Fe/H] $\lesssim -2.6$ in this catalog.

This shows that this catalogue is suitable for a variety of chemical characterizations of the metal-poor Galaxy ([Fe/H] < -0.75) and its components, as well as targeted searches of stellar populations such as the most metal-poor stars. Accordingly, spectroscopic observations and detailed kinematic analyses are currently underway to further characterize the low-metallicity tail of the metallicity distribution function and to obtain detailed chemical abundances of the population of stars with [Fe/H] < -3.0. This will contribute to our understanding of the origin and evolution of the oldest components of the Milky Way.

Chapter 9

The Metal-Poor Metallicity Distribution of the Ancient Milky Way

The content of this chapter was submitted for publication in the Astrophysical Journal Letters on October 2020, and was accepted for publication in December 2020.

Abstract

We present a low metallicity map of the Milky Way consisting of ∼111,000 giants with $-3.5 \lesssim$ [Fe/H] $\lesssim -0.75$, based on public photometry from the second data release of the SkyMapper survey. These stars extend out to ∼7 kpc from the solar neighborhood and cover the main Galactic stellar populations, including the thick disk and the inner halo. Notably, this map can reliably differentiate metallicities down to [Fe/H] ~ -3.0, and thus provides an unprecedented view into the ancient, metal-poor Milky Way. Among the more metal-rich stars in our sample ([Fe/H] > -2.0), we recover a clear spatial dependence of decreasing mean metallicity as a function of scale height that maps onto the thick disk component of the Milky Way. When only considering the very metal-poor stars in our sample ([Fe/H] < -2), we recover no such spatial dependence in their mean metallicity out to a scale height of $|Z| \sim 7$ kpc. We find that the metallicity distribution function (MDF) of the most metal-poor stars in our sample ($-3.0 <$ [Fe/H] < -2.3) is well fit with an exponential profile with a slope of $\Delta \log(N)/\Delta$[Fe/H] $= 1.52 \pm 0.05$, and shifts to $\Delta \log(N)/\Delta$[Fe/H] $= 1.53 \pm 0.10$ after accounting for target selection effects. For [Fe/H] < -2.3, the MDF is largely insensitive to scale height $|Z|$ out to ~ 5 kpc, showing that very and extremely metal-poor stars are in every galactic component.

9.1 Introduction

Many studies have focused on comprehensively characterizing the nature of the Milky Way's galactic components, which include the bulge [387], the thin and thick disk [431], the metal-weak tail of the thick disk, and the inner and outer halo [432] through determining spatial properties (e.g., scale heights, densities), stellar chemical abundances (e.g., metallicities), kinematic properties, and when possible, dating using age measurements. The halo is of particular interest for galactic archaeology studies that e.g., aim to understand the galaxy's early evolution. Firstly, a relatively large portion of the halo is composed of ancient very and extremely metal-poor stars ([Fe/H] < -2.0 and < -3.0, respectively), which are pivotal for studies of early chemical evolution [99]. Secondly, theoretical simulations of galaxy formation [433] have shown that the halo bears the signatures of the Milky Way's assembly from smaller "building block" galaxies.

Astrometric data from the *Gaia* mission [111, 114] has shown e.g., the existence of stellar kinematic signatures as a result from earlier accretion events [434, 435, 436] but there remains the need for precise metallicities *down to the extremely metal-poor regime* ([Fe/H] ~ -3.0) for many stars for a full chemodynamic picture of early structures still present in the current Milky Way. Recent spectroscopic and photometric surveys have began to remedy this. Spectroscopic surveys for which metallicities have been derived for large samples of stars include LAMOST [437], RAVE [438], GALAH [439], SDSS/SEGUE [327, 414], and APOGEE [423]. Photometric surveys are far more complete than spectroscopic surveys and thus offer better prospects for mapping chemical structure because the relative rarity of extremely metal-poor stars means that these are generally poorly represented in any sample. Ivezić et al. [419] created a metallicity map of the Northern sky based on SDSS broadband photometry of ~ 5.6 million stars. The disk and halo as well as the Monoceros stream cleanly differentiate in metallicity vs. height above the Galactic plane, confirming the galactic components and stellar populations. However, the SDSS photometry only enabled metallicity determination down to [Fe/H] ~ -2.0.

More recent photometric surveys, such as the SkyMapper Southern Sky Survey [127] and the Pristine survey [125], have instead developed the use of metallicity-sensitive filters surrounding the Ca II K line that enable metallicity measurements in the very and even extremely metal-poor regime. These have led to notable results, including identification of the most metal-poor stars in the halo [132, 234] and the bulge [387, 417], and the metallicity distribution function of extremely metal-poor stars [418].

Additional spatial maps of the metallicity of the Northern hemisphere were presented in [420], analogous to those in Ivezić et al. [419], but extending to lower metallicities ([Fe/H] ~ -3.0). Similarly, spatial maps of the Southern sky as a function of metallicity were presented in Casagrande et al. [145] and Huang et al. [416] using photometry from Data Release 1.1 from the SkyMapper Survey [9]. However, these maps only claimed metallicity precision down to [Fe/H] ~ -2.0 or [Fe/H] ~ -2.5, and were limited by the relatively shallow magnitudes in SkyMapper DR1.1.

Here we explore the oldest and most metal-poor stellar population spread across the galaxy with a series of metallicity maps of the Southern sky based on the recently released SkyMapper Southern Sky Survey Data Release 2 (DR2) [407]. The metallicity sensitive imaging filters [135] enable a significant metallicity resolution down to [Fe/H] ~ -3.3. Using techniques developed in Chiti et al. [39] to extract precise metallicities from the intermediate-band SkyMapper v and broadband u, g, i filters, we derived photometric metallicities for every giant star with $g < 17$ and [Fe/H] < -0.75 in the full catalog (Chiti et al. ApJS subm.). We here focus on a subset of well-selected $\sim 111,000$ metal-poor red giants with quality metallicity measurements to map out the ancient components of the Galaxy.

9.2 Observational Data and Photometric Metallicities

The SkyMapper Southern Sky Survey DR2 contains $\sim$ 500 million astrophysical sources [407]. We downloaded photometry for every star brighter than $g = 17$ in this catalog, de-reddened the data following the bandpass coefficients on the SkyMapper

website[1], and derived photometric stellar parameters of these stars (log g, [Fe/H]) following the methods presented in Chiti et al. [39]. In summary, this involved matching the observed photometry to a grid of synthetic photometry spanning a broad range of stellar parameters ($1.0 < \log g < 3.0$, $4000\,\mathrm{K} <$ $< 5700\,\mathrm{K}$, $-4.0 <$[Fe/H] < -0.75). We excluded all stars with initial[2] photometric [Fe/H] ≥ -0.75, [Fe/H] ≤ -3.75, and < 3.0, and $0.35 < g - i < 1.2$ (corresponding to our limits) to largely limit our sample to metal-poor red giant stars. We furthermore excluded stars with random uncertainties of >0.5 dex in their photometric metallicity and those in regions of high reddening (galactic latitude $|b| < 10^{\circ}$ and E(B−V) > 0.35 in Schlegel et al. 63). This resulted in a sample of 593,668 stars. Finally, we find that we systematically overestimate the metallicities of very metal-poor ([Fe/H] < -2.0) stars when $g - i < 0.65$, upon comparison to high-resolution samples [3, 62]. To avoid this issue, we conservatively only retain stars with $g - i > 0.65$, resulting in 308,702 stars. We refer the reader to Chiti et al. (ApJS, subm.) for further details on the full catalog.

We adopted photogeometric distances to every star in our sample from ?] over using inverted parallax-based distances (see Mardini et al. 440 for a recent discussion). To ensure distance measurements of sufficient quality, we only included stars that have distance uncertainties less than the 20% level. We then excluded stars with absolute SkyMapper g magnitude > 5 and a location on a color-magnitude diagram consistent with a metallicity [Fe/H] > -0.75 (Chiti et al. ApJS Subm.), which further limits contamination from cool dwarf stars and more metal-rich interlopers. This resulted in a final sample of 111,149 stars extending down to $g \sim 17$.

To validate the metallicities in our sample, we compared our metallicities to those from multiple other surveys. Details are given in Chiti et al. (ApJS subm.), but we list relevant comparisons here. For $-2.5 <$ [Fe/H] < -0.75, when only considering stars with uncertainties on their photometric metallicities < 0.5 dex, our metallicities are on average lower than those reported in the LAMOST survey by 0.05 dex. The

[1]http://skymapper.anu.edu.au/filter-transformations/

[2]We note that $\sim 5\%$ of stars have photometric metallicities up to 0.1 dex higher than [Fe/H] $= -0.75$ due to a metallicity correction based on the spatial location of stars (see Section 2.3 of Chiti et al. ApJS subm.).

standard deviation of the residuals between our photometric metallicities and those in the LAMOST survey is 0.25 dex, indicating great agreement. Similarly, upon comparing to metallicities from the combined APOGEE and GALAH surveys over the same metallicity regime, we find, on average, lower metallicities by 0.21 dex. The metallicity residuals have a standard deviation of 0.25 dex.

We demonstrate that our metallicities are robust when [Fe/H] < -2.5 following high-resolution observations of 74 initial metal-poor candidates selected from SkyMapper DR1.1 and DR2 data [9, 407] as an early test sample. We derived their stellar parameters following standard spectral analysis techniques [59] for these stars based on Magellan/MIKE [195] high-resolution ($R \sim 22,000$) snapshot spectra that were reduced using the CarPy pipeline [196]. Full results will be reported in X. Ou et al. (in prep) but we show results (red points) in Figure 9-1 for the 21 stars that we recovered in the DR2 catalog after our quality cuts. The comparison is excellent, with an average metallicity offset between the two samples of 0.09 dex and a standard deviation in the residuals of 0.17 dex. In Figure 9-1, we also compare our values to the high-resolution samples of to Barklem et al. [65], Marino et al. [64], and Ezzeddine et al. [62] for stars with covering the range of our photometric metallicities ([Fe/H] > -3.75). Results largely follow what is presented in the comparisons to APOGEE and LAMOST and X. Ou et al. (in prep), but the Barklem et al. [65] comparison shows an offset of 0.25 dex, largely due to them lacking an empirical correction on [59]. The standard deviation of the residuals of our photometric metallicities and the high-resolution spectroscopic studies is 0.29 dex.

We note that in Chiti et al. ApJS subm., we find that the completeness of our sample is independent of metallicity down to [Fe/H] ~ -3.0. Consequently, when presenting quantitative analysis (e.g., fitting an exponential slope) of the metallicity distribution function of our sample, we only include photometric metallicities down to [Fe/H] $= -3.0$ in the fitting procedures.

An additional bias is related to target selection effects, since metal-poor stars are brighter than metal-rich stars at the same effective temperature. Consequently, our sample may be preferentially biased toward low-metallicity stars at larger distances

as our quality cuts will exclude more metal-rich stars at larger distances. As an illustration of this effect, stars right at the threshold of our distance quality cut (uncertainties at the 18% to 20% level) have a median distance of 6.4 kpc when $-1.25 < \mathrm{[Fe/H]} < -0.75$, but a median distance of 8.9 kpc when $-2.75 < \mathrm{[Fe/H]} < -2.25$. However, this selection preference toward metal-poor stars is not significant within a distance of ∼5.0 kpc, as we find that at distances between 4.0 kpc and 5.0 kpc, a roughly constant fraction of $< 1\%$ of stars are excluded from our full catalog by our quality cut as a function of metallicity. A weak trend with metallicity appears at distances between 5.0 kpc and 6.0 kpc, in which 6% of stars are excluded with higher metallicities ($\mathrm{[Fe/H]} > -1.25$), but only 2% of stars are excluded with low metallicities ($\mathrm{[Fe/H]} < -1.75$). This suggests a slight preferential selection of low metallicity stars at distances beyond ∼5.0 kpc, but no bias at distances nearer.

9.3 Metal-Poor Stars in the Milky Way

Our low-metallicity map ($\mathrm{[Fe/H]} \leq -0.75$) of the Milky Way is shown in Figure 9-2 as a function of scale height ($|Z|$) and distance from the Galactic center (R). Using `astropy` [139], we transformed the coordinates of each star into the R, Z plane, assuming the Sun's location of 8.1 kpc away from the Galactic center and 22 pc above the Galactic midplane [441]. Each location of this map is colored by the average metallicity of stars in the corresponding spatial bin (300 pc by 300 pc in size). The disk/halo separation is immediately easy to recognize, due to the transition of the average metallicity from $\mathrm{[Fe/H]} \gtrsim -1.25$ to $\mathrm{[Fe/H]} \lesssim -1.25$ above $|Z| \sim 2.8$ kpc. This compares well to the metallicity map presented in Ivezić et al. [419], whom also find a sharp break at $|Z| \sim 3$ kpc above which the mean metallicity drops below $\mathrm{[Fe/H]} \sim -1.25$.

In Figure 9-3, we show metallicity maps for several metallicity ranges (1 dex increments from $\mathrm{[Fe/H]} = -1.0$ to $\mathrm{[Fe/H]} = -4.0$) to display the structure of the Galaxy at progressively lower metallicities. The Milky Way disk is still clearly noticeable in our highest metallicity bin ($-2.0 < \mathrm{[Fe/H]} < -1.0$), along with a diffuse

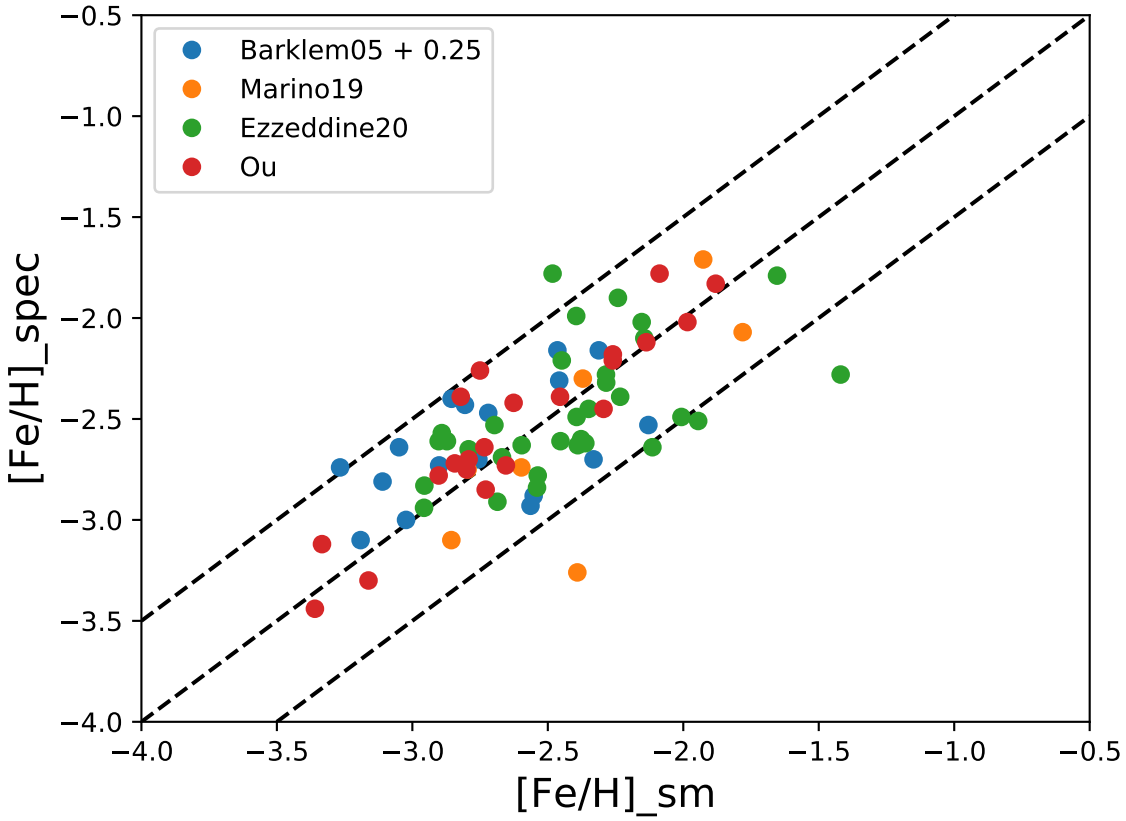

Figure 9-1 Comparison of [Fe/H] metallicities between our photometric SM results and high-resolution measurements of stars in Barklem et al. [65], Marino et al. [64], Ezzeddine et al. [62] and X. Ou et al. (in prep). The agreement is excellent, with Δ[Fe/H] = 0.04±0.03. The standard deviation of the residuals between the metallicities is 0.29 dex. Dashed lines indicate ±0.5 dex to guide the eye, and the metallicities in Barklem et al. [65] have been increased by 0.25 dex to account for an empirical correction on [59].

population of more metal-poor stars ($-2.0 <$ [Fe/H] < -1.5) that follow no obvious spatial structure. Continuing this trend, the stars in the two lowest metallicity bins ($-3.0 <$ [Fe/H] < -2.0 and $-4.0 <$ [Fe/H] < -3.0) appear to show no spatial correlation with their mean metallicity.

To illustrate this trend, in the right panel of Figure 9-3, we plot the mean metallicity of each of these metallicity bins as a function of scale height $|Z|$. While the mean metallicity of our most metal-rich bin shows a decreasing mean metallicity as a function of $|Z|$, the more metal-poor bins do not, suggesting no significant spatial correlation with metallicity below [Fe/H] $= -2.0$. Overall, this figure confirms that the

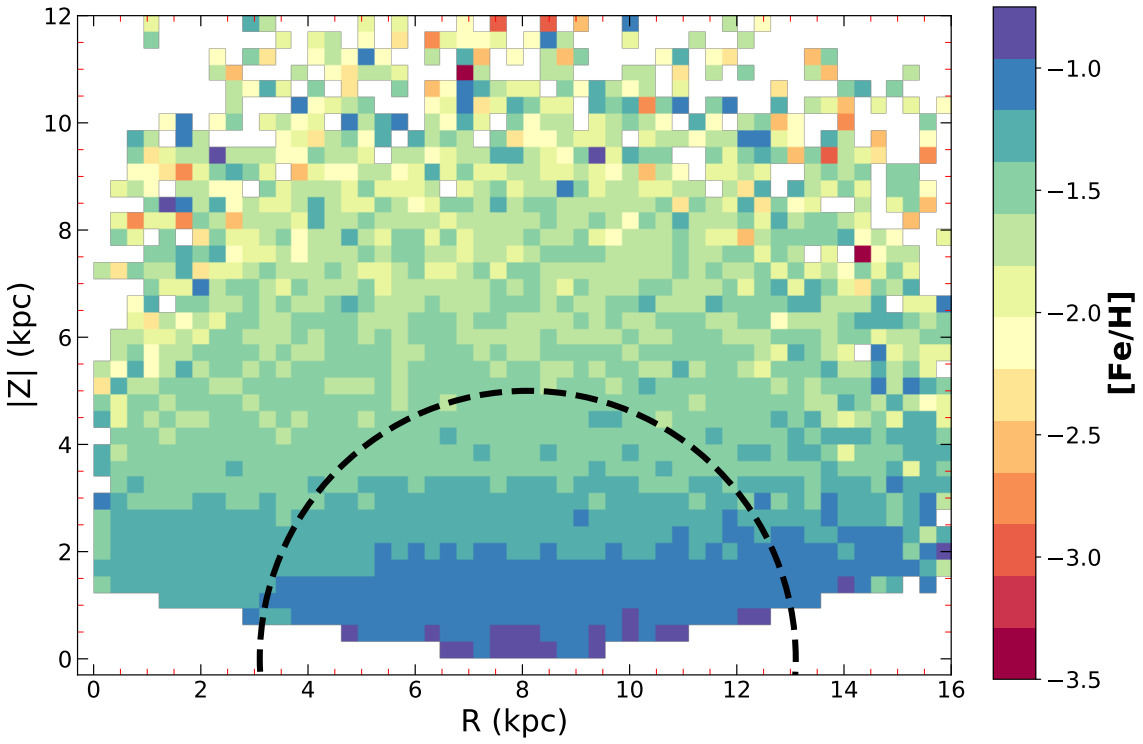

Figure 9-2 Top: Low metallicity map of stars with [Fe/H] ≤ -0.75 in the R-$|Z|$ plane, where R is the galactocentric distance and $|Z|$ is the absolute value of the height above the galactic plane. A clear, decreasing metallicitiy gradient is apparent as a function of $|Z|$, and the Milky Way disk is visible via a drop-off in average metallicity above $|Z| \sim 2.8$ kpc. Each cell in the plot has dimensions of 300 pc by 300 pc, and is colored by the mean metallicity of stars contained within its region. The dashed semicircle includes stars with distances < 5.0 kpc, within which target selection effects do not appreciably bias the metallicity of the sample (see Section 9.2 for discussion).

most metal-poor stars are spatially distributed in all of the Galactic components, but their search in certain components (e.g., the disk) is simply impeded by the wealth of the more metal-rich stars. In fact, 0.8% of stars in our sample have [Fe/H] < -2.5 when $|Z| < 3$ kpc, but comprise 2.7% of stars when $|Z| > 3$ kpc.

In Figure 9-4, we present the metallicity distribution function (MDF) of our sample of metal-poor giants. We now include stars with a loosened distance quality cut (uncertainty of $< 40\%$), since those giants with unreliable distances are most likely to be associated with the outer halo and populate the most metal-poor regime of the MDF. As mentioned in Section 9.2, we only include stars with [Fe/H] > -3.0 when fitting profiles to the MDF, given incompleteness effects when [Fe/H] < -3.0.

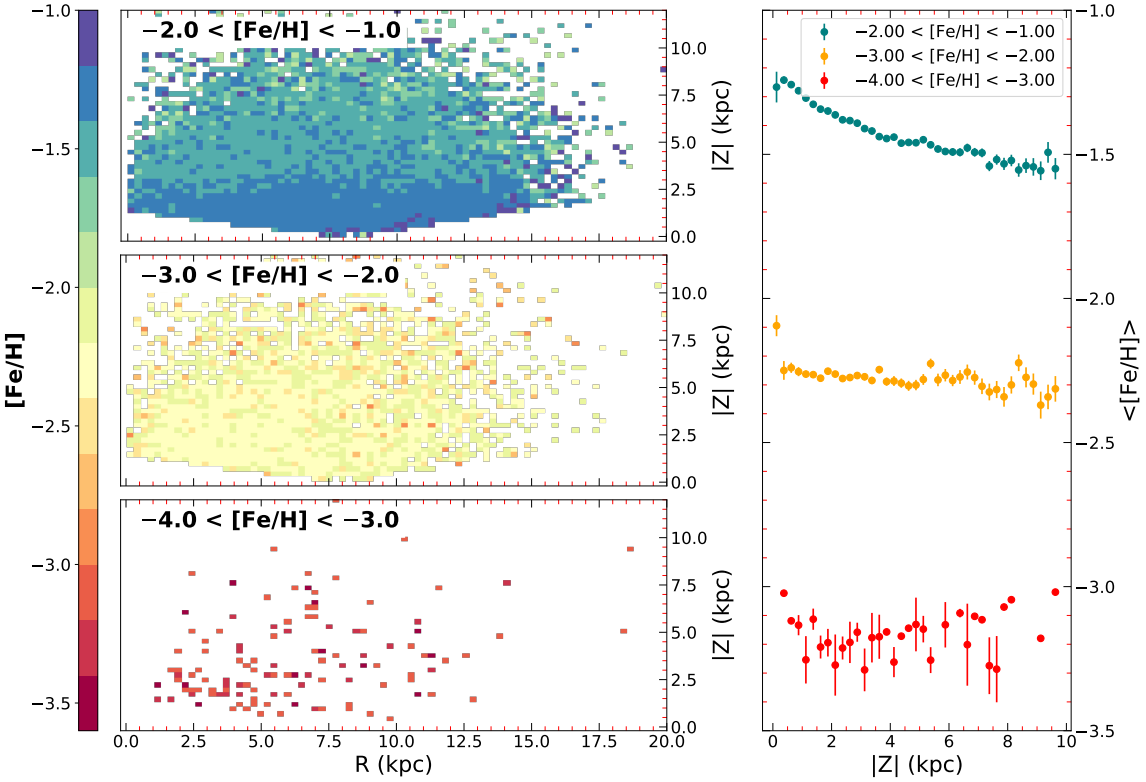

Figure 9-3 Left panels: Low metallicity maps of stars in different metallicity ranges. The thick disk is easily apparent among stars with $-2.0 < [\mathrm{Fe/H}] < -1.0$. No significant structure is present among stars with $[\mathrm{Fe/H}] < -2.0$. Right panel: Mean metallicities of stars as a function of scale height $|Z|$, within 0.25 kpc bins in $|Z|$ that correspond to the respective left panels. The disk region induces a clear metallicity gradient (top) that makes way for no significant change in [Fe/H] with increasing $|Z|$.

Below $[\mathrm{Fe/H}] = -1.5$, the MDF smoothly decreases exponentially towards lower metallicities. Down to $[\mathrm{Fe/H}] \sim -2.3$, this behavior is well described by an exponential function with a slope of $(\Delta(\log N))/(\Delta[\mathrm{Fe/H}]) = 0.98 \pm 0.01$. This slope was derived through a MCMC procedure by implementing the likelihood function for a truncated exponential distribution (equation 8.1.17 in Cohen 442) in the python package emcee [248]. Then, the derived exponential slope was converted from $\Delta(\ln N)/\Delta[\mathrm{Fe/H}]$, as was returned from this likelihood function, to $\Delta(\log N)/\Delta[\mathrm{Fe/H}]$. This slope suggests that the number of the metal-poor stars drops by a factor of ∼10 for every dex decrease in [Fe/H], supporting conventional wisdom that a factor of ∼ 10 fewer stars exist for each 1 dex drop in metallicity. Below $[\mathrm{Fe/H}] = -2.3$, the slope steepens to $(\Delta(\log N))/(\Delta[\mathrm{Fe/H}]) = 1.52 \pm 0.05$, implying that stars with metallicities below

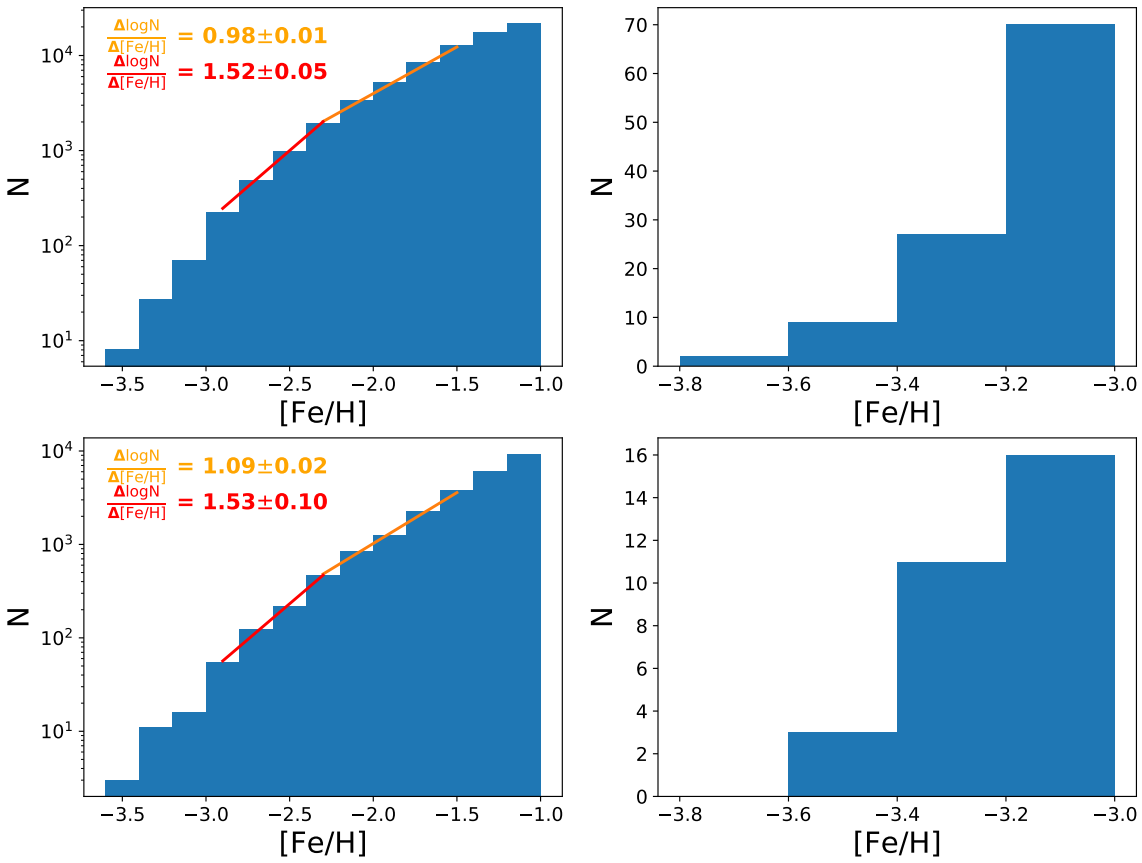

Figure 9-4 Top left: Metallicity distribution function (MDF) below [Fe/H] < -0.75 of $\sim$122,000 metal-poor giants. Best-fitting exponential fits are shown, $(\Delta(\log N))/(\Delta[\mathrm{Fe/H}]) = 0.98 \pm 0.01$ when $-2.3 <$ [Fe/H] < -1.5 and $(\Delta(\log N))/(\Delta[\mathrm{Fe/H}]) = 1.52 \pm 0.05$ when $-3.0 <$ [Fe/H] < -2.3. Fitting for the more metal-poor regime only includes stars [Fe/H] > -3.0, to avoid incompleteness effects (see Section 9.2 for discussion). Top right: MDF of stars with [Fe/H] < -3.0 in our sample. Bottom left and right: Same as top row, but only including stars with distances $<$5.0 kpc to minimize target selection effects (see Section 9.2 for discussion).

this cutoff are progressively more difficult to find as this corresponds to a drop by a factor of ∼33 for every dex decrease in [Fe/H]. This translates into a frequency of 1.5% of finding stars with [Fe/H] ~ -3.0 and 0.2% when [Fe/H] ~ -3.5 among stars with [Fe/H] < -1.5 within our sample. Overall, the MDF is remarkably smooth down to the lowest [Fe/H], as was also found in previous studies based on smaller samples [355, 443, 430, 234], and other large photometric studies [444, 418].

Only including stars with distances $< 5.0\,\mathrm{kpc}$, to account for target selection effects, results in a slope of $(\Delta(\log N))/(\Delta[\mathrm{Fe/H}])) = 1.09 \pm 0.02$ when $-2.3 <$ [Fe/H] < -1.5 and $(\Delta(\log N))/(\Delta[\mathrm{Fe/H}])) = 1.53 \pm 0.10$ when $-3.0 <$ [Fe/H] < -2.3. We note that the slope at the more metal-poor end is negligibly different, suggesting a robustness to target selection effects. However, the slope at the more metal-rich end is notably steeper. While this steepening plausibly does arise from addressing target selection effects that exclude metal-rich stars at large distances, it may also be caused by the exclusion of spatially distant stars that have an underlying MDF that is preferentially metal-poor [e.g., 419].

Our derived exponential slope of the MDF is consistent with that of previous spectroscopic studies [443, 445], but is steeper than what is found in others [444, 418]. By taking the relative ratio of the MDF in Schörck et al. [443] at [Fe/H] $= -3.0$ and [Fe/H] $= -2.3$ suggests an exponential slope of $(\Delta(\log N))/(\Delta[\mathrm{Fe/H}]) \sim 1.73$, which is comparable to our result of $\Delta \log(N)/\Delta[\mathrm{Fe/H}] = 1.52 \pm 0.05$ or 1.53 ± 0.10 in that regime. A similar calculation for the MDF presented in Allende Prieto et al. [445] suggests an exponential slope of $(\Delta(\log N))/(\Delta[\mathrm{Fe/H}]) \sim 1.66$. However, the same analysis returns an exponential slope of 0.98 from An et al. [444], and Youakim et al. [418] present a value of 1.0 ± 0.1, with which our derived slope is somewhat discrepant. This suggests that underlying selection effects between our samples might be affecting the slope. For instance, this study only focuses on relatively cool giant stars within $\sim 7\,\mathrm{kpc}$, whereas other studies purely focus on stars in the halo ($> 6\,\mathrm{kpc}$ away).

We also investigate how the shape of the MDF varies as a function of height above the galactic plane. In Figure 9-5, we show MDFs for four different scale heights. The closest range is $0.8 < |Z| < 1.2\,\mathrm{kpc}$, followed by $1.5 < |Z| < 2.0\,\mathrm{kpc}$, $3.0 < |Z| <$

4.0 kpc, and $5 < |Z| < 7$ kpc. At low $|Z|$, the thick disk component clearly dominates the higher [Fe/H] end of the distribution, but wanes beyond 2 kpc. By 3 kpc the more metal-rich population associated with the thick disk population no longer dominates the distribution, and the metal weak tail of the thick disk becomes apparent around [Fe/H] ~ -1.3. Finally, beyond 5 kpc, the halo dominates, with the MDF peaking at [Fe/H] ~ -1.5 and showing a significant metal-poor tail. The more metal-rich thick disk population appears to be entirely removed.

In Figure 9-5, we also fit the very metal-poor tail of the MDF ([Fe/H] < -2.3) with an exponential slope to see if variations occur with scale height. We find four slopes: $(\Delta(\log N))/(\Delta[\mathrm{Fe/H}]) = 1.41 \pm 0.19$ when $0.8 < |Z| < 1.2$ kpc, 1.63 ± 0.13 when $1.5 < |Z| < 2.0$ kpc, 1.46 ± 0.12 when $3.0 < |Z| < 4.0$ kpc, and 1.59 ± 0.13 when $5 < |Z| < 7$ kpc. Upon performing a chi-squared test of the hypothesis that the slope is constant as a function of $|Z|$, we find no evidence to reject that hypothesis. Consequently, from our analysis, there is no strong evidence that the behavior of the very metal-poor tail of the MDF varies as a function of scale height.

Finally, we note that metallicities derived from SkyMapper photometry are biased high in the case of carbon-enhanced stars, which would plausibly steepen our MDF since carbon-enhanced stars are more prevalent at low metallicities. To estimate whether this affect could appreciably alter our MDF, we used the sample of Placco et al. [8] to investigate the carbon abundance ([C/Fe]) of stars between $-3.0 <$[Fe/H]< -2.0. We find that the average carbon abundance of stars increases by 0.13 dex between [Fe/H] $= -2.0$ and [Fe/H] $= -3.0$. At a typical = 4500 K, such an increase in the carbon abundance stars with [Fe/H] $= -3.0$ would only increase the photometric metallicity by 0.07 dex. Consequently, while we do acknowledge that individual outliers with extremely high carbon abundances would appear to have much higher metallicities, at a population level, the metallicity of a typical star is not significantly affected.

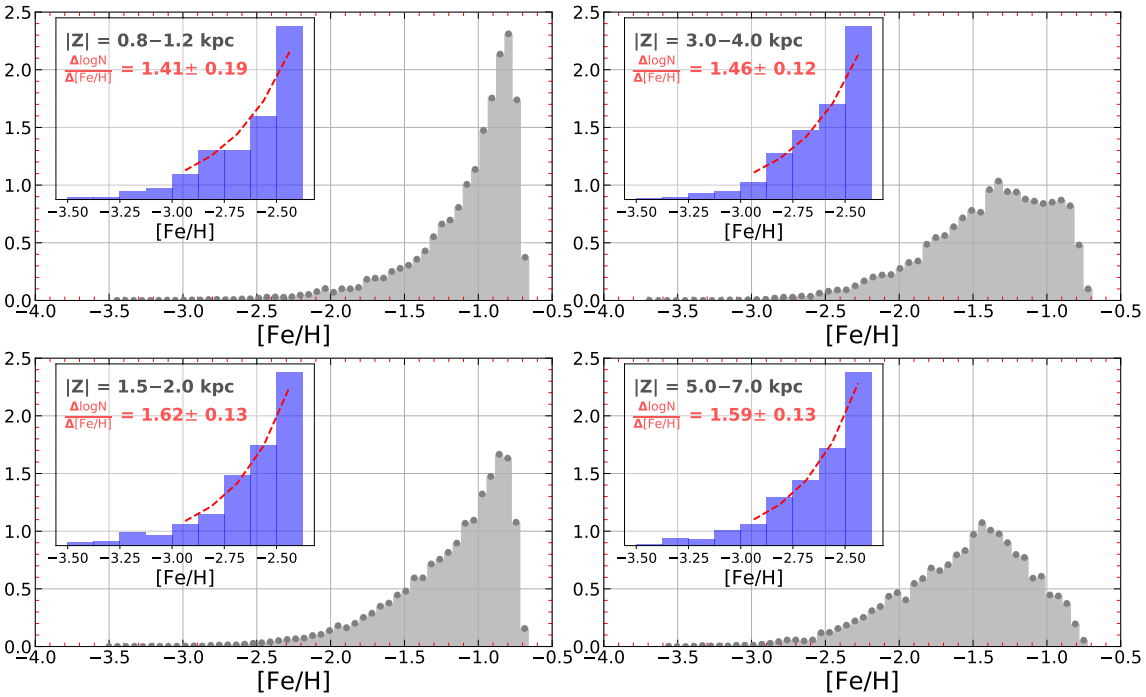

Figure 9-5 Metallicity distribution of ∼122,000 stars, arranged as a function of distance from the Galactic plane in four different ranges, mimicking the inner thick disk (top left), the outer thick disk (bottom left), the metal-weak tail of the thick disk (top right), and the halo (bottom right). Insets show the MDFs of stars with [Fe/H] < -2.3, with the best fitting exponential slope indicated.

9.4 Summary and Conclusion

We have presented a low-metallicity map of the Milky Way based on photometric metallicities obtained from new public SkyMapper DR2 data of ∼111,000 red giants in the Southern sky with $-3.75 \lesssim$ [Fe/H] $\lesssim -0.75$ and $g < 17$ out to ~ 7 kpc from the solar neighborhood. Based on a comparison with new high-resolution spectra as well as using several literature samples and surveys, we demonstrate this sample achieves reliable metallicity precision (σ ∼0.24 dex to 0.29 dex) down to [Fe/H] ~ -3.3. We display the spatial distribution of stars within the very and extremely metal-poor regimes providing an unprecedented view into the ancient, metal-poor Milky Way.

We find clear signatures of the components of the Milky Way in our dataset. Notably, the thick disk prominently appears in our population of stars with [Fe/H] > -1.50 (see Figure 9-3), and the transition from the thick disk to the inner halo is reflected in a sharp drop in metallicities around $|Z| \sim 2.8$ kpc (see Figure 9-2). The average metallicities of stars in our sample progressively decrease out to $|Z| \sim 7$ kpc. At even larger distances, we do not have enough coverage to confidently map out metallicity averages but observe hints of an additional small decrease, as expected for the outer halo. It is worth pointing out that a smooth distribution of very and extremely metal-poor stars exists across the entire sky covered by this sample, even within the more metal-rich thick disk. This highlights that the most metal-poor stars are well spread across the galaxy, likely owing to their orbital properties that regularly bring to the inner portions of the Galaxy. We explore this topic in a separate paper (M. Mardini et al. 2020, in prep), in which we quantify the kinematic properties of our sample of stars and find that ∼200 stars with [Fe/H] < -2.3 in our sample have orbits consistent with membership to the thick disk. This result further highlights that very and extremely metal-poor stars exist in the thick disk of the galaxy.

We are also able to quantify the shape of the MDF for [Fe/H] < -1.5. It is well fit by two exponential profiles with a slope of $\Delta \log(N)/\Delta$[Fe/H] $= 0.98 \pm 0.01$ for stars with $-2.3 <$ [Fe/H] < -1.5, and $\Delta \log(N)/\Delta$[Fe/H] $= 1.52 \pm 0.05$ when $-3.0 <$ [Fe/H] < -2.3. When only including stars within 5.0 kpc, to account for

biases from target selection, we derive slopes of $\Delta \log(N)/\Delta[\mathrm{Fe/H}] = 1.09 \pm 0.02$ for stars with $-2.3 < [\mathrm{Fe/H}] < -1.0$, and $\Delta \log(N)/\Delta[\mathrm{Fe/H}] = 1.53 \pm 0.10$ when $-3.0 < [\mathrm{Fe/H}] < -2.3$. In both cases, the MDF steepens at low metallicities, highlighting the difficulty of finding the most metal-poor stars. More intuitively, the slope from our entire sample implies that the number of metal-poor stars drops by a factor of $\sim$10 for every dex decrease in [Fe/H] when $-2.3 < [\mathrm{Fe/H}] < -1.0$ and a factor of $\sim$33 for every dex decrease in [Fe/H] when $-3.0 < [\mathrm{Fe/H}] < -2.3$. Unsurprisingly, we also find that the relative frequency of the most metal-poor stars increases as a function of $|Z|$, as 0.8% of stars in our sample have $[\mathrm{Fe/H}] < -2.5$ when $|Z| < 3\,\mathrm{kpc}$ but comprise 2.7% of stars when $|Z| > 3\,\mathrm{kpc}$. Finally, we find some evidence that the MDF for stars with $[\mathrm{Fe/H}] < -2.3$ is largely insensitive to scale height $|Z|$ out to $\sim 5\,\mathrm{kpc}$, suggesting that the most metal-poor stars are spatially distributed in every galactic component. Overall, our sample contains $\sim$140 giants with $[\mathrm{Fe/H}] < -3.0$, and $\sim$35 with $[\mathrm{Fe/H}] < -3.3$. Detailed follow-up studies of these stars are underway which should help to reveal the full extent of the nature and origin of the ancient component of our Milky Way.

Chapter 10

Conclusion

This thesis has presented several studies of the metal-poor stellar populations of the Milky Way and its satellite dwarf galaxies. Notably, this work has demonstrated that targeted, efficient photometric searches for metal-poor stars in UFDs eliminates the traditional inefficiencies related to identifying stars for study in these relic galaxies (Chapter 2). The application of these photometric techniques to just one UFD, Tucana II, doubled its population of known member stars and revealed a previously inaccessible, diffuse "halo" of stars out to $\sim$9 half-light radii from the center of this system (Chapters 3 and 4). This detection is the first direct evidence that some of the earliest galaxies may have inhabited extended, massive dark matter halos, and showed that this tiny ($\sim$ 3000 stars) relic system may have formed through the merger of even smaller galaxies. I also present work that greatly increased ($\sim$tripled) the number of known extremely metal-poor stars in the Sculptor dwarf galaxy (Chapter 5) and the number of very metal-poor stars in the Sagittarius dwarf galaxy (Chapters 6 and 7). These studies showed that Sculptor, much like the Milky Way halo, hosts a population of carbon-enhanced stars at the lowest metallicities ([Fe/H] < -3.0). This suggests some level of universality in early chemical evolution, or that the carbon-enhanced stars in the Milky Way halo plausibly originated from accreted analogs of dwarf spheroidal galaxies. The studies of the Sagittarius dwarf galaxy do not show this carbon-enhanced signature in the very metal-poor regime, but a larger sample, especially in the [Fe/H] < -3.0 regime, is needed for robust conclusions.

In Chapters 8 and 9, I present photometrically-derived metallicities of hundreds of thousands of stars in the Milky Way and present a low-metallicity map of our Galaxy out to $\sim 8\,\mathrm{kpc}$ using these metallicities and *Gaia* EDR3 data [111, 114, 115]. This work demonstrates the feasibility of deriving precise photometric metallicities down to the extremely metal-poor regime using public survey data with metallicity-sensitive imaging filters. The next generations of astronomical surveys (e.g., LSST) will have imaging filters that are demonstratively metallicity-sensitive, and luckily, the photometric methods presented in this thesis are highly modular and can readily be extended to these datasets for the next generation of Galactic Archaeology studies. This, in tandem with the next generation of 30 m class telescopes and large, multi-fiber surveys (e.g., Subaru/PFS, DESI) will comprehensively map the Milky Way halo and its satellite galaxies and will certainly reveal a plethora of serendipitous discoveries. Unsurprisingly, I remain eager to see what these next generations of studies will reveal,

Bibliography

[1] Matthew G. Walker, Mario Mateo, Edward W. Olszewski, Sergey Koposov, Vasily Belokurov, Prashin Jethwa, David L. Nidever, Vincent Bonnivard, III Bailey, John I., and Eric F. Bell. Magellan/M2FS Spectroscopy of Tucana 2 and Grus 1. ApJ, 819(1):53, Mar 2016. doi: 10.3847/0004-637X/819/1/53.

[2] Alexander P. Ji, Anna Frebel, Rana Ezzeddine, and Andrew R. Casey. Chemical Diversity in the Ultra-faint Dwarf Galaxy Tucana II. ApJ, 832(1):L3, Nov 2016. doi: 10.3847/2041-8205/832/1/L3.

[3] Heather R. Jacobson, Stefan Keller, Anna Frebel, Andrew R. Casey, Martin Asplund, Michael S. Bessell, Gary S. Da Costa, Karin Lind, Anna F. Marino, and John E. Norris. High-Resolution Spectroscopic Study of Extremely Metal-Poor Star Candidates from the SkyMapper Survey. ApJ, 807(2):171, Jul 2015. doi: 10.1088/0004-637X/807/2/171.

[4] Evan N. Kirby, Michelle Guo, Andrew J. Zhang, Michelle Deng, Judith G. Cohen, Puragra Guhathakurta, Matthew D. Shetrone, Young Sun Lee, and Luca Rizzi. Carbon in Red Giants in Globular Clusters and Dwarf Spheroidal Galaxies. ApJ, 801(2):125, Mar 2015. doi: 10.1088/0004-637X/801/2/125.

[5] J. D. Simon, H. R. Jacobson, A. Frebel, I. B. Thompson, J. J. Adams, and S. A. Shectman. Chemical Signatures of the First Supernovae in the Sculptor Dwarf Spheroidal Galaxy. ApJ, 802:93, April 2015. doi: 10.1088/0004-637X/802/2/93.

[6] P. Jablonka, P. North, L. Mashonkina, V. Hill, Y. Revaz, M. Shetrone, E. Starkenburg, M. Irwin, E. Tolstoy, G. Battaglia, K. Venn, A. Helmi, F. Primas, and P. François. The early days of the Sculptor dwarf spheroidal galaxy. A&A, 583:A67, November 2015. doi: 10.1051/0004-6361/201525661.

[7] O. A. Gonzalez, M. Rejkuba, M. Zoccali, V. Hill, G. Battaglia, C. Babusiaux, D. Minniti, B. Barbuy, A. Alves-Brito, A. Renzini, A. Gomez, and S. Ortolani. Alpha element abundances and gradients in the Milky Way bulge from FLAMES-GIRAFFE spectra of 650 K giants. A&A, 530:A54, June 2011. doi: 10.1051/0004-6361/201116548.

[8] V. M. Placco, A. Frebel, T. C. Beers, and R. J. Stancliffe. Carbon-enhanced Metal-poor Star Frequencies in the Galaxy: Corrections for the Effect of Evo-

lutionary Status on Carbon Abundances. ApJ, 797:21, December 2014. doi: 10.1088/0004-637X/797/1/21.

[9] C. Wolf, C. A. Onken, L. C. Luvaul, B. P. Schmidt, M. S. Bessell, S.-W. Chang, G. S. Da Costa, D. Mackey, T. Martin-Jones, S. J. Murphy, T. Preston, R. A. Scalzo, L. Shao, J. Smillie, P. Tisserand, M. C. White, and F. Yuan. SkyMapper Southern Survey: First Data Release (DR1). PASA, 35:e010, February 2018. doi: 10.1017/pasa.2018.5.

[10] A. Dotter, B. Chaboyer, D. Jevremović, V. Kostov, E. Baron, and J. W. Ferguson. The Dartmouth Stellar Evolution Database. ApJS, 178:89–101, September 2008. doi: 10.1086/589654.

[11] E. Carretta, A. Bragaglia, R. Gratton, V. D'Orazi, and S. Lucatello. Intrinsic iron spread and a new metallicity scale for globular clusters. A&A, 508(2): 695–706, Dec 2009. doi: 10.1051/0004-6361/200913003.

[12] Anirudh Chiti, Anna Frebel, Alexander P. Ji, Helmut Jerjen, Dongwon Kim, and John E. Norris. Chemical Abundances of New Member Stars in the Tucana II Dwarf Galaxy. ApJ, 857(1):74, Apr 2018. doi: 10.3847/1538-4357/aab4fc.

[13] Sergey E. Koposov, Vasily Belokurov, Gabriel Torrealba, and N. Wyn Evans. Beasts of the Southern Wild: Discovery of Nine Ultra Faint Satellites in the Vicinity of the Magellanic Clouds. ApJ, 805(2):130, Jun 2015. doi: 10.1088/0004-637X/805/2/130.

[14] Aaron Dotter. MESA Isochrones and Stellar Tracks (MIST) 0: Methods for the Construction of Stellar Isochrones. ApJS, 222(1):8, January 2016. doi: 10.3847/0067-0049/222/1/8.

[15] Jieun Choi, Aaron Dotter, Charlie Conroy, Matteo Cantiello, Bill Paxton, and Benjamin D. Johnson. Mesa Isochrones and Stellar Tracks (MIST). I. Solar-scaled Models. ApJ, 823(2):102, June 2016. doi: 10.3847/0004-637X/823/2/102.

[16] A. Frebel. Stellar archaeology: Exploring the Universe with metal-poor stars. *Astronomische Nachrichten*, 331:474–488, May 2010. doi: 10.1002/asna.201011362.

[17] I. U. Roederer, G. W. Preston, I. B. Thompson, S. A. Shectman, C. Sneden, G. S. Burley, and D. D. Kelson. A Search for Stars of Very Low Metal Abundance. VI. Detailed Abundances of 313 Metal-poor Stars. AJ, 147:136, June 2014. doi: 10.1088/0004-6256/147/6/136.

[18] A. Koch, A. McWilliam, E. K. Grebel, D. B. Zucker, and V. Belokurov. The Highly Unusual Chemical Composition of the Hercules Dwarf Spheroidal Galaxy. ApJ, 688:L13, November 2008. doi: 10.1086/595001.

[19] S. Feltzing, K. Eriksson, J. Kleyna, and M. I. Wilkinson. Evidence of enrichment by individual SN from elemental abundance ratios in the very metal-poor dSph galaxy Boötes I. A&A, 508:L1–L4, December 2009. doi: 10.1051/0004-6361/200912833.

[20] A. Frebel, E. N. Kirby, and J. D. Simon. Linking dwarf galaxies to halo building blocks with the most metal-poor star in Sculptor. Nature, 464:72–75, March 2010. doi: 10.1038/nature08772.

[21] A. Frebel, J. D. Simon, M. Geha, and B. Willman. High-Resolution Spectroscopy of Extremely Metal-Poor Stars in the Least Evolved Galaxies: Ursa Major II and Coma Berenices. ApJ, 708:560–583, January 2010. doi: 10.1088/0004-637X/708/1/560.

[22] A. Frebel, J. D. Simon, and E. N. Kirby. Segue 1: An Unevolved Fossil Galaxy from the Early Universe. ApJ, 786:74, May 2014. doi: 10.1088/0004-637X/786/1/74.

[23] J. E. Norris, G. Gilmore, R. F. G. Wyse, D. Yong, and A. Frebel. An Extremely Carbon-rich, Extremely Metal-poor Star in the Segue 1 System. ApJ, 722:L104–L109, October 2010. doi: 10.1088/2041-8205/722/1/L104.

[24] J. E. Norris, D. Yong, G. Gilmore, and R. F. G. Wyse. Boo-1137an Extremely Metal-Poor Star in the Ultra-Faint Dwarf Spheroidal Galaxy Boötes I. ApJ, 711:350–360, March 2010. doi: 10.1088/0004-637X/711/1/350.

[25] J. D. Simon, A. Frebel, A. McWilliam, E. N. Kirby, and I. B. Thompson. High-resolution Spectroscopy of Extremely Metal-poor Stars in the Least Evolved Galaxies: Leo IV. ApJ, 716:446–452, June 2010. doi: 10.1088/0004-637X/716/1/446.

[26] G. Gilmore, J. E. Norris, L. Monaco, D. Yong, R. F. G. Wyse, and D. Geisler. Elemental Abundances and their Implications for the Chemical Enrichment of the Boötes I Ultrafaint Galaxy. ApJ, 763:61, January 2013. doi: 10.1088/0004-637X/763/1/61.

[27] A. Koch, S. Feltzing, D. Adén, and F. Matteucci. Neutron-capture element deficiency of the Hercules dwarf spheroidal galaxy. A&A, 554:A5, June 2013. doi: 10.1051/0004-6361/201220742.

[28] M. N. Ishigaki, W. Aoki, N. Arimoto, and S. Okamoto. Chemical compositions of six metal-poor stars in the ultra-faint dwarf spheroidal galaxy Boötes I. A&A, 562:A146, February 2014. doi: 10.1051/0004-6361/201322796.

[29] A. Koch and R. M. Rich. A Chemical Confirmation of the Faint Boötes II Dwarf Spheroidal Galaxy. ApJ, 794:89, October 2014. doi: 10.1088/0004-637X/794/1/89.

[30] I. U. Roederer and E. N. Kirby. Detailed abundance analysis of the brightest star in Segue 2, the least massive galaxy. MNRAS, 440:2665–2675, May 2014. doi: 10.1093/mnras/stu491.

[31] A. P. Ji, A. Frebel, J. D. Simon, and A. Chiti. Complete Element Abundances of Nine Stars in the r-process Galaxy Reticulum II. ApJ, 830:93, October 2016. doi: 10.3847/0004-637X/830/2/93.

[32] A. P. Ji, A. Frebel, J. D. Simon, and A. Chiti. Complete Element Abundances of Nine Stars in the r-process Galaxy Reticulum II. ApJ, 830:93, October 2016. doi: 10.3847/0004-637X/830/2/93.

[33] T. T. Hansen, J. D. Simon, J. L. Marshall, T. S. Li, D. Carollo, D. L. DePoy, D. Q. Nagasawa, R. A. Bernstein, A. Drlica-Wagner, F. B. Abdalla, S. Allam, J. Annis, K. Bechtol, A. Benoit-Lévy, D. Brooks, E. Buckley-Geer, A. Carnero Rosell, M. Carrasco Kind, J. Carretero, C. E. Cunha, L. N. da Costa, S. Desai, T. F. Eifler, A. Fausti Neto, B. Flaugher, J. Frieman, J. García-Bellido, E. Gaztanaga, D. W. Gerdes, D. Gruen, R. A. Gruendl, J. Gschwend, G. Gutierrez, D. J. James, E. Krause, K. Kuehn, N. Kuropatkin, O. Lahav, R. Miquel, A. A. Plazas, A. K. Romer, E. Sanchez, B. Santiago, V. Scarpine, R. C. Smith, M. Soares-Santos, F. Sobreira, E. Suchyta, M. E. C. Swanson, G. Tarle, A. R. Walker, and DES Collaboration. An r-process Enhanced Star in the Dwarf Galaxy Tucana III. ApJ, 838:44, March 2017. doi: 10.3847/1538-4357/aa634a.

[34] E. N. Kirby, J. G. Cohen, J. D. Simon, P. Guhathakurta, A. O. Thygesen, and G. E. Duggan. Triangulum II. Not Especially Dense After All. ApJ, 838:83, April 2017. doi: 10.3847/1538-4357/aa6570.

[35] K. A. Venn, E. Starkenburg, L. Malo, N. Martin, and B. P. M. Laevens. Gemini/GRACES spectroscopy of stars in Tri II. MNRAS, 466:3741–3752, April 2017. doi: 10.1093/mnras/stw3198.

[36] D. Q. Nagasawa, J. L. Marshall, T. S. Li, T. T. Hansen, J. D. Simon, R. A. Bernstein, E. Balbinot, A. Drlica-Wagner, A. B. Pace, L. E. Strigari, C. M. Pellegrino, D. L. DePoy, N. B. Suntzeff, K. Bechtol, A. R. Walker, T. M. C. Abbott, F. B. Abdalla, S. Allam, J. Annis, A. Benoit-Lévy, E. Bertin, D. Brooks, A. Carnero Rosell, M. Carrasco Kind, J. Carretero, C. E. Cunha, C. B. D'Andrea, L. N. da Costa, C. Davis, S. Desai, P. Doel, T. F. Eifler, B. Flaugher, P. Fosalba, J. Frieman, J. García-Bellido, E. Gaztanaga, D. W. Gerdes, D. Gruen, R. A. Gruendl, J. Gschwend, G. Gutierrez, W. G. Hartley, K. Honscheid, D. J. James, T. Jeltema, E. Krause, K. Kuehn, S. Kuhlmann, N. Kuropatkin, M. March, R. Miquel, B. Nord, A. Roodman, E. Sanchez, B. Santiago, V. Scarpine, R. Schindler, M. Schubnell, I. Sevilla-Noarbe, M. Smith, R. C. Smith, M. Soares-Santos, F. Sobreira, E. Suchyta, G. Tarle, D. Thomas, D. L. Tucker, R. H. Wechsler, R. C. Wolf, and B. Yanny. Chemical Abundance Analysis of Three α-poor, Metal-poor Stars

in the Ultrafaint Dwarf Galaxy Horologium I. ApJ, 852:99, January 2018. doi: 10.3847/1538-4357/aaa01d.

[37] K. Bechtol, A. Drlica-Wagner, E. Balbinot, A. Pieres, J. D. Simon, B. Yanny, B. Santiago, R. H. Wechsler, J. Frieman, and A. R. Walker. Eight New Milky Way Companions Discovered in First-year Dark Energy Survey Data. ApJ, 807 (1):50, Jul 2015. doi: 10.1088/0004-637X/807/1/50.

[38] Joe Wolf, Gregory D. Martinez, James S. Bullock, Manoj Kaplinghat, Marla Geha, Ricardo R. Muñoz, Joshua D. Simon, and Frank F. Avedo. Accurate masses for dispersion-supported galaxies. MNRAS, 406(2):1220–1237, August 2010. doi: 10.1111/j.1365-2966.2010.16753.x.

[39] Anirudh Chiti, Anna Frebel, Helmut Jerjen, Dongwon Kim, and John E. Norris. Stellar Metallicities from SkyMapper Photometry I: A Study of the Tucana II Ultra-faint Dwarf Galaxy. ApJ, 891(1):8, March 2020. doi: 10.3847/1538-4357/ab6d72.

[40] Bill Paxton, Lars Bildsten, Aaron Dotter, Falk Herwig, Pierre Lesaffre, and Frank Timmes. Modules for Experiments in Stellar Astrophysics (MESA). ApJS, 192(1):3, January 2011. doi: 10.1088/0067-0049/192/1/3.

[41] Bill Paxton, Matteo Cantiello, Phil Arras, Lars Bildsten, Edward F. Brown, Aaron Dotter, Christopher Mankovich, M. H. Montgomery, Dennis Stello, F. X. Timmes, and Richard Townsend. Modules for Experiments in Stellar Astrophysics (MESA): Planets, Oscillations, Rotation, and Massive Stars. ApJS, 208(1):4, September 2013. doi: 10.1088/0067-0049/208/1/4.

[42] Bill Paxton, Pablo Marchant, Josiah Schwab, Evan B. Bauer, Lars Bildsten, Matteo Cantiello, Luc Dessart, R. Farmer, H. Hu, N. Langer, R. H. D. Townsend, Dean M. Townsley, and F. X. Timmes. Modules for Experiments in Stellar Astrophysics (MESA): Binaries, Pulsations, and Explosions. ApJS, 220 (1):15, September 2015. doi: 10.1088/0067-0049/220/1/15.

[43] Alessandro Bressan, Paola Marigo, Léo. Girardi, Bernardo Salasnich, Claudia Dal Cero, Stefano Rubele, and Ambra Nanni. PARSEC: stellar tracks and isochrones with the PAdova and TRieste Stellar Evolution Code. MNRAS, 427 (1):127–145, November 2012. doi: 10.1111/j.1365-2966.2012.21948.x.

[44] Yang Chen, Léo Girardi, Alessandro Bressan, Paola Marigo, Mauro Barbieri, and Xu Kong. Improving PARSEC models for very low mass stars. MNRAS, 444(3):2525–2543, November 2014. doi: 10.1093/mnras/stu1605.

[45] Jing Tang, Alessandro Bressan, Philip Rosenfield, Alessandra Slemer, Paola Marigo, Léo Girardi, and Luciana Bianchi. New PARSEC evolutionary tracks of massive stars at low metallicity: testing canonical stellar evolution in nearby star-forming dwarf galaxies. MNRAS, 445(4):4287–4305, December 2014. doi: 10.1093/mnras/stu2029.

[46] Yang Chen, Alessandro Bressan, Léo Girardi, Paola Marigo, Xu Kong, and Antonio Lanza. PARSEC evolutionary tracks of massive stars up to 350 $M_?$ at metallicities $0.0001 \leq Z \leq 0.04$. MNRAS, 452(1):1068–1080, September 2015. doi: 10.1093/mnras/stv1281.

[47] Paola Marigo, Léo Girardi, Alessandro Bressan, Philip Rosenfield, Bernhard Aringer, Yang Chen, Marco Dussin, Ambra Nanni, Giada Pastorelli, Thaíse S. Rodrigues, Michele Trabucchi, Sara Bladh, Julianne Dalcanton, Martin A. T. Groenewegen, Josefina Montalbán, and Peter R. Wood. A New Generation of PARSEC-COLIBRI Stellar Isochrones Including the TP-AGB Phase. ApJ, 835 (1):77, January 2017. doi: 10.3847/1538-4357/835/1/77.

[48] Giada Pastorelli, Paola Marigo, Léo Girardi, Yang Chen, Stefano Rubele, Michele Trabucchi, Bernhard Aringer, Sara Bladh, Alessandro Bressan, Josefina Montalbán, Martha L. Boyer, Julianne J. Dalcanton, Kjell Eriksson, Martin A. T. Groenewegen, Susanne Höfner, Thomas Lebzelter, Ambra Nanni, Philip Rosenfield, Peter R. Wood, and Maria-Rosa L. Cioni. Constraining the thermally pulsing asymptotic giant branch phase with resolved stellar populations in the Small Magellanic Cloud. MNRAS, 485(4):5666–5692, June 2019. doi: 10.1093/mnras/stz725.

[49] M. A. Czekaj, A. C. Robin, F. Figueras, X. Luri, and M. Haywood. The Besançon Galaxy model renewed. I. Constraints on the local star formation history from Tycho data. A&A, 564:A102, April 2014. doi: 10.1051/0004-6361/201322139.

[50] M. G. Coleman, G. S. Da Costa, and J. Bland-Hawthorn. The Absence of Extratidal Structure in the Sculptor Dwarf Spheroidal Galaxy. AJ, 130:1065–1082, September 2005. doi: 10.1086/432662.

[51] E. N. Kirby, P. Guhathakurta, J. D. Simon, M. C. Geha, C. M. Rockosi, C. Sneden, J. G. Cohen, S. T. Sohn, S. R. Majewski, and M. Siegel. Multi-element Abundance Measurements from Medium-resolution Spectra. II. Catalog of Stars in Milky Way Dwarf Satellite Galaxies. ApJS, 191:352–375, December 2010. doi: 10.1088/0067-0049/191/2/352.

[52] T. C. Beers, S. Rossi, J. E. Norris, S. G. Ryan, and T. Shefler. Estimation of Stellar Metal Abundance. II. A Recalibration of the Ca II K Technique, and the Autocorrelation Function Method. AJ, 117:981–1009, February 1999. doi: 10.1086/300727.

[53] T. Masseron, B. Plez, S. Van Eck, R. Colin, I. Daoutidis, M. Godefroid, P.-F. Coheur, P. Bernath, A. Jorissen, and N. Christlieb. CH in stellar atmospheres: an extensive linelist. A&A, 571:A47, November 2014. doi: 10.1051/0004-6361/201423956.

[54] W. Aoki, T. C. Beers, N. Christlieb, J. E. Norris, S. G. Ryan, and S. Tsangarides. Carbon-enhanced Metal-poor Stars. I. Chemical Compositions of 26 Stars. ApJ, 655:492–521, January 2007. doi: 10.1086/509817.

[55] A. Frebel, N. Christlieb, J. E. Norris, C. Thom, T. C. Beers, and J. Rhee. Discovery of HE 1523-0901, a Strongly r-Process-enhanced Metal-poor Star with Detected Uranium. ApJ, 660:L117–L120, May 2007. doi: 10.1086/518122.

[56] P. Jofré, U. Heiter, C. Soubiran, S. Blanco-Cuaresma, C. C. Worley, E. Pancino, T. Cantat-Gaudin, L. Magrini, M. Bergemann, J. I. González Hernández, V. Hill, C. Lardo, P. de Laverny, K. Lind, T. Masseron, D. Montes, A. Mucciarelli, T. Nordlander, A. Recio Blanco, J. Sobeck, R. Sordo, S. G. Sousa, H. Tabernero, A. Vallenari, and S. Van Eck. Gaia FGK benchmark stars: Metallicity. A&A, 564:A133, April 2014. doi: 10.1051/0004-6361/201322440.

[57] C. J. Hansen, M. El-Souri, L. Monaco, S. Villanova, P. Bonifacio, E. Caffau, and L. Sbordone. Ages and Heavy Element Abundances from Very Metal-poor Stars in the Sagittarius Dwarf Galaxy. ApJ, 855:83, March 2018. doi: 10.3847/1538-4357/aa978f.

[58] C. Boeche and E. K. Grebel. SP_Ace: a new code to derive stellar parameters and elemental abundances. A&A, 587:A2, March 2016. doi: 10.1051/0004-6361/201526758.

[59] Anna Frebel, Andrew R. Casey, Heather R. Jacobson, and Qinsi Yu. Deriving Stellar Effective Temperatures of Metal-poor Stars with the Excitation Potential Method. ApJ, 769(1):57, May 2013. doi: 10.1088/0004-637X/769/1/57.

[60] Bill Paxton, Josiah Schwab, Evan B. Bauer, Lars Bildsten, Sergei Blinnikov, Paul Duffell, R. Farmer, Jared A. Goldberg, Pablo Marchant, Elena Sorokina, Anne Thoul, Richard H. D. Townsend, and F. X. Timmes. Modules for Experiments in Stellar Astrophysics (MESA): Convective Boundaries, Element Diffusion, and Massive Star Explosions. ApJS, 234(2):34, February 2018. doi: 10.3847/1538-4365/aaa5a8.

[61] Peter S. Ferguson and Louis E. Strigari. Three-dimensional structure of the Sagittarius dwarf spheroidal core from RR Lyrae. MNRAS, 495(4):4124–4134, May 2020. doi: 10.1093/mnras/staa1404.

[62] Rana Ezzeddine, Kaitlin Rasmussen, Anna Frebel, Anirudh Chiti, Karina Hinojisa, Vinicius M. Placco, Alexander P. Ji, Timothy C. Beers, Terese T. Hansen, Ian U. Roederer, Charli M. Sakari, and Jorge Melendez. The R-Process Alliance: First Magellan/MIKE Release from the Southern Search for R-process-enhanced Stars. ApJ, 898(2):150, August 2020. doi: 10.3847/1538-4357/ab9d1a.

[63] D. J. Schlegel, D. P. Finkbeiner, and M. Davis. Maps of Dust Infrared Emission for Use in Estimation of Reddening and Cosmic Microwave Background Radiation Foregrounds. ApJ, 500:525–553, June 1998. doi: 10.1086/305772.

[64] A. F. Marino, G. S. Da Costa, A. R. Casey, M. Asplund, M. S. Bessell, A. Frebel, S. C. Keller, K. Lind, A. D. Mackey, S. J. Murphy, T. Nordlander, J. E. Norris, B. P. Schmidt, and D. Yong. Keck HIRES spectroscopy of SkyMapper commissioning survey candidate extremely metal-poor stars. MNRAS, 485(4): 5153–5167, June 2019. doi: 10.1093/mnras/stz645.

[65] P. S. Barklem, N. Christlieb, T. C. Beers, V. Hill, M. S. Bessell, J. Holmberg, B. Marsteller, S. Rossi, F. J. Zickgraf, and D. Reimers. The Hamburg/ESO R-process enhanced star survey (HERES). II. Spectroscopic analysis of the survey sample. A&A, 439(1):129–151, August 2005. doi: 10.1051/0004-6361:20052967.

[66] Planck Collaboration, P. A. R. Ade, N. Aghanim, M. Arnaud, M. Ashdown, J. Aumont, C. Baccigalupi, A. J. Banday, R. B. Barreiro, J. G. Bartlett, N. Bartolo, E. Battaner, R. Battye, K. Benabed, A. Benoît, A. Benoit-Lévy, J. P. Bernard, M. Bersanelli, P. Bielewicz, J. J. Bock, A. Bonaldi, L. Bonavera, J. R. Bond, J. Borrill, F. R. Bouchet, F. Boulanger, M. Bucher, C. Burigana, R. C. Butler, E. Calabrese, J. F. Cardoso, A. Catalano, A. Challinor, A. Chamballu, R. R. Chary, H. C. Chiang, J. Chluba, P. R. Christensen, S. Church, D. L. Clements, S. Colombi, L. P. L. Colombo, C. Combet, A. Coulais, B. P. Crill, A. Curto, F. Cuttaia, L. Danese, R. D. Davies, R. J. Davis, P. de Bernardis, A. de Rosa, G. de Zotti, J. Delabrouille, F. X. Désert, E. Di Valentino, C. Dickinson, J. M. Diego, K. Dolag, H. Dole, S. Donzelli, O. Doré, M. Douspis, A. Ducout, J. Dunkley, X. Dupac, G. Efstathiou, F. Elsner, T. A. Enßlin, H. K. Eriksen, M. Farhang, J. Fergusson, F. Finelli, O. Forni, M. Frailis, A. A. Fraisse, E. Franceschi, A. Frejsel, S. Galeotta, S. Galli, K. Ganga, C. Gauthier, M. Gerbino, T. Ghosh, M. Giard, Y. Giraud-Héraud, E. Giusarma, E. Gjerløw, J. González-Nuevo, K. M. Górski, S. Gratton, A. Gregorio, A. Gruppuso, J. E. Gudmundsson, J. Hamann, F. K. Hansen, D. Hanson, D. L. Harrison, G. Helou, S. Henrot-Versillé, C. Hernández-Monteagudo, D. Herranz, S. R. Hildebrandt, E. Hivon, M. Hobson, W. A. Holmes, A. Hornstrup, W. Hovest, Z. Huang, K. M. Huffenberger, G. Hurier, A. H. Jaffe, T. R. Jaffe, W. C. Jones, M. Juvela, E. Keihänen, R. Keskitalo, T. S. Kisner, R. Kneissl, J. Knoche, L. Knox, M. Kunz, H. Kurki-Suonio, G. Lagache, A. Lähteenmäki, J. M. Lamarre, A. Lasenby, M. Lattanzi, C. R. Lawrence, J. P. Leahy, R. Leonardi, J. Lesgourgues, F. Levrier, A. Lewis, M. Liguori, P. B. Lilje, M. Linden-Vørnle, M. López-Caniego, P. M. Lubin, J. F. Macías-Pérez, G. Maggio, D. Maino, N. Mandolesi, A. Mangilli, A. Marchini, M. Maris, P. G. Martin, M. Martinelli, E. Martínez-González, S. Masi, S. Matarrese, P. McGehee, P. R. Meinhold, A. Melchiorri, J. B. Melin, L. Mendes, A. Mennella, M. Migliaccio, M. Millea, S. Mitra, M. A. Miville-Deschênes, A. Moneti, L. Montier, G. Morgante, D. Mortlock, A. Moss, D. Munshi, J. A. Murphy, P. Naselsky, F. Nati, P. Natoli, C. B. Netterfield, H. U. Nørgaard-Nielsen, F. Noviello, D. Novikov, I. Novikov, C. A. Oxborrow, F. Paci, L. Pagano, F. Pajot, R. Paladini, D. Paoletti, B. Partridge, F. Pasian, G. Patanchon, T. J. Pearson, O. Perdereau, L. Perotto, F. Perrotta, V. Pettorino, F. Piacentini, M. Piat, E. Pierpaoli, D. Pietrobon, S. Plaszczynski,

E. Pointecouteau, G. Polenta, L. Popa, G. W. Pratt, G. Prézeau, S. Prunet, J. L. Puget, J. P. Rachen, W. T. Reach, R. Rebolo, M. Reinecke, M. Remazeilles, C. Renault, A. Renzi, I. Ristorcelli, G. Rocha, C. Rosset, M. Rossetti, G. Roudier, B. Rouillé d'Orfeuil, M. Rowan-Robinson, J. A. Rubiño-Martín, B. Rusholme, N. Said, V. Salvatelli, L. Salvati, M. Sandri, D. Santos, M. Savelainen, G. Savini, D. Scott, M. D. Seiffert, P. Serra, E. P. S. Shellard, L. D. Spencer, M. Spinelli, V. Stolyarov, R. Stompor, R. Sudiwala, R. Sunyaev, D. Sutton, A. S. Suur-Uski, J. F. Sygnet, J. A. Tauber, L. Terenzi, L. Toffolatti, M. Tomasi, M. Tristram, T. Trombetti, M. Tucci, J. Tuovinen, M. Türler, G. Umana, L. Valenziano, J. Valiviita, F. Van Tent, P. Vielva, F. Villa, L. A. Wade, B. D. Wandelt, I. K. Wehus, M. White, S. D. M. White, A. Wilkinson, D. Yvon, A. Zacchei, and A. Zonca. Planck 2015 results. XIII. Cosmological parameters. A&A, 594:A13, September 2016. doi: 10.1051/0004-6361/201525830.

[67] M. Tegmark. Doppler Peaks on all that: CMB Anisotropies and What They Can Tell Us. In S. Bonometto, J. R. Primack, and A. Provenzale, editors, *Dark Matter in the Universe*, page 379, January 1996.

[68] Annika H. G. Peter. Dark Matter: A Brief Review. *arXiv e-prints*, art. arXiv:1201.3942, January 2012.

[69] R. Barkana and A. Loeb. In the beginning: the first sources of light and the reionization of the universe. Phys. Rep., 349(2):125–238, July 2001. doi: 10.1016/S0370-1573(01)00019-9.

[70] Volker Bromm and Naoki Yoshida. The First Galaxies. ARA&A, 49(1):373–407, September 2011. doi: 10.1146/annurev-astro-081710-102608.

[71] Linhua Jiang, Nobunari Kashikawa, Shu Wang, Gregory Walth, Luis C. Ho, Zheng Cai, Eiichi Egami, Xiaohui Fan, Kei Ito, Yongming Liang, Daniel Schaerer, and Daniel P. Stark. Evidence for GN-z11 as a luminous galaxy at redshift 10.957. *Nature Astronomy*, 5:256–261, January 2021. doi: 10.1038/s41550-020-01275-y.

[72] Judd D. Bowman, Alan E. E. Rogers, Raul A. Monsalve, Thomas J. Mozdzen, and Nivedita Mahesh. An absorption profile centred at 78 megahertz in the sky-averaged spectrum. Nature, 555(7694):67–70, March 2018. doi: 10.1038/nature25792.

[73]

[74] Naoki Yoshida, Kazuyuki Omukai, Lars Hernquist, and Tom Abel. Formation of Primordial Stars in a ΛCDM Universe. ApJ, 652(1):6–25, November 2006. doi: 10.1086/507978.

[75] Thomas H. Greif, Jarrett L. Johnson, Volker Bromm, and Ralf S. Klessen. The First Supernova Explosions: Energetics, Feedback, and Chemical Enrichment. ApJ, 670(1):1–14, November 2007. doi: 10.1086/522028.

[76] Volker Bromm, Paolo S. Coppi, and Richard B. Larson. The Formation of the First Stars. I. The Primordial Star-forming Cloud. ApJ, 564(1):23–51, January 2002. doi: 10.1086/323947.

[77] Mattis Magg, Tilman Hartwig, Bhaskar Agarwal, Anna Frebel, Simon C. O. Glover, Brendan F. Griffen, and Ralf S. Klessen. Predicting the locations of possible long-lived low-mass first stars: importance of satellite dwarf galaxies. MNRAS, 473(4):5308–5323, February 2018. doi: 10.1093/mnras/stx2729.

[78] Antonino Del Popolo and Morgan Le Delliou. Small Scale Problems of the ΛCDM Model: A Short Review. *Galaxies*, 5(1):17, February 2017. doi: 10.3390/galaxies5010017.

[79] Jennifer A. Johnson. Populating the periodic table: Nucleosynthesis of the elements. *Science*, 363(6426):474–478, February 2019. doi: 10.1126/science.aau9540.

[80] B. Cseh, M. Lugaro, V. D'Orazi, D. B. de Castro, C. B. Pereira, A. I. Karakas, L. Molnár, E. Plachy, R. Szabó, M. Pignatari, and S. Cristallo. The s process in AGB stars as constrained by a large sample of barium stars. A&A, 620:A146, December 2018. doi: 10.1051/0004-6361/201834079.

[81] N. R. Tanvir, A. J. Levan, A. S. Fruchter, J. Hjorth, R. A. Hounsell, K. Wiersema, and R. L. Tunnicliffe. A 'kilonova' associated with the short-duration γ-ray burst GRB 130603B. Nature, 500(7464):547–549, August 2013. doi: 10.1038/nature12505.

[82] A. P. Ji, A. Frebel, A. Chiti, and J. D. Simon. R-process enrichment from a single event in an ancient dwarf galaxy. Nature, 531:610–613, March 2016. doi: 10.1038/nature17425.

[83] M. R. Drout, A. L. Piro, B. J. Shappee, C. D. Kilpatrick, J. D. Simon, C. Contreras, D. A. Coulter, R. J. Foley, M. R. Siebert, N. Morrell, K. Boutsia, F. Di Mille, T. W. S. Holoien, D. Kasen, J. A. Kollmeier, B. F. Madore, A. J. Monson, A. Murguia-Berthier, Y. C. Pan, J. X. Prochaska, E. Ramirez-Ruiz, A. Rest, C. Adams, K. Alatalo, E. Bañados, J. Baughman, T. C. Beers, R. A. Bernstein, T. Bitsakis, A. Campillay, T. T. Hansen, C. R. Higgs, A. P. Ji, G. Maravelias, J. L. Marshall, C. Moni Bidin, J. L. Prieto, K. C. Rasmussen, C. Rojas-Bravo, A. L. Strom, N. Ulloa, J. Vargas-González, Z. Wan, and D. D. Whitten. Light curves of the neutron star merger GW170817/SSS17a: Implications for r-process nucleosynthesis. *Science*, 358(6370):1570–1574, December 2017. doi: 10.1126/science.aaq0049.

[84] Alexander P. Ji, Maria R. Drout, and Terese T. Hansen. The Lanthanide Fraction Distribution in Metal-poor Stars: A Test of Neutron Star Mergers as the Dominant r-process Site. ApJ, 882(1):40, September 2019. doi: 10.3847/1538-4357/ab3291.

[85] Benoit Côté, Marius Eichler, Almudena Arcones, Camilla J. Hansen, Paolo Simonetti, Anna Frebel, Chris L. Fryer, Marco Pignatari, Moritz Reichert, Krzysztof Belczynski, and Francesca Matteucci. Neutron Star Mergers Might Not Be the Only Source of r-process Elements in the Milky Way. ApJ, 875(2): 106, April 2019. doi: 10.3847/1538-4357/ab10db.

[86] Daniel M. Siegel, Jennifer Barnes, and Brian D. Metzger. Collapsars as a major source of r-process elements. Nature, 569(7755):241–244, May 2019. doi: 10.1038/s41586-019-1136-0.

[87]

[88] K. Iwamoto, F. Brachwitz, K. Nomoto, N. Kishimoto, H. Umeda, W. R. Hix, and F.-K. Thielemann. Nucleosynthesis in Chandrasekhar Mass Models for Type IA Supernovae and Constraints on Progenitor Systems and Burning-Front Propagation. ApJS, 125:439–462, December 1999. doi: 10.1086/313278.

[89] E. N. Kirby, J. G. Cohen, G. H. Smith, S. R. Majewski, S. T. Sohn, and P. Guhathakurta. Multi-element Abundance Measurements from Medium-resolution Spectra. IV. Alpha Element Distributions in Milky Way Satellite Galaxies. ApJ, 727:79, February 2011. doi: 10.1088/0004-637X/727/2/79.

[90] Kayhan Gültekin, Douglas O. Richstone, Karl Gebhardt, Tod R. Lauer, Scott Tremaine, M. C. Aller, Ralf Bender, Alan Dressler, S. M. Faber, Alexei V. Filippenko, Richard Green, Luis C. Ho, John Kormendy, John Magorrian, Jason Pinkney, and Christos Siopis. The M-σ and M-L Relations in Galactic Bulges, and Determinations of Their Intrinsic Scatter. ApJ, 698(1):198–221, June 2009. doi: 10.1088/0004-637X/698/1/198.

[91] Linda S. Sparke and III Gallagher, John S. *Galaxies in the Universe: An Introduction*. 2007.

[92] Chengdong Li and Gang Zhao. The Evolution of the Galactic Thick Disk with the LAMOST Survey. ApJ, 850(1):25, November 2017. doi: 10.3847/1538-4357/aa93f4.

[93] A. M. Ghez, S. Salim, N. N. Weinberg, J. R. Lu, T. Do, J. K. Dunn, K. Matthews, M. R. Morris, S. Yelda, E. E. Becklin, T. Kremenek, M. Milosavljevic, and J. Naiman. Measuring Distance and Properties of the Milky Way's Central Supermassive Black Hole with Stellar Orbits. ApJ, 689(2):1044–1062, December 2008. doi: 10.1086/592738.

[94] Silvia Garbari, Justin I. Read, and George Lake. Limits on the local dark matter density. MNRAS, 416(3):2318–2340, September 2011. doi: 10.1111/j.1365-2966.2011.19206.x.

[95] Michael R. Hayden, Jon A. Holtzman, Jo Bovy, Steven R. Majewski, Jennifer A. Johnson, Carlos Allende Prieto, Timothy C. Beers, Katia Cunha, Peter M.

Frinchaboy, Ana E. García Pérez, Léo Girardi, Fred R. Hearty, Young Sun Lee, David Nidever, Ricardo P. Schiavon, Katharine J. Schlesinger, Donald P. Schneider, Mathias Schultheis, Matthew Shetrone, Verne V. Smith, Gail Zasowski, Dmitry Bizyaev, Diane Feuillet, Sten Hasselquist, Karen Kinemuchi, Elena Malanushenko, Viktor Malanushenko, Robert O'Connell, Kaike Pan, and Keivan Stassun. Chemical Cartography with APOGEE: Large-scale Mean Metallicity Maps of the Milky Way Disk. AJ, 147(5):116, May 2014. doi: 10.1088/0004-6256/147/5/116.

[96] J. Ted Mackereth, Jo Bovy, Henry W. Leung, Ricardo P. Schiavon, Wilma H. Trick, William J. Chaplin, Katia Cunha, Diane K. Feuillet, Steven R. Majewski, Marie Martig, Andrea Miglio, David Nidever, Marc H. Pinsonneault, Victor Silva Aguirre, Jennifer Sobeck, Jamie Tayar, and Gail Zasowski. Dynamical heating across the Milky Way disc using APOGEE and Gaia. MNRAS, 489(1): 176–195, October 2019. doi: 10.1093/mnras/stz1521.

[97] Roeland P. van der Marel. The Large Magellanic Cloud: structure and kinematics. In Mario Livio and Thomas M. Brown, editors, *The Local Group as an Astrophysical Laboratory*, volume 17, pages 47–71, January 2006.

[98] Nate Bastian and Carmela Lardo. Multiple Stellar Populations in Globular Clusters. ARA&A, 56:83–136, September 2018. doi: 10.1146/annurev-astro-081817-051839.

[99] A. Frebel and J. E. Norris. Near-Field Cosmology with Extremely Metal-Poor Stars. ARA&A, 53:631–688, August 2015. doi: 10.1146/annurev-astro-082214-122423.

[100]

[101] C. Chiappini. First stars and reionization: Spinstars. *Astronomische Nachrichten*, 334(6):595–604, June 2013. doi: 10.1002/asna.201311902.

[102] A. Heger and S. E. Woosley. Nucleosynthesis and Evolution of Massive Metal-free Stars. ApJ, 724:341–373, November 2010. doi: 10.1088/0004-637X/724/1/341.

[103] Miho N. Ishigaki, Nozomu Tominaga, Chiaki Kobayashi, and Ken'ichi Nomoto. The Initial Mass Function of the First Stars Inferred from Extremely Metal-poor Stars. ApJ, 857(1):46, April 2018. doi: 10.3847/1538-4357/aab3de.

[104] Rana Ezzeddine, Anna Frebel, and Bertrand Plez. Ultra-metal-poor Stars: Spectroscopic Determination of Stellar Atmospheric Parameters Using Iron Non-LTE Line Abundances. ApJ, 847(2):142, October 2017. doi: 10.3847/1538-4357/aa8875.

[105] Arnab Rai Choudhuri. *Astrophysics for Physicists*. 2010.

[106] B. Willman, M. R. Blanton, A. A. West, J. J. Dalcanton, D. W. Hogg, D. P. Schneider, N. Wherry, B. Yanny, and J. Brinkmann. A New Milky Way Companion: Unusual Globular Cluster or Extreme Dwarf Satellite? AJ, 129:2692–2700, June 2005. doi: 10.1086/430214.

[107] V. Belokurov, D. B. Zucker, N. W. Evans, J. T. Kleyna, S. Koposov, S. T. Hodgkin, M. J. Irwin, G. Gilmore, M. I. Wilkinson, M. Fellhauer, D. M. Bramich, P. C. Hewett, S. Vidrih, J. T. A. De Jong, J. A. Smith, H.-W. Rix, E. F. Bell, R. F. G. Wyse, H. J. Newberg, P. A. Mayeur, B. Yanny, C. M. Rockosi, O. Y. Gnedin, D. P. Schneider, T. C. Beers, J. C. Barentine, H. Brewington, J. Brinkmann, M. Harvanek, S. J. Kleinman, J. Krzesinski, D. Long, A. Nitta, and S. A. Snedden. Cats and Dogs, Hair and a Hero: A Quintet of New Milky Way Companions. ApJ, 654:897–906, January 2007. doi: 10.1086/509718.

[108] MAGIC Collaboration, M. L. Ahnen, S. Ansoldi, L. A. Antonelli, P. Antoranz, A. Babic, B. Banerjee, P. Bangale, U. Barres de Almeida, J. A. Barrio, J. Becerra González, W. Bednarek, E. Bernardini, B. Biasuzzi, A. Biland, O. Blanch, S. Bonnefoy, G. Bonnoli, F. Borracci, T. Bretz, E. Carmona, A. Carosi, A. Chatterjee, R. Clavero, P. Colin, E. Colombo, J. L. Contreras, J. Cortina, S. Covino, P. Da Vela, F. Dazzi, A. De Angelis, B. De Lotto, E. de Oña Wilhelmi, C. Delgado Mendez, F. Di Pierro, D. Dominis Prester, D. Dorner, M. Doro, S. Einecke, D. Eisenacher Glawion, D. Elsaesser, A. Fernández-Barral, D. Fidalgo, M. V. Fonseca, L. Font, K. Frantzen, C. Fruck, D. Galindo, R. J. García López, M. Garczarczyk, D. Garrido Terrats, M. Gaug, P. Giammaria, N. Godinović, A. González Muñoz, D. Guberman, A. Hahn, Y. Hanabata, M. Hayashida, J. Herrera, J. Hose, D. Hrupec, G. Hughes, W. Idec, K. Kodani, Y. Konno, H. Kubo, J. Kushida, A. La Barbera, D. Lelas, E. Lindfors, S. Lombardi, F. Longo, M. López R. López-Coto, A. López-Oramas, E. Lorenz, P. Majumdar, M. Makariev, K. Mallot, G. Maneva, M. Manganaro, K. Mannheim, L. Maraschi, B. Marcote, M. Mariotti, M. Martínez, D. Mazin, U. Menzel, J. M. Miranda, R. Mirzoyan, A. Moralejo, E. Moretti, D. Nakajima, V. Neustroev, A. Niedzwiecki, M. Nievas Rosillo, K. Nilsson, K. Nishijima, K. Noda, R. Orito, A. Overkemping, S. Paiano, J. Palacio, M. Palatiello, D. Paneque, R. Paoletti, J. M. Paredes, X. Paredes-Fortuny, M. Persic, J. Poutanen, P. G. Prada Moroni, E. Prandini, I. Puljak, W. Rhode, M. Ribó, J. Rico, J. Rodriguez Garcia, T. Saito, K. Satalecka, C. Schultz, T. Schweizer, S. N. Shore, A. Sillanpää, J. Sitarek, I. Snidaric, D. Sobczynska, A. Stamerra, T. Steinbring, M. Strzys, L. Takalo, H. Takami, F. Tavecchio, P. Temnikov, T. Terzić, D. Tescaro, M. Teshima, J. Thaele, D. F. Torres, T. Toyama, A. Treves, V. Verguilov, I. Vovk, J. E. Ward, M. Will, M. H. Wup, R. Zanins, J. Aleksić, M. Wood, B. Anderson, E. D. Bloom, J. Cohen-Tanugi, A. Drlica-Wagner, M. N. Mazziotta, M. Sánchez-Condeai, and L. Strigarian. Limits to dark matter annihilation cross-section from a combined analysis of MAGIC and Fermi-LAT observations of dwarf satellite galaxies. J. Cosmology Astropart. Phys., 2016(2):039, February 2016. doi: 10.1088/1475-7516/2016/02/039.

[109] Thomas M. Brown, Jason Tumlinson, Marla Geha, Joshua D. Simon, Luis C. Vargas, Don A. VandenBerg, Evan N. Kirby, Jason S. Kalirai, Roberto J. Avila, Mario Gennaro, Henry C. Ferguson, Ricardo R. Muñoz, Puragra Guhathakurta, and Alvio Renzini. The Quenching of the Ultra-faint Dwarf Galaxies in the Reionization Era. ApJ, 796(2):91, December 2014. doi: 10.1088/0004-637X/796/2/91.

[110] Alis Deason, Andrew Wetzel, and Shea Garrison-Kimmel. Satellite Dwarf Galaxies in a Hierarchical Universe: The Prevalence of Dwarf-Dwarf Major Mergers. ApJ, 794(2):115, October 2014. doi: 10.1088/0004-637X/794/2/115.

[111] Gaia Collaboration, T. Prusti, J. H. J. de Bruijne, A. G. A. Brown, A. Vallenari, C. Babusiaux, C. A. L. Bailer-Jones, U. Bastian, M. Biermann, D. W. Evans, and et al. The Gaia mission. A&A, 595:A1, November 2016. doi: 10.1051/0004-6361/201629272.

[112] Gaia Collaboration, A. G. A. Brown, A. Vallenari, T. Prusti, J. H. J. de Bruijne, C. Babusiaux, C. A. L. Bailer-Jones, M. Biermann, D. W. Evans, L. Eyer, and et al. Gaia Data Release 2. Summary of the contents and survey properties. A&A, 616:A1, August 2018. doi: 10.1051/0004-6361/201833051.

[113] Christopher A. Onken, Christian Wolf, Michael S. Bessell, Seo-Won Chang, Gary S. Da Costa, Lance C. Luvaul, Dougal Mackey, Brian P. Schmidt, and Li Shao. SkyMapper Southern Survey: Second Data Release (DR2). *arXiv e-prints*, art. arXiv:2008.10359, August 2020.

[114] Gaia Collaboration, A. G. A. Brown, A. Vallenari, T. Prusti, J. H. J. de Bruijne, C. Babusiaux, and M. Biermann. Gaia Early Data Release 3: Summary of the contents and survey properties. *arXiv e-prints*, art. arXiv:2012.01533, December 2020.

[115] C. A. L. Bailer-Jones, J. Rybizki, M. Fouesneau, M. Demleitner, and R. Andrae. Estimating Distances from Parallaxes. V. Geometric and Photogeometric Distances to 1.47 Billion Stars in Gaia Early Data Release 3. AJ, 161(3):147, March 2021. doi: 10.3847/1538-3881/abd806.

[116] E. N. Kirby, J. D. Simon, M. Geha, P. Guhathakurta, and A. Frebel. Uncovering Extremely Metal-Poor Stars in the Milky Way's Ultrafaint Dwarf Spheroidal Satellite Galaxies. ApJ, 685:L43, September 2008. doi: 10.1086/592432.

[117] E. N. Kirby, G. A. Lanfranchi, J. D. Simon, J. G. Cohen, and P. Guhathakurta. Multi-element Abundance Measurements from Medium-resolution Spectra. III. Metallicity Distributions of Milky Way Dwarf Satellite Galaxies. ApJ, 727:78, February 2011. doi: 10.1088/0004-637X/727/2/78.

[118] K. A. Venn, M. D. Shetrone, M. J. Irwin, V. Hill, P. Jablonka, E. Tolstoy, B. Lemasle, M. Divell, E. Starkenburg, B. Letarte, C. Baldner, G. Battaglia, A. Helmi, A. Kaufer, and F. Primas. Nucleosynthesis and the Inhomogeneous

Chemical Evolution of the Carina Dwarf Galaxy. ApJ, 751:102, June 2012. doi: 10.1088/0004-637X/751/2/102.

[119] D. Romano, M. Bellazzini, E. Starkenburg, and R. Leaman. Chemical enrichment in very low metallicity environments: Boötes I. MNRAS, 446:4220–4231, February 2015. doi: 10.1093/mnras/stu2427.

[120] I. Escala, A. Wetzel, E. N. Kirby, P. F. Hopkins, X. Ma, C. Wheeler, D. Kereš, C.-A. Faucher-Giguère, and E. Quataert. Modelling chemical abundance distributions for dwarf galaxies in the Local Group: the impact of turbulent metal diffusion. MNRAS, 474:2194–2211, February 2018. doi: 10.1093/mnras/stx2858.

[121] Joshua D. Simon. The Faintest Dwarf Galaxies. *arXiv e-prints*, art. arXiv:1901.05465, Jan 2019.

[122] A. Frebel and V. Bromm. Chemical Signatures of the First Galaxies: Criteria for One-shot Enrichment. ApJ, 759:115, November 2012. doi: 10.1088/0004-637X/759/2/115.

[123] Deokkeun An, Timothy C. Beers, Jennifer A. Johnson, Marc H. Pinsonneault, Young Sun Lee, Jo Bovy, Željko Ivezić, Daniela Carollo, and Matthew Newby. The Stellar Metallicity Distribution Function of the Galactic Halo from SDSS Photometry. ApJ, 763(1):65, Jan 2013. doi: 10.1088/0004-637X/763/1/65.

[124] Andrew B. Pace and Ting S. Li. Proper Motions of Milky Way Ultra-faint Satellites with Gaia DR2 DES DR1. ApJ, 875(1):77, Apr 2019. doi: 10.3847/1538-4357/ab0aee.

[125] Else Starkenburg, Nicolas Martin, Kris Youakim, David S. Aguado, Carlos Allende Prieto, Anke Arentsen, Edouard J. Bernard, Piercarlo Bonifacio, Elisabetta Caffau, and Raymond G. Carlberg. The Pristine survey - I. Mining the Galaxy for the most metal-poor stars. MNRAS, 471(3):2587–2604, Nov 2017. doi: 10.1093/mnras/stx1068.

[126] Barbara J. Anthony-Twarog, John B. Laird, Don Payne, and Bruce A. Twarog. CA II H and K Filter Photometry on the UVBY System. I. The Standard System. AJ, 101:1902, May 1991. doi: 10.1086/115815.

[127] S. C. Keller, B. P. Schmidt, M. S. Bessell, P. G. Conroy, P. Francis, A. Granlund, E. Kowald, A. P. Oates, T. Martin-Jones, and T. Preston. The SkyMapper Telescope and The Southern Sky Survey. PASA, 24(1):1–12, May 2007. doi: 10.1071/AS07001.

[128] D. D. Whitten, V. M. Placco, T. C. Beers, A. L. Chies-Santos, C. Bonatto, J. Varela, D. Cristóbal-Hornillos, A. Ederoclite, T. Masseron, and Y. S. Lee. J-PLUS: Identification of low-metallicity stars with artificial neural networks using SPHINX. A&A, 622:A182, Feb 2019. doi: 10.1051/0004-6361/201833368.

[129] S. C. Keller, M. S. Bessell, A. Frebel, A. R. Casey, M. Asplund, H. R. Jacobson, K. Lind, J. E. Norris, D. Yong, and A. Heger. A single low-energy, iron-poor supernova as the source of metals in the star SMSS J031300.36-670839.3. Nature, 506(7489):463–466, Feb 2014. doi: 10.1038/nature12990.

[130] T. Nordlander, M. S. Bessell, G. S. Da Costa, A. D. Mackey, M. Asplund, A. R. Casey, A. Chiti, R. Ezzeddine, A. Frebel, K. Lind, A. F. Marino, S. J. Murphy, J. E. Norris, B. P. Schmidt, and D. Yong. The lowest detected stellar Fe abundance: the halo star SMSS J160540.18-144323.1. MNRAS, 488(1): L109–L113, September 2019. doi: 10.1093/mnrasl/slz109.

[131] K. Youakim, E. Starkenburg, D. S. Aguado, N. F. Martin, M. Fouesneau, J. I. González Hernández, C. Allende Prieto, P. Bonifacio, M. Gentile, and C. Kielty. The Pristine survey - III. Spectroscopic confirmation of an efficient search for extremely metal-poor stars. MNRAS, 472(3):2963–2974, Dec 2017. doi: 10.1093/mnras/stx2005.

[132] Else Starkenburg, David S. Aguado, Piercarlo Bonifacio, Elisabetta Caffau, Pascale Jablonka, Carmela Lardo, Nicolas Martin, Rubén Sánchez-Janssen, Federico Sestito, and Kim A. Venn. The Pristine survey IV: approaching the Galactic metallicity floor with the discovery of an ultra-metal-poor star. MNRAS, 481(3):3838–3852, Dec 2018. doi: 10.1093/mnras/sty2276.

[133] Nicolas Longeard, Nicolas Martin, Else Starkenburg, Rodrigo A. Ibata, Michelle L. M. Collins, Marla Geha, Benjamin P. M. Laevens, R. Michael Rich, David S. Aguado, and Anke Arentsen. Pristine dwarf galaxy survey - I. A detailed photometric and spectroscopic study of the very metal-poor Draco II satellite. MNRAS, 480(2):2609–2627, Oct 2018. doi: 10.1093/mnras/sty1986.

[134] Nicolas Longeard, Nicolas Martin, Else Starkenburg, Rodrigo A. Ibata, Michelle L. M. Collins, Benjamin P. M. Laevens, Dougal Mackey, R. Michael Rich, David S. Aguado, and Anke Arentsen. The Pristine Dwarf-Galaxy survey - II. In-depth observational study of the faint Milky Way satellite Sagittarius II. *arXiv e-prints*, art. arXiv:1902.02780, Feb 2019.

[135] M. Bessell, G. Bloxham, B. Schmidt, S. Keller, P. Tisserand, and P. Francis. SkyMapper Filter Set: Design and Fabrication of Large-Scale Optical Filters. PASP, 123:789, July 2011. doi: 10.1086/660849.

[136] S. Murphy, S. Keller, B. Schmidt, P. Tisserand, M. Bessell, P. Francis, and G. Da Costa. SkyMapper and the Southern Sky Survey: A Valuable Resource for Stellar Astrophysics. In S. J. Murphy and M. S. Bessell, editors, *The Eighth Pacific Rim Conference on Stellar Astrophysics: A Tribute to Kam-Ching Leung*, volume 404 of *Astronomical Society of the Pacific Conference Series*, page 356, Aug 2009.

[137] Anirudh Chiti and Anna Frebel. Four Metal-poor Stars in the Sagittarius Dwarf Spheroidal Galaxy. ApJ, 875(2):112, Apr 2019. doi: 10.3847/1538-4357/ab0f9f.

[138] S. B. Howell. *Handbook of CCD Astronomy*. March 2006.

[139] The Astropy Collaboration, A. M. Price-Whelan, B. M. Sipőcz, H. M. Günther, P. L. Lim, S. M. Crawford, S. Conseil, D. L. Shupe, M. W. Craig, N. Dencheva, A. Ginsburg, J. T. VanderPlas, L. D. Bradley, D. Pérez-Suárez, M. de Val-Borro, T. L. Aldcroft, K. L. Cruz, T. P. Robitaille, E. J. Tollerud, C. Ardelean, T. Babej, M. Bachetti, A. V. Bakanov, S. P. Bamford, G. Barentsen, P. Barmby, A. Baumbach, K. L. Berry, F. Biscani, M. Boquien, K. A. Bostroem, L. G. Bouma, G. B. Brammer, E. M. Bray, H. Breytenbach, H. Buddelmeijer, D. J. Burke, G. Calderone, J. L. Cano Rodríguez, M. Cara, J. V. M. Cardoso, S. Cheedella, Y. Copin, D. Crichton, D. DÁvella, C. Deil, É. Depagne, J. P. Dietrich, A. Donath, M. Droettboom, N. Earl, T. Erben, S. Fabbro, L. A. Ferreira, T. Finethy, R. T. Fox, L. H. Garrison, S. L. J. Gibbons, D. A. Goldstein, R. Gommers, J. P. Greco, P. Greenfield, A. M. Groener, F. Grollier, A. Hagen, P. Hirst, D. Homeier, A. J. Horton, G. Hosseinzadeh, L. Hu, J. S. Hunkeler, Ž. Ivezić, A. Jain, T. Jenness, G. Kanarek, S. Kendrew, N. S. Kern, W. E. Kerzendorf, A. Khvalko, J. King, D. Kirkby, A. M. Kulkarni, A. Kumar, A. Lee, D. Lenz, S. P. Littlefair, Z. Ma, D. M. Macleod, M. Mastropietro, C. McCully, S. Montagnac, B. M. Morris, M. Mueller, S. J. Mumford, D. Muna, N. A. Murphy, S. Nelson, G. H. Nguyen, J. P. Ninan, M. Nöthe, S. Ogaz, S. Oh, J. K. Parejko, N. Parley, S. Pascual, R. Patil, A. A. Patil, A. L. Plunkett, J. X. Prochaska, T. Rastogi, V. Reddy Janga, J. Sabater, P. Sakurikar, M. Seifert, L. E. Sherbert, H. Sherwood-Taylor, A. Y. Shih, J. Sick, M. T. Silbiger, S. Singanamalla, L. P. Singer, P. H. Sladen, K. A. Sooley, S. Sornarajah, O. Streicher, P. Teuben, S. W. Thomas, G. R. Tremblay, J. E. H. Turner, V. Terrón, M. H. van Kerkwijk, A. de la Vega, L. L. Watkins, B. A. Weaver, J. B. Whitmore, J. Woillez, and V. Zabalza. The Astropy Project: Building an inclusive, open-science project and status of the v2.0 core package. *ArXiv e-prints*, January 2018.

[140] D. Lang, D. W. Hogg, K. Mierle, M. Blanton, and S. Roweis. Astrometry.net: Blind Astrometric Calibration of Arbitrary Astronomical Images. AJ, 139: 1782–1800, May 2010. doi: 10.1088/0004-6256/139/5/1782.

[141] E. Bertin. Automatic Astrometric and Photometric Calibration with SCAMP. In C. Gabriel, C. Arviset, D. Ponz, and S. Enrique, editors, *Astronomical Data Analysis Software and Systems XV*, volume 351 of *Astronomical Society of the Pacific Conference Series*, page 112, July 2006.

[142] E. Bertin and S. Arnouts. SExtractor: Software for source extraction. A&AS, 117:393–404, June 1996. doi: 10.1051/aas:1996164.

[143] E. Bertin, Y. Mellier, M. Radovich, G. Missonnier, P. Didelon, and B. Morin. The TERAPIX Pipeline. In D. A. Bohlender, D. Durand, and T. H. Handley, editors, *Astronomical Data Analysis Software and Systems XI*, volume 281 of *Astronomical Society of the Pacific Conference Series*, page 228, 2002.

[144] David J. Schlegel, Douglas P. Finkbeiner, and Marc Davis. Maps of Dust Infrared Emission for Use in Estimation of Reddening and Cosmic Microwave Background Radiation Foregrounds. ApJ, 500(2):525–553, Jun 1998. doi: 10.1086/305772.

[145] L. Casagrande, C. Wolf, A. D. Mackey, T. Nordland er, D. Yong, and M. Bessell. SkyMapper stellar parameters for Galactic Archaeology on a grand-scale. MNRAS, 482(2):2770–2787, January 2019. doi: 10.1093/mnras/sty2878.

[146] A. Drlica-Wagner, I. Sevilla-Noarbe, E. S. Rykoff, R. A. Gruendl, B. Yanny, D. L. Tucker, B. Hoyle, A. Carnero Rosell, G. M. Bernstein, K. Bechtol, M. R. Becker, A. Benoit-Lévy, E. Bertin, M. Carrasco Kind, C. Davis, J. de Vicente, H. T. Diehl, D. Gruen, W. G. Hartley, B. Leistedt, T. S. Li, J. L. Marshall, E. Neilsen, M. M. Rau, E. Sheldon, J. Smith, M. A. Troxel, S. Wyatt, Y. Zhang, T. M. C. Abbott, F. B. Abdalla, S. Allam, M. Banerji, D. Brooks, E. Buckley-Geer, D. L. Burke, D. Capozzi, J. Carretero, C. E. Cunha, C. B. D'Andrea, L. N. da Costa, D. L. DePoy, S. Desai, J. P. Dietrich, P. Doel, A. E. Evrard, A. Fausti Neto, B. Flaugher, P. Fosalba, J. Frieman, J. García-Bellido, D. W. Gerdes, T. Giannantonio, J. Gschwend, G. Gutierrez, K. Honscheid, D. J. James, T. Jeltema, K. Kuehn, S. Kuhlmann, N. Kuropatkin, O. Lahav, M. Lima, H. Lin, M. A. G. Maia, P. Martini, R. G. McMahon, P. Melchior, F. Menanteau, R. Miquel, R. C. Nichol, R. L. C. Ogand o, A. A. Plazas, A. K. Romer, A. Roodman, E. Sanchez, V. Scarpine, R. Schindler, M. Schubnell, M. Smith, R. C. Smith, M. Soares-Santos, F. Sobreira, E. Suchyta, G. Tarle, V. Vikram, A. R. Walker, R. H. Wechsler, J. Zuntz, and DES Collaboration. Dark Energy Survey Year 1 Results: The Photometric Data Set for Cosmology. ApJS, 235(2):33, Apr 2018. doi: 10.3847/1538-4365/aab4f5.

[147] R. Alvarez and B. Plez. Near-infrared narrow-band photometry of M-giant and Mira stars: models meet observations. A&A, 330:1109–1119, February 1998.

[148] B. Plez. Turbospectrum: Code for spectral synthesis. Astrophysics Source Code Library, May 2012.

[149] B. Gustafsson, B. Edvardsson, K. Eriksson, U. G. Jørgensen, rA. Nordlund, and B. Plez. A grid of MARCS model atmospheres for late-type stars. I. Methods and general properties. A&A, 486:951–970, August 2008. doi: 10.1051/0004-6361:200809724.

[150] N. E. Piskunov, F. Kupka, T. A. Ryabchikova, W. W. Weiss, and C. S. Jeffery. VALD: The Vienna Atomic Line Data Base. A&AS, 112:525, September 1995.

[151] T. Ryabchikova, N. Piskunov, R. L. Kurucz, H. C. Stempels, U. Heiter, Y. Pakhomov, and P. S. Barklem. A major upgrade of the VALD database. Phys. Scr, 90(5):054005, May 2015. doi: 10.1088/0031-8949/90/5/054005.

[152] James S. A. Brooke, Ram S. Ram, Colin M. Western, Gang Li, David W. Schwenke, and Peter F. Bernath. Einstein A Coefficients and Oscillator

Strengths for the A $^2\Pi$-X $^2\Sigma^+$ (Red) and B$^2\Sigma^+$-X$^2\Sigma^+$ (Violet) Systems and Rovibrational Transitions in the X $^2\Sigma^+$ State of CN. ApJS, 210(2):23, Feb 2014. doi: 10.1088/0067-0049/210/2/23.

[153] Christopher Sneden, Sara Lucatello, Ram S. Ram, James S. A. Brooke, and Peter Bernath. Line Lists for the A $^2\Pi$-X $^2\Sigma^+$ (Red) and B $^2\Sigma^+$-X $^2\Sigma^+$ (Violet) Systems of CN, ^{13}C^{14}N, and ^{12}C^{15}N, and Application to Astronomical Spectra. ApJS, 214(2):26, Oct 2014. doi: 10.1088/0067-0049/214/2/26.

[154] James S. A. Brooke, Peter F. Bernath, Timothy W. Schmidt, and George B. Bacskay. Line strengths and updated molecular constants for the C_2 Swan system. J. Quant. Spec. Radiat. Transf., 124:11–20, Jul 2013. doi: 10.1016/j.jqsrt.2013.02.025.

[155] Ram S. Ram, James S. A. Brooke, Peter F. Bernath, Christopher Sneden, and Sara Lucatello. Improved Line Data for the Swan System ^{12}C^{13}C Isotopologue. ApJS, 211(1):5, Mar 2014. doi: 10.1088/0067-0049/211/1/5.

[156] Luke D. Keller, Catherine A. Pilachowski, and Christopher Sneden. ^{12}C/^{13}C in Metal-poor Field Halo Giants. AJ, 122(5):2554–2560, Nov 2001. doi: 10.1086/323548.

[157] N. Grevesse, M. Asplund, and A. J. Sauval. The Solar Chemical Composition. Space Sci. Rev., 130:105–114, June 2007. doi: 10.1007/s11214-007-9173-7.

[158] C. Rodrigo, E. Solano, and A. Bayo. SVO Filter Profile Service Version 1.0. IVOA Working Draft 15 October 2012, October 2012.

[159] L. Casagrande and D. A. VandenBerg. Synthetic stellar photometry - I. General considerations and new transformations for broad-band systems. MNRAS, 444:392–419, October 2014. doi: 10.1093/mnras/stu1476.

[160] S. C. Keller, Skymapper Team, and Aegis Team. SkyMapper and Galactic Archaeology. In W. Aoki, M. Ishigaki, T. Suda, T. Tsujimoto, and N. Arimoto, editors, *Galactic Archaeology: Near-Field Cosmology and the Formation of the Milky Way*, volume 458 of *Astronomical Society of the Pacific Conference Series*, page 409, Aug 2012.

[161] Jinmi Yoon, Timothy C. Beers, Vinicius M. Placco, Kaitlin C. Rasmussen, Daniela Carollo, Siyu He, Terese T. Hansen, Ian U. Roederer, and Jeff Zeanah. Observational Constraints on First-star Nucleosynthesis. I. Evidence for Multiple Progenitors of CEMP-No Stars. ApJ, 833(1):20, Dec 2016. doi: 10.3847/0004-637X/833/1/20.

[162] William E. Harris. A New Catalog of Globular Clusters in the Milky Way. *arXiv e-prints*, art. arXiv:1012.3224, Dec 2010.

[163] William E. Harris. A Catalog of Parameters for Globular Clusters in the Milky Way. AJ, 112:1487, Oct 1996. doi: 10.1086/118116.

[164] J. Salgado, J. González-Núñez, R. Gutiérrez-Sánchez, J. C. Segovia, J. Durán, J. L. Hernández, and C. Arviset. The ESA Gaia Archive: Data Release 1. *Astronomy and Computing*, 21:22–26, October 2017. doi: 10.1016/j.ascom.2017.08.002.

[165] S. Desai, R. Armstrong, J. J. Mohr, D. R. Semler, J. Liu, E. Bertin, S. S. Allam, W. A. Barkhouse, G. Bazin, E. J. Buckley-Geer, M. C. Cooper, S. M. Hansen, F. W. High, H. Lin, Y.-T. Lin, C.-C. Ngeow, A. Rest, J. Song, D. Tucker, and A. Zenteno. The Blanco Cosmology Survey: Data Acquisition, Processing, Calibration, Quality Diagnostics, and Data Release. ApJ, 757:83, September 2012. doi: 10.1088/0004-637X/757/1/83.

[166] Nicolas F. Martin, Jelte T. A. de Jong, and Hans-Walter Rix. A Comprehensive Maximum Likelihood Analysis of the Structural Properties of Faint Milky Way Satellites. *The Astrophysical Journal*, 684(2):1075–1092, Sep 2008. doi: 10.1086/590336.

[167] Daniel Foreman-Mackey, David W. Hogg, Dustin Lang, and Jonathan Goodman. emcee: The MCMC Hammer. *Publications of the Astronomical Society of the Pacific*, 125(925):306, Mar 2013. doi: 10.1086/670067.

[168] Jonathan Goodman and Jonathan Weare. Ensemble samplers with affine invariance. *Communications in Applied Mathematics and Computational Science*, 5(1):65–80, Jan 2010. doi: 10.2140/camcos.2010.5.65.

[169] C. Sneden, A. McWilliam, G. W. Preston, J. J. Cowan, D. L. Burris, and B. J. Armosky. The Ultra–Metal-poor, Neutron-Capture–rich Giant Star CS 22892-052. ApJ, 467:819, August 1996. doi: 10.1086/177656.

[170] T. C. Beers and N. Christlieb. The Discovery and Analysis of Very Metal-Poor Stars in the Galaxy. ARA&A, 43:531–580, September 2005. doi: 10.1146/annurev.astro.42.053102.134057.

[171] V. Bromm, N. Yoshida, L. Hernquist, and C. F. McKee. The formation of the first stars and galaxies. Nature, 459:49–54, May 2009. doi: 10.1038/nature07990.

[172] F. Spite and M. Spite. Abundance of lithium in unevolved halo stars and old disk stars - Interpretation and consequences. A&A, 115:357–366, November 1982.

[173] K. Freeman and J. Bland-Hawthorn. The New Galaxy: Signatures of Its Formation. ARA&A, 40:487–537, 2002. doi: 10.1146/annurev.astro.40.060401.093840.

[174] A. Frebel and J. E. Norris. *Metal-Poor Stars and the Chemical Enrichment of the Universe*, page 55. 2013. doi: 10.1007/978-94-007-5612-0_3.

[175] T. Karlsson, V. Bromm, and J. Bland-Hawthorn. Pregalactic metal enrichment: The chemical signatures of the first stars. *Reviews of Modern Physics*, 85:809–848, April 2013. doi: 10.1103/RevModPhys.85.809.

[176] E. Tolstoy, V. Hill, and M. Tosi. Star-Formation Histories, Abundances, and Kinematics of Dwarf Galaxies in the Local Group. ARA&A, 47:371–425, September 2009. doi: 10.1146/annurev-astro-082708-101650.

[177] V. Belokurov. Galactic Archaeology: The dwarfs that survived and perished. *New Astronomy Review*, 57:100–121, September 2013. doi: 10.1016/j.newar.2013.07.001.

[178] J. D. Simon and M. Geha. The Kinematics of the Ultra-faint Milky Way Satellites: Solving the Missing Satellite Problem. ApJ, 670:313–331, November 2007. doi: 10.1086/521816.

[179] E. N. Kirby, J. G. Cohen, P. Guhathakurta, L. Cheng, J. S. Bullock, and A. Gallazzi. The Universal Stellar Mass-Stellar Metallicity Relation for Dwarf Galaxies. ApJ, 779:102, December 2013. doi: 10.1088/0004-637X/779/2/102.

[180] T. K. Starkenburg and A. Helmi. Dark influences: imprints of dark satellites on dwarf galaxies. A&A, 575:A59, March 2015. doi: 10.1051/0004-6361/201425082.

[181] D. B. Zucker, V. Belokurov, N. W. Evans, J. T. Kleyna, M. J. Irwin, M. I. Wilkinson, M. Fellhauer, D. M. Bramich, G. Gilmore, H. J. Newberg, B. Yanny, J. A. Smith, P. C. Hewett, E. F. Bell, H.-W. Rix, O. Y. Gnedin, S. Vidrih, R. F. G. Wyse, B. Willman, E. K. Grebel, D. P. Schneider, T. C. Beers, A. Y. Kniazev, J. C. Barentine, H. Brewington, J. Brinkmann, M. Harvanek, S. J. Kleinman, J. Krzesinski, D. Long, A. Nitta, and S. A. Snedden. A Curious Milky Way Satellite in Ursa Major. ApJ, 650:L41–L44, October 2006. doi: 10.1086/508628.

[182] S. M. Walsh, H. Jerjen, and B. Willman. A Pair of Boötes: A New Milky Way Satellite. ApJ, 662:L83–L86, June 2007. doi: 10.1086/519684.

[183] B. Willman. In Pursuit of the Least Luminous Galaxies. *Advances in Astronomy*, 2010:285454, 2010. doi: 10.1155/2010/285454.

[184] A. Drlica-Wagner, K. Bechtol, E. S. Rykoff, E. Luque, A. Queiroz, Y.-Y. Mao, R. H. Wechsler, J. D. Simon, B. Santiago, B. Yanny, E. Balbinot, S. Dodelson, A. Fausti Neto, D. J. James, T. S. Li, M. A. G. Maia, J. L. Marshall, A. Pieres, K. Stringer, A. R. Walker, T. M. C. Abbott, F. B. Abdalla, S. Allam, A. Benoit-Lévy, G. M. Bernstein, E. Bertin, D. Brooks, E. Buckley-Geer, D. L. Burke, A. Carnero Rosell, M. Carrasco Kind, J. Carretero, M. Crocce, L. N. da Costa, S. Desai, H. T. Diehl, J. P. Dietrich, P. Doel, T. F. Eifler, A. E. Evrard, D. A. Finley, B. Flaugher, P. Fosalba, J. Frieman, E. Gaztanaga, D. W. Gerdes, D. Gruen, R. A. Gruendl, G. Gutierrez, K. Honscheid, K. Kuehn,

N. Kuropatkin, O. Lahav, P. Martini, R. Miquel, B. Nord, R. Ogando, A. A. Plazas, K. Reil, A. Roodman, M. Sako, E. Sanchez, V. Scarpine, M. Schubnell, I. Sevilla-Noarbe, R. C. Smith, M. Soares-Santos, F. Sobreira, E. Suchyta, M. E. C. Swanson, G. Tarle, D. Tucker, V. Vikram, W. Wester, Y. Zhang, J. Zuntz, and DES Collaboration. Eight Ultra-faint Galaxy Candidates Discovered in Year Two of the Dark Energy Survey. ApJ, 813:109, November 2015. doi: 10.1088/0004-637X/813/2/109.

[185] D. Kim and H. Jerjen. Horologium II: A Second Ultra-faint Milky Way Satellite in the Horologium Constellation. ApJ, 808:L39, August 2015. doi: 10.1088/2041-8205/808/2/L39.

[186] D. Kim, H. Jerjen, D. Mackey, G. S. Da Costa, and A. P. Milone. A Heros Dark Horse: Discovery of an Ultra-faint Milky Way Satellite in Pegasus. ApJ, 804:L44, May 2015. doi: 10.1088/2041-8205/804/2/L44.

[187] B. P. M. Laevens, N. F. Martin, R. A. Ibata, H.-W. Rix, E. J. Bernard, E. F. Bell, B. Sesar, A. M. N. Ferguson, E. F. Schlafly, C. T. Slater, W. S. Burgett, K. C. Chambers, H. Flewelling, K. A. Hodapp, N. Kaiser, R.-P. Kudritzki, R. H. Lupton, E. A. Magnier, N. Metcalfe, J. S. Morgan, P. A. Price, J. L. Tonry, R. J. Wainscoat, and C. Waters. A New Faint Milky Way Satellite Discovered in the Pan-STARRS1 3π Survey. ApJ, 802:L18, April 2015. doi: 10.1088/2041-8205/802/2/L18.

[188] B. P. M. Laevens, N. F. Martin, E. J. Bernard, E. F. Schlafly, B. Sesar, H.-W. Rix, E. F. Bell, A. M. N. Ferguson, C. T. Slater, W. E. Sweeney, R. F. G. Wyse, A. P. Huxor, W. S. Burgett, K. C. Chambers, P. W. Draper, K. A. Hodapp, N. Kaiser, E. A. Magnier, N. Metcalfe, J. L. Tonry, R. J. Wainscoat, and C. Waters. Sagittarius II, Draco II and Laevens 3: Three New Milky Way Satellites Discovered in the Pan-STARRS 1 3π Survey. ApJ, 813:44, November 2015. doi: 10.1088/0004-637X/813/1/44.

[189] A. Drlica-Wagner, K. Bechtol, S. Allam, D. L. Tucker, R. A. Gruendl, M. D. Johnson, A. R. Walker, D. J. James, D. L. Nidever, K. A. G. Olsen, R. H. Wechsler, M. R. L. Cioni, B. C. Conn, K. Kuehn, T. S. Li, Y.-Y. Mao, N. F. Martin, E. Neilsen, N. E. D. Noel, A. Pieres, J. D. Simon, G. S. Stringfellow, R. P. van der Marel, and B. Yanny. An Ultra-faint Galaxy Candidate Discovered in Early Data from the Magellanic Satellites Survey. ApJ, 833:L5, December 2016. doi: 10.3847/2041-8205/833/1/L5.

[190] D. Homma, M. Chiba, S. Okamoto, Y. Komiyama, M. Tanaka, M. Tanaka, M. N. Ishigaki, M. Akiyama, N. Arimoto, J. A. Garmilla, R. H. Lupton, M. A. Strauss, H. Furusawa, S. Miyazaki, H. Murayama, A. J. Nishizawa, M. Takada, T. Usuda, and S.-Y. Wang. A New Milky Way Satellite Discovered in the Subaru/Hyper Suprime-Cam Survey. ApJ, 832:21, November 2016. doi: 10.3847/0004-637X/832/1/21.

[191] D. Homma, M. Chiba, S. Okamoto, Y. Komiyama, M. Tanaka, M. Tanaka, M. N. Ishigaki, K. Hayashi, N. Arimoto, J. A. Garmilla, R. H. Lupton, M. A. Strauss, S. Miyazaki, S.-Y. Wang, and H. Murayama. Searches for new Milky Way satellites from the first two years of data of the Subaru/Hyper Suprime-Cam survey: Discovery of Cetus III. PASJ, 70:S18, January 2018. doi: 10.1093/pasj/psx050.

[192] N. F. Martin, J. T. A. de Jong, and H.-W. Rix. A Comprehensive Maximum Likelihood Analysis of the Structural Properties of Faint Milky Way Satellites. ApJ, 684:1075-1092, September 2008. doi: 10.1086/590336.

[193] R. Alvarez and B. Plez. Near-infrared narrow-band photometry of M-giant and Mira stars: models meet observations. A&A, 330:1109–1119, February 1998.

[194] M. Bessell and S. Murphy. Spectrophotometric Libraries, Revised Photonic Passbands, and Zero Points for UBVRI, Hipparcos, and Tycho Photometry. PASP, 124:140, February 2012. doi: 10.1086/664083.

[195] Rebecca Bernstein, Stephen A. Shectman, Steven M. Gunnels, Stefan Mochnacki, and Alex E. Athey. MIKE: A Double Echelle Spectrograph for the Magellan Telescopes at Las Campanas Observatory. In Masanori Iye and Alan F. M. Moorwood, editors, *Instrument Design and Performance for Optical/Infrared Ground-based Telescopes*, volume 4841 of *Society of Photo-Optical Instrumentation Engineers (SPIE) Conference Series*, pages 1694–1704, March 2003. doi: 10.1117/12.461502.

[196] D. D. Kelson. Optimal Techniques in Two-dimensional Spectroscopy: Background Subtraction for the 21st Century. PASP, 115:688–699, June 2003. doi: 10.1086/375502.

[197] A. R. Casey. *A Tale of Tidal Tales in the Milky Way*. PhD thesis, Australian National University, May 2014.

[198] C. A. Sneden. *Carbon and Nitrogen Abundances in Metal-Poor Stars*. PhD thesis, The University of Texas at Austin., 1973.

[199] J. S. Sobeck, R. P. Kraft, C. Sneden, G. W. Preston, J. J. Cowan, G. H. Smith, I. B. Thompson, S. A. Shectman, and G. S. Burley. The Abundances of Neutron-capture Species in the Very Metal-poor Globular Cluster M15: A Uniform Analysis of Red Giant Branch and Red Horizontal Branch Stars. AJ, 141:175, June 2011. doi: 10.1088/0004-6256/141/6/175.

[200] F. Castelli and R. L. Kurucz. New Grids of ATLAS9 Model Atmospheres. *preprint (astro-ph/0405087)*, May 2004.

[201] V. Hill, B. Plez, R. Cayrel, T. C. Beers, B. Nordström, J. Andersen, M. Spite, F. Spite, B. Barbuy, P. Bonifacio, E. Depagne, P. François, and F. Primas. First stars. I. The extreme r-element rich, iron-poor halo giant CS 31082-001.

Implications for the r-process site(s) and radioactive cosmochronology. A&A, 387:560–579, May 2002. doi: 10.1051/0004-6361:20020434.

[202] E. A. Den Hartog, J. E. Lawler, C. Sneden, and J. J. Cowan. Improved Laboratory Transition Probabilities for Nd II and Application to the Neodymium Abundances of the Sun and Three Metal-poor Stars. ApJS, 148:543–566, October 2003. doi: 10.1086/376940.

[203] I. I. Ivans, J. Simmerer, C. Sneden, J. E. Lawler, J. J. Cowan, R. Gallino, and S. Bisterzo. Near-Ultraviolet Observations of HD 221170: New Insights into the Nature of r-Process-rich Stars. ApJ, 645:613–633, July 2006. doi: 10.1086/504069.

[204] J. E. Lawler, E. A. Den Hartog, C. Sneden, and J. J. Cowan. Improved Laboratory Transition Probabilities for Sm II and Application to the Samarium Abundances of the Sun and Three r-Process-rich, Metal-poor Stars. ApJS, 162: 227–260, January 2006. doi: 10.1086/498213.

[205] J. E. Lawler, C. Sneden, J. J. Cowan, I. I. Ivans, and E. A. Den Hartog. Improved Laboratory Transition Probabilities for Ce II, Application to the Cerium Abundances of the Sun and Five r-Process-Rich, Metal-Poor Stars, and Rare Earth Lab Data Summary. ApJS, 182:51–79, May 2009. doi: 10.1088/0067-0049/182/1/51.

[206] C. Sneden, J. E. Lawler, J. J. Cowan, I. I. Ivans, and E. A. Den Hartog. New Rare Earth Element Abundance Distributions for the Sun and Five r-Process-Rich Very Metal-Poor Stars. ApJS, 182:80–96, May 2009. doi: 10.1088/0067-0049/182/1/80.

[207] M. Asplund, N. Grevesse, A. J. Sauval, and P. Scott. The Chemical Composition of the Sun. ARA&A, 47:481–522, September 2009. doi: 10.1146/annurev.astro.46.060407.145222.

[208] J. F Kenney. *Mathematics of Statistics, Pt. 1.* Van Nostrand, Princeton, NJ, 3 edition, 1962. ISBN B0007HR7SY.

[209] Y. S. Lee, T. C. Beers, T. Sivarani, C. Allende Prieto, L. Koesterke, R. Wilhelm, P. Re Fiorentin, C. A. L. Bailer-Jones, J. E. Norris, C. M. Rockosi, B. Yanny, H. J. Newberg, K. R. Covey, H.-T. Zhang, and A.-L. Luo. The SEGUE Stellar Parameter Pipeline. I. Description and Comparison of Individual Methods. AJ, 136:2022–2049, November 2008. doi: 10.1088/0004-6256/136/5/2022.

[210] A. Abohalima and A. Frebel. JINAbase: A database for chemical abundances of metal-poor stars. *ArXiv e-prints*, November 2017.

[211] P. François, L. Monaco, P. Bonifacio, C. Moni Bidin, D. Geisler, and L. Sbordone. Abundance ratios of red giants in low-mass ultra-faint dwarf spheroidal galaxies. A&A, 588:A7, April 2016. doi: 10.1051/0004-6361/201527181.

[212] S. Wanajo. The r-process in Proto-neutron-star Wind Revisited. ApJ, 770:L22, June 2013. doi: 10.1088/2041-8205/770/2/L22.

[213] N. Tominaga, K. Maeda, H. Umeda, K. Nomoto, M. Tanaka, N. Iwamoto, T. Suzuki, and P. A. Mazzali. The Connection between Gamma-Ray Bursts and Extremely Metal-poor Stars: Black Hole-forming Supernovae with Relativistic Jets. ApJ, 657:L77–L80, March 2007. doi: 10.1086/513193.

[214] R. J. Cooke and P. Madau. Carbon-enhanced Metal-poor Stars: Relics from the Dark Ages. ApJ, 791:116, August 2014. doi: 10.1088/0004-637X/791/2/116.

[215] A. Chiti, J. D. Simon, A. Frebel, I. B. Thompson, S. A. Shectman, M. Mateo, J. I. Bailey, III, J. D. Crane, and M. Walker. Detection of a Population of Carbon-enhanced Metal-poor Stars in the Sculptor Dwarf Spheroidal Galaxy. ApJ, 856:142, April 2018. doi: 10.3847/1538-4357/aab663.

[216] L. C. Vargas, M. Geha, E. N. Kirby, and J. D. Simon. The Distribution of Alpha Elements in Ultra-faint Dwarf Galaxies. ApJ, 767:134, April 2013. doi: 10.1088/0004-637X/767/2/134.

[217] J. D. Simon, T. S. Li, A. Drlica-Wagner, K. Bechtol, J. L. Marshall, D. J. James, M. Y. Wang, L. Strigari, E. Balbinot, K. Kuehn, A. R. Walker, T. M. C. Abbott, S. Allam, J. Annis, A. Benoit-Lévy, D. Brooks, E. Buckley-Geer, D. L. Burke, A. Carnero Rosell, M. Carrasco Kind, J. Carretero, C. E. Cunha, C. B. D'Andrea, L. N. da Costa, D. L. DePoy, S. Desai, P. Doel, E. Fernandez, B. Flaugher, J. Frieman, J. García-Bellido, E. Gaztanaga, D. A. Goldstein, D. Gruen, G. Gutierrez, N. Kuropatkin, M. A. G. Maia, P. Martini, F. Menanteau, C. J. Miller, R. Miquel, E. Neilsen, B. Nord, R. Ogando, A. A. Plazas, A. K. Romer, E. S. Rykoff, E. Sanchez, B. Santiago, V. Scarpine, M. Schubnell, I. Sevilla-Noarbe, R. C. Smith, F. Sobreira, E. Suchyta, M. E. C. Swanson, G. Tarle, L. Whiteway, B. Yanny, and DES Collaboration. Nearest Neighbor: The Low-mass Milky Way Satellite Tucana III. ApJ, 838(1):11, March 2017. doi: 10.3847/1538-4357/aa5be7.

[218] Anirudh Chiti, Anna Frebel, Joshua D. Simon, Denis Erkal, Laura J. Chang, Lina Necib, Alexander P. Ji, Helmut Jerjen, Dongwon Kim, and John E. Norris. An extended halo around an ancient dwarf galaxy. *Nature Astronomy*, February 2021. doi: 10.1038/s41550-020-01285-w.

[219] Beth Willman, Julianne J. Dalcanton, David Martinez-Delgado, Andrew A. West, Michael R. Blanton, David W. Hogg, J. C. Barentine, Howard J. Brewington, Michael Harvanek, S. J. Kleinman, Jurek Krzesinski, Dan Long, Jr. Neilsen, Eric H., Atsuko Nitta, and Stephanie A. Snedden. A New Milky Way Dwarf Galaxy in Ursa Major. ApJ, 626(2):L85–L88, June 2005. doi: 10.1086/431760.

[220] Ferah Munshi, Alyson M. Brooks, Charlotte Christensen, Elaad Applebaum, Kelly Holley-Bockelmann, Thomas R. Quinn, and James Wadsley. Dancing in

the Dark: Uncertainty in Ultrafaint Dwarf Galaxy Predictions from Cosmological Simulations. ApJ, 874(1):40, March 2019. doi: 10.3847/1538-4357/ab0085.

[221] Coral Wheeler, Philip F. Hopkins, Andrew B. Pace, Shea Garrison-Kimmel, Michael Boylan-Kolchin, Andrew Wetzel, James S. Bullock, Dušan Kereš, Claude-André Faucher-Giguère, and Eliot Quataert. Be it therefore resolved: cosmological simulations of dwarf galaxies with 30 solar mass resolution. MNRAS, 490(3):4447–4463, December 2019. doi: 10.1093/mnras/stz2887.

[222] Martin P. Rey, Andrew Pontzen, Oscar Agertz, Matthew D. A. Orkney, Justin I. Read, Amélie Saintonge, and Christian Pedersen. EDGE: The Origin of Scatter in Ultra-faint Dwarf Stellar Masses and Surface Brightnesses. ApJ, 886(1):L3, November 2019. doi: 10.3847/2041-8213/ab53dd.

[223] Ricardo R. Muñoz, Patrick Côté, Felipe A. Santana, Marla Geha, Joshua D. Simon, Grecco A. Oyarzún, Peter B. Stetson, and S. G. Djorgovski. A MegaCam Survey of Outer Halo Satellites. III. Photometric and Structural Parameters. ApJ, 860(1):66, June 2018. doi: 10.3847/1538-4357/aac16b.

[224] Anna Frebel, John E. Norris, Gerard Gilmore, and Rosemary F. G. Wyse. The Chemical Evolution of the Bootes I Ultra-faint Dwarf Galaxy. ApJ, 826(2):110, August 2016. doi: 10.3847/0004-637X/826/2/110.

[225] John E. Norris, Rosemary F. G. Wyse, Gerard Gilmore, David Yong, Anna Frebel, Mark I. Wilkinson, V. Belokurov, and Daniel B. Zucker. Chemical Enrichment in the Faintest Galaxies: The Carbon and Iron Abundance Spreads in the Boötes I Dwarf Spheroidal Galaxy and the Segue 1 System. ApJ, 723(2): 1632–1650, November 2010. doi: 10.1088/0004-637X/723/2/1632.

[226] J. L. Marshall, S. Burles, I. B. Thompson, S. A. Shectman, B. C. Bigelow, G. Burley, C. Birk, J. Estrada, P. Jones, M. Smith, V. Kowal, J. Castillo, R. Storts, and G. Ortiz. The MagE spectrograph. In *Ground-based and Airborne Instrumentation for Astronomy II*, volume 7014 of Proc. SPIE, page 701454, July 2008. doi: 10.1117/12.789972.

[227] A. Dressler, B. Bigelow, T. Hare, B. Sutin, I. Thompson, G. Burley, H. Epps, A. Oemler, A. Bagish, C. Birk, K. Clardy, S. Gunnels, D. Kelson, S. Shectman, and D. Osip. IMACS: The Inamori-Magellan Areal Camera and Spectrograph on Magellan-Baade. PASP, 123:288–332, March 2011. doi: 10.1086/658908.

[228] E. Tolstoy, M. J. Irwin, A. Helmi, G. Battaglia, P. Jablonka, V. Hill, K. A. Venn, M. D. Shetrone, B. Letarte, A. A. Cole, F. Primas, P. Francois, N. Arimoto, K. Sadakane, A. Kaufer, T. Szeifert, and T. Abel. Two Distinct Ancient Components in the Sculptor Dwarf Spheroidal Galaxy: First Results from the Dwarf Abundances and Radial Velocities Team. ApJ, 617:L119–L122, December 2004. doi: 10.1086/427388.

[229] T. S. Li, J. D. Simon, K. Kuehn, A. B. Pace, D. Erkal, K. Bechtol, B. Yanny, A. Drlica-Wagner, J. L. Marshall, C. Lidman, E. Balbinot, D. Carollo, S. Jenkins, C. E. Martínez-Vázquez, N. Shipp, K. M. Stringer, A. K. Vivas, A. R. Walker, R. H. Wechsler, F. B. Abdalla, S. Allam, J. Annis, S. Avila, E. Bertin, D. Brooks, E. Buckley-Geer, D. L. Burke, A. Carnero Rosell, M. Carrasco Kind, J. Carretero, C. E. Cunha, C. B. D'Andrea, L. N. da Costa, C. Davis, J. De Vicente, P. Doel, T. F. Eifler, A. E. Evrard, B. Flaugher, J. Frieman, J. García-Bellido, E. Gaztanaga, D. W. Gerdes, D. Gruen, R. A. Gruendl, J. Gschwend, G. Gutierrez, W. G. Hartley, D. L. Hollowood, K. Honscheid, D. J. James, E. Krause, M. A. G. Maia, M. March, F. Menanteau, R. Miquel, A. A. Plazas, E. Sanchez, B. Santiago, V. Scarpine, R. Schindler, M. Schubnell, I. Sevilla-Noarbe, M. Smith, R. C. Smith, M. Soares-Santos, F. Sobreira, E. Suchyta, M. E. C. Swanson, G. Tarle, D. L. Tucker, and DES Collaboration. The First Tidally Disrupted Ultra-faint Dwarf Galaxy?: A Spectroscopic Analysis of the Tucana III Stream. ApJ, 866(1):22, October 2018. doi: 10.3847/1538-4357/aadf91.

[230] J. I. Read and D. Erkal. Abundance matching with the mean star formation rate: there is no missing satellites problem in the Milky Way above $M_{200} \sim 10^9$ $M_\odot$. MNRAS, 487(4):5799–5812, August 2019. doi: 10.1093/mnras/stz1320.

[231] P. Jethwa, D. Erkal, and V. Belokurov. The upper bound on the lowest mass halo. MNRAS, 473(2):2060–2083, January 2018. doi: 10.1093/mnras/stx2330.

[232] Oscar Agertz, Andrew Pontzen, Justin I. Read, Martin P. Rey, Matthew Orkney, Joakim Rosdahl, Romain Teyssier, Robbert Verbeke, Michael Kretschmer, and Sarah Nickerson. EDGE: the mass-metallicity relation as a critical test of galaxy formation physics. MNRAS, 491(2):1656–1672, January 2020. doi: 10.1093/mnras/stz3053.

[233] Mattis Magg, Tilman Hartwig, Bhaskar Agarwal, Anna Frebel, Simon C. O. Glover, Brendan F. Griffen, and Ralf S. Klessen. Predicting the locations of possible long-lived low-mass first stars: importance of satellite dwarf galaxies. MNRAS, 473(4):5308–5323, February 2018. doi: 10.1093/mnras/stx2729.

[234] G. S. Da Costa, M. S. Bessell, A. D. Mackey, T. Nordland er, M. Asplund, A. R. Casey, A. Frebel, K. Lind, A. F. Marino, S. J. Murphy, J. E. Norris, B. P. Schmidt, and D. Yong. The SkyMapper DR1.1 search for extremely metal-poor stars. MNRAS, 489(4):5900–5918, November 2019. doi: 10.1093/mnras/stz2550.

[235] S. Murphy, S. Keller, B. Schmidt, P. Tisserand, M. Bessell, P. Francis, and G. Da Costa. SkyMapper and the Southern Sky Survey: A Valuable Resource for Stellar Astrophysics. In S. J. Murphy and M. S. Bessell, editors, *The Eighth Pacific Rim Conference on Stellar Astrophysics: A Tribute to Kam-Ching Leung*, volume 404 of *Astronomical Society of the Pacific Conference Series*, page 356, August 2009.

[236] Joshua D. Simon. Gaia Proper Motions and Orbits of the Ultra-faint Milky Way Satellites. ApJ, 863(1):89, August 2018. doi: 10.3847/1538-4357/aacdfb.

[237] E. Bertin. Automated Morphometry with SExtractor and PSFEx. In I. N. Evans, A. Accomazzi, D. J. Mink, and A. H. Rots, editors, *Astronomical Data Analysis Software and Systems XX*, volume 442 of *Astronomical Society of the Pacific Conference Series*, page 435, July 2011.

[238] B. Flaugher, H. T. Diehl, K. Honscheid, T. M. C. Abbott, O. Alvarez, R. Angstadt, J. T. Annis, M. Antonik, O. Ballester, L. Beaufore, G. M. Bernstein, R. A. Bernstein, B. Bigelow, M. Bonati, D. Boprie, D. Brooks, E. J. Buckley-Geer, J. Campa, L. Cardiel-Sas, F. J. Castander, J. Castilla, H. Cease, J. M. Cela-Ruiz, S. Chappa, E. Chi, C. Cooper, L. N. da Costa, E. Dede, G. Derylo, D. L. DePoy, J. de Vicente, P. Doel, A. Drlica-Wagner, J. Eiting, A. E. Elliott, J. Emes, J. Estrada, A. Fausti Neto, D. A. Finley, R. Flores, J. Frieman, D. Gerdes, M. D. Gladders, B. Gregory, G. R. Gutierrez, J. Hao, S. E. Holland, S. Holm, D. Huffman, C. Jackson, D. J. James, M. Jonas, A. Karcher, I. Karliner, S. Kent, R. Kessler, M. Kozlovsky, R. G. Kron, D. Kubik, K. Kuehn, S. Kuhlmann, K. Kuk, O. Lahav, A. Lathrop, J. Lee, M. E. Levi, P. Lewis, T. S. Li, I. Mandrichenko, J. L. Marshall, G. Martinez, K. W. Merritt, R. Miquel, F. Muñoz, E. H. Neilsen, R. C. Nichol, B. Nord, R. Ogando, J. Olsen, N. Palaio, K. Patton, J. Peoples, A. A. Plazas, J. Rauch, K. Reil, J.-P. Rheault, N. A. Roe, H. Rogers, A. Roodman, E. Sanchez, V. Scarpine, R. H. Schindler, R. Schmidt, R. Schmitt, M. Schubnell, K. Schultz, P. Schurter, L. Scott, S. Serrano, T. M. Shaw, R. C. Smith, M. Soares-Santos, A. Stefanik, W. Stuermer, E. Suchyta, A. Sypniewski, G. Tarle, J. Thaler, R. Tighe, C. Tran, D. Tucker, A. R. Walker, G. Wang, M. Watson, C. Weaverdyck, W. Wester, R. Woods, B. Yanny, and DES Collaboration. The Dark Energy Camera. AJ, 150:150, November 2015. doi: 10.1088/0004-6256/150/5/150.

[239] E. Morganson, R. A. Gruendl, F. Menanteau, M. Carrasco Kind, Y. C. Chen, G. Daues, A. Drlica-Wagner, D. N. Friedel, M. Gower, M. W. G. Johnson, M. D. Johnson, R. Kessler, F. Paz-Chinchón, D. Petravick, C. Pond, B. Yanny, S. Allam, R. Armstrong, W. Barkhouse, K. Bechtol, A. Benoit-Lévy, G. M. Bernstein, E. Bertin, E. Buckley-Geer, R. Covarrubias, S. Desai, H. T. Diehl, D. A. Goldstein, D. Gruen, T. S. Li, H. Lin, J. Marriner, J. J. Mohr, E. Neilsen, C. C. Ngeow, K. Paech, E. S. Rykoff, M. Sako, I. Sevilla-Noarbe, E. Sheldon, F. Sobreira, D. L. Tucker, W. Wester, and DES Collaboration. The Dark Energy Survey Image Processing Pipeline. PASP, 130(989):074501, July 2018. doi: 10.1088/1538-3873/aab4ef.

[240] T. S. Li, J. D. Simon, A. Drlica-Wagner, K. Bechtol, M. Y. Wang, J. García-Bellido, J. Frieman, J. L. Marshall, D. J. James, L. Strigari, A. B. Pace, E. Balbinot, Y. Zhang, T. M. C. Abbott, S. Allam, A. Benoit-Lévy, G. M. Bernstein, E. Bertin, D. Brooks, D. L. Burke, A. Carnero Rosell, M. Carrasco Kind, J. Carretero, C. E. Cunha, C. B. D'Andrea, L. N. da Costa, D. L. DePoy,

S. Desai, H. T. Diehl, T. F. Eifler, B. Flaugher, D. A. Goldstein, D. Gruen, R. A. Gruendl, J. Gschwend, G. Gutierrez, E. Krause, K. Kuehn, H. Lin, M. A. G. Maia, M. March, F. Menanteau, R. Miquel, A. A. Plazas, A. K. Romer, E. Sanchez, B. Santiago, M. Schubnell, I. Sevilla-Noarbe, R. C. Smith, F. Sobreira, E. Suchyta, G. Tarle, D. Thomas, D. L. Tucker, A. R. Walker, R. H. Wechsler, W. Wester, B. Yanny, and DES Collaboration. Farthest Neighbor: The Distant Milky Way Satellite Eridanus II. ApJ, 838(1):8, March 2017. doi: 10.3847/1538-4357/aa6113.

[241] A. Oemler, K. Clardy, D. Kelson, G. Walth, and E. Villanueva. COSMOS: Carnegie Observatories System for MultiObject Spectroscopy, May 2017.

[242] Michael C. Cooper, Jeffrey A. Newman, Marc Davis, Douglas P. Finkbeiner, and Brian F. Gerke. spec2d: DEEP2 DEIMOS Spectral Pipeline, March 2012.

[243] Jeffrey A. Newman, Michael C. Cooper, Marc Davis, S. M. Faber, Alison L. Coil, Puragra Guhathakurta, David C. Koo, Andrew C. Phillips, Charlie Conroy, Aaron A. Dutton, Douglas P. Finkbeiner, Brian F. Gerke, David J. Rosario, Benjamin J. Weiner, C. N. A. Willmer, Renbin Yan, Justin J. Harker, Susan A. Kassin, N. P. Konidaris, Kamson Lai, Darren S. Madgwick, K. G. Noeske, Gregory D. Wirth, A. J. Connolly, N. Kaiser, Evan N. Kirby, Brian C. Lemaux, Lihwai Lin, Jennifer M. Lotz, G. A. Luppino, C. Marinoni, Daniel J. Matthews, Anne Metevier, and Ricardo P. Schiavon. The DEEP2 Galaxy Redshift Survey: Design, Observations, Data Reduction, and Redshifts. ApJS, 208(1):5, September 2013. doi: 10.1088/0067-0049/208/1/5.

[244] C. Chubak, G. Marcy, D. A. Fischer, A. W. Howard, H. Isaacson, J. A. Johnson, and J. T. Wright. Precise Radial Velocities of 2046 Nearby FGKM Stars and 131 Standards. *arXiv e-prints*, art. arXiv:1207.6212, July 2012.

[245] Astropy Collaboration, T. P. Robitaille, E. J. Tollerud, P. Greenfield, M. Droettboom, E. Bray, T. Aldcroft, M. Davis, A. Ginsburg, A. M. Price-Whelan, W. E. Kerzendorf, A. Conley, N. Crighton, K. Barbary, D. Muna, H. Ferguson, F. Grollier, M. M. Parikh, P. H. Nair, H. M. Unther, C. Deil, J. Woillez, S. Conseil, R. Kramer, J. E. H. Turner, L. Singer, R. Fox, B. A. Weaver, V. Zabalza, Z. I. Edwards, K. Azalee Bostroem, D. J. Burke, A. R. Casey, S. M. Crawford, N. Dencheva, J. Ely, T. Jenness, K. Labrie, P. L. Lim, F. Pierfederici, A. Pontzen, A. Ptak, B. Refsdal, M. Servillat, and O. Streicher. Astropy: A community Python package for astronomy. A&A, 558:A33, October 2013. doi: 10.1051/0004-6361/201322068.

[246] Astropy Collaboration, T. P. Robitaille, E. J. Tollerud, P. Greenfield, M. Droettboom, E. Bray, T. Aldcroft, M. Davis, A. Ginsburg, A. M. Price-Whelan, W. E. Kerzendorf, A. Conley, N. Crighton, K. Barbary, D. Muna, H. Ferguson, F. Grollier, M. M. Parikh, P. H. Nair, H. M. Unther, C. Deil, J. Woillez, S. Conseil, R. Kramer, J. E. H. Turner, L. Singer, R. Fox, B. A. Weaver, V. Zabalza,

Z. I. Edwards, K. Azalee Bostroem, D. J. Burke, A. R. Casey, S. M. Crawford, N. Dencheva, J. Ely, T. Jenness, K. Labrie, P. L. Lim, F. Pierfederici, A. Pontzen, A. Ptak, B. Refsdal, M. Servillat, and O. Streicher. Astropy: A community Python package for astronomy. A&A, 558:A33, October 2013. doi: 10.1051/0004-6361/201322068.

[247] Matthew G. Walker, Mario Mateo, Edward W. Olszewski, Rebecca Bernstein, Xiao Wang, and Michael Woodroofe. Internal Kinematics of the Fornax Dwarf Spheroidal Galaxy. AJ, 131(4):2114–2139, April 2006. doi: 10.1086/500193.

[248] Daniel Foreman-Mackey, David W. Hogg, Dustin Lang, and Jonathan Goodman. emcee: The MCMC Hammer. PASP, 125(925):306, March 2013. doi: 10.1086/670067.

[249] R. Carrera, E. Pancino, C. Gallart, and A. del Pino. The near-infrared Ca II triplet as a metallicity indicator - II. Extension to extremely metal-poor metallicity regimes. MNRAS, 434:1681–1691, September 2013. doi: 10.1093/mnras/stt1126.

[250] D. Tody. The IRAF Data Reduction and Analysis System. In D. L. Crawford, editor, *Instrumentation in astronomy VI*, volume 627 of Proc. SPIE, page 733, January 1986. doi: 10.1117/12.968154.

[251] D. Tody. IRAF in the Nineties. In R. J. Hanisch, R. J. V. Brissenden, and J. Barnes, editors, *Astronomical Data Analysis Software and Systems II*, volume 52 of *Astronomical Society of the Pacific Conference Series*, page 173, January 1993.

[252] R. L. Kurucz. Including all the lines. *Canadian Journal of Physics*, 89:417–428, April 2011. doi: 10.1139/p10-104.

[253] C. Sneden, J. J. Cowan, C. Kobayashi, M. Pignatari, J. E. Lawler, E. A. Den Hartog, and M. P. Wood. Iron-group Abundances in the Metal-poor Main-Sequence Turnoff Star HD˜84937. ApJ, 817:53, January 2016. doi: 10.3847/0004-637X/817/1/53.

[254] T. M. C. Abbott, F. B. Abdalla, S. Allam, A. Amara, J. Annis, J. Asorey, S. Avila, O. Ballester, M. Banerji, W. Barkhouse, L. Baruah, M. Baumer, K. Bechtol, M. R. Becker, A. Benoit-Lévy, G. M. Bernstein, E. Bertin, J. Blazek, S. Bocquet, D. Brooks, D. Brout, E. Buckley-Geer, D. L. Burke, V. Busti, R. Campisano, L. Cardiel-Sas, A. Carnero Rosell, M. Carrasco Kind, J. Carretero, F. J. Castander, R. Cawthon, C. Chang, X. Chen, C. Conselice, G. Costa, M. Crocce, C. E. Cunha, C. B. D'Andrea, L. N. da Costa, R. Das, G. Daues, T. M. Davis, C. Davis, J. De Vicente, D. L. DePoy, J. DeRose, S. Desai, H. T. Diehl, J. P. Dietrich, S. Dodelson, P. Doel, A. Drlica-Wagner, T. F. Eifler, A. E. Elliott, A. E. Evrard, A. Farahi, A. Fausti Neto, E. Fernandez, D. A. Finley, B. Flaugher, R. J. Foley, P. Fosalba, D. N. Friedel,

J. Frieman, J. García-Bellido, E. Gaztanaga, D. W. Gerdes, T. Giannantonio, M. S. S. Gill, K. Glazebrook, D. A. Goldstein, M. Gower, D. Gruen, R. A. Gruendl, J. Gschwend, R. R. Gupta, G. Gutierrez, S. Hamilton, W. G. Hartley, S. R. Hinton, J. M. Hislop, D. Hollowood, K. Honscheid, B. Hoyle, D. Huterer, B. Jain, D. J. James, T. Jeltema, M. W. G. Johnson, M. D. Johnson, T. Kacprzak, S. Kent, G. Khullar, M. Klein, A. Kovacs, A. M. G. Koziol, E. Krause, A. Kremin, R. Kron, K. Kuehn, S. Kuhlmann, N. Kuropatkin, O. Lahav, J. Lasker, T. S. Li, R. T. Li, A. R. Liddle, M. Lima, H. Lin, P. López-Reyes, N. MacCrann, M. A. G. Maia, J. D. Maloney, M. Manera, M. March, J. Marriner, J. L. Marshall, P. Martini, T. McClintock, T. McKay, R. G. McMahon, P. Melchior, F. Menanteau, C. J. Miller, R. Miquel, J. J. Mohr, E. Morganson, J. Mould, E. Neilsen, R. C. Nichol, F. Nogueira, B. Nord, P. Nugent, L. Nunes, R. L. C. Ogando, L. Old, A. B. Pace, A. Palmese, F. Paz-Chinchón, H. V. Peiris, W. J. Percival, D. Petravick, A. A. Plazas, J. Poh, C. Pond, A. Porredon, A. Pujol, A. Refregier, K. Reil, P. M. Ricker, R. P. Rollins, A. K. Romer, A. Roodman, P. Rooney, A. J. Ross, E. S. Rykoff, M. Sako, M. L. Sanchez, E. Sanchez, B. Santiago, A. Saro, V. Scarpine, D. Scolnic, S. Serrano, I. Sevilla-Noarbe, E. Sheldon, N. Shipp, M. L. Silveira, M. Smith, R. C. Smith, J. A. Smith, M. Soares-Santos, F. Sobreira, J. Song, A. Stebbins, E. Suchyta, M. Sullivan, M. E. C. Swanson, G. Tarle, J. Thaler, D. Thomas, R. C. Thomas, M. A. Troxel, D. L. Tucker, V. Vikram, A. K. Vivas, A. R. Walker, R. H. Wechsler, J. Weller, W. Wester, R. C. Wolf, H. Wu, B. Yanny, A. Zenteno, Y. Zhang, J. Zuntz, DES Collaboration, S. Juneau, M. Fitzpatrick, R. Nikutta, D. Nidever, K. Olsen, A. Scott, and NOAO Data Lab. The Dark Energy Survey: Data Release 1. ApJS, 239(2):18, December 2018. doi: 10.3847/1538-4365/aae9f0.

[255] A. G. Moskowitz and M. G. Walker. Stellar Density Profiles of Dwarf Spheroidal Galaxies. ApJ, 892(1):27, March 2020. doi: 10.3847/1538-4357/ab7459.

[256] D. Crnojević, D. J. Sand, D. Zaritsky, K. Spekkens, B. Willman, and J. R. Hargis. Deep Imaging of Eridanus II and Its Lone Star Cluster. ApJ, 824(1): L14, June 2016. doi: 10.3847/2041-8205/824/1/L14.

[257] Blair C. Conn, Helmut Jerjen, Dongwon Kim, and Mischa Schirmer. On the Nature of Ultra-faint Dwarf Galaxy Candidates. I. DES1, Eridanus III, and Tucana V. ApJ, 852(2):68, January 2018. doi: 10.3847/1538-4357/aa9eda.

[258] E. Luque, B. Santiago, A. Pieres, J. L. Marshall, A. B. Pace, R. Kron, A. Drlica-Wagner, A. Queiroz, E. Balbinot, M. dal Ponte, A. Fausti Neto, L. N. da Costa, M. A. G. Maia, A. R. Walker, F. B. Abdalla, S. Allam, J. Annis, K. Bechtol, A. Benoit-Lévy, E. Bertin, D. Brooks, A. Carnero Rosell, M. Carrasco Kind, J. Carretero, M. Crocce, C. Davis, P. Doel, T. F. Eifler, B. Flaugher, J. García-Bellido, D. W. Gerdes, D. Gruen, R. A. Gruendl, G. Gutierrez, K. Honscheid, D. J. James, K. Kuehn, N. Kuropatkin, R. Miquel, R. C. Nichol, A. A. Plazas, E. Sanchez, V. Scarpine, R. Schindler, I. Sevilla-Noarbe, M. Smith, M. Soares-Santos, F. Sobreira, E. Suchyta, G. Tarle, and D. Thomas. Deep SOAR follow-

up photometry of two Milky Way outer-halo companions discovered with Dark Energy Survey. MNRAS, 478(2):2006–2018, August 2018. doi: 10.1093/mnras/sty1039.

[259] Burçin Mutlu-Pakdil, David J. Sand, Jeffrey L. Carlin, Kristine Spekkens, Nelson Caldwell, Denija Crnojević, Allison K. Hughes, Beth Willman, and Dennis Zaritsky. A Deeper Look at the New Milky Way Satellites: Sagittarius II, Reticulum II, Phoenix II, and Tucana III. ApJ, 863(1):25, August 2018. doi: 10.3847/1538-4357/aacd0e.

[260] Helmut Jerjen, Blair Conn, Dongwon Kim, and Mischa Schirmer. On the Nature of Ultra-faint Dwarf Galaxy Candidates. III. Horologium I, Pictor I, Grus I, and Phoenix II. *arXiv e-prints*, art. arXiv:1809.02259, September 2018.

[261] A. Katherina Vivas, Clara Martínez-Vázquez, and Alistair R. Walker. Gaia RR Lyrae Stars in Nearby Ultra-faint Dwarf Satellite Galaxies. ApJS, 247(1):35, March 2020. doi: 10.3847/1538-4365/ab67c0.

[262] S. L. J. Gibbons, V. Belokurov, and N. W. Evans. 'Skinny Milky Way please', says Sagittarius. MNRAS, 445(4):3788–3802, December 2014. doi: 10.1093/mnras/stu1986.

[263] D. Erkal, V. Belokurov, C. F. P. Laporte, S. E. Koposov, T. S. Li, C. J. Grillmair, N. Kallivayalil, A. M. Price-Whelan, N. W. Evans, K. Hawkins, D. Hendel, C. Mateu, J. F. Navarro, A. del Pino, C. T. Slater, S. T. Sohn, and Orphan Aspen Treasury Collaboration. The total mass of the Large Magellanic Cloud from its perturbation on the Orphan stream. MNRAS, 487(2):2685–2700, August 2019. doi: 10.1093/mnras/stz1371.

[264] D. Erkal, T. S. Li, S. E. Koposov, V. Belokurov, E. Balbinot, K. Bechtol, B. Buncher, A. Drlica-Wagner, K. Kuehn, J. L. Marshall, C. E. Martínez-Vázquez, A. B. Pace, N. Shipp, J. D. Simon, K. M. Stringer, A. K. Vivas, R. H. Wechsler, B. Yanny, F. B. Abdalla, S. Allam, J. Annis, S. Avila, E. Bertin, D. Brooks, E. Buckley-Geer, D. L. Burke, A. Carnero Rosell, M. Carrasco Kind, J. Carretero, C. B. D'Andrea, L. N. da Costa, C. Davis, J. De Vicente, P. Doel, T. F. Eifler, A. E. Evrard, B. Flaugher, J. Frieman, J. García-Bellido, E. Gaztanaga, D. W. Gerdes, D. Gruen, R. A. Gruendl, J. Gschwend, G. Gutierrez, W. G. Hartley, D. L. Hollowood, K. Honscheid, D. J. James, E. Krause, M. A. G. Maia, M. March, F. Menanteau, R. Miquel, R. L. C. Ogando, A. A. Plazas, E. Sanchez, B. Santiago, V. Scarpine, R. Schindler, I. Sevilla-Noarbe, M. Smith, R. C. Smith, M. Soares-Santos, F. Sobreira, E. Suchyta, M. E. C. Swanson, G. Tarle, D. L. Tucker, and A. R. Walker. Modelling the Tucana III stream - a close passage with the LMC. MNRAS, 481(3):3148–3159, December 2018. doi: 10.1093/mnras/sty2518.

[265] Paul J. McMillan. The mass distribution and gravitational potential of the Milky Way. MNRAS, 465(1):76–94, February 2017. doi: 10.1093/mnras/stw2759.

[266] Walter Dehnen and James J. Binney. Local stellar kinematics from HIPPARCOS data. MNRAS, 298(2):387–394, August 1998. doi: 10.1046/j.1365-8711.1998.01600.x.

[267] Lars Hernquist. An Analytical Model for Spherical Galaxies and Bulges. ApJ, 356:359, June 1990. doi: 10.1086/168845.

[268] Nitya Kallivayalil, Roeland P. van der Marel, Gurtina Besla, Jay Anderson, and Charles Alcock. Third-epoch Magellanic Cloud Proper Motions. I. Hubble Space Telescope/WFC3 Data and Orbit Implications. ApJ, 764(2):161, February 2013. doi: 10.1088/0004-637X/764/2/161.

[269] Roeland P. van der Marel, David R. Alves, Eduardo Hardy, and Nicholas B. Suntzeff. New Understanding of Large Magellanic Cloud Structure, Dynamics, and Orbit from Carbon Star Kinematics. AJ, 124(5):2639–2663, November 2002. doi: 10.1086/343775.

[270] G. Pietrzyński, D. Graczyk, W. Gieren, I. B. Thompson, B. Pilecki, A. Udalski, I. Soszyński, S. Kozłowski, P. Konorski, K. Suchomska, G. Bono, P. G. Prada Moroni, S. Villanova, N. Nardetto, F. Bresolin, R. P. Kudritzki, J. Storm, A. Gallenne, R. Smolec, D. Minniti, M. Kubiak, M. K. Szymański, R. Poleski, Ł. Wyrzykowski, K. Ulaczyk, P. Pietrukowicz, M. Górski, and P. Karczmarek. An eclipsing-binary distance to the Large Magellanic Cloud accurate to two per cent. Nature, 495(7439):76–79, March 2013. doi: 10.1038/nature11878.

[271] Jo Bovy. galpy: Galactic dynamics package, November 2014.

[272] Jeremy J. Webb, Jo Bovy, Raymond G. Carlberg, and Mark Gieles. Modelling the effects of dark matter substructure on globular cluster evolution with the tidal approximation. MNRAS, 488(4):5748–5762, October 2019. doi: 10.1093/mnras/stz2118.

[273] J. I. Read and P. Steger. How to break the density-anisotropy degeneracy in spherical stellar systems. MNRAS, 471(4):4541–4558, November 2017. doi: 10.1093/mnras/stx1798.

[274] James Binney and Scott Tremaine. *Galactic Dynamics: Second Edition*. 2008.

[275] Laura J. Chang and Lina Necib. Dark Matter Density Profiles in Dwarf Galaxies: Linking Jeans Modeling Systematics and Observation. *arXiv e-prints*, art. arXiv:2009.00613, September 2020.

[276] Julio F. Navarro, Carlos S. Frenk, and Simon D. M. White. A Universal Density Profile from Hierarchical Clustering. ApJ, 490(2):493–508, December 1997. doi: 10.1086/304888.

[277] V. Bonnivard, D. Maurin, and M. G. Walker. Contamination of stellar-kinematic samples and uncertainty about dark matter annihilation profiles in

ultrafaint dwarf galaxies: the example of Segue I. MNRAS, 462(1):223–234, October 2016. doi: 10.1093/mnras/stw1691.

[278] L. P. Osipkov. Spherical systems of gravitating bodies with ellipsoidal velocity distribution. *Pisma v Astronomicheskii Zhurnal*, 5:77–80, February 1979.

[279] D. Merritt. Spherical stellar systems with spheroidal velocity distributions. AJ, 90:1027–1037, June 1985. doi: 10.1086/113810.

[280] Andrew P. Hearin, Duncan Campbell, Erik Tollerud, Peter Behroozi, Benedikt Diemer, Nathan J. Goldbaum, Elise Jennings, Alexie Leauthaud, Yao-Yuan Mao, Surhud More, John Parejko, Manodeep Sinha, Brigitta Sipöcz, and Andrew Zentner. Forward Modeling of Large-scale Structure: An Open-source Approach with Halotools. AJ, 154(5):190, November 2017. doi: 10.3847/1538-3881/aa859f.

[281] Aaron A. Dutton and Andrea V. Macciò. Cold dark matter haloes in the Planck era: evolution of structural parameters for Einasto and NFW profiles. MNRAS, 441(4):3359–3374, July 2014. doi: 10.1093/mnras/stu742.

[282] A. McWilliam. Abundance Ratios and Galactic Chemical Evolution. ARA&A, 35:503–556, 1997. doi: 10.1146/annurev.astro.35.1.503.

[283] E. N. Kirby, J. G. Cohen, G. H. Smith, S. R. Majewski, S. T. Sohn, and P. Guhathakurta. Multi-element Abundance Measurements from Medium-resolution Spectra. IV. Alpha Element Distributions in Milky Way Satellite Galaxies. ApJ, 727:79, February 2011. doi: 10.1088/0004-637X/727/2/79.

[284] K. Freeman and J. Bland-Hawthorn. The New Galaxy: Signatures of Its Formation. ARA&A, 40:487–537, 2002. doi: 10.1146/annurev.astro.40.060401.093840.

[285] V. Bromm and R. B. Larson. The First Stars. ARA&A, 42:79–118, September 2004. doi: 10.1146/annurev.astro.42.053102.134034.

[286] J. G. Cohen and W. Huang. The Chemical Evolution of the Draco Dwarf Spheroidal Galaxy. ApJ, 701:1053–1075, August 2009. doi: 10.1088/0004-637X/701/2/1053.

[287] J. G. Cohen and W. Huang. The Chemical Evolution of the Ursa Minor Dwarf Spheroidal Galaxy. ApJ, 719:931–949, August 2010. doi: 10.1088/0004-637X/719/1/931.

[288] E. N. Kirby, P. Guhathakurta, M. Bolte, C. Sneden, and M. C. Geha. Multi-element Abundance Measurements from Medium-resolution Spectra. I. The Sculptor Dwarf Spheroidal Galaxy. ApJ, 705:328–346, November 2009. doi: 10.1088/0004-637X/705/1/328.

[289] J. D. Simon, A. Frebel, A. McWilliam, E. N. Kirby, and I. B. Thompson. High-resolution Spectroscopy of Extremely Metal-poor Stars in the Least Evolved Galaxies: Leo IV. ApJ, 716:446–452, June 2010. doi: 10.1088/0004-637X/716/1/446.

[290] M. Tafelmeyer, P. Jablonka, V. Hill, M. Shetrone, E. Tolstoy, M. J. Irwin, G. Battaglia, A. Helmi, E. Starkenburg, K. A. Venn, T. Abel, P. Francois, A. Kaufer, P. North, F. Primas, and T. Szeifert. Extremely metal-poor stars in classical dwarf spheroidal galaxies: Fornax, Sculptor, and Sextans. A&A, 524: A58, December 2010. doi: 10.1051/0004-6361/201014733.

[291] D. K. Lai, Y. S. Lee, M. Bolte, S. Lucatello, T. C. Beers, J. A. Johnson, T. Sivarani, and C. M. Rockosi. The [Fe/H], [C/Fe], and [α/Fe] Distributions of the Boötes I Dwarf Spheroidal Galaxy. ApJ, 738:51, September 2011. doi: 10.1088/0004-637X/738/1/51.

[292] M. Shetrone, K. A. Venn, E. Tolstoy, F. Primas, V. Hill, and A. Kaufer. VLT/UVES Abundances in Four Nearby Dwarf Spheroidal Galaxies. I. Nucleosynthesis and Abundance Ratios. AJ, 125:684–706, February 2003. doi: 10.1086/345966.

[293] E. Tolstoy, K. A. Venn, M. Shetrone, F. Primas, V. Hill, A. Kaufer, and T. Szeifert. VLT/UVES Abundances in Four Nearby Dwarf Spheroidal Galaxies. II. Implications for Understanding Galaxy Evolution. AJ, 125:707–726, February 2003. doi: 10.1086/345967.

[294] D. Geisler, V. V. Smith, G. Wallerstein, G. Gonzalez, and C. Charbonnel. "Sculptor-ing" the Galaxy? The Chemical Compositions of Red Giants in the Sculptor Dwarf Spheroidal Galaxy. AJ, 129:1428–1442, March 2005. doi: 10.1086/427540.

[295] G. Battaglia, A. Helmi, E. Tolstoy, M. Irwin, V. Hill, and P. Jablonka. The Kinematic Status and Mass Content of the Sculptor Dwarf Spheroidal Galaxy. ApJ, 681:L13, July 2008. doi: 10.1086/590179.

[296] E. Starkenburg, V. Hill, E. Tolstoy, J. I. González Hernández, M. Irwin, A. Helmi, G. Battaglia, P. Jablonka, M. Tafelmeyer, M. Shetrone, K. Venn, and T. de Boer. The NIR Ca ii triplet at low metallicity. Searching for extremely low-metallicity stars in classical dwarf galaxies. A&A, 513:A34, April 2010. doi: 10.1051/0004-6361/200913759.

[297] D. Romano and E. Starkenburg. Chemical evolution of Local Group dwarf galaxies in a cosmological context - I. A new modelling approach and its application to the Sculptor dwarf spheroidal galaxy. MNRAS, 434:471–487, September 2013. doi: 10.1093/mnras/stt1033.

[298] T. C. Beers, G. W. Preston, and S. A. Shectman. A search for stars of very low metal abundance. II. AJ, 103:1987–2034, June 1992. doi: 10.1086/116207.

[299] S. Rossi, T. C. Beers, and C. Sneden. Carbon Abundances for Metal-Poor Stars Based on Medium-Resolution Spectra. In B. K. Gibson, R. S. Axelrod, and M. E. Putman, editors, *The Third Stromlo Symposium: The Galactic Halo*, volume 165 of *Astronomical Society of the Pacific Conference Series*, page 264, 1999.

[300] W. Aoki, J. E. Norris, S. G. Ryan, T. C. Beers, and H. Ando. The Chemical Composition of Carbon-rich, Very Metal Poor Stars: A New Class of Mildly Carbon Rich Objects without Excess of Neutron-Capture Elements. ApJ, 567: 1166–1182, March 2002. doi: 10.1086/338756.

[301] S. G. Ryan. Carbon-rich, Extremely Metal-Poor Population II stars. In C. Charbonnel, D. Schaerer, and G. Meynet, editors, *CNO in the Universe*, volume 304 of *Astronomical Society of the Pacific Conference Series*, page 128, 2003.

[302] J. G. Cohen, S. Shectman, I. Thompson, A. McWilliam, N. Christlieb, J. Melendez, F.-J. Zickgraf, S. Ramírez, and A. Swenson. The Frequency of Carbon Stars among Extremely Metal-poor Stars. ApJ, 633:L109–L112, November 2005. doi: 10.1086/498502.

[303] S. Lucatello, S. Tsangarides, T. C. Beers, E. Carretta, R. G. Gratton, and S. G. Ryan. The Binary Frequency Among Carbon-enhanced, s-Process-rich, Metal-poor Stars. ApJ, 625:825–832, June 2005. doi: 10.1086/428104.

[304] T. T. Hansen, J. Andersen, B. Nordström, T. C. Beers, V. M. Placco, J. Yoon, and L. A. Buchhave. The role of binaries in the enrichment of the early Galactic halo. III. Carbon-enhanced metal-poor stars - CEMP-s stars. A&A, 588:A3, April 2016. doi: 10.1051/0004-6361/201527409.

[305] J. E. Norris, D. Yong, M. S. Bessell, N. Christlieb, M. Asplund, G. Gilmore, R. F. G. Wyse, T. C. Beers, P. S. Barklem, A. Frebel, and S. G. Ryan. The Most Metal-poor Stars. IV. The Two Populations with [Fe/H] ˜ -3.0. ApJ, 762: 28, January 2013. doi: 10.1088/0004-637X/762/1/28.

[306] E. Starkenburg, V. Hill, E. Tolstoy, P. François, M. J. Irwin, L. Boschman, K. A. Venn, T. J. L. de Boer, B. Lemasle, P. Jablonka, G. Battaglia, P. Groot, and L. Kaper. The extremely low-metallicity tail of the Sculptor dwarf spheroidal galaxy. A&A, 549:A88, January 2013. doi: 10.1051/0004-6361/201220349.

[307] Á. Skúladóttir, E. Tolstoy, S. Salvadori, V. Hill, M. Pettini, M. D. Shetrone, and E. Starkenburg. The first carbon-enhanced metal-poor star found in the Sculptor dwarf spheroidal. A&A, 574:A129, February 2015. doi: 10.1051/0004-6361/201424782.

[308] C. Lardo, G. Battaglia, E. Pancino, D. Romano, T. J. L. de Boer, E. Starkenburg, E. Tolstoy, M. J. Irwin, P. Jablonka, and M. Tosi. Carbon and nitrogen abundances of individual stars in the Sculptor dwarf spheroidal galaxy. A&A, 585:A70, January 2016. doi: 10.1051/0004-6361/201527391.

[309] C. Salgado, G. S. Da Costa, D. Yong, and J. E. Norris. Scl-1013644: a CEMP-s star in the Sculptor Dwarf Spheroidal Galaxy. MNRAS, August 2016. doi: 10.1093/mnras/stw1986.

[310] R. D. Cannon, B. Niss, and H. U. Norgaard-Nielsen. The Discovery of Two Carbon Stars in the Carina Dwarf Galaxy. MNRAS, 196:1P, July 1981. doi: 10.1093/mnras/196.1.1P.

[311] J. R. Mould, R. D. Cannon, J. A. Frogel, and M. Aaronson. Carbon stars in the Carina dwarf spheroidal galaxy. ApJ, 254:500–506, March 1982. doi: 10.1086/159759.

[312] J. A. Frogel, V. M. Blanco, J. G. Cohen, and M. F. McCarthy. The late-type stellar content of the Fornax and Sculptor dwarf galaxies. ApJ, 252:133–146, January 1982. doi: 10.1086/159540.

[313] H. B. Richer and B. E. Westerlund. Carbon stars in Local Group galaxies. ApJ, 264:114–125, January 1983. doi: 10.1086/160578.

[314] M. Aaronson, P. W. Hodge, and E. W. Olszewski. Carbon stars and the seven dwarfs. ApJ, 267:271–279, April 1983. doi: 10.1086/160865.

[315] V. M. Blanco and M. F. McCarthy. The distribution of carbon and M-type giants in the Magellanic Clouds. AJ, 88:1442–1457, October 1983. doi: 10.1086/113433.

[316] M. Azzopardi, J. Lequeux, and B. E. Westerlund. New carbon stars in spheroidal galaxies. I - Sculptor, Carina, Leo I and Leo II systems. A&A, 144:388–394, March 1985.

[317] M. Azzopardi, J. Lequeux, and B. E. Westerlund. New carbon stars in spheroidal galaxies. II - Draco, Ursa Minor and new data on Sculptor, Carina, and Leo I. A&A, 161:232–236, June 1986.

[318] M. D. Shetrone, G. H. Smith, L. M. Stanford, M. H. Siegel, and H. E. Bond. Carbon Abundances for Red Giants in the Draco Dwarf Spheroidal Galaxy. AJ, 145:123, May 2013. doi: 10.1088/0004-6256/145/5/123.

[319] A. Susmitha, A. Koch, and T. Sivarani. Abundance analysis of a CEMP-no star in the Carina dwarf spheroidal galaxy. *ArXiv e-prints*, June 2017.

[320] G. Battaglia. *Chemistry and kinematics of stars in Local Group galaxies*. PhD thesis, Kapteyn Astronomical Institute, University of Groningen, September 2007.

[321] P. Marigo, L. Girardi, A. Bressan, M. A. T. Groenewegen, L. Silva, and G. L. Granato. Evolution of asymptotic giant branch stars. II. Optical to far-infrared isochrones with improved TP-AGB models. A&A, 482:883–905, May 2008. doi: 10.1051/0004-6361:20078467.

[322] M. Mateo, J. I. Bailey, J. Crane, S. Shectman, I. Thompson, I. Roederer, B. Bigelow, and S. Gunnels. M2FS: the Michigan/Magellan Fiber System. In *Ground-based and Airborne Instrumentation for Astronomy IV*, volume 8446 of Proc. SPIE, page 84464Y, September 2012. doi: 10.1117/12.926448.

[323] G. A. Oyarzún, G. A. Blanc, V. González, M. Mateo, J. I. Bailey, III, S. L. Finkelstein, P. Lira, J. D. Crane, and E. W. Olszewski. How Lyman Alpha Emission Depends on Galaxy Stellar Mass. ApJ, 821:L14, April 2016. doi: 10.3847/2041-8205/821/1/L14.

[324] M. G. Walker, M. Mateo, and E. W. Olszewski. Stellar Velocities in the Carina, Fornax, Sculptor, and Sextans dSph Galaxies: Data From the Magellan/MMFS Survey. AJ, 137:3100–3108, February 2009. doi: 10.1088/0004-6256/137/2/3100.

[325] T. C. Beers, J. A. Kage, G. W. Preston, and S. A. Shectman. Estimation of stellar metal abundance. I - Calibration of the CA II K index. AJ, 100:849–883, September 1990. doi: 10.1086/115568.

[326] K. U. Ratnatunga and K. C. Freeman. Field K giants in Galactic halo. II - Improved abundance and kinematic parameters. ApJ, 339:126–148, April 1989. doi: 10.1086/167282.

[327] Daniel J. Eisenstein, David H. Weinberg, Eric Agol, Hiroaki Aihara, Carlos Allende Prieto, Scott F. Anderson, James A. Arns, Éric Aubourg, Stephen Bailey, Eduardo Balbinot, Robert Barkhouser, Timothy C. Beers, Andreas A. Berlind, Steven J. Bickerton, Dmitry Bizyaev, Michael R. Blanton, John J. Bochanski, Adam S. Bolton, Casey T. Bosman, Jo Bovy, W. N. Brandt, Ben Breslauer, Howard J. Brewington, J. Brinkmann, Peter J. Brown, Joel R. Brownstein, Dan Burger, Nicolas G. Busca, Heather Campbell, Phillip A. Cargile, William C. Carithers, Joleen K. Carlberg, Michael A. Carr, Liang Chang, Yanmei Chen, Cristina Chiappini, Johan Comparat, Natalia Connolly, Marina Cortes, Rupert A. C. Croft, Katia Cunha, Luiz N. da Costa, James R. A. Davenport, Kyle Dawson, Nathan De Lee, Gustavo F. Porto de Mello, Fernand o de Simoni, Janice Dean, Saurav Dhital, Anne Ealet, Garrett L. Ebelke, Edward M. Edmondson, Jacob M. Eiting, Stephanie Escoffier, Massimiliano Esposito, Michael L. Evans, Xiaohui Fan, Bruno Femenía Castellá, Leticia Dutra Ferreira, Greg Fitzgerald, Scott W. Fleming, Andreu Font-Ribera, Eric B. Ford, Peter M. Frinchaboy, Ana Elia García Pérez, B. Scott Gaudi, Jian Ge, Luan Ghezzi, Bruce A. Gillespie, G. Gilmore, Léo Girardi, J. Richard Gott, Andrew Gould, Eva K. Grebel, James E. Gunn, Jean-Christophe Hamilton, Paul Harding, David W. Harris, Suzanne L. Hawley, Frederick R. Hearty, Joseph F. Hennawi, Jonay I. González Hernández, Shirley Ho, David W. Hogg, Jon A. Holtzman, Klaus Honscheid, Naohisa Inada, Inese I. Ivans, Linhua Jiang, Peng Jiang, Jennifer A. Johnson, Cathy Jordan, Wendell P. Jordan, Guinevere Kauffmann, Eyal Kazin, David Kirkby, Mark A. Klaene, G. R. Knapp, Jean-Paul

Kneib, C. S. Kochanek, Lars Koesterke, Juna A. Kollmeier, Richard G. Kron, Hubert Lampeitl, Dustin Lang, James E. Lawler, Jean-Marc Le Goff, Brian L. Lee, Young Sun Lee, Jarron M. Leisenring, Yen-Ting Lin, Jian Liu, Daniel C. Long, Craig P. Loomis, Sara Lucatello, Britt Lundgren, Robert H. Lupton, Bo Ma, Zhibo Ma, Nicholas MacDonald, Claude Mack, Suvrath Mahadevan, Marcio A. G. Maia, Steven R. Majewski, Martin Makler, Elena Malanushenko, Viktor Malanushenko, Rachel Mand elbaum, Claudia Maraston, Daniel Margala, Paul Maseman, Karen L. Masters, Cameron K. McBride, Patrick McDonald, Ian D. McGreer, Richard G. McMahon, Olga Mena Requejo, Brice Ménard, Jordi Miralda-Escudé, Heather L. Morrison, Fergal Mullally, Demitri Muna, Hitoshi Murayama, Adam D. Myers, Tracy Naugle, Angelo Fausti Neto, Duy Cuong Nguyen, Robert C. Nichol, David L. Nidever, Robert W. O'Connell, Ricardo L. C. Ogando, Matthew D. Olmstead, Daniel J. Oravetz, Nikhil Padmanabhan, Martin Paegert, Nathalie Palanque-Delabrouille, Kaike Pan, Parul Pandey, John K. Parejko, Isabelle Pâris, Paulo Pellegrini, Joshua Pepper, Will J. Percival, Patrick Petitjean, Robert Pfaffenberger, Janine Pforr, Stefanie Phleps, Christophe Pichon, Matthew M. Pieri, Francisco Prada, Adrian M. Price-Whelan, M. Jordan Raddick, Beatriz H. F. Ramos, I. Neill Reid, Celine Reyle, James Rich, Gordon T. Richards, George H. Rieke, Marcia J. Rieke, Hans-Walter Rix, Annie C. Robin, Helio J. Rocha-Pinto, Constance M. Rockosi, Natalie A. Roe, Emmanuel Rollinde, Ashley J. Ross, Nicholas P. Ross, Bruno Rossetto, Ariel G. Sánchez, Basilio Santiago, Conor Sayres, Ricardo Schiavon, David J. Schlegel, Katharine J. Schlesinger, Sarah J. Schmidt, Donald P. Schneider, Kris Sellgren, Alaina Shelden, Erin Sheldon, Matthew Shetrone, Yiping Shu, John D. Silverman, Jennifer Simmerer, Audrey E. Simmons, Thirupathi Sivarani, M. F. Skrutskie, Anže Slosar, Stephen Smee, Verne V. Smith, Stephanie A. Snedden, Keivan G. Stassun, Oliver Steele, Matthias Steinmetz, Mark H. Stockett, Todd Stollberg, Michael A. Strauss, Alexander S. Szalay, Masayuki Tanaka, Aniruddha R. Thakar, Daniel Thomas, Jeremy L. Tinker, Benjamin M. Tofflemire, Rita Tojeiro, Christy A. Tremonti, Mariana Vargas Magaña, Licia Verde, Nicole P. Vogt, David A. Wake, Xiaoke Wan, Ji Wang, Benjamin A. Weaver, Martin White, Simon D. M. White, John C. Wilson, John P. Wisniewski, W. Michael Wood-Vasey, Brian Yanny, Naoki Yasuda, Christophe Yèche, Donald G. York, Erick Young, Gail Zasowski, Idit Zehavi, and Bo Zhao. SDSS-III: Massive Spectroscopic Surveys of the Distant Universe, the Milky Way, and Extra-Solar Planetary Systems. AJ, 142(3):72, September 2011. doi: 10.1088/0004-6256/142/3/72.

[328] C. P. Ahn, R. Alexandroff, C. Allende Prieto, F. Anders, S. F. Anderson, T. Anderton, B. H. Andrews, É. Aubourg, S. Bailey, F. A. Bastien, and et al. The Tenth Data Release of the Sloan Digital Sky Survey: First Spectroscopic Data from the SDSS-III Apache Point Observatory Galactic Evolution Experiment. ApJS, 211:17, April 2014. doi: 10.1088/0067-0049/211/2/17.

[329] K. Jordi, E. K. Grebel, and K. Ammon. Empirical color transformations be-

tween SDSS photometry and other photometric systems. A&A, 460:339–347, December 2006. doi: 10.1051/0004-6361:20066082.

[330] D. Yong, I. U. Roederer, F. Grundahl, G. S. Da Costa, A. I. Karakas, J. E. Norris, W. Aoki, C. K. Fishlock, A. F. Marino, A. P. Milone, and L. J. Shingles. Iron and neutron-capture element abundance variations in the globular cluster M2 (NGC 7089)$^{?}$. MNRAS, 441:3396–3416, July 2014. doi: 10.1093/mnras/stu806.

[331] B. W. Carney. The Constancy of [alpha/Fe] in Globular Clusters of Differing [Fe/H] and Age. PASP, 108:900, October 1996. doi: 10.1086/133811.

[332] E. N. Kirby, P. Guhathakurta, and C. Sneden. Metallicity and Alpha-Element Abundance Measurement in Red Giant Stars from Medium-Resolution Spectra. ApJ, 682:1217-1233, August 2008. doi: 10.1086/589627.

[333] S. Rossi, T. C. Beers, C. Sneden, T. Sevastyanenko, J. Rhee, and B. Marsteller. Estimation of Carbon Abundances in Metal-Poor Stars. I. Application to the Strong G-Band Stars of Beers, Preston, and Shectman. AJ, 130:2804–2823, December 2005. doi: 10.1086/497164.

[334] F. Kupka, N. Piskunov, T. A. Ryabchikova, H. C. Stempels, and W. W. Weiss. VALD-2: Progress of the Vienna Atomic Line Data Base. A&AS, 138:119–133, July 1999. doi: 10.1051/aas:1999267.

[335] A. Kramida, Yu. Ralchenko, J. Reader, and and NIST ASD Team. NIST Atomic Spectra Database (ver. 5.2), [Online]. Available: `http://physics.nist.gov/asd` [2014, October 17]. National Institute of Standards and Technology, Gaithersburg, MD., 2014.

[336] R. L. Kurucz. Atomic and Molecular Data for Opacity Calculations. *Revista Mexicana de Astronomia y Astrofisica*, 23:45, March 1992.

[337] U. G. Jorgensen, M. Larsson, A. Iwamae, and B. Yu. Line intensities for CH and their application to stellar atmospheres. A&A, 315:204–211, November 1996.

[338] E. Anders and N. Grevesse. Abundances of the elements - Meteoritic and solar. Geochim. Cosmochim. Acta, 53:197–214, January 1989. doi: 10.1016/0016-7037(89)90286-X.

[339] N. Grevesse and A. J. Sauval. Standard Solar Composition. Space Sci. Rev., 85:161–174, May 1998. doi: 10.1023/A:1005161325181.

[340] R. D. McClure and A. W. Woodsworth. The binary nature of the barium and CH stars. III - Orbital parameters. ApJ, 352:709–723, April 1990. doi: 10.1086/168573.

[341] W. Aoki, T. C. Beers, N. Christlieb, J. E. Norris, S. G. Ryan, and S. Tsangarides. Carbon-enhanced Metal-poor Stars. I. Chemical Compositions of 26 Stars. ApJ, 655:492–521, January 2007. doi: 10.1086/509817.

[342] M. Limongi, A. Chieffi, and P. Bonifacio. On the Origin of HE 0107-5240, the Most Iron-deficient Star Presently Known. ApJ, 594:L123–L126, September 2003. doi: 10.1086/378734.

[343] H. Umeda and K. Nomoto. First-generation black-hole-forming supernovae and the metal abundance pattern of a very iron-poor star. Nature, 422:871–873, April 2003. doi: 10.1038/nature01571.

[344] N. Iwamoto, H. Umeda, N. Tominaga, K. Nomoto, and K. Maeda. The First Chemical Enrichment in the Universe and the Formation of Hyper Metal-Poor Stars. *Science*, 309:451–453, July 2005. doi: 10.1126/science.1112997.

[345] R. Hirschi. Very low-metallicity massive stars:. Pre-SN evolution models and primary nitrogen production. A&A, 461:571–583, January 2007. doi: 10.1051/0004-6361:20065356.

[346] G. Meynet, R. Hirschi, S. Ekstrom, A. Maeder, C. Georgy, P. Eggenberger, and C. Chiappini. Are C-rich ultra iron-poor stars also He-rich? A&A, 521:A30, October 2010. doi: 10.1051/0004-6361/200913377.

[347] C. C. Joggerst, A. Almgren, J. Bell, A. Heger, D. Whalen, and S. E. Woosley. The Nucleosynthetic Imprint of 15-40 M $_{sun}$ Primordial Supernovae on Metal-Poor Stars. ApJ, 709:11–26, January 2010. doi: 10.1088/0004-637X/709/1/11.

[348] N. Tominaga, N. Iwamoto, and K. Nomoto. Abundance Profiling of Extremely Metal-poor Stars and Supernova Properties in the Early Universe. ApJ, 785:98, April 2014. doi: 10.1088/0004-637X/785/2/98.

[349] E. N. Kirby and J. G. Cohen. Detailed Abundances of Two Very Metal-poor Stars in Dwarf Galaxies. AJ, 144:168, December 2012. doi: 10.1088/0004-6256/144/6/168.

[350] Ken'ichi Nomoto, Nozomu Tominaga, Hideyuki Umeda, Chiaki Kobayashi, and Keiichi Maeda. Nucleosynthesis yields of core-collapse supernovae and hypernovae, and galactic chemical evolution. Nucl. Phys. A, 777:424–458, October 2006. doi: 10.1016/j.nuclphysa.2006.05.008.

[351] V. M. Placco, A. Frebel, T. C. Beers, J. Yoon, A. Chiti, A. Heger, C. Chan, A. R. Casey, and N. Christlieb. Observational Constraints on First-Star Nucleosynthesis. II. Spectroscopy of an Ultra metal-poor CEMP-no Star. ApJ, 833:21, December 2016. doi: 10.3847/0004-637X/833/1/21.

[352] Eline Tolstoy, Vanessa Hill, and Monica Tosi. Star-Formation Histories, Abundances, and Kinematics of Dwarf Galaxies in the Local Group. *Annual*

Review of Astronomy and Astrophysics, 47:371–425, September 2009. doi: 10.1146/annurev-astro-082708-101650.

[353] T. C. Beers, G. W. Preston, and S. A. Shectman. A search for stars of very low metal abundance. I. AJ, 90:2089–2102, October 1985. doi: 10.1086/113917.

[354] N. Christlieb. Finding the Most Metal-poor Stars of the Galactic Halo with the Hamburg/ESO Objective-prism Survey (With 6 Figures). In R. E. Schielicke, editor, *Reviews in Modern Astronomy*, volume 16 of *Reviews in Modern Astronomy*, page 191, 2003. doi: 10.1002/9783527617647.ch8.

[355] A. Frebel, N. Christlieb, J. E. Norris, T. C. Beers, M. S. Bessell, J. Rhee, C. Fechner, B. Marsteller, S. Rossi, C. Thom, L. Wisotzki, and D. Reimers. Bright Metal-poor Stars from the Hamburg/ESO Survey. I. Selection and Follow-up Observations from 329 Fields. ApJ, 652:1585–1603, December 2006. doi: 10.1086/508506.

[356] Y. S. Lee, T. C. Beers, T. Sivarani, C. Allende Prieto, L. Koesterke, R. Wilhelm, P. Re Fiorentin, C. A. L. Bailer-Jones, J. E. Norris, C. M. Rockosi, B. Yanny, H. J. Newberg, K. R. Covey, H.-T. Zhang, and A.-L. Luo. The SEGUE Stellar Parameter Pipeline. I. Description and Comparison of Individual Methods. AJ, 136:2022–2049, November 2008. doi: 10.1088/0004-6256/136/5/2022.

[357] Carlos Allende Prieto, Thirupathi Sivarani, Timothy C. Beers, Young Sun Lee, Lars Koesterke, Matthew Shetrone, Christopher Sneden, David L. Lambert, Ronald Wilhelm, Constance M. Rockosi, David K. Lai, Brian Yanny, Inese I. Ivans, Jennifer A. Johnson, Wako Aoki, Coryn A. L. Bailer-Jones, and Paola Re Fiorentin. The SEGUE Stellar Parameter Pipeline. III. Comparison with High-Resolution Spectroscopy of SDSS/SEGUE Field Stars. AJ, 136:2070–2082, November 2008. doi: 10.1088/0004-6256/136/5/2070.

[358] W. Aoki, T. C. Beers, Y. S. Lee, S. Honda, H. Ito, M. Takada-Hidai, A. Frebel, T. Suda, M. Y. Fujimoto, D. Carollo, and T. Sivarani. High-resolution Spectroscopy of Extremely Metal-poor Stars from SDSS/SEGUE. I. Atmospheric Parameters and Chemical Compositions. AJ, 145:13, January 2013. doi: 10.1088/0004-6256/145/1/13.

[359] D. S. Aguado, C. Allende Prieto, J. I. González Hernández, R. Carrera, R. Rebolo, M. Shetrone, D. L. Lambert, and E. Fernández-Alvar. Follow-up observations of extremely metal-poor stars identified from SDSS. A&A, 593:A10, August 2016. doi: 10.1051/0004-6361/201628371.

[360] Jon P. Fulbright, Rosemary F. G. Wyse, Gregory R. Ruchti, G. F. Gilmore, Eva Grebel, O. Bienaymé, J. Binney, J. Bland-Hawthorn, R. Campbell, K. C. Freeman, B. K. Gibson, A. Helmi, U. Munari, J. F. Navarro, Q. A. Parker, W. Reid, G. M. Seabroke, A. Siebert, A. Siviero, M. Steinmetz, F. G. Watson, M. Williams, and T. Zwitter. The RAVE Survey: Rich in Very Metal-poor Stars. ApJ, 724:L104–L108, November 2010. doi: 10.1088/2041-8205/724/1/L104.

[361] D. S. Aguado, J. I. González Hernández, C. Allende Prieto, and R. Rebolo. WHT follow-up observations of extremely metal-poor stars identified from SDSS and LAMOST. A&A, 605:A40, September 2017. doi: 10.1051/0004-6361/201730654.

[362] Haining Li, Kefeng Tan, and Gang Zhao. A Catalog of 10,000 Very Metal-poor Stars from LAMOST DR3. *The Astrophysical Journal Supplement Series*, 238: 16, October 2018. doi: 10.3847/1538-4365/aada4a.

[363] Abdu Abohalima and Anna Frebel. JINAbase—A Database for Chemical Abundances of Metal-poor Stars. *The Astrophysical Journal Supplement Series*, 238: 36, October 2018. doi: 10.3847/1538-4365/aadfe9.

[364] D. D. Whitten, V. M. Placco, T. C. Beers, A. L. Chies-Santos, C. Bonatto, J. Varela, D. Cristóbal-Hornillos, A. Ederoclite, T. Masseron, Y. S. Lee, S. Akras, M. Borges Fernandes, J. A. Caballero, A. J. Cenarro, P. Coelho, M. V. Costa-Duarte, S. Daflon, R. A. Dupke, R. Lopes de Oliveira, C. López-Sanjuan, A. Marín-Franch, C. Mendes de Oliveira, M. Moles, A. A. Orsi, S. Rossi, L. Sodré, and H. Vázquez Ramió. J-PLUS: Identification of low-metallicity stars with artificial neural networks using SPHINX. *arXiv e-prints*, November 2018.

[365] T. Nordlander, A. M. Amarsi, K. Lind, M. Asplund, P. S. Barklem, A. R. Casey, R. Collet, and J. Leenaarts. 3D NLTE analysis of the most iron-deficient star, SMSS0313-6708. A&A, 597:A6, January 2017. doi: 10.1051/0004-6361/201629202.

[366] R. A. Ibata, G. Gilmore, and M. J. Irwin. A dwarf satellite galaxy in Sagittarius. Nature, 370:194–196, July 1994. doi: 10.1038/370194a0.

[367] P. Bonifacio, V. Hill, P. Molaro, L. Pasquini, P. Di Marcantonio, and P. Santin. First results of UVES at VLT: abundances in the Sgr dSph. A&A, 359:663–668, July 2000.

[368] P. Bonifacio, L. Sbordone, G. Marconi, L. Pasquini, and V. Hill. The Sgr dSph hosts a metal-rich population. A&A, 414:503–514, February 2004. doi: 10.1051/0004-6361:20031692.

[369] L. Monaco, M. Bellazzini, P. Bonifacio, F. R. Ferraro, G. Marconi, E. Pancino, L. Sbordone, and S. Zaggia. The Ital-FLAMES survey of the Sagittarius dwarf spheroidal galaxy. I. Chemical abundances of bright RGB stars. A&A, 441: 141–151, October 2005. doi: 10.1051/0004-6361:20053333.

[370] L. Sbordone, P. Bonifacio, R. Buonanno, G. Marconi, L. Monaco, and S. Zaggia. The exotic chemical composition of the Sagittarius dwarf spheroidal galaxy. A&A, 465:815–824, April 2007. doi: 10.1051/0004-6361:20066385.

[371] M. Bellazzini, R. A. Ibata, S. C. Chapman, A. D. Mackey, L. Monaco, M. J. Irwin, N. F. Martin, G. F. Lewis, and E. Dalessandro. The Nucleus of the Sagittarius Dsph Galaxy and M54: a Window on the Process of Galaxy Nucleation. AJ, 136:1147–1170, September 2008. doi: 10.1088/0004-6256/136/3/1147.

[372] E. Carretta, A. Bragaglia, R. G. Gratton, S. Lucatello, M. Bellazzini, G. Catanzaro, F. Leone, Y. Momany, G. Piotto, and V. D'Orazi. Detailed abundances of a large sample of giant stars in M 54 and in the Sagittarius nucleus. A&A, 520:A95, September 2010. doi: 10.1051/0004-6361/201014924.

[373] A. McWilliam, G. Wallerstein, and M. Mottini. Chemistry of the Sagittarius Dwarf Galaxy: A Top-light Initial Mass Function, Outflows, and the R-process. ApJ, 778:149, December 2013. doi: 10.1088/0004-637X/778/2/149.

[374] S. Hasselquist, M. Shetrone, V. Smith, J. Holtzman, A. McWilliam, J. G. Fernández-Trincado, T. C. Beers, S. R. Majewski, D. L. Nidever, B. Tang, P. B. Tissera, E. Fernández Alvar, C. Allende Prieto, A. Almeida, B. Anguiano, G. Battaglia, L. Carigi, G. Delgado Inglada, P. Frinchaboy, D. A. García-Hernández, D. Geisler, D. Minniti, V. M. Placco, M. Schultheis, J. Sobeck, and S. Villanova. APOGEE Chemical Abundances of the Sagittarius Dwarf Galaxy. ApJ, 845:162, August 2017. doi: 10.3847/1538-4357/aa7ddc.

[375] A. Mucciarelli, M. Bellazzini, R. Ibata, D. Romano, S. C. Chapman, and L. Monaco. Chemical abundances in the nucleus of the Sagittarius dwarf spheroidal galaxy. A&A, 605:A46, September 2017. doi: 10.1051/0004-6361/201730707.

[376] A. Kunder and B. Chaboyer. Distance to the Sagittarius Dwarf Galaxy Using Macho Project RR Lyrae Stars. AJ, 137:4478–4486, May 2009. doi: 10.1088/0004-6256/137/5/4478.

[377] Gaia Collaboration, A. Helmi, F. van Leeuwen, P. J. McMillan, D. Massari, T. Antoja, A. C. Robin, L. Lindegren, U. Bastian, F. Arenou, and et al. Gaia Data Release 2. Kinematics of globular clusters and dwarf galaxies around the Milky Way. A&A, 616:A12, August 2018. doi: 10.1051/0004-6361/201832698.

[378] S. C. Keller, Skymapper Team, and Aegis Team. SkyMapper and Galactic Archaeology. In W. Aoki, M. Ishigaki, T. Suda, T. Tsujimoto, and N. Arimoto, editors, *Galactic Archaeology: Near-Field Cosmology and the Formation of the Milky Way*, volume 458 of *Astronomical Society of the Pacific Conference Series*, page 409, August 2012.

[379] S. W. Campbell, B. T. MacLean, V. D'Orazi, L. Casagrande, G. M. de Silva, D. Yong, P. L. Cottrell, and J. C. Lattanzio. NGC 6752 AGB stars revisited. I. Improved AGB temperatures remove apparent overionisation of Fe I. A&A, 605:A98, September 2017. doi: 10.1051/0004-6361/201731101.

[380] A. Koch and A. McWilliam. A Differential Chemical Element Analysis of the Metal-poor Globular Cluster NGC 6397. AJ, 142:63, August 2011. doi: 10.1088/0004-6256/142/2/63.

[381] S. C. Trager, I. R. King, and S. Djorgovski. Catalogue of Galactic globular-cluster surface-brightness profiles. AJ, 109:218–241, January 1995. doi: 10.1086/117268.

[382] J. L. Tonry, C. W. Stubbs, K. R. Lykke, P. Doherty, I. S. Shivvers, W. S. Burgett, K. C. Chambers, K. W. Hodapp, N. Kaiser, R.-P. Kudritzki, E. A. Magnier, J. S. Morgan, P. A. Price, and R. J. Wainscoat. The Pan-STARRS1 Photometric System. ApJ, 750:99, May 2012. doi: 10.1088/0004-637X/750/2/99.

[383] Y. S. Lee, T. C. Beers, T. Sivarani, C. Allende Prieto, L. Koesterke, R. Wilhelm, P. Re Fiorentin, C. A. L. Bailer-Jones, J. E. Norris, C. M. Rockosi, B. Yanny, H. J. Newberg, K. R. Covey, H.-T. Zhang, and A.-L. Luo. The SEGUE Stellar Parameter Pipeline. I. Description and Comparison of Individual Methods. AJ, 136:2022–2049, November 2008. doi: 10.1088/0004-6256/136/5/2022.

[384] A. J. Pickles. A Stellar Spectral Flux Library: 1150-25000 rA. PASP, 110:863–878, July 1998. doi: 10.1086/316197.

[385] F. Castelli and R. L. Kurucz. New Grids of ATLAS9 Model Atmospheres. *arXiv Astrophysics e-prints*, May 2004.

[386] Daniela Carollo, Timothy C. Beers, Jo Bovy, Thirupathi Sivarani, John E. Norris, Ken C. Freeman, Wako Aoki, Young Sun Lee, and Catherine R. Kennedy. Carbon-enhanced Metal-poor Stars in the Inner and Outer Halo Components of the Milky Way. ApJ, 744(2):195, January 2012. doi: 10.1088/0004-637X/744/2/195.

[387] L. M. Howes, A. R. Casey, M. Asplund, S. C. Keller, D. Yong, D. M. Nataf, R. Poleski, K. Lind, C. Kobayashi, C. I. Owen, M. Ness, M. S. Bessell, G. S. da Costa, B. P. Schmidt, P. Tisserand, A. Udalski, M. K. Szymański, I. Soszyński, G. Pietrzyński, K. Ulaczyk, Ł. Wyrzykowski, P. Pietrukowicz, J. Skowron, S. Kozłowski, and P. Mróz. Extremely metal-poor stars from the cosmic dawn in the bulge of the Milky Way. Nature, 527:484–487, November 2015. doi: 10.1038/nature15747.

[388] A. Koch, A. McWilliam, G. W. Preston, and I. B. Thompson. Metal-poor stars towards the Galactic bulge: A population potpourri. A&A, 587:A124, March 2016. doi: 10.1051/0004-6361/201527413.

[389] N. Tominaga, H. Umeda, and K. Nomoto. Supernova Nucleosynthesis in Population III 13-50 M_{solar} Stars and Abundance Patterns of Extremely Metal-poor Stars. ApJ, 660:516–540, May 2007. doi: 10.1086/513063.

[390] Anirudh Chiti, Kylie Y. Hansen, and Anna Frebel. Discovery of 18 Stars with -3.10 < [Fe/H] < -1.45 in the Sagittarius Dwarf Galaxy. ApJ, 901(2):164, October 2020. doi: 10.3847/1538-4357/abb1ae.

[391] Alis J. Deason, Yao-Yuan Mao, and Risa H. Wechsler. The Eating Habits of Milky Way-mass Halos: Destroyed Dwarf Satellites and the Metallicity Distribution of Accreted Stars. ApJ, 821(1):5, April 2016. doi: 10.3847/0004-637X/821/1/5.

[392] Kaley Brauer, Alexander P. Ji, Anna Frebel, Gregory A. Dooley, Facundo A. Gómez, and Brian W. O'Shea. The Origin of r-process Enhanced Metal-poor Halo Stars In Now-destroyed Ultra-faint Dwarf Galaxies. ApJ, 871(2):247, February 2019. doi: 10.3847/1538-4357/aafafb.

[393] Matthew D. Shetrone, Patrick Côté, and W. L. W. Sargent. Abundance Patterns in the Draco, Sextans, and Ursa Minor Dwarf Spheroidal Galaxies. ApJ, 548(2):592–608, February 2001. doi: 10.1086/319022.

[394] Jon. P. Fulbright, R. Michael Rich, and Sandra Castro. Draco 119: A Remarkable Heavy-Element-deficient Giant. ApJ, 612(1):447–453, September 2004. doi: 10.1086/421712.

[395] W. Aoki, N. Arimoto, K. Sadakane, E. Tolstoy, G. Battaglia, P. Jablonka, M. Shetrone, B. Letarte, M. Irwin, V. Hill, P. Francois, K. Venn, F. Primas, A. Helmi, A. Kaufer, M. Tafelmeyer, T. Szeifert, and C. Babusiaux. Chemical composition of extremely metal-poor stars in the Sextans dwarf spheroidal galaxy. A&A, 502(2):569–578, August 2009. doi: 10.1051/0004-6361/200911959.

[396] M. Aoki, W. Aoki, and P. François. Chemical abundance analysis of extremely metal-poor stars in the Sextans dwarf spheroidal galaxy. A&A, 636:A111, April 2020. doi: 10.1051/0004-6361/201936535.

[397] Uğur Ural, Gabriele Cescutti, Andreas Koch, Jan Kleyna, Sofia Feltzing, and Mark I. Wilkinson. An inefficient dwarf: chemical abundances and the evolution of the Ursa Minor dwarf spheroidal galaxy. MNRAS, 449(1):761–770, May 2015. doi: 10.1093/mnras/stv294.

[398] R. Theler, P. Jablonka, R. Lucchesi, C. Lardo, P. North, M. Irwin, G. Battaglia, V. Hill, E. Tolstoy, K. Venn, A. Helmi, A. Kaufer, F. Primas, and M. Shetrone. The chemical evolution of the dwarf Spheroidal galaxy Sextans. *arXiv e-prints*, art. arXiv:1911.08627, November 2019.

[399] Rodrigo A. Ibata, Gerard Gilmore, and Michael J. Irwin. Sagittarius: the nearest dwarf galaxy. MNRAS, 277(3):781–800, December 1995. doi: 10.1093/mnras/277.3.781.

[400] Eugene Vasiliev and Vasily Belokurov. The last breath of the Sagittarius dSph. *arXiv e-prints*, art. arXiv:2006.02929, June 2020.

[401] J. D. Simon, A. Drlica-Wagner, T. S. Li, B. Nord, M. Geha, K. Bechtol, E. Balbinot, E. Buckley-Geer, H. Lin, J. Marshall, B. Santiago, L. Strigari, M. Wang, R. H. Wechsler, B. Yanny, T. Abbott, A. H. Bauer, G. M. Bernstein, E. Bertin, D. Brooks, D. L. Burke, D. Capozzi, A. Carnero Rosell, M. Carrasco Kind, C. B. D'Andrea, L. N. da Costa, D. L. DePoy, S. Desai, H. T. Diehl, S. Dodelson, C. E. Cunha, J. Estrada, A. E. Evrard, A. Fausti Neto, E. Fernandez, D. A. Finley, B. Flaugher, J. Frieman, E. Gaztanaga, D. Gerdes, D. Gruen, R. A. Gruendl, K. Honscheid, D. James, S. Kent, K. Kuehn, N. Kuropatkin, O. Lahav, M. A. G. Maia, M. March, P. Martini, C. J. Miller, R. Miquel, R. Ogando, A. K. Romer, A. Roodman, E. S. Rykoff, M. Sako, E. Sanchez, M. Schubnell, I. Sevilla, R. C. Smith, M. Soares-Santos, F. Sobreira, E. Suchyta, M. E. C. Swanson, G. Tarle, J. Thaler, D. Tucker, V. Vikram, A. R. Walker, W. Wester, and DES Collaboration. Stellar Kinematics and Metallicities in the Ultra-faint Dwarf Galaxy Reticulum II. ApJ, 808(1):95, July 2015. doi: 10.1088/0004-637X/808/1/95.

[402] Matthew G. Walker, Edward W. Olszewski, and Mario Mateo. Bayesian analysis of resolved stellar spectra: application to MMT/Hectochelle observations of the Draco dwarf spheroidal. MNRAS, 448(3):2717–2732, April 2015. doi: 10.1093/mnras/stv099.

[403] T. J. L. de Boer, V. Belokurov, and S. Koposov. The star formation history of the Sagittarius stream. MNRAS, 451(4):3489–3503, August 2015. doi: 10.1093/mnras/stv946.

[404] Louise M. Howes, Martin Asplund, Stefan C. Keller, Andrew R. Casey, David Yong, Karin Lind, Anna Frebel, Austin Hays, Alan Alves-Brito, Michael S. Bessell, Luca Casagrande, Anna F. Marino, David M. Nataf, Christopher I. Owen, Gary S. Da Costa, Brian P. Schmidt, and Patrick Tisserand. The EMBLA survey - metal-poor stars in the Galactic bulge. MNRAS, 460(1):884–901, July 2016. doi: 10.1093/mnras/stw1004.

[405] Steven R. Majewski, M. F. Skrutskie, Martin D. Weinberg, and James C. Ostheimer. A Two Micron All Sky Survey View of the Sagittarius Dwarf Galaxy. I. Morphology of the Sagittarius Core and Tidal Arms. ApJ, 599(2):1082–1115, December 2003. doi: 10.1086/379504.

[406] Eline Tolstoy, M. J. Irwin, A. Helmi, G. Battaglia, P. Jablonka, V. Hill, K. A. Venn, M. D. Shetrone, B. Letarte, A. A. Cole, F. Primas, P. Francois, N. Arimoto, K. Sadakane, A. Kaufer, T. Szeifert, and T. Abel. Two Distinct Ancient Components in the Sculptor Dwarf Spheroidal Galaxy: First Results from the Dwarf Abundances and Radial Velocities Team. ApJ, 617(2):L119–L122, December 2004. doi: 10.1086/427388.

[407] Christopher A. Onken, Christian Wolf, Michael S. Bessell, Seo-Won Chang, Gary S. Da Costa, Lance C. Luvaul, Dougal Mackey, Brian P. Schmidt, and Li Shao. SkyMapper Southern Survey: Second data release (DR2). PASA, 36: e033, August 2019. doi: 10.1017/pasa.2019.27.

[408] Carlos Allende Prieto, Timothy C. Beers, Ronald Wilhelm, Heidi Jo Newberg, Constance M. Rockosi, Brian Yanny, and Young Sun Lee. A Spectroscopic Study of the Ancient Milky Way: F- and G-Type Stars in the Third Data Release of the Sloan Digital Sky Survey. ApJ, 636(2):804–820, January 2006. doi: 10.1086/498131.

[409] H. E. Bond. Where is population III ? ApJ, 248:606–611, September 1981. doi: 10.1086/159186.

[410] J. N. Bahcall and R. M. Soneira. The universe at faint magnitudes. I. Models for the Galaxy and the predicted star counts. ApJS, 44:73–110, September 1980. doi: 10.1086/190685.

[411] F. D. A. Hartwick. The Chemical Evolution of the Galactic Halo. ApJ, 209: 418–423, October 1976. doi: 10.1086/154735.

[412] Sean G. Ryan and John E. Norris. Subdwarf Studies. III. The Halo Metallicity Distribution. AJ, 101:1865–1878, May 1991. doi: 10.1086/115812.

[413] N. Christlieb, T. Schörck, A. Frebel, T. C. Beers, L. Wisotzki, and D. Reimers. The stellar content of the Hamburg/ESO survey. IV. Selection of candidate metal-poor stars. A&A, 484(3):721–732, June 2008. doi: 10.1051/0004-6361: 20078748.

[414] Brian Yanny, Constance Rockosi, Heidi Jo Newberg, Gillian R. Knapp, Jennifer K. Adelman-McCarthy, Bonnie Alcorn, Sahar Allam, Carlos Allende Prieto, Deokkeun An, Kurt S. J. Anderson, Scott Anderson, Coryn A. L. Bailer-Jones, Steve Bastian, Timothy C. Beers, Eric Bell, Vasily Belokurov, Dmitry Bizyaev, Norm Blythe, John J. Bochanski, William N. Boroski, Jarle Brinchmann, J. Brinkmann, Howard Brewington, Larry Carey, Kyle M. Cudworth, Michael Evans, N. W. Evans, Evalyn Gates, B. T. Gänsicke, Bruce Gillespie, Gerald Gilmore, Ada Nebot Gomez-Moran, Eva K. Grebel, Jim Greenwell, James E. Gunn, Cathy Jordan, Wendell Jordan, Paul Harding, Hugh Harris, John S. Hendry, Diana Holder, Inese I. Ivans, Željko Ivezič, Sebastian Jester, Jennifer A. Johnson, Stephen M. Kent, Scot Kleinman, Alexei Kniazev, Jurek Krzesinski, Richard Kron, Nikolay Kuropatkin, Svetlana Lebedeva, Young Sun Lee, R. French Leger, Sébastien Lépine, Steve Levine, Huan Lin, Daniel C. Long, Craig Loomis, Robert Lupton, Olena Malanushenko, Viktor Malanushenko, Bruce Margon, David Martinez-Delgado, Peregrine McGehee, Dave Monet, Heather L. Morrison, Jeffrey A. Munn, Jr. Neilsen, Eric H., Atsuko Nitta, John E. Norris, Dan Oravetz, Russell Owen, Nikhil Padmanabhan, Kaike Pan, R. S. Peterson, Jeffrey R. Pier, Jared Platson, Paola Re Fiorentin,

Gordon T. Richards, Hans-Walter Rix, David J. Schlegel, Donald P. Schneider, Matthias R. Schreiber, Axel Schwope, Valena Sibley, Audrey Simmons, Stephanie A. Snedden, J. Allyn Smith, Larry Stark, Fritz Stauffer, M. Steinmetz, C. Stoughton, Mark SubbaRao, Alex Szalay, Paula Szkody, Aniruddha R. Thakar, Thirupathi Sivarani, Douglas Tucker, Alan Uomoto, Dan Vanden Berk, Simon Vidrih, Yogesh Wadadekar, Shannon Watters, Ron Wilhelm, Rosemary F. G. Wyse, Jean Yarger, and Dan Zucker. SEGUE: A Spectroscopic Survey of 240,000 Stars with g = 14-20. AJ, 137(5):4377–4399, May 2009. doi: 10.1088/0004-6256/137/5/4377.

[415] G. Cordoni, G. S. Da Costa, D. Yong, A. D. Mackey, A. F. Marino, S. Monty, T. Nordlander, J. E. Norris, M. Asplund, M. S. Bessell, A. R. Casey, A. Frebel, K. Lind, S. J. Murphy, B. P. Schmidt, X. D. Gao, T. Xylakis-Dornbusch, A. M. Amarsi, and A. P. Milone. Exploring the Galaxy's halo and very metal-weak thick disk with SkyMapper and Gaia DR2. MNRAS, November 2020. doi: 10.1093/mnras/staa3417.

[416] Y. Huang, B. Q. Chen, H. B. Yuan, H. W. Zhang, M. S. Xiang, C. Wang, H. F. Wang, C. Wolf, G. C. Liu, and X. W. Liu. Milky Way Tomography with the SkyMapper Southern Survey. I. Atmospheric Parameters and Distances of One Million Red Giants. ApJS, 243(1):7, July 2019. doi: 10.3847/1538-4365/ab1f72.

[417] Anke Arentsen, Else Starkenburg, Nicolas F. Martin, David S. Aguado, Daniel B. Zucker, Carlos Allende Prieto, Vanessa Hill, Kim A. Venn, Raymond G. Carlberg, Jonay I. González Hernández, Lyudmila I. Mashonkina, Julio F. Navarro, Rubén Sánchez-Janssen, Mathias Schultheis, Guillaume F. Thomas, Kris Youakim, Geraint F. Lewis, Jeffrey D. Simpson, Zhen Wan, Roger E. Cohen, Doug Geisler, and Julia E. O'Connell. The Pristine Inner Galaxy Survey (PIGS) II: Uncovering the most metal-poor populations in the inner Milky Way. MNRAS, 496(4):4964–4978, July 2020. doi: 10.1093/mnras/staa1661.

[418] K. Youakim, E. Starkenburg, N. F. Martin, G. Matijevič, D. S. Aguado, C. Allende Prieto, A. Arentsen, P. Bonifacio, R. G. Carlberg, J. I. González Hernández, V. Hill, G. Kordopatis, C. Lardo, J. F. Navarro, P. Jablonka, R. Sánchez Janssen, F. Sestito, G. F. Thomas, and K. Venn. The Pristine Survey - VIII. The metallicity distribution function of the Milky Way halo down to the extremely metal-poor regime. MNRAS, 492(4):4986–5002, March 2020. doi: 10.1093/mnras/stz3619.

[419] Željko Ivezić, Branimir Sesar, Mario Jurić, Nicholas Bond, Julianne Dalcanton, Constance M. Rockosi, Brian Yanny, Heidi J. Newberg, Timothy C. Beers, Carlos Allende Prieto, Ron Wilhelm, Young Sun Lee, Thirupathi Sivarani, John E. Norris, Coryn A. L. Bailer-Jones, Paola Re Fiorentin, David Schlegel, Alan Uomoto, Robert H. Lupton, Gillian R. Knapp, James E. Gunn, Kevin R. Covey, J. Allyn Smith, Gajus Miknaitis, Mamoru Doi, Masayuki Tanaka, Masataka Fukugita, Steve Kent, Douglas Finkbeiner, Jeffrey A. Munn, Jeffrey R.

Pier, Tom Quinn, Suzanne Hawley, Scott Anderson, Furea Kiuchi, Alex Chen, James Bushong, Harkirat Sohi, Daryl Haggard, Amy Kimball, John Barentine, Howard Brewington, Mike Harvanek, Scott Kleinman, Jurek Krzesinski, Dan Long, Atsuko Nitta, Stephanie Snedden, Brian Lee, Hugh Harris, Jonathan Brinkmann, Donald P. Schneider, and Donald G. York. The Milky Way Tomography with SDSS. II. Stellar Metallicity. ApJ, 684(1):287–325, September 2008. doi: 10.1086/589678.

[420] Deokkeun An and Timothy C. Beers. A Blueprint for the Milky Way's Stellar Populations: The Power of Large Photometric and Astrometric Surveys. ApJ, 897(1):39, July 2020. doi: 10.3847/1538-4357/ab8d39.

[421] Adam Ginsburg, Brigitta M. Sipőcz, C. E. Brasseur, Philip S. Cowperthwaite, Matthew W. Craig, Christoph Deil, James Guillochon, Giannina Guzman, Simon Liedtke, Pey Lian Lim, Kelly E. Lockhart, Michael Mommert, Brett M. Morris, Henrik Norman, Madhura Parikh, Magnus V. Persson, Thomas P. Robitaille, Juan-Carlos Segovia, Leo P. Singer, Erik J. Tollerud, Miguel de Val-Borro, Ivan Valtchanov, Julien Woillez, Astroquery Collaboration, and a subset of astropy Collaboration. astroquery: An Astronomical Web-querying Package in Python. AJ, 157(3):98, March 2019. doi: 10.3847/1538-3881/aafc33.

[422] Michael R. Blanton, Matthew A. Bershady, Bela Abolfathi, Franco D. Albareti, Carlos Allende Prieto, Andres Almeida, Javier Alonso-García, Friedrich Anders, Scott F. Anderson, Brett Andrews, Erik Aquino-Ortíz, Alfonso Aragón-Salamanca, Maria Argudo-Fernández, Eric Armengaud, Eric Aubourg, Vladimir Avila-Reese, Carles Badenes, Stephen Bailey, Kathleen A. Barger, Jorge Barrera-Ballesteros, Curtis Bartosz, Dominic Bates, Falk Baumgarten, Julian Bautista, Rachael Beaton, Timothy C. Beers, Francesco Belfiore, Chad F. Bender, Andreas A. Berlind, Mariangela Bernardi, Florian Beutler, Jonathan C. Bird, Dmitry Bizyaev, Guillermo A. Blanc, Michael Blomqvist, Adam S. Bolton, Médéric Boquien, Jura Borissova, Remco van den Bosch, Jo Bovy, William N. Brandt, Jonathan Brinkmann, Joel R. Brownstein, Kevin Bundy, Adam J. Burgasser, Etienne Burtin, Nicolás G. Busca, Michele Cappellari, Maria Leticia Delgado Carigi, Joleen K. Carlberg, Aurelio Carnero Rosell, Ricardo Carrera, Nancy J. Chanover, Brian Cherinka, Edmond Cheung, Yilen Gómez Maqueo Chew, Cristina Chiappini, Peter Doohyun Choi, Drew Chojnowski, Chia-Hsun Chuang, Haeun Chung, Rafael Fernando Cirolini, Nicolas Clerc, Roger E. Cohen, Johan Comparat, Luiz da Costa, Marie-Claude Cousinou, Kevin Covey, Jeffrey D. Crane, Rupert A. C. Croft, Irene Cruz-Gonzalez, Daniel Garrido Cuadra, Katia Cunha, Guillermo J. Damke, Jeremy Darling, Roger Davies, Kyle Dawson, Axel de la Macorra, Flavia Dell'Agli, Nathan De Lee, Timothée Delubac, Francesco Di Mille, Aleks Diamond-Stanic, Mariana Cano-Díaz, John Donor, Juan José Downes, Niv Drory, Hélion du Mas des Bourboux, Christopher J. Duckworth, Tom Dwelly, Jamie Dyer, Garrett Ebelke, Arthur D. Eigenbrot, Daniel J. Eisenstein, Eric Emsellem, Mike Eracleous, Stephanie Escoffier, Michael L. Evans, Xiaohui Fan, Emma Fernández-Alvar,

J. G. Fernandez-Trincado, Diane K. Feuillet, Alexis Finoguenov, Scott W. Fleming, Andreu Font-Ribera, Alexander Fredrickson, Gordon Freischlad, Peter M. Frinchaboy, Carla E. Fuentes, Lluís Galbany, R. Garcia-Dias, D. A. García-Hernández, Patrick Gaulme, Doug Geisler, Joseph D. Gelfand, Héctor Gil-Marín, Bruce A. Gillespie, Daniel Goddard, Violeta Gonzalez-Perez, Kathleen Grabowski, Paul J. Green, Catherine J. Grier, James E. Gunn, Hong Guo, Julien Guy, Alex Hagen, ChangHoon Hahn, Matthew Hall, Paul Harding, Sten Hasselquist, Suzanne L. Hawley, Fred Hearty, Jonay I. Gonzalez Hernández, Shirley Ho, David W. Hogg, Kelly Holley-Bockelmann, Jon A. Holtzman, Parker H. Holzer, Joseph Huehnerhoff, Timothy A. Hutchinson, Ho Seong Hwang, Héctor J. Ibarra-Medel, Gabriele da Silva Ilha, Inese I. Ivans, KeShawn Ivory, Kelly Jackson, Trey W. Jensen, Jennifer A. Johnson, Amy Jones, Henrik Jönsson, Eric Jullo, Vikrant Kamble, Karen Kinemuchi, David Kirkby, Francisco-Shu Kitaura, Mark Klaene, Gillian R. Knapp, Jean-Paul Kneib, Juna A. Kollmeier, Ivan Lacerna, Richard R. Lane, Dustin Lang, David R. Law, Daniel Lazarz, Youngbae Lee, Jean-Marc Le Goff, Fu-Heng Liang, Cheng Li, Hongyu Li, Jianhui Lian, Marcos Lima, Lihwai Lin, Yen-Ting Lin, Sara Bertran de Lis, Chao Liu, Miguel Angel C. de Icaza Lizaola, Dan Long, Sara Lucatello, Britt Lundgren, Nicholas K. MacDonald, Alice Deconto Machado, Chelsea L. MacLeod, Suvrath Mahadevan, Marcio Antonio Geimba Maia, Roberto Maiolino, Steven R. Majewski, Elena Malanushenko, Viktor Malanushenko, Arturo Manchado, Shude Mao, Claudia Maraston, Rui Marques-Chaves, Thomas Masseron, Karen L. Masters, Cameron K. McBride, Richard M. McDermid, Brianne McGrath, Ian D. McGreer, Nicolás Medina Peña, Matthew Melendez, Andrea Merloni, Michael R. Merrifield, Szabolcs Meszaros, Andres Meza, Ivan Minchev, Dante Minniti, Takamitsu Miyaji, Surhud More, John Mulchaey, Francisco Müller-Sánchez, Demitri Muna, Ricardo R. Munoz, Adam D. Myers, Preethi Nair, Kirpal Nandra, Janaina Correa do Nascimento, Alenka Negrete, Melissa Ness, Jeffrey A. Newman, Robert C. Nichol, David L. Nidever, Christian Nitschelm, Pierros Ntelis, Julia E. O'Connell, Ryan J. Oelkers, Audrey Oravetz, Daniel Oravetz, Zach Pace, Nelson Padilla, Nathalie Palanque-Delabrouille, Pedro Alonso Palicio, Kaike Pan, John K. Parejko, Taniya Parikh, Isabelle Pâris, Changbom Park, Alim Y. Patten, Sebastien Peirani, Marcos Pellejero-Ibanez, Samantha Penny, Will J. Percival, Ismael Perez-Fournon, Patrick Petitjean, Matthew M. Pieri, Marc Pinsonneault, Alice Pisani, Radosław Poleski, Francisco Prada, Abhishek Prakash, Anna Bárbara de Andrade Queiroz, M. Jordan Raddick, Anand Raichoor, Sand ro Barboza Rembold, Hannah Richstein, Rogemar A. Riffel, Rogério Riffel, Hans-Walter Rix, Annie C. Robin, Constance M. Rockosi, Sergio Rodríguez-Torres, A. Roman-Lopes, Carlos Román-Zúñiga, Margarita Rosado, Ashley J. Ross, Graziano Rossi, John Ruan, Rossana Ruggeri, Eli S. Rykoff, Salvador Salazar-Albornoz, Mara Salvato, Ariel G. Sánchez, D. S. Aguado, José R. Sánchez-Gallego, Felipe A. Santana, Basílio Xavier Santiago, Conor Sayres, Ricardo P. Schiavon, Jaderson da Silva Schimoia, Edward F. Schlafly, David J. Schlegel, Donald P. Schneider, Mathias Schultheis, William J.

Schuster, Axel Schwope, Hee-Jong Seo, Zhengyi Shao, Shiyin Shen, Matthew Shetrone, Michael Shull, Joshua D. Simon, Danielle Skinner, M. F. Skrutskie, Anže Slosar, Verne V. Smith, Jennifer S. Sobeck, Flavia Sobreira, Garrett Somers, Diogo Souto, David V. Stark, Keivan Stassun, Fritz Stauffer, Matthias Steinmetz, Thaisa Storchi-Bergmann, Alina Streblyanska, Guy S. Stringfellow, Genaro Suárez, Jing Sun, Nao Suzuki, Laszlo Szigeti, Manuchehr Taghizadeh-Popp, Baitian Tang, Charling Tao, Jamie Tayar, Mita Tembe, Johanna Teske, Aniruddha R. Thakar, Daniel Thomas, Benjamin A. Thompson, Jeremy L. Tinker, Patricia Tissera, Rita Tojeiro, Hector Hernandez Toledo, Sylvain de la Torre, Christy Tremonti, Nicholas W. Troup, Octavio Valenzuela, Inma Martinez Valpuesta, Jaime Vargas-González, Mariana Vargas-Magaña, Jose Alberto Vazquez, Sandro Villanova, M. Vivek, Nicole Vogt, David Wake, Rene Walterbos, Yuting Wang, Benjamin Alan Weaver, Anne-Marie Weijmans, David H. Weinberg, Kyle B. Westfall, David G. Whelan, Vivienne Wild, John Wilson, W. M. Wood-Vasey, Dominika Wylezalek, Ting Xiao, Renbin Yan, Meng Yang, Jason E. Ybarra, Christophe Yèche, Nadia Zakamska, Olga Zamora, Pauline Zarrouk, Gail Zasowski, Kai Zhang, Gong-Bo Zhao, Zheng Zheng, Zheng Zheng, Xu Zhou, Zhi-Min Zhou, Guangtun B. Zhu, Manuela Zoccali, and Hu Zou. Sloan Digital Sky Survey IV: Mapping the Milky Way, Nearby Galaxies, and the Distant Universe. AJ, 154(1):28, July 2017. doi: 10.3847/1538-3881/aa7567.

[423] Steven R. Majewski, Ricardo P. Schiavon, Peter M. Frinchaboy, Carlos Allende Prieto, Robert Barkhouser, Dmitry Bizyaev, Basil Blank, Sophia Brunner, Adam Burton, Ricardo Carrera, S. Drew Chojnowski, Kátia Cunha, Courtney Epstein, Greg Fitzgerald, Ana E. García Pérez, Fred R. Hearty, Chuck Henderson, Jon A. Holtzman, Jennifer A. Johnson, Charles R. Lam, James E. Lawler, Paul Maseman, Szabolcs Mészáros, Matthew Nelson, Duy Coung Nguyen, David L. Nidever, Marc Pinsonneault, Matthew Shetrone, Stephen Smee, Verne V. Smith, Todd Stolberg, Michael F. Skrutskie, Eric Walker, John C. Wilson, Gail Zasowski, Friedrich Anders, Sarbani Basu, Stephane Beland, Michael R. Blanton, Jo Bovy, Joel R. Brownstein, Joleen Carlberg, William Chaplin, Cristina Chiappini, Daniel J. Eisenstein, Yvonne Elsworth, Diane Feuillet, Scott W. Fleming, Jessica Galbraith-Frew, Rafael A. García, D. Aníbal García-Hernández, Bruce A. Gillespie, Léo Girardi, James E. Gunn, Sten Hasselquist, Michael R. Hayden, Saskia Hekker, Inese Ivans, Karen Kinemuchi, Mark Klaene, Suvrath Mahadevan, Savita Mathur, Benoît Mosser, Demitri Muna, Jeffrey A. Munn, Robert C. Nichol, Robert W. O'Connell, John K. Parejko, A. C. Robin, Helio Rocha-Pinto, Matthias Schultheis, Aldo M. Serenelli, Neville Shane, Victor Silva Aguirre, Jennifer S. Sobeck, Benjamin Thompson, Nicholas W. Troup, David H. Weinberg, and Olga Zamora. The Apache Point Observatory Galactic Evolution Experiment (APOGEE). AJ, 154(3):94, September 2017. doi: 10.3847/1538-3881/aa784d.

[424] Sven Buder, Sanjib Sharma, Janez Kos, Anish M. Amarsi, Thomas Nordlander, Karin Lind, Sarah L. Martell, Martin Asplund, Joss Bland-Hawthorn, An-

drew R. Casey, Gayandhi M. De Silva, Valentina D'Orazi, Ken C. Freeman, Michael R. Hayden, Geraint F. Lewis, Jane Lin, Katharine. J. Schlesinger, Jeffrey D. Simpson, Dennis Stello, Daniel B. Zucker, Tomaz Zwitter, Kevin L. Beeson, Tobias Buck, Luca Casagrande, Jake T. Clark, Klemen Cotar, Gary S. Da Costa, Richard de Grijs, Diane Feuillet, Jonathan Horner, Shourya Khanna, Prajwal R. Kafle, Fan Liu, Benjamin T. Montet, Govind Nandakumar, David M. Nataf, Melissa K. Ness, Lorenzo Spina, Gregor Traven, Thor Tepper-Garcia, Yuan-Sen Ting, Rok Vogrincic, Robert A. Wittenmyer, Marusa Zerjal, and the GALAH collaboration. The GALAH+ Survey: Third Data Release. *arXiv e-prints*, art. arXiv:2011.02505, November 2020.

[425] G. Zhao, Y.-Q. Chen, J.-R. Shi, Y.-C. Liang, J.-L. Hou, L. Chen, H.-W. Zhang, and A.-G. Li. Stellar Abundance and Galactic Chemical Evolution through LAMOST Spectroscopic Survey. Chinese J. Astron. Astrophys., 6:265–280, June 2006. doi: 10.1088/1009-9271/6/3/01.

[426] G. Zhao, Y.-H. Zhao, Y.-Q. Chu, Y.-P. Jing, and L.-C. Deng. LAMOST spectral survey An overview. *Research in Astronomy and Astrophysics*, 12:723–734, July 2012. doi: 10.1088/1674-4527/12/7/002.

[427] X.-Q. Cui, Y.-H. Zhao, Y.-Q. Chu, G.-P. Li, Q. Li, L.-P. Zhang, H.-J. Su, Z.-Q. Yao, Y.-N. Wang, X.-Z. Xing, X.-N. Li, Y.-T. Zhu, G. Wang, B.-Z. Gu, A.-L. Luo, X.-Q. Xu, Z.-C. Zhang, G.-R. Liu, H.-T. Zhang, D.-H. Yang, S.-Y. Cao, H.-Y. Chen, J.-J. Chen, K.-X. Chen, Y. Chen, J.-R. Chu, L. Feng, X.-F. Gong, Y.-H. Hou, H.-Z. Hu, N.-S. Hu, Z.-W. Hu, L. Jia, F.-H. Jiang, X. Jiang, Z.-B. Jiang, G. Jin, A.-H. Li, Y. Li, Y.-P. Li, G.-Q. Liu, Z.-G. Liu, W.-Z. Lu, Y.-D. Mao, L. Men, Y.-J. Qi, Z.-X. Qi, H.-M. Shi, Z.-H. Tang, Q.-S. Tao, D.-Q. Wang, D. Wang, G.-M. Wang, H. Wang, J.-N. Wang, J. Wang, J.-L. Wang, J.-P. Wang, L. Wang, S.-Q. Wang, Y. Wang, Y.-F. Wang, L.-Z. Xu, Y. Xu, S.-H. Yang, Y. Yu, H. Yuan, X.-Y. Yuan, C. Zhai, J. Zhang, Y.-X. Zhang, Y. Zhang, M. Zhao, F. Zhou, G.-H. Zhou, J. Zhu, and S.-C. Zou. The Large Sky Area Multi-Object Fiber Spectroscopic Telescope (LAMOST). *Research in Astronomy and Astrophysics*, 12:1197–1242, September 2012. doi: 10.1088/1674-4527/12/9/003.

[428] M. B. Taylor. TOPCAT & STIL: Starlink Table/VOTable Processing Software. In P. Shopbell, M. Britton, and R. Ebert, editors, *Astronomical Data Analysis Software and Systems XIV*, volume 347 of *Astronomical Society of the Pacific Conference Series*, page 29, December 2005.

[429] Ana E. García Pérez, Carlos Allende Prieto, Jon A. Holtzman, Matthew Shetrone, Szabolcs Mészáros, Dmitry Bizyaev, Ricardo Carrera, Katia Cunha, D. A. García-Hernández, Jennifer A. Johnson, Steven R. Majewski, David L. Nidever, Ricardo P. Schiavon, Neville Shane, Verne V. Smith, Jennifer Sobeck, Nicholas Troup, Olga Zamora, David H. Weinberg, Jo Bovy, Daniel J. Eisenstein, Diane Feuillet, Peter M. Frinchaboy, Michael R. Hayden, Fred R. Hearty,

Duy C. Nguyen, Robert W. O'Connell, Marc H. Pinsonneault, John C. Wilson, and Gail Zasowski. ASPCAP: The APOGEE Stellar Parameter and Chemical Abundances Pipeline. AJ, 151(6):144, June 2016. doi: 10.3847/0004-6256/151/6/144.

[430] David Yong, John E. Norris, M. S. Bessell, N. Christlieb, M. Asplund, Timothy C. Beers, P. S. Barklem, Anna Frebel, and S. G. Ryan. The Most Metal-poor Stars. II. Chemical Abundances of 190 Metal-poor Stars Including 10 New Stars with [Fe/H] <= -3.5. ApJ, 762(1):26, January 2013. doi: 10.1088/0004-637X/762/1/26.

[431] L. Duong, K. C. Freeman, M. Asplund, L. Casagrande, S. Buder, K. Lind, M. Ness, J. Bland-Hawthorn, G. M. De Silva, V. D'Orazi, J. Kos, G. F. Lewis, J. Lin, S. L. Martell, K. Schlesinger, S. Sharma, J. D. Simpson, D. B. Zucker, T. Zwitter, B. Anguiano, G. S. Da Costa, E. Hyde, J. Horner, P. R. Kafle, D. M. Nataf, W. Reid, D. Stello, Y. S. Ting, and R. F. G. Wyse. The GALAH survey: properties of the Galactic disc(s) in the solar neighbourhood. MNRAS, 476(4):5216–5232, June 2018. doi: 10.1093/mnras/sty525.

[432] Daniela Carollo, Timothy C. Beers, Young Sun Lee, Masashi Chiba, John E. Norris, Ronald Wilhelm, Thirupathi Sivarani, Brian Marsteller, Jeffrey A. Munn, Coryn A. L. Bailer-Jones, Paola Re Fiorentin, and Donald G. York. Two stellar components in the halo of the Milky Way. Nature, 450(7172):1020–1025, December 2007. doi: 10.1038/nature06460.

[433] James S. Bullock and Kathryn V. Johnston. Tracing Galaxy Formation with Stellar Halos. I. Methods. ApJ, 635(2):931–949, December 2005. doi: 10.1086/497422.

[434] V. Belokurov, D. Erkal, N. W. Evans, S. E. Koposov, and A. J. Deason. Co-formation of the disc and the stellar halo. MNRAS, 478(1):611–619, July 2018. doi: 10.1093/mnras/sty982.

[435] G. C. Myeong, E. Vasiliev, G. Iorio, N. W. Evans, and V. Belokurov. Evidence for two early accretion events that built the Milky Way stellar halo. MNRAS, 488(1):1235–1247, September 2019. doi: 10.1093/mnras/stz1770.

[436] Zhen Yuan, G. C. Myeong, Timothy C. Beers, N. W. Evans, Young Sun Lee, Projjwal Banerjee, Dmitrii Gudin, Kohei Hattori, Haining Li, Tadafumi Matsuno, Vinicius M. Placco, M. C. Smith, Devin D. Whitten, and Gang Zhao. Dynamical Relics of the Ancient Galactic Halo. ApJ, 891(1):39, March 2020. doi: 10.3847/1538-4357/ab6ef7.

[437] Gang Zhao, Yong-Heng Zhao, Yao-Quan Chu, Yi-Peng Jing, and Li-Cai Deng. LAMOST spectral survey — An overview. *Research in Astronomy and Astrophysics*, 12(7):723–734, July 2012. doi: 10.1088/1674-4527/12/7/002.

[438] Matthias Steinmetz, Guillaume Guiglion, Paul J. McMillan, Gal Matijevič, Harry Enke, Georges Kordopatis, Tomaž Zwitter, Marica Valentini, Cristina Chiappini, Luca Casagrande, Jennifer Wojno, Borja Anguiano, Olivier Bienaymé, Albert Bijaoui, James Binney, Donna Burton, Paul Cass, Patrick de Laverny, Kristin Fiegert, Kenneth Freeman, Jon P. Fulbright, Brad K. Gibson, Gerard Gilmore, Eva K. Grebel, Amina Helmi, Andrea Kunder, Ulisse Munari, Julio F. Navarro, Quentin Parker, Gregory R. Ruchti, Alejandra Recio-Blanco, Warren Reid, George M. Seabroke, Alessandro Siviero, Arnaud Siebert, Milorad Stupar, Fred Watson, Mary E. K. Williams, Rosemary F. G. Wyse, Friedrich Anders, Teresa Antoja, Danijela Birko, Joss Bland-Hawthorn, Diego Bossini, Rafael A. García, Ismael Carrillo, William J. Chaplin, Yvonne Elsworth, Benoit Famaey, Ortwin Gerhard, Paula Jofre, Andreas Just, Savita Mathur, Andrea Miglio, Ivan Minchev, Giacomo Monari, Benoit Mosser, Andreas Ritter, Thaise S. Rodrigues, Ralf-Dieter Scholz, Sanjib Sharma, Kseniia Sysoliatina, and RAVE Collaboration. The Sixth Data Release of the Radial Velocity Experiment (RAVE). II. Stellar Atmospheric Parameters, Chemical Abundances, and Distances. AJ, 160(2):83, August 2020. doi: 10.3847/1538-3881/ab9ab8.

[439] G. M. De Silva, K. C. Freeman, J. Bland-Hawthorn, S. Martell, E. Wylie de Boer, M. Asplund, S. Keller, S. Sharma, D. B. Zucker, T. Zwitter, B. Anguiano, C. Bacigalupo, D. Bayliss, M. A. Beavis, M. Bergemann, S. Campbell, R. Cannon, D. Carollo, L. Casagrande, A. R. Casey, G. Da Costa, V. D'Orazi, A. Dotter, L. Duong, A. Heger, M. J. Ireland, P. R. Kafle, J. Kos, J. Lattanzio, G. F. Lewis, J. Lin, K. Lind, U. Munari, D. M. Nataf, S. O'Toole, Q. Parker, W. Reid, K. J. Schlesinger, A. Sheinis, J. D. Simpson, D. Stello, Y. S. Ting, G. Traven, F. Watson, R. Wittenmyer, D. Yong, and M. Žerjal. The GALAH survey: scientific motivation. MNRAS, 449(3):2604–2617, May 2015. doi: 10.1093/mnras/stv327.

[440] Mohammad K. Mardini, Vinicius M. Placco, Ali Taani, Haining Li, and Gang Zhao. Metal-poor Stars Observed with the Automated Planet Finder Telescope. II. Chemodynamical Analysis of Six Low-metallicity Stars in the Halo System of the Milky Way. ApJ, 882(1):27, Sep 2019. doi: 10.3847/1538-4357/ab3047.

[441] Gravity Collaboration, R. Abuter, A. Amorim, N. Anugu, M. Bauböck, M. Benisty, J. P. Berger, N. Blind, H. Bonnet, W. Brandner, A. Buron, C. Collin, F. Chapron, Y. Clénet, V. Coudé Du Foresto, P. T. de Zeeuw, C. Deen, F. Delplancke-Ströbele, R. Dembet, J. Dexter, G. Duvert, A. Eckart, F. Eisenhauer, G. Finger, N. M. Förster Schreiber, P. Fédou, P. Garcia, R. Garcia Lopez, F. Gao, E. Gendron, R. Genzel, S. Gillessen, P. Gordo, M. Habibi, X. Haubois, M. Haug, F. Haußmann, Th. Henning, S. Hippler, M. Horrobin, Z. Hubert, N. Hubin, A. Jimenez Rosales, L. Jochum, K. Jocou, A. Kaufer, S. Kellner, S. Kendrew, P. Kervella, Y. Kok, M. Kulas, S. Lacour, V. Lapeyrère, B. Lazareff, J. B. Le Bouquin, P. Léna, M. Lippa, R. Lenzen, A. Mérand, E. Müler, U. Neumann, T. Ott, L. Palanca, T. Paumard, L. Pasquini, K. Perraut, G. Perrin, O. Pfuhl, P. M. Plewa, S. Rabien, A. Ramírez, J. Ramos,

C. Rau, G. Rodríguez-Coira, R. R. Rohloff, G. Rousset, J. Sanchez-Bermudez, S. Scheithauer, M. Schöller, N. Schuler, J. Spyromilio, O. Straub, C. Straubmeier, E. Sturm, L. J. Tacconi, K. R. W. Tristram, F. Vincent, S. von Fellenberg, I. Wank, I. Waisberg, F. Widmann, E. Wieprecht, M. Wiest, E. Wiezorrek, J. Woillez, S. Yazici, D. Ziegler, and G. Zins. Detection of the gravitational redshift in the orbit of the star S2 near the Galactic centre massive black hole. A&A, 615:L15, July 2018. doi: 10.1051/0004-6361/201833718.

[442] A. Clifford Cohen. *Truncated and Censored Samples: Theory and Applications*. Taylor & Francis Group, Boca Raton, 1991.

[443] T. Schörck, N. Christlieb, J. G. Cohen, T. C. Beers, S. Shectman, I. Thompson, A. McWilliam, M. S. Bessell, J. E. Norris, J. Meléndez, S. Ramírez, D. Haynes, P. Cass, M. Hartley, K. Russell, F. Watson, F. J. Zickgraf, B. Behnke, C. Fechner, B. Fuhrmeister, P. S. Barklem, B. Edvardsson, A. Frebel, L. Wisotzki, and D. Reimers. The stellar content of the Hamburg/ESO survey. V. The metallicity distribution function of the Galactic halo. A&A, 507(2):817–832, November 2009. doi: 10.1051/0004-6361/200810925.

[444] Deokkeun An, Timothy C. Beers, Rafael M. Santucci, Daniela Carollo, Vinicius M. Placco, Young Sun Lee, and Silvia Rossi. The Fractions of Inner- and Outer-halo Stars in the Local Volume. ApJ, 813(2):L28, November 2015. doi: 10.1088/2041-8205/813/2/L28.

[445] C. Allende Prieto, E. Fernández-Alvar, K. J. Schlesinger, Y. S. Lee, H. L. Morrison, D. P. Schneider, T. C. Beers, D. Bizyaev, G. Ebelke, E. Malanushenko, V. Malanushenko, D. Oravetz, K. Pan, A. Simmons, J. Simmerer, J. Sobeck, and A. C. Robin. Deep SDSS optical spectroscopy of distant halo stars. I. Atmospheric parameters and stellar metallicity distribution. A&A, 568:A7, August 2014. doi: 10.1051/0004-6361/201424053.